Tunable magnetic anisotropy and magnetotransport properties of epitaxial oxide ferromagnetic heterostructures

Inaugural - Dissertation zur

Erlangung des Doktorgrades

der Mathematisch - Naturwissenschaftlichen Fakultät

der Universität zu Köln

vorgelegt von
Lena Wysocki

aus Solingen

Köln, 2022

Diese Arbeit stellt eine von der mathematisch-naturwissenschaftlichen Fakultät der Universität zu Köln angenommene Dissertation dar.

Gutachter: Prof. Dr. Ir. Paul H. M. van Loosdrecht
Gutachterin: Prof. Dr. Kathrin Dörr
Vorsitzender der Prüfungskommission: Prof. Dr. Jan Jolie
Beisitzerin: Dr. Andrea Bliesener

Tag der mündlichen Prüfung: 21.06.2022

Contents

List of abbreviations

DMI	Dzyaloshinskii-Moriya interaction
DE	double exchange mechanism
PMA	perpendicular magnetic anisotropy
CMR	colossal magnetoresistance
AMR	anisotropic magnetoresistance
DWR	domain wall magnetoresistance
MIT	metal-to-insulator transition
MLs	monolayers
SRO	$SrRuO_3$
SIO	$SrIrO_3$
SZO	$SrZrO_3$
STO	$SrTiO_3$
LSAT	$(LaAlO_3)_{0.3}(Sr_2TaAlO_6)_{0.7}$
PLD	pulsed-laser deposition
KrF	krypton fluoride
PMMA	poly (methyl methacrylate)
RHEED	reflection high-energy electron diffraction
AFM	atomic force microscopy
MFM	magnetic force microscopy
SQUID	superconducting quantum interference device
p-MOKE	polar magneto-optical Kerr efffect
TEM	transmission electron microscopy

Part I

Introduction and fundamental concepts

Chapter 1

Introduction

Perovskite oxides exhibit a great diversity of functional properties ranging from insulating, semiconducting, metallic to superconducting, from ferro- to antiferromagnetism.[1–4]

They show colossal magnetoresistivity, multiferroicity, catalytic characteristics, and thermoelectricity.[1,2,4] These properties pave the way for their application in a variety of functional devices, for instance from the fields of magnetoelectronics, spintronics, or optoelectronics.[2,3] The common ABO_3 crystal structure and the corresponding lattice mismatch of typically a few percent enable the epitaxial stacking of dissimilar perovskite oxides with high interfacial quality.[1] Such epitaxial interfaces inherently break the inversion symmetry and can induce strain and charge transfer, modify the B-O-B angles and bond lengths, and result in A-site displacements.[1] These can thereby significantly alter the structural, electronic, and magnetic characteristics of the individual layers.[1] Additionally, new phenomena can emerge at these interfaces being absent in bare films, such as non-collinear magnetism, as it was stabilized for instance by charge transfer at the interface of $La_{2/3}Sr_{1/3}MnO_3$-$LaNiO_3$[5] or interfacial Dzyaloshinskii-Moriya interaction at $LaMnO_3$-$SrIrO_3$ interfaces.[6]

Thanks to the improvement of thin film deposition techniques and *in situ* growth monitoring possibilities, the growth of high quality epitaxial thin films and heterostructures with reproducible properties was achieved.[1]

The use of the materials in reliable devices can only be realized when the material characteristics are well understood and controllable.

In the focus of this thesis are the two perovskite oxides strontium ruthenate ($SrRuO_3$) and Ru-substituted strontium lanthanum manganite ($La_{0.67}Sr_{0.33}Ru_yMn_{1-y}O_3$), which are promising candidates to host magnetic skyrmions in epitaxial thin films and heterostructures.[7,8]

Due to their topological protection, the smallness, and the possibility of controlled creation and annihilation, magnetic skyrmions are considered as potential building blocks for future magnetic storage devices or reservoir computing.[9–12] In contrast to metallic multilayers where free electrons are typically strongly screened, the manipulation of magnetic skyrmions by electric fields is expected to function effectively in insulating or bad metallic all-oxide heterostructures.[13] Thus, the stabilization of skyrmions in perovskite oxide heterostructures is of great technological interest due to the potential of non-volatile magnetic storage devices with reduced power consumption but high information storage density.[9]

The itinerant $4d$ ferromagnet $SrRuO_3$, that has a remarkably large conductivity among the family of oxides, was recently studied extensively due to the proposal that nanometer-sized Néel skyrmions can form in ultrathin films or when it is interfaced with the strong spin-orbit coupling $SrIrO_3$.[7,13,14] Here, the existence of skyrmions in $SrRuO_3$ layers was primarily concluded from the observation of peculiar hump-like features in the Hall resistance loops. However, the existence of skyrmions in $SrRuO_3$-based heterostructures is still under debate and also addressed with original contributions within the framework of this thesis.

Mixed valence manganites show rich electric and magnetic phase diagrams upon temperature and composition on the A-site. Its spin polarization close to unity, the colossal magnetoresistance, and the ferromagnetic transition temperature above room temperature make $La_{0.67}Sr_{0.33}MnO_3$ (LSMO) a highly interesting material in the context of miniaturized spintronic applications.[4] Orbital, electronic, and lattice degree of freedom are strongly coupled, which offers the possibility to modify the magnetic and magnetotransport properties efficiently.[4] One example is the magnetic anisotropy in LSMO thin films or heterostructures, which can be tailored by variation of epitaxial strain, B-site substitution, or film thickness.[4,15] The realization of moderate perpendicular magnetic anisotropy is one of the key ingredients to stabilize magnetic skyrmions in magnetic multilayers. If the Dzyaloshinskii–Moriya interaction, generated at the interface of the magnetic thin film with a strong spin-orbit coupled layer, is of comparable strength with the Heisenberg exchange interaction in the ferromagnet and the magnetic anisotropy, non-trivial spin textures, such as magnetic skyrmions or chiral domain walls, might be stabilized.

Features mimicking a skyrmion-generated topological Hall effect were indeed observed in the Hall hysteresis loops of 30 nm thick $La_{0.7}Sr_{0.3}Mn_{0.95}Ru_{0.05}O_3$ films, deposited under compressive strain on LSAT(100).[8]

Motivated by this observation, the tailoring of the magnetic anisotropy in

$La_{0.7}Sr_{0.3}Mn_{1-y}Ru_yO_3$ thin films and its impact on the magnetotransport was studied by varying the film thickness in the scope of this dissertation.

The topic of magnetism in thin films is introduced by giving two examples of tuning knobs to tailor the magnetic state of epitaxial heterostructures: the magnetic anisotropy and the coupling between the individual magnetic layers (Chapter 2.1). Subsequently, most relevant magnetotransport phenomena that can be observed in magnetic conductors, such as the studied perovskite oxides, are presented. Since the focus of this thesis is on the magnetic and magnetotransport properties of epitaxial heterostructures based on the two ferromagnetic perovskite oxides $SrRuO_3$ and $La_{0.67}Sr_{0.33}Mn_{1-y}Ru_yO_3$, a short overview of the structural, magnetic and magnetotransport properties will be given in Chapter 2.2. The experimental methods that are most relevant in the framework of this thesis are presented in Chapter 3.

Motivated by the proposal of a skyrmion-generated topological Hall effect in $SrRuO_3$-$SrIrO_3$ bilayers, the real-space magnetic imaging was addressed in Chapter 4 by a magnetic force microscopy study combined with magnetotransport investigations of a capped $SrRuO_3$-$SrIrO_3$ bilayer and a bare $SrRuO_3$ reference thin film.

One motivation for the design of epitaxial oxide multilayers was to stabilize a skyrmion phase at elevated temperatures, as it was achieved in metallic multilayers due to dipolar interactions and interlayer exchange coupling.[16–19] The investigation of the type and strength of the magnetic interlayer coupling in $SrRuO_3$-based heterostructures is discussed in Chapter 5.

Unconventional features in the Hall resistance were recently taken as an experimental proof of skyrmion phases. The possible pitfall of such procedure motivated Chapter 6. The presented magnetotransport investigations of $SrRuO_3$-$SrIrO_3$ heterostructures illustrate that unconventional features resembling a topological Hall effect can be generated in all-oxide multilayers without the presence of skyrmions.

The last part of this thesis focuses on Ru-substituted lanthanum strontium manganite thin films. The possibility to tune the magnetic anisotropy of $La_{0.7}Sr_{0.3}MnO_3$ thin films by comparably small modifications of the heterostructure design makes the material class highly interesting in the context of the stabilization of non-collinear magnetic textures. The tailoring of the magnetic anisotropy in $La_{0.67}Sr_{0.33}Ru_yMn_{1-y}O_3$ thin films, by thickness variations, temperature, and Ru content, is discussed in Chapter 7. It is shown that moderate

perpendicular magnetic anisotropy can be induced in $La_{0.67}Sr_{0.33}Mn_{0.95}Ru_{0.05}O_3$ thin films at low temperatures, when they are deposited under weak compressive epitaxial strain and are of intermediate thicknesses.
Chapter 8 is dedicated to the magnetic and magnetotransport properties of one specific LSMO thin film of this series, a 42.5 nm thick $La_{0.67}Sr_{0.33}Ru_{0.05}Mn_{0.95}O_3$ film, where in-plane anisotropic magnetoresistances are related to the magnetic anisotropy and the corresponding magnetic domain structure.

References

[1] F. M. Granozio, G. Koster, and G. Rijnders: *Functional oxide interfaces*, MRS Bulletin **38**, 1017–1023 (2013).

[2] M. Bibes and A. Barthélémy: *Oxide spintronics*, IEEE Transactions on Electron Devices **54**, 1003–1023 (2007).

[3] H. He, Z. Yang, Y. Xu, A. T. Smith, G. Yang, and L. Sun: *Perovskite oxides as transparent semiconductors: A review*, Nano Convergence **7**, 32 (2020).

[4] A.-M. Haghiri-Gosnet and J.-P. Renard: *CMR manganites: physics, thin films and devices*, J. Phys. D: Appl. Phys. **36**, R127 (2003).

[5] J. D. Hoffman, B. J. Kirby, J. Kwon, G. Fabbris, D. Meyers, J. W. Freeland, I. Martin, O. G. Heinonen, P. Steadman, H. Zhou, C. M. Schlepütz, M. P. M. Dean, S. G. E. te Velthuis, J.-M. Zuo, and A. Bhattacharya: *Oscillatory noncollinear magnetism induced by interfacial charge transfer in superlattices composed of metallic oxides*, Phys. Rev. X **6**, 041038 (2016).

[6] E. Skoropata, J. Nichols, J. M. Ok, R. V. Chopdekar, E. S. Choi, A. Rastogi, C. Sohn, X. Gao, S. Yoon, T. Farmer, R. D. Desautels, Y. Choi, D. Haskel, J. W. Freeland, S. Okamoto, M. Brahlek, and H. N. Lee: *Interfacial tuning of chiral magnetic interactions for large topological Hall effects in $LaMnO_3/SrIrO_3$ heterostructures*, Science Advances **6**, eaaz3902 (2020).

[7] J. Matsuno, N. Ogawa, K. Yasuda, F. Kagawa, W. Koshibae, N. Nagaosa, Y. Tokura, and M. Kawasaki: *Interface-driven topological Hall effect in $SrRuO_3$ - $SrIrO_3$ bilayer*, Science Advances **2**, e1600304 (2016).

[8] M. Nakamura, D. Morikawa, X. Yu, F. Kagawa, T.-h. Arima, Y. Tokura, and M. Kawasaki: *Emergence of Topological Hall Effect in Half-Metallic Manganite Thin Films by Tuning Perpendicular Magnetic Anisotropy*, Journal of the Physical Society of Japan **87**, 074704 (2018).

[9] C. Back, V. Cros, H. Ebert, K. Everschor-Sitte, A. Fert, M. Garst, T. Ma, S. Mankovsky, T. L. Monchesky, M. Mostovoy, N. Nagaosa, S. S. P. Parkin, C. Pfleiderer, N. Reyren, A. Rosch, Y. Taguchi, Y. Tokura, K. von Bergmann, and J. Zang: *The 2020 skyrmionics roadmap*, Journal of Physics D: Applied Physics **53**, 363001 (2020).

[10] A. Fert, V. Cros, and J. Sampaio: *Skyrmions on the track*, Nature Nanotechnology **8**, 152–156 (2013).

[11] R. Tomasello, E. Martinez, R. Zivieri, L. Torres, M. Carpentieri, and G. Finocchio: *A strategy for the design of skyrmion racetrack memories*, Scientific Reports **4**, 6784 (2014).

[12] G. Bourianoff, D. Pinna, M. Sitte, and K. Everschor-Sitte: *Potential implementation of reservoir computing models based on magnetic skyrmions*, AIP Advances **8**, 055602 (2018).

[13] Y. Ohuchi, J. Matsuno, N. Ogawa, Y. Kozuka, M. Uchida, Y. Tokura, and M. Kawasaki: *Electric-field control of anomalous and topological Hall effects in oxide bilayer thin films*, Nature Communications **9**, 213 (2018).

[14] K.-Y. Meng, A. S. Ahmed, M. Baćani, A.-O. Mandru, X. Zhao, N. Bagués, B. D. Esser, J. Flores, D. W. McComb, H. J. Hug, and F. Yang: *Observation of Nanoscale Skyrmions in* $SrIrO_3$ */* $SrRuO_3$ *Bilayers*, Nano Letters **19**, 3169–3175 (2019).

[15] B. Kim, D. Kwon, J. H. Song, Y. Hikita, B. G. Kim, and H. Y. Hwang: *Finite size effect and phase diagram of ultra-thin* $La_{0.7}Sr_{0.3}MnO_3$, Solid State Communications **150**, 598–601 (2010).

[16] C. Moreau-Luchaire, C. Moutafis, N. Reyren, J. Sampaio, C. A. Vaz, N. Van Horne, K. Bouzehouane, K. Garcia, C. Deranlot, P. Warnicke, P. Wohlhüter, J. M. George, M. Weigand, J. Raabe, V. Cros, and A. Fert: *Additive interfacial chiral interaction in multilayers for stabilization of small individual skyrmions at room temperature*, Nature Nanotechnology **11**, 444–448 (2016).

[17] A. Soumyanarayanan, M. Raju, A. L. G. Oyarce, A. K. C. Tan, M. Y. Im, A. P. Petrović, P. Ho, K. H. Khoo, M. Tran, C. K. Gan, F. Ernult, and C. Panagopoulos: *Tunable room-temperature magnetic skyrmions in Ir/Fe/Co/Pt multilayers*, Nature Materials **16**, 898–904 (2017).

[18] A. K. Nandy, N. S. Kiselev, and S. Blügel: *Interlayer Exchange Coupling: A General Scheme Turning Chiral Magnets into Magnetic Multilayers Carrying Atomic-Scale Skyrmions*, Physical Review Letters **116**, 177202 (2016).

[19] S. D. Pollard, J. A. Garlow, J. Yu, Z. Wang, Y. Zhu, and H. Yang: *Observation of stable Néel skyrmions in cobalt/palladium multilayers with Lorentz transmission electron microscopy*, Nature Communications **8**, 14761 (2017).

Chapter 2

Fundamentals

Contents

The aim of this chapter is the presentation of the basic physical properties of magnetic thin films which are relevant for the research presented in this thesis. Firstly, the most important contributions that determine the magnetic anisotropy in magnetic thin films are discussed. The different mechanisms of the magnetic interlayer coupling, which will be investigated for $SrRuO_3$-$SrIrO_3$ heterostructures in Chapter 5, are presented subsequently. The purpose of Chapter 2.1.3 is to introduce magnetotransport phenomena that are observed in magnetic conductors. The two main perovskite oxides under study, $SrRuO_3$ and $La_{0.7}Sr_{0.3}Mn_{1-y}Ru_yO_3$, are presented in Subsection 2.2. Due to the scientific debate on peculiar features in the Hall effect in $SrRuO_3$ thin films, this topic is in the focus of Chapter 2.2.1.

2.1 Magnetism and magnetotransport in thin films

The magnetic state of a system is dictated by the minimization of the total (free) energy E_{tot} (if thermal fluctuations and higher order exchange interactions can be neglected):[1]

$$E_{\text{tot}} = E_{\text{ex}} + E_{\text{DMI}} + E_{\text{ani}} + E_{\text{z}} \tag{2.1}$$

with the symmetric Heisenberg exchange energy E_{ex}, the antisymmetric Dzyaloshinskii-Moriya exchange energy E_{DMI}, and the anisotropy energy E_{ani}. The Zeeman energy E_{z} represents the energy change in presence of a magnetic field and is minimized for the alignment of the magnetic moments along the applied magnetic field. The subsequent chapter will focus on the magnetic anisotropy E_{ani}.

2.1.1 Magnetic anisotropy

Due to the presence of spin-orbit coupling and dipole-dipole interactions, the magnetic energy of a system depends on the orientation of the magnetization with respect to sample specific directions, determined by crystallographic axes or sample geometry.[2] This energetic preference of the magnetization orientation is named magnetic anisotropy and leads to the existence of magnetic hard and easy axes (or planes).[3] The different contributions that determine the total magnetic anisotropy, such as the magnetocrystalline, shape, and the magnetoelastic anisotropy, will be discussed subsequently.

Magnetocrystalline anisotropy

Magnetocrystalline anisotropy (MCA) describes the preferential alignment of the magnetization $\boldsymbol{M}$ along crystallographic directions[2,3] and originates from the interplay of the crystal field and spin-orbit coupling.[2,3] The crystal field, which is dictated by the crystal stucture, causes the existence of a preferred orientation of the orbital moment. Due to spin-orbit coupling, this leads to an energetically favorable alignment of the total magnetic moment with respect to the crystal axes.[2,3]

Because of the complexity of theoretical *ab initio* band structure calculations of the magnetocrystalline anisotropy, phenomenological descriptions are often considered instead.[3] The magnetocrystalline anisotropy energy, which has to reflect the symmetry of the crystal lattice and electronic structure, can be expressed in terms of an expansion:[3]

$$E_{\mathrm{mc}} = K_0 + K_1 f_1 \left(\widehat{\boldsymbol{M}}\,(\boldsymbol{r})\right) + K_2 f_2 \left(\widehat{\boldsymbol{M}}\,(\boldsymbol{r})\right) + ... \tag{2.2}$$

with the anisotropy constants K_{i}. The functions f_{i} depend on the magnetization orientation $\widehat{\boldsymbol{M}}$ with $\widehat{\boldsymbol{M}} = \boldsymbol{M}/M$. This is typically described by the cosine of the angle α_i which is enclosed between the magnetization direction and the cartesian axes ($\widehat{M_i} = \cos\alpha_i$).[3] In inversion symmetric systems, only even functions f_i are allowed in Equation (2.2).

If a magnetic system has an easy axis $\boldsymbol{u}$, but is isotropic in the corresponding plane perpendicular to this axis, the system shows uniaxial magnetic anisotropy. Such a situation is often seen in systems that have a single axis of high symmetry.[3] If the easy axis of the system is given by $\boldsymbol{u}$, with $\boldsymbol{u}$ along the z direction, and Φ the angle between the anisotropy axis $\boldsymbol{u}$ and the direction of magnetization $\boldsymbol{M}$, the uniaxial magnetic anisotropy is given by:[3]

$$E_{\mathrm{mc}}^{\mathrm{uni}} = K_0^{\mathrm{uni}} + K_1^{\mathrm{uni}} \sin^2\Phi + K_2^{\mathrm{uni}} \sin^4\Phi + ... \tag{2.3}$$

with the uniaxial anisotropy constant of first and second order K_1^{uni} and K_2^{uni}, respectively.

Magnetoelastic anisotropy

If stress is applied on a magnetic specimen, for instance by epitaxial strain due to the heteroepitaxial growth on a substrate, the symmetry may be reduced, which can allow anisotropy terms that are forbidden in the unstrained film.[4] Under the assumption that the magnetic system is elastically isotropic with magnetostriction coefficient λ, the energy contribution (per unit volume) originating from magnetoelastic anisotropy is:[2]

$$E_{\mathrm{ms}} = -\frac{3}{2}\lambda\sigma\cos^2\Theta \tag{2.4}$$

Θ describes the angle between the magnetization and the direction of uniform strain. σ is the stress, which can be expressed in terms of the strain ϵ by the elastic modulus E: $\sigma = E\epsilon$.[2]

Shape anisotropy

In a uniformly magnetized sample of finite dimensions, uncompensated magnetic poles will form at the surfaces that generate the so-called demagnetization field.[2] It is proportional to the magnetization $\boldsymbol{M}$, but oriented in opposite direction:[2]

$$\boldsymbol{H}_d = -\widehat{N}\boldsymbol{M} \tag{2.5}$$

with the demagnetization tensor $\widehat{N}$, which is determined by the geometry of the magnetic specimen. The energy associated with the demagnetization field is given by:[2]

$$E_d = -\frac{1}{2V}\mu_0 \int \boldsymbol{H}_\mathrm{d}\boldsymbol{M}dV \tag{2.6}$$

In case of magnetic thin films with lateral extension in x- and y-direction in the infinite plane limit, all tensor elements, except for $N_{zz} = 1$, are zero.[2,3] Then, the shape anisotropy energy per unit volume V of the film is:[2]

$$E_d = \frac{1}{2}\mu_0\boldsymbol{M^2}\cos^2\Theta \tag{2.7}$$

with the angle Θ between the film normal and the magnetization direction. Thus, the demagnetization energy is minimized in magnetic thin films[1] when the magnetization is aligned in the thin film plane.[2]

Surface anisotropy and roughness induced magnetic anisotropy

At surfaces or interfaces between dissimilar materials, the environment of the magnetic ions differs from the surrounding of the magnetic ions in the bulk, which is reflected in the magnetic surface anisotropy (MSA). Due to the ratio of surface and bulk, the MSA gets particularly important, sometimes even dominating, in ultrathin films and multilayers.[6] The surface anisotropy is related to the missing bonds at the surfaces and the induced strains in the bonds with the surface atoms.[6,7] In Néel's phenomenological model, the surface atoms environment thus has reduced symmetry, which leads to additional anisotropy contributions.[8]

The existence of surfaces also impacts on the dipole-dipole interactions, which differ for the magnetic moments in the bulk and at boundaries.[5] Draaisma and de Jonge showed that the magnetic continuum approach is no longer valid

---

[1] Referring to Draaisma and de Jonge, ultrathin films should not be treated as a magnetic continuum but rather as discrete magnetic dipoles on a lattice.[2,5]

in case of ultrathin magnetic films, which they treated as discrete magnetic dipoles on a regular lattice instead.[5] They demonstrated that the existence of surfaces leads to the appearance of an additional dipole-dipole-related surface anisotropy contribution.[5] Furthermore, it was shown that the magnetic anisotropy contributions of the surface and the volume can be disentangled due to the distinct scaling with the film thickness.[5]

Not only the surfaces, but also the details of the surface morphology impact on the total magnetic anisotropy.[6] Substrates with a step-terrace-like structure are often utilized in the epitaxial thin film deposition in order to ensure pseudomorphic crystal growth. In case of high-quality thin film growth, the magnetic film surface maintains the substrate-induced structure so that the environment of the magnetic ions on the surface is dependent on the exact position on the sample, i.e. on the flat terrace or at the step edge.[6] At step edges, the locally broken bonds and missing atoms were considered to modify the magnetocrystalline anisotropy,[9] referring to Néel's model. Also the local contribution to the magneto-elastic anisotropy varies at the step edges, since the existence of terraces causes strain within the magnetic film[10] and influences the strain relaxation.[9] Furthermore, the magnetostatic shape anisotropy differs locally in presence of non-coplanar surfaces[11] due to the increased local roughness.[9,10] In 25 nm thick $La_{0.67}Sr_{0.33}MnO_3$ thin films deposited on vicinal (0.24°) $SrTiO_3(100)$ substrates, the terraces were found for instance to lead to in-plane uniaxial anisotropy at room temperature with the easy axis aligned along the step-edge direction and the hard axis perpendicular to the step edges.[9]

Determination of the effective magnetic anisotropy

The different contributions of the effective magnetic anisotropy constant K_{eff} can be phenomenologically categorized into volume and surface terms. In the so-called coherent strain regime, when the imposed strain is small, the volume anisotropy contains the magnetocrystalline anisotropy K_{mc}, the strain anisotropy $K_{\mathrm{ms}}^{\mathrm{coh}}$, and the shape anisotropy K_{d}.[2] The effective anisotropy constant K_{eff} is then the sum of the volume contributions and the surface anisotropy constant K_{surface}:

$$K_{\mathrm{eff}} = K_{\mathrm{mc}} + K_{\mathrm{ms}}^{\mathrm{coh}} + K_{\mathrm{d}} + K_{\mathrm{surface}} \tag{2.8}$$

K_{surface} scales with the film thickness t as $1/t$.[6] In case of a stepped surface with terraces of width d, K_{surface} contains an additional contribution that scales with $1/(dt)$.[6]

The required energy to reorient the magnetization by $d\boldsymbol{M}$ in a magnetic field $\boldsymbol{H}$ is $\mu_0 \boldsymbol{H} \cdot d\boldsymbol{M}$.[2] Following Johnson *et al.* and Yi *et al.*, the effective (perpendicular) magnetic anisotropy energy can then be determined experimentally by the calculation of the area between the out-of-plane and in-plane magnetic hysteresis loops (in the first quadrant of the hysteresis loop).[2,12] As illustrated in Fig. 2.1, the perpendicular anisotropy energy density is:

$$K_{\text{perp}} = \mu_0 \int_0^{H_s} M_{\text{OOP}}\, dH - \mu_0 \int_0^{H_s} M_{\text{IP}}\, dH \tag{2.9}$$

However, this method can be problematic when the applied magnetic field is insufficient to saturate the magnetic sample in the hard axis orientation. Angular dependent measurements with fixed applied magnetic field and the corresponding fitting are used alternatively in order to determine the effective magnetic anisotropy.[2]

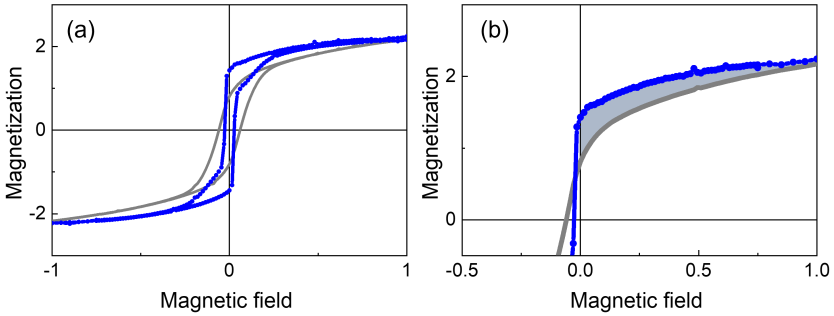

Figure 2.1: (a) Magnetic hysteresis loops with the magnetic field applied perpendicular (blue) and parallel (grey) to the surface of a fictous thin film. (b) Zoom-in to highlight the area enclosed by the OOP- and IP hysteresis loops used to experimentally determine the perpendicular magnetic anisotropy. The calculation of the PMA is based on the procedure described in Ref. [12]. Figure inspired from Ref. [12].

2.1.2 Mechanisms of magnetic interlayer coupling

When magnetic layers are epitaxially stacked in a heterostructure, the magnetic coupling between the layers can influence the properties of the entire heterostructure.

Initially motivated by the observation of antiferromagnetic coupling between Fe films through a Cr spacer[13,14] and further driven by its relevance for several applications, intense research was performed on the experimental and theoretical understanding of the magnetic interlayer coupling. The magnetic coupling of two ferromagnetic layers which are separated by a non-magnetic spacer can be mediated by various mechanisms.

Several theoretical models were developed to describe the indirect exchange coupling mechanism, such as the spin-current model by Slonczewski,[15] valid for insulating spacers at T=0, or the Ruderman-Kittel-Kasuya-Yosida (RKKY) model, which is capable to explain the oscillatory dependence of the coupling strength depending on the metallic spacer thickness.[16–18]

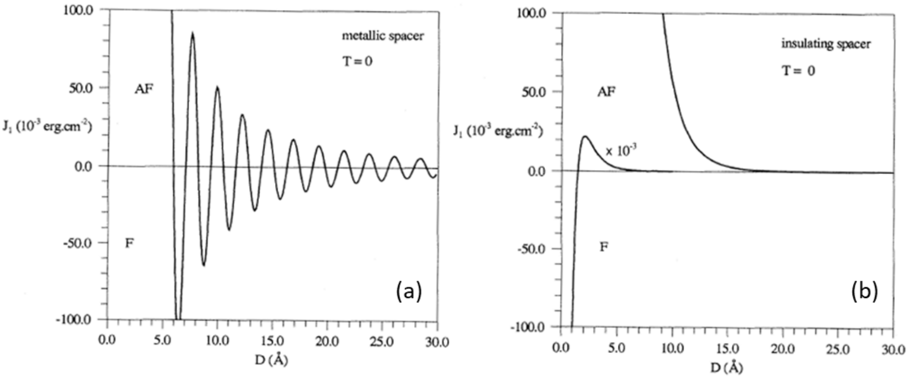

Figure 2.2: Thickness dependence of the interlayer exchange coupling strength J_1, calculated within the quantum interference model by Bruno, for metallic (a) or insulating spacers (b) at $T = 0$. The thickness of the ferromagnetic layers was infinite, the Fermi energy was 7 eV, the exchange splitting 1.5 eV; $U = 0$ for (a) and U - $\epsilon_F = 0.1$ eV for the insulating spacer in (b). Figure adapted from Ref. [14]. Reprinted subfigures with permission from P. Bruno, Physical Review B **52**, 411 (1995), Copyright 1995 by the American Physical Society.

A generalized description of the interlayer exchange coupling (IEC) for metallic and insulating spacers, including the above mentioned models as special cases, was achieved by the concept of the complex Fermi surface, introduced by Bruno.[14,19] In his *Theory of interlayer magnetic coupling*, the IEC originates from the quantum interferences of electron waves caused by multiple spin-dependent reflections at the interfaces of the ferromagnetic layers and the (dia- or paramagnetic) spacer.[14,19]

This (analytical) quantum interference approach starts from the free electron model, where the bottom of the majority bands of the two ferromagnetic layers, assumed to have identical properties, is defined as zero energy. The spacer has a potential U and the exchange splitting is the potential of the minority bands. When the magnetizations of the two ferromagnetic layers make an angle Θ, the interlayer coupling energy per unit area for the two layers A and B was expanded as:[14,19]

$$E_{AB} = J_0 + J_1 \cos\Theta + J_2 \cos^2\Theta + ... \tag{2.10}$$

where J_0 is the non-magnetic coupling and J_2 the biquadratic coupling.

According to Ref. [14], the Heisenberg coupling constant J_1, in the limit of large spacer thickness D and for semi-infinitely thick ferromagnetic layers, is given by:

$$J_1(T) = \frac{\hbar^2 k_F^2}{4\pi^2 m D^2} \operatorname{Im}(\Delta r^2 e^{2ik_F D}) \frac{\frac{2\pi k_B T D m}{\hbar^2 k_F}}{\sinh \frac{2\pi k_B T D m}{\hbar^2 k_F}} \tag{2.11}$$

with the Fermi wave vector of the spacer k_F, the spin-asymmetry of the reflected amplitudes at the FM-NM interfaces Δr^2, the electron mass m, and the Boltzmann constant k_B. In case of an insulating spacer, Equation (2.11) is valid only at temperatures lower than $T_1 = \frac{\hbar^2 k_F}{2k_B m D}$.[14] While the Fermi wave vector $k_F = \sqrt{2m(\epsilon_F - U)/\hbar^2}$ is real for metallic spacers, $k_F = i\sqrt{2m(U - \epsilon_F)/\hbar^2}$ is imaginary for an insulating spacer.[14] Therefore, Equation (2.11) predicts an oscillatory dependence of the IEC on spacer thickness for metallic spacers, but an exponential decrease for increasing spacer thickness for insulating spacers (see Fig. 2.2).[14,19] Given by the last factor in Equation (2.11), a temperature-induced decrease of the IEC strength is expected for metallic spacers, while it increases in the case of insulating spacers.

The extension of this approach to finite ferromagnetic layer thicknesses additionally predicts oscillations of the coupling strength on the thickness of the ferromagnetic layer.[14] At T=0, J calculated by the quantum interference model is reduced to the result proposed by Slonczewski.[14,15,19]

For the description of the general theory of interlayer exchange by quantum interference for realistic multiband systems, the reader is referred to Ref. [14].

Independent of the electronic properties of the spacer, direct exchange coupling can be realized by the formation of areas where the two magnetic layers are in direct contact, because the spacer thickness vanishes[20] (compare Fig. 2.3 (d)). These so-called pinholes acting as direct connection between the two magnetic layers lead to ferromagnetic coupling.[21,22] Their formation probability is increased for decreasing spacer thickness and therefore most important for heterostructures with ultrathin spacers.[23,24]

Additionally, magnetostatic interactions are capable to influence the magnetic interlayer coupling significantly.[25,26] Such magnetostatic interactions due to magnetic stray fields can be induced by local nonuniformity of the magnetization in the ferromagnetic layers due to the interface topography[27,28] or when the layers exhibit multiple magnetic domains instead of a single-domain state.[29–31]

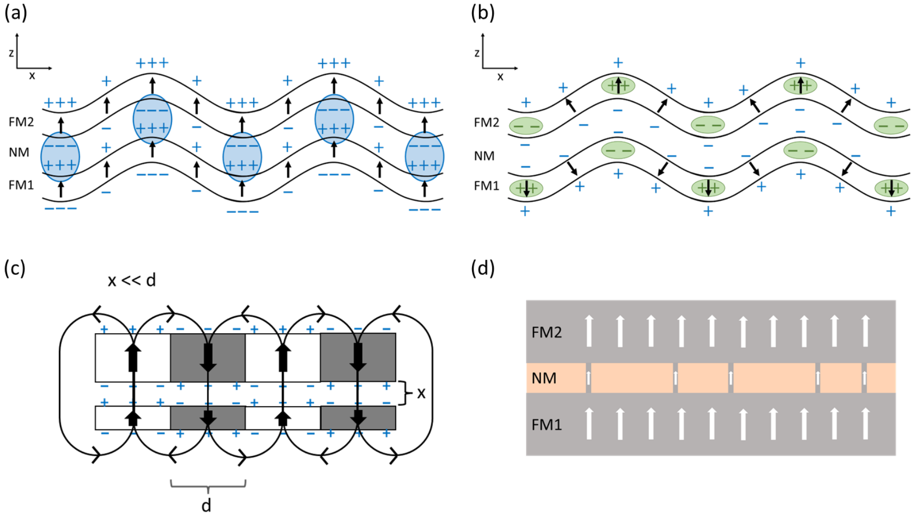

Figure 2.3: The magnetic layers separated by a non-magnetic spacer can be coupled magnetostatically by orange-peel coupling. In case of weak perpendicular magnetic anisotropy (with respect to the exchange stiffness), the alignment is parallel (a), whereas it is antiparallel (b) when the perpendicular magnetic anisotropy is strong. (c) Magnetostatic stray field coupling of the two ferromagnetic layers induced by the presence of magnetic domains of width *d*. Direct ferromagnetic coupling of the ferromagnetic layer FM1 and FM2 via pinholes (d). Figures (a) and (b) are based on Ref. [28]. Figure (c) is based on Ref. [30]. Figure (d) is inspired from Ref. [22].

Here, the shape of the sample and the magnetic domains impact on the stray field coupling,[25,32] which was found to become relevant for submicron-sized devices.[32]

Another origin of magnetostatic interactions in thin film heterostructures is (correlated) surface roughness, which can be introduced for instance by the usage of vicinal substrates that possess a step-terrace like structure.[33] Furthermore, wavy interfacial roughness can be obtained by strain relaxation in epitaxial heterostructures.[34] The subsequent layers of a heterostructure will approximately follow the surface roughness of the initially deposited thin film, leading to correlated roughness of the layers. This was taken as one basic assumption of the orange-peel coupling model, developed by Néel.[27] In case of in-plane magnetized layers, the magnetic exchange will favor the parallel alignment of the magnetic moments within the individual layers which leads to the formation of surface charges due to the interface roughness. The interaction between the surface charges through the non-magnetic spacer will then favor the parallel alignment of the magnetic moments of the two magnetic layers.[27]

Here, the orange-peel coupling field is:[35]

$$H_{OP} = \frac{\pi^2}{\sqrt{2}}\Big(\frac{h^2}{\lambda t_f}\Big) M_s \exp\left(\frac{-2\pi\sqrt{2}t_s}{\lambda}\right) \tag{2.12}$$

with the thickness of the spacer layer t_s, the thickness and the magnetization of the free layer[2] t_F and M_s. λ and h are the wavelength and the amplitude of the sinusoidal roughness profile.[35] According to Equation (2.12), the orange-peel coupling field decreases exponentially with the spacer thickness t_s. Large values of H_OP can be obtained for large magnetizations M_s and when the square of the rougness amplitude h is significantly larger than the product of the roughness wavelength λ and the free layer thickness t_f.

As shown by Moritz *et al.*,[28] ferromagnetic or antiferromagnetic coupling can be favored for magnetic layers having perpendicular magnetic anisotropy. Whether the alignment of the magnetizations in the coupled layers is parallel or antiparallel depends on the relative strength of the magnetic anisotropy and the exchange stiffness as well as on the details of the interfacial roughness. When the magnetic anisotropy is weak, the magnetization is aligned parallel to the

---

[2] Schrag *et al.* used Equation (2.12) in their work on magnetic tunnel junctions to describe the magnetic interlayer coupling between a NiFe layer and a Co layer.[35] While the magnetization of the Co layer was pinned to the magnetization direction of an enclosed magnetic structure, the magnetization of the free layer was not pinned to this underlying structure and could be reoriented more easily by the application of a magnetic field.

average surface normal (cf. Fig. 2.3 (a)). In presence of correlated interface roughness, this leads again to the existence of surface charges with opposite orientation when the magnetizations of the two magnetic layers are oriented parallel. In contrast, the magnetic moments are locally aligned perpendicular to the thin film surface in the case of strong magnetic anisotropy.[28] As presented in Fig. 2.3 (b), this will create in-plane components of the magnetization[28,36] and therefore volume charges. Due to the interfaces being uniformly charged this time, the dominant magnetostatic interaction is induced by the volume charge densities that oscillate in the direction of the interface waviness. For antiparallel alignment of the magnetization in the two layers, the volume charge densities oscillate out-of-phase, which is energetically favorable so that antiparallel alignment of the magnetic layers is favored in the case of strong perpendicular magnetic anisotropy.[28]

Magnetostatic coupling between magnetic layers can also be created by the interaction of magnetic stray fields when the magnetization structure of the layers is non-uniform due to the existence of magnetic domains. While in systems with perpendicular magnetic anisotropy these stray fields are generated mostly by the magnetic domains themselves,[29,30,37] the domain walls create strong stray fields in magnetic systems with in-plane magnetic anisotropy.[26,38–41] The decrease of the nucleation field in the magnetically soft layer in presence of domain walls in the magnetically harder layer and its effect on the soft layer magnetization reversal has been attributed to magnetic stray fields.[38,41] Furthermore, the creation of replicated domains was demonstrated to be induced by magnetic stray fields.[29,31,40,42] Baltz *et al.* showed in Co/Pt multilayers that the multi-domain state induced magnetostatic stray field coupling can only be strong when the magnetic domain size is much larger than the thickness of the separating spacer,[30] as presented in Fig. 2.3 (c).

Experimental determination of the coupling strength

The type and strength of the magnetic coupling between the ferromagnetic layers of heterostructures can be assessed by the performance of major and minor magnetic hystereses loops. Required for this technique are measurable differences in the coercive fields of the individual layers. In case of weakly or decoupled magnetic layers, the magnetization of a heterostructure with two

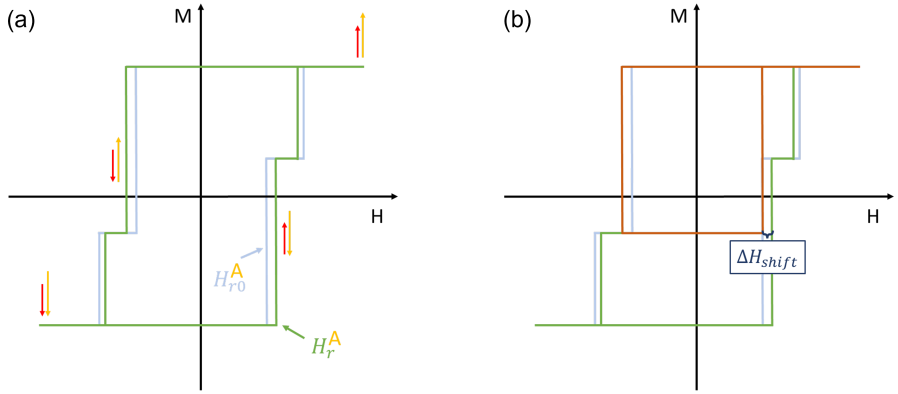

Figure 2.4: Sketch of the basic idea of the major and minor loop investigations in order to determine the interlayer coupling strength experimentally. Shown in (a) is the magnetic hysteresis loop in case of fully decoupled layers (light blue) and weakly ferromagnetically coupled layers (green). $\mathrm{H}_{\mathrm{r}}^{\mathrm{A}}$ and $\mathrm{H}_{\mathrm{r0}}^{\mathrm{A}}$ are the switching fields of the magnetically softer layer in case of weakly ferromagnetically coupled and decoupled layers, respectively. (b) Minor hysteresis loop (orange) of a heterostructure composed of two weakly ferromagnetically coupled layers. $\Delta H_{\mathrm{shift}}$ corresponds to the difference of $\mathrm{H}_{\mathrm{r}}^{\mathrm{A}}$ and $\mathrm{H}_{\mathrm{r0}}^{\mathrm{A}}$. Figure inspired from Ref. [43].

ferromagnetic layers, measured along the magnetic easy axis, reverses its orientation in a two-step process, as sketched in Fig. 2.4 (a). The step at smaller magnetic field is then related to the switching of the magnetically softer layer. To perform a minor loop, the whole heterostructure is magnetized in sufficient magnetic fields and the field is subsequently reduced, reversed, and swept to the middle of the observed first plateau. At this reversal field, it is assumed that the magnetically softer layer has fully reversed its magnetization, while the harder layer is still magnetized opposite to the applied magnetic field. Subsequently, the magnetic field is swept back to saturation, as displayed in Fig. 2.4 (b). Following the calculations by van der Heijden *et al.*,[43] the interlayer coupling strength can be calculated by:

$$J_{\mathrm{C}} = \mu_0 (H_{\mathrm{r}}^{\mathrm{A}} - H_{\mathrm{r0}}^{\mathrm{A}}) M_{\mathrm{soft,rev}} t = \mu_0 \Delta H_{\mathrm{shift}} M_{\mathrm{soft,rev}} t \tag{2.13}$$

with the thickness t and the magnetization (in saturation) of the magnetically softer layer $M_{\mathrm{soft,rev}}$. The minor loop shift $\Delta H_{\mathrm{shift}}$ is the difference of the coercive fields of the magnetically softer layer during the major loop H_r^A and of the minor loop $H_{\mathrm{r0}}^{\mathrm{A}}$.

If ΔH_{shift} is positive, the interlayer coupling is ferromagnetic, while a negative minor loop shift indicates antiferromagnetic interlayer coupling.

2.1.3 Introduction to magnetotransport phenomena in magnetic (half-)metals

The electrical resistivity ρ of a conductor is modified in presence of a magnetic field, which is typically expressed by the magnetoresistance:[3]

$$\mathrm{MR} = \frac{\rho(\mathrm{B}) - \rho(0)}{\rho(0)} = \frac{\Delta\rho}{\rho(0)} \tag{2.14}$$

$\rho(0)$ is the resistivity in absence of an external magnetic field. Depending on the angle between the applied magnetic field $\boldsymbol{B}$ and the electric current direction $\boldsymbol{J}$, transversal ($\boldsymbol{B} \perp \boldsymbol{J}$) and longitudinal magnetoresistance ($\boldsymbol{B} \parallel \boldsymbol{J}$) can be studied.[3] Various mechanisms, whose relative strengths are determined by the magnetic and electronic properties of the material under study, contribute to the total magnetoresistance.

In presence of a magnetic field[3] $\boldsymbol{B}$, the Lorentz force leads to the deflection of electrons and thereby to the decrease of the charge carrier mean free path. The field-induced increase of the resistance corresponds to a positive magnetoresistance, which can be described by the Kohler rule:[3,44,45]

$$\frac{\Delta\rho}{\rho_0} = F(\frac{B}{\rho_0}) \tag{2.15}$$

with the resistivity in absence of a magnetic field ρ_0 and the material specific function F. This so-called normal magnetoresistance is usually a small effect and is maximized for high quality single crystals with low ρ_0.[44]

However, the normal MR is often accompanied by other MR effects in ferromagnetic conductors.[44] In (single-domain) ferromagnetic conductors, the magnetoresistance is typically negative, due to the magnetic field induced suppression of spin fluctuations.[44]

Mixed-valence manganites became prominent due to the unusually large magnitude of the negative magnetoresistance, reaching orders of magnitude close to the metal-to-insulator transition,[46] as presented exemplarily in Fig. 2.5 (a) for a $La_{2/3}Sr_{1/3}MnO_3$ (LSMO) thin film, deposited on $NdGaO_3$ (110).[47]

---

[3] The magnetic field corresponds to $\boldsymbol{B}= \mu_0(\boldsymbol{H_a}+\boldsymbol{H}_{\text{demag}}+\boldsymbol{M})$ in case of a ferromagnet.[44]

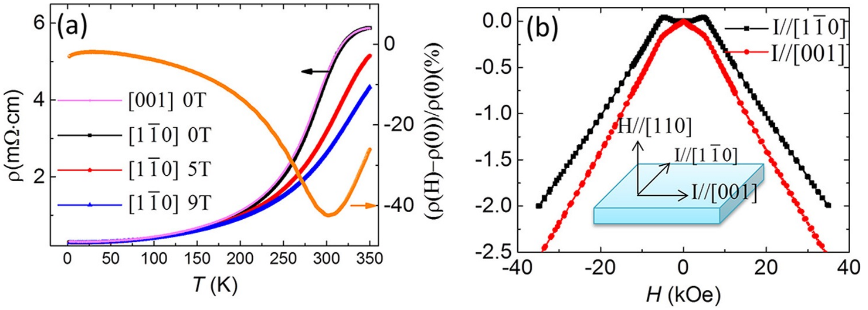

Figure 2.5: Magnetoresistance study of a $La_{2/3}Sr_{1/3}MnO_3$ thin film, deposited on $NdGaO_3$ (110): (a) Temperature dependent resistivity along [001] and [1$\bar{1}$0] under different magnetic fields. The magnetic field is along [110] direction. The orange curve is the MR ratio at 9 T vs temperature. (b) Field dependent MR ratio at I ∥ [1$\bar{1}$0] and I ∥ [001] with H ∥ [110]. Figures adapted from Ref. [47]. Reprinted from Z. Liao, M. Huijben, G. Koster, and G. Rijnders, APL Materials **2**, 096112 (2014), with the permission of AIP publishing.

This so-called colossal magnetoresistance (CMR) scales linearly with the external magnetic field[47,48] (cf. Fig. 2.5 (b)).
Considering the double exchange model, the conduction of mixed-valence manganites is very sensitive to the effective hopping probability of electrons between the Mn^{3+} and Mn^{4+} so that the electrical transport properties are strongly influenced by the magnetic ordering.[46,49] Upon temperature enhancement, the increased spin disorder causes a resistivity increase. However, the application of an external magnetic field is capable to reduce the spin disorder and thereby decrease the resistivity, which is particularly important close to the metal-to-insulator transition, which leads (in a simplified picture) to the observation of the CMR (see Fig. 2.5 (a)).[44]

Discovered by Thomson in 1857,[50] the anisotropic magnetoresistance (AMR) describes the dependence of the magnetoresistance on the angle between the current and the magnetization. The fundamental origin of the AMR is the influence of the spin-orbit interaction on the scattering between magnetic ions and charge carriers.[51,52] Depending on the material characteristics, the normal anisotropic magnetoresistance is maximum (minimum) when the current is parallel (orthogonal) to the magnetization.[52] Thus the AMR, which is defined by the normalized difference between in-plane resistivities for the current applied parallel and perpendicular to the magnetization ($(\rho_{\parallel}$ -$\rho_{\perp})/\rho_{\parallel}$), is positive for most metals.[51] The resistivity for a given angle Θ between the current direction and the magnetization is then:[52]

$$\rho(\Theta) = \rho_{\perp} + (\rho_{\parallel} - \rho_{\perp}) \cos^2 \Theta \tag{2.16}$$

In the diffusive transport regime, the AMR was explained by the spin-orbit interaction induced mixing of the minority and majority spin channels.[52] When the conductivity in ferromagnetic transition metals is mainly determined by the scattering rates of the *s*-electrons, which carry the current, into localized *d*-states, such spin-mixing causes anisotropy of the scattering events and thereby the distinct resistivities for electrons that move parallel or perpendicular to the magnetization.[52] However, magnetotransport studies in manganites revealed a negative anisotropic magnetoresistance and cannot be explained in this simple model.[51]

If a ferromagnetic specimen is not in a single-domain state, the present domain walls will create the domain wall resistance (DWR), which can yield positive or negative contributions.[53] Negative DWR[47,53–56] was attributed to the domain-wall-induced suppression of electron interference in the weakly localized regime.[54] This quantum mechanical effect is expected to be important at low temperature.[57]
While the positive DWR was initially related to the reflection of electrons at the domain walls,[47,55,58] recent models are based on spin-dependent scattering rates and potentials.[56] Van Gorkom *et al.* demonstrated that the sign of the DWR is determined by the spin-dependent scattering times of the two spin channels, considering the tailoring of the band structure due to the magnetization rotation inside the domain wall.[53,57]

Within the two-channels conduction model in ferromagnets, the positive DWR is attributed to the mixed spin conduction.[59,60] The noncollinearity of the magnetization within the domain walls was proposed to mix the majority and minority spin channels.[59] The resistivity is thereby increased due to the partial elimination of the short circuit of the spin channel with lower resistivity, which is usually achieved in case of a homogeneously magnetized ferromagnet.[56,60] Experimental studies of materials that show parallel magnetic stripe domains, such as LSMO films under compressive strain or FePd films, revealed DWR of

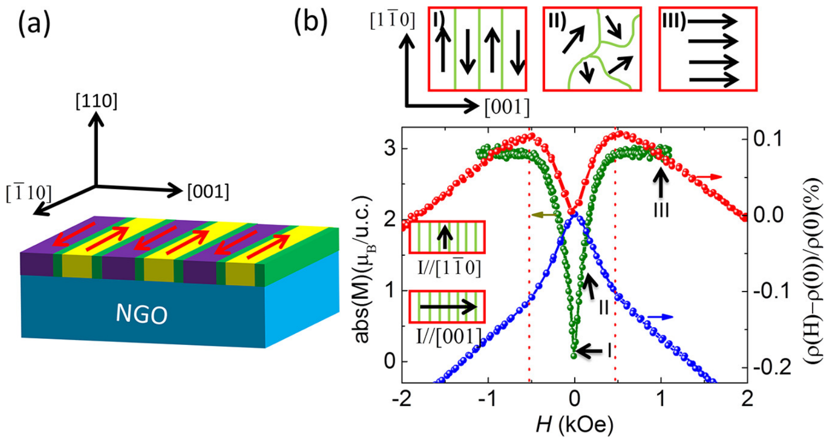

Figure 2.6: (a) Schematic structure of the magnetic stripe domain pattern in the $La_{2/3}Sr_{1/3}MnO_3$ thin film, deposited on $NdGaO_3$ (110). The green areas correspond to domain walls. (b) Comparison of the M(H) loop (green curve) and the magnetoresistance data when H ∥ [001] at 100 K. Reprinted from Ref. [47]: Z. Liao, M. Huijben, G. Koster, and G. Rijnders, APL Materials **2**, 096112 (2014), with the permission of AIP publishing.

tenth of percent[47,61] up to a few percent,[57] when the current is either parallel or perpendicular to the domain walls, as shown exemplarily in Fig. 2.6 for a $La_{2/3}Sr_{1/3}MnO_3$ thin film.[47]
In addition to the domain wall resistance that contributes to the MR, further extrinsic magnetoresistance effects appear due to the existence of magnetic domains. Berger *et al.* observed the increase of the resistivity when the current is applied perpendicular to the magnetic domain walls in a perpendicularly magnetized sample, which was attributed to the zig-zag movement of the electrons due to the changing Hall angles in alternating magnetic domains.[56,62]

The usual Hall effect[4] belongs to the group of transverse magnetoresistance effects. Here, the external magnetic field is applied perpendicular to the current and perpendicular to the sample surface[5]. Depending on the magnetic and electrical properties of a solid, the Hall resistivity ρ_{xy} contains various contributions. In case of a magnetic conductor, the ordinary Hall resistivity $\rho_{\mathrm{xy}}^{\mathrm{OHE}}$, the anomalous Hall resistivity $\rho_{\mathrm{xy}}^{\mathrm{AHE}}$, and in presence of topologically non-trivial spin textures the topological Hall effect $\rho_{\mathrm{xy}}^{\mathrm{THE}}$ determine the total

---

[4] Throughout this dissertation, the Hall resistivity ρ_{xy} describes the DC limit of the generally frequency dependent Hall effect $\rho_{\mathrm{xy}}(\omega)$.

[5] Only in case of planar Hall measurements, the magnetic field is applied in the film plane.

Hall resistivity. Pugh *et al.* suggested the empirical relation[63] between the different contributions that will be explained subsequently:

$$\rho_{\mathrm{xy}} = \rho_{\mathrm{xy}}^{\mathrm{OHE}} + \rho_{\mathrm{xy}}^{\mathrm{AHE}} + \rho_{\mathrm{xy}}^{\mathrm{THE}} \tag{2.17}$$

The ordinary Hall effect, discovered by Edwin Hall in 1879, appears when an electric current is flowing through a conductor in presence of a magnetic field that is applied perpendicular to the current direction.[64] The effect is related to the deflection of electrons due to the Lorentz force, which creates a transverse electric field that is in balance with the Lorentz force in equilibrium.[3] Since the ordinary Hall resistivity is proportional to the perpendicular component of the external magnetic field, the ordinary Hall constant is typically determined in experiments from the slope of the Hall resistance hysteresis loops (dR_{xy}/dB). In a single-carrier model, the ordinary Hall constant is proportional to the inverse of the charge carrier density. However, when two types of charges carry the electric current, as for instance in semimetals such as bulk $\mathrm{SrIrO_3}$,[65] the ordinary Hall coefficient R_H is given by:

$$R_H = \frac{\mu_h^2 n_h - \mu_e^2 n_e}{e(\mu_h n_h + \mu_e n_e)^2} \tag{2.18}$$

μ_e and n_e (μ_h and n_h) are the mobilities and carrier densities of the electrons (and holes).

The anomalous Hall conductivity arises from spin-orbit coupling in materials with broken time reversal symmetry, such as ferromagnets or paramagnets that are magnetized by an external magnetic field.[66] Generally, the intrinsic contribution originating from the (momentum space) Berry curvature (see Equation (2.20)) as well as extrinsic effects (skew scattering and side jumps) can contribute to the total anomalous Hall effect.[66] These extrinsic effects were related to asymmetric scattering events at impurities due to finite spin-orbit coupling.[66] Within the skew scattering mechanism, proposed by Smit,[67] the anomalous Hall resistivity is proportional to the longitudinal resistivity ρ_{xx}. In case of side-jump scattering, suggested by Berger,[68] $\rho_{\mathrm{AHE}}^{\mathrm{side}}$ scales with ρ_{xx}^2. The side-jump mechanism can be imagined as the lateral displacement of the electron wave package due to the approach of an impurity.[69] When the scattering in a magnetized conductor depends on the spin state, a finite spin current and thus a transverse charge current, is generated.[70] It was found that the extrinsic contributions of the anomalous Hall resistivity are proportional to the perpendicular component of the sample magnetization M_z:[66]

$$\rho_{\mathrm{AHE}}^{\mathrm{extr}} = (a\rho_{\mathrm{xx}} + b\rho_{\mathrm{xx}}^2)M_z \tag{2.19}$$

The intrinsic Hall conductivity was originally derived by Karplus and Luttinger[71] and recently improved by consideration of the theory of the momentum space Berry curvature.[66] As derived in Ref. [66], the intrinsic Hall conductivity $\sigma_{\mathrm{xy}}^{\mathrm{BP}}$ is proportional to the integral of the Berry curvature of the occupied conduction bands.

Then, the contribution to the anomalous Hall resistivity that is related to the intrinsic effect depends on $\sigma_{\mathrm{xy}}^{\mathrm{BP}}$, which itself is a function of the magnetization $\boldsymbol{M}$:[72]

$$\rho_{\mathrm{AHE}}^{\mathrm{intr}} = -\rho_{\mathrm{xx}}^2\sigma_{\mathrm{xy}}^{\mathrm{BP}}(\boldsymbol{M}) \tag{2.20}$$

The dependence of the intrinsic contribution on the electronic band structure emphasizes its sensitivity to the material characteristics and the possible strong temperature dependence.

If an electric current is applied to a magnetic specimen that hosts spin textures of non-trivial topology, as for instance Bloch or Néel-type skyrmions[73] (cf. Fig. 2.7 a) and b)), the Hall resistivity will contain the topological Hall resistivity contribution ρ_{THE}. In the adiabatic limit, the spin of an electron traversing through a spin texture with finite topological charge perfectly adapts the magnetization direction locally[74] (cf. Fig. 2.7 (c)) so that the electron picks up a (real space) Berry phase.[75–77] The trajectory of an electron passing through a magnetic skyrmion is presented in Fig. 2.7 c). By the performance of a transformation that reorients the quantization axis locally parallel to the magnetization direction, the situation can be described by the movement of an electron that interacts with an emergent magnetic field.[75,76,78] This emergent magnetic field[6], which laterally extends in x-y plane, is given by:[79]

$$B_z = \frac{\phi_0}{2}\boldsymbol{n}(\boldsymbol{r})\left(\frac{\partial\boldsymbol{n}(\boldsymbol{r})}{\partial x} \times \frac{\partial\boldsymbol{n}(\boldsymbol{r})}{\partial y}\right) \tag{2.21}$$

$\boldsymbol{n}(\boldsymbol{r}) = \frac{\boldsymbol{M}(\boldsymbol{r})}{|\boldsymbol{M}(\boldsymbol{r})|}$ describes the three-dimensional unit vector of the magnetization direction of the spin texture and $\phi_0 = h/2e$.

---

[6] For more details on the derivation, the reader is referred to Ref. [75, 79].

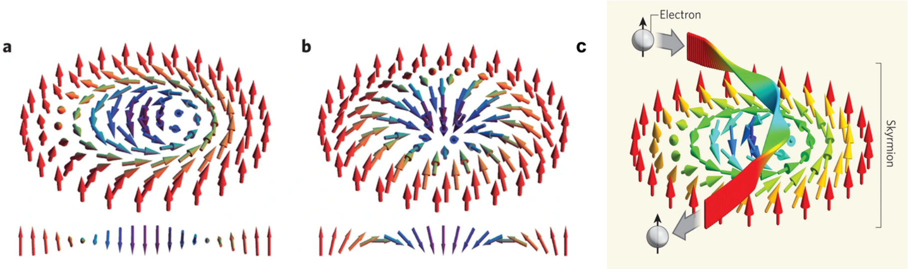

Figure 2.7: Illustrations of a Bloch-type (a) and Néel-type magnetic skyrmion (b). The cross sections of the vortices are shown in the lower panels of a) and b). Shown in c) is the trajectory of an electron moving through a magnetic skyrmion. The electron spin twists to adjust the local spin structure of the skyrmion (ribbon-like pattern). Due to the twisting, the travel direction of the electron is changed. Figures a) and b) reprinted from Ref. [73]; reprinted by permission from Springer Nature: Nature Materials **14**, 1116-1122 (2015), Néel-type skyrmion lattice with confined orientation in the polar magnetic semiconductor GaV_4S_8, I. Kézsmárki, S. Bordács, P. Milde, E. Neuber, L. M. Eng, J. S. White, H. M. Rønnow, C. D. Dewhurst, M. Mochizuki, K. Yanai, H. Nakamura, D. Ehlers, V. Tsurkan, A. Loidl, Copyright (2015). Figure c) is reproduced from Ref. [74]. Reprinted by permission from Springer Nature: Nature **465**, 880-881 (2010), Single skyrmions spotted, C. Pfleiderer and A. Rosch, Copyright (2010).

The topological charge N_{sk} is defined as:[75]

$$N_{\text{sk}} = \frac{1}{4\pi} \int \boldsymbol{n}(\boldsymbol{r}) \left(\frac{\partial \boldsymbol{n}(\boldsymbol{r})}{\partial x} \times \frac{\partial \boldsymbol{n}(\boldsymbol{r})}{\partial y} \right) d\boldsymbol{r}^2 \tag{2.22}$$

In the low field limit, the arising topological Hall resistivity $\rho_{\text{xy}}^{\text{THE}}$ is proportional to the effective emergent magnetic field $\overline{B_{\text{eff}}}$, which corresponds to B_{z} averaged over the area S of the spin texture.[79] Thus $\rho_{\text{xy}}^{\text{THE}}$ is proportional to the skyrmion density.[75,80] It follows that the skyrmion density can be determined experimentally by Hall effect studies if the existence of skyrmions is proven by complementary studies.[80] For skyrmion lattices with a skyrmion density n_{sk}, the topological Hall resistivity ρ_{THE} (in the adiabatic limit) is given by:[80,81]

$$\rho_{\text{THE}} = P R_0 \phi_0 n_{\text{sk}} \tag{2.23}$$

P is the spin polarization, ϕ_0 is one flux quantum, and R_0 denotes the material´s ordinary Hall constant.

The existence of a skyrmionic phase can be confirmed for instance by real space imaging such as Lorentz transmission microscopy,[82] or spin-polarized scanning tunneling microscopy.[83] Skyrmion lattices can be observed also by neutron scattering studies.[80] Additionally, Kerr microscopy[84] or magnetic force microscopy,[85] which typically sense the out-of-plane component of the magnetic stray field, can be used to detect signatures of magnetic skyrmions.

2.2 Ferromagnetic perovskite oxides

In the course of this dissertation, thin films and all-oxide epitaxial heterostructures are investigated, which are based on the two ferromagnets $SrRuO_3$ and ruthenium substituted $La_{0.67}Sr_{0.33}Mn_{1-y}Ru_yO_3$. The following section aims to introduce these perovskites briefly. Motivated by the prominent debate about the origin of peculiar features in the Hall effect of $SrRuO_3$-based thin films, the initial Subsection 2.2.1 gives a brief overview of the current understanding of the anomalous Hall effect in $SrRuO_3$ as well as the ongoing discussion about the origin of the peculiar Hall features.

2.2.1 Anomalous Hall effect in $SrRuO_3$ bulk and thin film heterostructures

The 4*d* perovskite oxide $SrRuO_3$ is an itinerant ferromagnet with a Curie temperature of 160 K for single crystals and up to 150 K for thin films.[72] Single crystals of $SrRuO_3$ possess orthorhombic crystal structure at room temperature with lattice parameters $a = 5.5670\,\text{Å}$, $b = 5.5304\,\text{Å}$, and $c = 7.8446\,\text{Å}$.[86] The corresponding pseudocubic lattice constant is $a_{pc} = 3.93\,\text{Å}$.[72]

In thin film heterostructures, the crystal structure can be tailored for instance by variations of the interfacial environment, substrate-induced epitaxial strain, thickness, and temperature.[72,87,88] Bulk $SrRuO_3$ and films of minimum 4 unit cells (uc) thickness[89] exhibit metallic behavior with a kink in the temperature-dependent resistivity at the Curie temperature.[72,90]

The Hall resistivity of $SrRuO_3$ is determined by the ordinary as well as the anomalous Hall resistivity.[66,72] The non-monotonic temperature dependence of the anomalous Hall effect in (orthorhombic) $SrRuO_3$, including a sign-change from negative to positive values upon temperature increase, has already been observed experimentally in the 1990's.[91,92] However, the description of the temperature dependence of the anomalous Hall resistivity by the extrinsic contributions of side jumps and skew scattering (Equation (2.19)) was not possible.[55] In 2003, Fang *et al.* proposed the intrinsic mechanism, which is

depending on the Berry curvature in crystal momentum space, as the origin of the non-monotonic temperature evolution of the anomalous Hall effect in $SrRuO_3$.[93] Based on the assumption that the temperature dependence of the intrinsic Hall conductivity σ_{xy} originates from the temperature evolution of the spin-splitting, which is proportional to the magnetization, $\sigma_{xy}(T)$ was inferred from $\sigma_{xy}(M(T))$.[93] First-principles calculations of σ_{xy} indeed showed non-monotonous dependence on the magnetization and resembled the features of $\sigma_{xy}(T)$ qualitatively.[93] This Berry phase picture was consistent with further experimental observations of the AHE in $SrRuO_3$ thin films and heterostructures[94–97] and capable to describe the scaling of the Hall conductivity with the magnetization.[98]
The sensitivity of the intrinsic anomalous Hall contribution to the band structure was also in agreement with several investigations that demonstrated the dependence of the anomalous Hall effect on sample properties, such as thin film thickness or crystal structure, which determine the electronic band structure.[88,95,96,99,100] While the non-monotonous temperature dependence of the AHE was commonly observed in orthorhombic $SrRuO_3$ crystals and thin films, epitaxially strained $SrRuO_3$ layers of tetragonal crystal structure exhibited positive anomalous Hall constants within the ferromagnetic temperature range.[88,95] Furthermore, the anomalous Hall constant was shown to depend on the thickness of the epitaxial thin films in a non-trivial manner.[99,100] Mizuno *et al.* induced changes of the electronic conduction band filling by the application of gate voltages, which led to modifications of the AHE magnitude and sign.[96] However deviations, for instance in the high carrier scattering regimes,[98] emphasized the incompleteness of the purely intrinsic description.[98,100,101]

In the past years, further theoretical studies predicted the existence of Weyl nodes in the band structure of $SrRuO_3$, acting as magnetic monopoles in momentum space, which yield strong contributions to the Berry curvature that determines the intrinsic anomalous Hall effect.[93,102–105] Fingerprints of the presence of Weyl fermions were experimentally observed in the spin dynamics, studied by neutron Brillouin scattering,[103] in the optical Hall conductivity, investigated by Faraday rotation in the terahertz range,[106] and in the magnetotransport.[107] Furthermore, angle-resolved photoemission spectroscopy verified the theoretical calculation of the band structure in the tight-binding model in the ultrathin (2D) limit.[105] Considering the Berry curvature enhancement due to the existence of Weyl nodes in the band structure, theoretical calculations demonstrated that the sign of the intrinsic anomalous Hall effect can be tailored by varying the film thickness,[105,108] magnetization and temperature,[105,108] chemical potential,[105] disorder,[108] or interfacial environment.[104,109]

In 2016, the research interest in the Hall effect of $SrRuO_3$ was renewed due to the observation of peculiar hump-like anomalies in the Hall resistivity hysteresis loops of $SrRuO_3$-$SrIrO_3$ bilayers.[81]
The peculiar features (see Fig. 2.8) were present only in bilayers with $SrRuO_3$ layers of 4-6 MLs thickness.[81] Since the unconventional behavior could not be explained by the anomalous Hall effect of the $SrRuO_3$ film, which was assumed to be proportional to the perpendicular component of the sample magnetization, the effect was attributed to a topological Hall effect generated by the presence of skyrmions.[81] The existence of an interfacial DMI, enabling the generation of Néel-type skyrmions, was inferred based on the fulfillment of the broken spatial inversion symmetry at the bilayer interface in combination with the strong spin-orbit coupling of the $5d$ Iridium ions in the ultrathin $SrIrO_3$ layers[81] (but only for 4-6 MLs thick $SrRuO_3$ layers). In order to support the explanation of the THE-like features in the Hall resistivity by the formation of skyrmions, magnetic force microscopy of a 5 uc $SrRuO_3$/ 2 uc $SrIrO_3$ was performed. The observation of tiny (< 10 nm) objects of spherical shape present in consecutive difference images was interpreted as indication of skyrmions.[81]
Furthermore, the efficient modulation of the topological Hall effect anomalies were shown in the inverse $SrRuO_3/SrIrO_3$ structure by the application of a gate voltage.[110]
Initiated by this proposal of tiny skyrmions, several magnetotransport studies were performed on ultrathin bare $SrRuO_3$ films[111–123] or $SrRuO_3$-$SrIrO_3$ heterostructures,[104,109,110,124–127] which drew contradictory conclusions either in favor of the existence of magnetic skyrmions,[81,110,112,113,121,125,127,128] or Berry curvature effects in momentum space.[111,116–118]
An alternative interpretation of the hump-like anomalies present in the Hall measurements is the summation of multiple conduction channels that contribute to the total anomalous Hall resistivity[109,129–131] (see Fig. 2.9). The existence of multiple anomalous Hall channels in $SrRuO_3$ layers was related to spatially inhomogeneous magnetoelectric characteristics,[116,118–120,126,132,133] e.g. due to thickness variations in ultrathin $SrRuO_3$ layers[119,132,133] or interfacial modifications.[109]

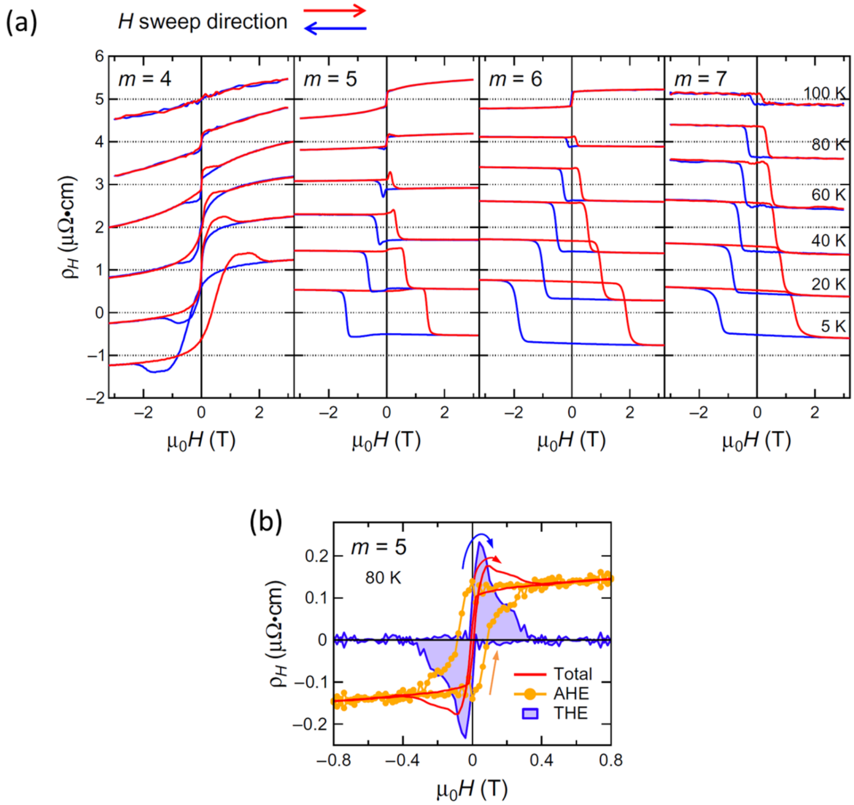

Figure 2.8: (a) Magnetic field dependence of the Hall resistivity (ρ_H) of the $(\mathrm{SrRuO_3})_m$-$(\mathrm{SrIrO_3})_2$ bilayers (m = 4, 5, 6, and 7) at various temperatures. Red and blue represent sweep directions of the magnetic field. The ordinary Hall term is subtracted by the linear fitting in a higher magnetic field region. (b) Contribution from AHE (yellow) and THE (blue) of the $(\mathrm{SrRuO_3})_m$-$(\mathrm{SrIrO_3})_2$ bilayer with m = 5 at 80 K. Figure adapted from Ref. [81], published under a Creative Commons Attribution NonCommerical license 4.0 (CC BY-NC), ©2016, K.-Y. Meng, A. S. Ahmed, M. Baćani, A.-O. Mandru, X. Zhao, N. Bagués, B. D. Esser, J. Flores, D. W. McComb, H. J. Hug, and F. Yang: Observation of Nanoscale Skyrmions in $\mathrm{SrIrO_3}$ / $\mathrm{SrRuO_3}$ Bilayers, Nano Letters 19, 3169– 3175 (2019), doi: 10.1021/acs.nanolett.9b00596.

Based on the HAADF-STEM study of a high-quality 30 nm $\mathrm{SrRuO_3}$ film that revealed the existence of strain-relaxation-induced distinct structural regions, Miao *et al.* attributed the THE-like Hall anomalies to the combination of AHE contributions from distinct domains.[120] Also the relation to off-stoichiometry leading to inhomogeneous ferromagnetism was discussed.[111,134]

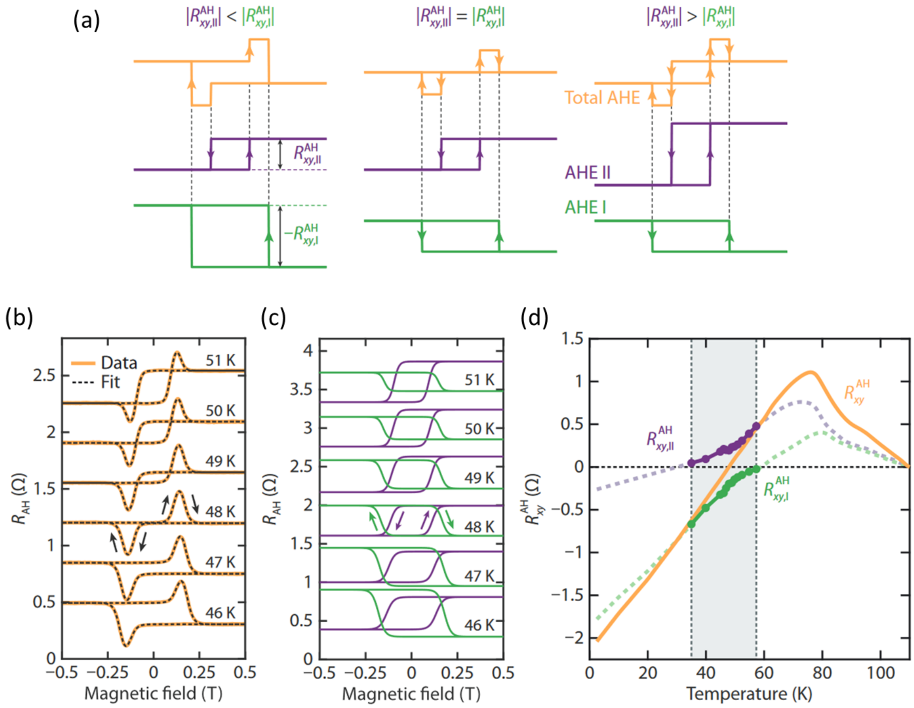

Figure 2.9: (a) Schematics of the two-channels anomalous Hall effect model for distinct sizes of the Hall resistance for the two channels I and II. (b) Anomalous Hall resistance loops of a $SrRuO_3/SrIrO_3$ bilayer (yellow). Plotted with the dashed line is the fit associated with the two-channel model. (c) Both anomalous Hall channels extracted from the fits in (b). Anomalous Hall resistances of channel I (green) and II (purple) of the determined fits as function of temperature (d). Figures adapted from Ref. [109] (published under Creative Commons Attribution 4.0 International license, ©2020, D. J. Groenendijk, C. Autieri, T. C. van Thiel , W. Brzezicki, J. R. Hortensius , D. Afanasiev, N. Gauquelin, P. Barone , K. H. W. van den Bos, S. van Aert , J. Verbeeck, A. Filippetti, S. Picozzi, M. Cuoco, and A. D. Caviglia, Berry phase engineering at oxide interfaces, Physical Review Research **2**, 023404 (2020), doi:10.1103/PhysRevResearch.2.023404.).

Kim *et al.* suggested that the existence of regions with distinct magneto-electric and magnetic properties arises from the non-random distribution of off-stoichiometry in 30 nm thick $SrRuO_3$ films.[134] Regions with smaller defect densities were proposed to have a larger AHE sign-change temperature and the coercive field was shown to depend on the stoichiometry.[134] The existence of intrinsic and extrinsic anomalous Hall mechanisms in $SrRuO_3$ ultrathin films was proposed as further possible origin for the peak-like features, which was concluded from the modulations of the THE-like anomalies by the application of gate voltages that showed identical effects on the humps and on the saturated anomalous Hall resistivity.[117]

In addition to the Hall studies of systems that involve a single $SrRuO_3$ layer, the study by van Thiel *et al.* as well as our study, which will be addressed in detail in Chapter 6, showed the generation of hump-like features of the Hall loops by heterostructuring two $SrRuO_3$ layers with distinct switching fields and anomalous Hall constants, separated by nonmagnetic spacers.[130,131]

The observation of Hall signals akin to a topological Hall effect were not only observed in $SrRuO_3$ films or when interfaced with $SrIrO_3$, but also in superlattices with other ferromagnets,[135] multiferroics,[136] or nonmagnetic insulators.[108] In case of the interfacing of $SrRuO_3$ with $Pr_{0.7}Ca_{0.3}MnO_3$,[135] the structure of the $SrRuO_3$ was found to be modified by tailoring of the oxygen octahedra tilt angles. The Hall anomalies were then attributed to the superposition of Hall voltages originating from the observed orthorhombic- and tetragonal-like parts of the $SrRuO_3$ layer.[135]

However, the origin of the peculiar anomalies mimicking a topological Hall effect is still under debate.

In order to shed light on this discussion that was sometimes based mainly on magnetotransport studies only,[121,124,128] real space imaging techniques were applied.

Nanometer-sized, isolated bubble-like domains were observed in magnetic force microscopy studies of a 10 uc $SrRuO_3$/2 uc $SrIrO_3$ bilayer (see Fig. 2.10), appearing in the same magnetic field region where the THE-like features on the order of $0.15\,\mu\Omega\,\mathrm{cm}$ were seen.[125] This agreement led to the conclusion of the existence of magnetic skyrmions.[125] On the other hand, the skyrmion diameter of about 6 nm at 5 K, which was calculated from the maximum of the resistivity hump,[125] was smaller than the experimental resolution of 10 nm and smaller than the average size of the magnetic bubbles of less than 20 nm observed in the MFM images.[125]

In contrast to the study by Meng *et al.*, the magnetic force microscopy study of a capped ultrathin $SrRuO_3$-$SrIrO_3$ heterostructure revealed the existence of THE-like features without the formation of magnetic skyrmions,[132] as further discussed in Chapter 4.

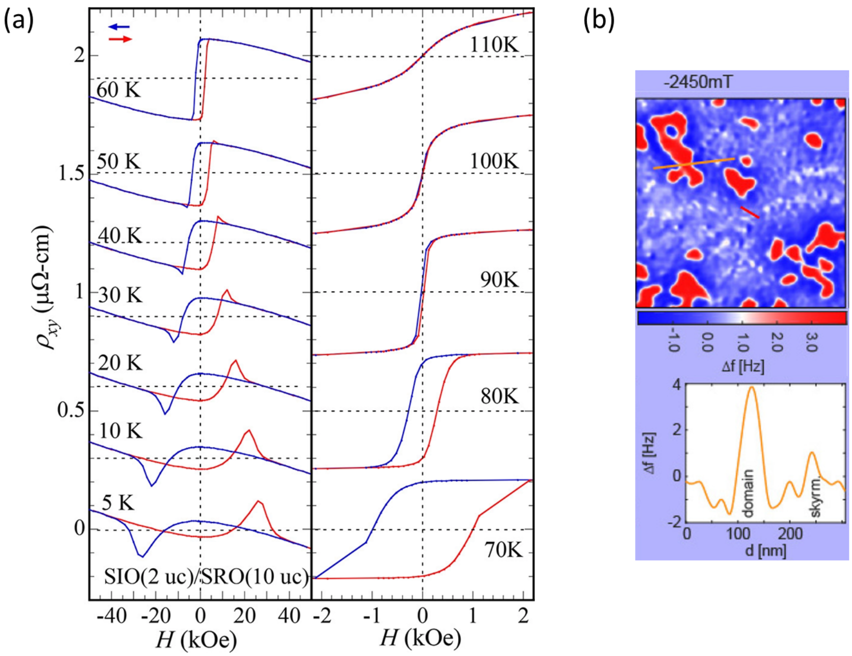

Figure 2.10: (a) Hall effect study of a 10 uc $SrRuO_3$/ 2 uc $SrIrO_3$ bilayer. (b) MFM image of the same bilayer at 10 K, taken at −2450 mT. The bottom row shows a cross section taken along the orange line in the MFM image. Figures adapted from Ref. [125]. Adapted with permission from K.-Y. Meng, A. S. Ahmed, M. Baćani, A.-O. Mandru, X. Zhao, N. Bagués, B. D. Esser, J. Flores, D. W. McComb, H. J. Hug, and F. Yang: Observation of Nanoscale Skyrmions in $SrIrO_3$ / $SrRuO_3$ Bilayers, Nano Lett. 2019, 19, 3169-3175, Copyright 2019 American Chemical Society.

The ongoing debate about the origin of the frequently observed THE-like Hall features is manifested by several studies on similar $SrRuO_3$-based systems that give contradictory interpretations of the experimental data. Skoropata *et al.* observed anomalies in the Hall effect after low-energy helium irradiation of 20 nm $SrRuO_3$ films.[137] Due to the depth-dependent magnetization gradient in the film, revealed by polarized neutron reflectometry, they attributed the peculiar features to the summation of multiple Hall channels.[137] In contrast, Wang *et al.* related the THE-like features in 60 nm $SrRuO_3$, irradiated by helium ions, to DMI arising from the broken inversion symmetry generated by the defect engineering.[112]

The defects were found to modify the oxygen octahedral tilts and thereby induce an orthorhombic-tetragonal phase transition within the film.[112] Similarly, Li *et al.* showed experimentally the controlled proton insertion in $SrRuO_3$ thin films by ionic liquid gating and thereby generated a gradient of the concentration of protons across the film thickness, which was proposed to account for the observed THE-like Hall features.[114]

While off-stoichiometry or non-homogeneous stoichiometry was considered in several studies in $SrRuO_3$ thin films to generate multiple anomalous Hall conduction channels, reproducing the peculiar Hall loop anomalies,[111,134] the interface between stoichiometric and oxygen deficient regions was suggested to induce interfacial DMI.[138] In the study by Lu *et al.*, oxygen vacancies diffused from the $SrTiO_3$ substrate to the $SrRuO_3$, which caused the formation of regions with distinct stoichiometry.[138] The argumentation was supported by density functional theory (DFT) and the finding of few, isolated magnetic bubbles as well as THE-like features, observed by MFM and transport investigations, respectively.[138]

Also when thin $SrRuO_3$ layers were interfaced with a ferroelectric, peculiar Hall anomalies were observed.[139] Induced by the ferroelectricity, the ionic displacement in $BaTiO_3$ was found to continue for some monolayers in $SrRuO_3$ and was proposed to create DMI at the $SrRuO_3/BaTiO_3$ interface, since it breaks the inversion symmetry.[139] On the other hand, Ren *et al.* showed the possibility to explain the transport anomalies by multiple Hall channels in the inhomogeneous $SrRuO_3$ layer in $SrRuO_3$-$BiFeO_3$ bilayers.[136] Confirmed by band structure calculations, it was furthermore demonstrated that the anomalous Hall effect in $SrRuO_3$ can be varied by polarization-field-induced effects in $SrRuO_3$-$BiFeO_3$-heterostructures.[136]

Recently, also Néel-type chiral domain walls were proposed to account for the THE-like features in 4 uc thick $SrRuO_3$ thin films, deposited on $SrTiO_3$.[115] Here, resonant soft x-ray scattering investigations at the oxygen K edge, supported by theoretical simulations, were utilized to demonstrate the existence of a chiral Néel-type spin structure.[115] The formation of periodic chiral domains was proposed by Seddon *et al.* in $SrRuO_3$-$PbTiO_3$ bilayers, based on MFM investigations and DFT.[140]

Moreover, THE-like features were observed in ultrathin $SrRuO_3$ thin films, which were capped by $SrTiO_3$, not only at low temperatures, but also above the ferromagnetic transition temperature.[141] Supported by Monte-Carlo- Simulations, the observation of the peculiar Hall features in the paramagnetic phase was attributed to spin chirality fluctuations.[141]

Despite the variety of both experimental and theoretical studies as well as the improvement of the understanding of the anomalous Hall effect in $SrRuO_3$, a consensus on the true origin of the Hall anomalies mimicking a topological Hall effect does not exist up to now.

2.2.2 $La_{1-x}Sr_xMnO_3$

$La_{1-x}Sr_xMnO_3$(LSMO) crystallizes in a (distorted) ABO_3-perovskite structure, with the La^{3+} and Sr^{2+} ions located on the A-sites.[46] The Mn ions are on the B-sites, surrounded by six oxygen ions that build the MnO_6 octahedra. Due to the different ionic radii, the MnO_6 octahedra are rotated so that the crystal structure of LSMO gets distorted and deviates from the ideal cubic perovskite structure (cf. Fig. 2.11 (a)).[46] This distortion is described by the Goldschmidt tolerance factor t, which is governed by the ionic radii of the cations r_i: $t = (r_A + r_O)/(\sqrt{2}(r_B + r_O))$. r_O is the ionic radius of O^{2-}.[142]

Lanthanum strontium manganite crystals exhibit a rich structural, magnetic, and electronic phase diagram as function of the strontium concentration x, as presented in Fig. 2.12 (b).

Upon increase of x and/or temperature[7], the structural transition from an orthorhombic crystal structure ($t < 0.96$[143]) to rhombohedral structure ($0.96 < t < 1$[143]) was observed in LSMO single crystals.[144,145] This transition takes place at room temperature for Sr concentration $x = 0.175$ (cf. Fig. 2.11 (b))[144] or can be induced thermally when $0.15 < x < 0.2$.[145]

The octahedral rotations of the rhombohedral crystal structure, with $R\overline{3}c$ space group symmetry, are described by Glazer's tilt system by $a^-a^-a^-$, corresponding to out-of-phase rotations around the cubic <100> crystal axes.[146]

The lattice parameters of $La_{0.7}Sr_{0.3}MnO_3$ are $a = b = c = 0.5471\,\text{nm}$ with $\alpha = \beta = \gamma = 60.43°$.[146,147] If the rhombohedral unit cell is described in a pseudocubic manner by a tilted fcc cell,[148] the corresponding pseudocubic lattice parameter is $a_{pc} = 0.3876\,\text{nm}$.[149]

---

[7] Since the magnetism in LSMO is dictated by the double exchange mechanism and thereby strongly depends on the Mn-O-Mn bond angle, the manipulation of the crystal structure by the application of magnetic fields in a suitable temperature and composition range was shown by Asamitsu *et al.*[145]

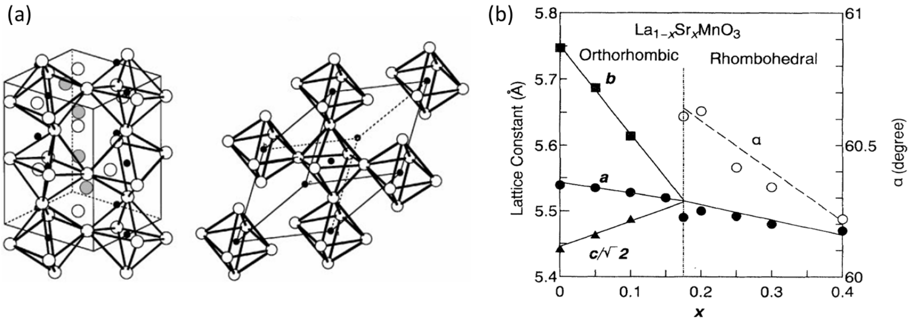

Figure 2.11: (a) Schematic structures of distorted perovskites of manganite; orthorhombic (left) and rhombohedral (right). Figure adapted from Ref. [143]. (b) Lattice parameters for $La_{1-x}Sr_xMnO_3$ crystals at room temperature. Figure (b) reproduced from Ref. [144]. Figure (a) reprinted from Journal of Magnetism and Magnetic Materials **200** (1999), Y. Tokura, Y. Tomioka: Colossal magnetoresistive manganites, p. 1-23, Copyright (1999), with permission from Elsevier. Figure (b) reprinted with permission from A. Urushibara, Y. Moritomo, T. Arima, A. Asamitsu, G. Kido, and Y. Tokura, Physical Review B **51**, 14103 (1995), Copyright 1995 by the American Physical Society.

Magnetism and electronic properties

While the *3d* orbital state is fivefold degenerate in case of isolated manganese ions, a cubic crystal field induces the splitting into the three lower lying t_{2g} and two higher lying e_g levels (cf. Fig. 2.12 (a)).[46] Determined by the concentration of the divalent Sr^{2+}, the Mn ions are present in a mixed valence state of Mn^{3+} and Mn^{4+} in order to achieve charge neutrality of the LSMO crystal. According to Hund's rule, only the t_{2g} orbitals are occupied by three electrons in case of Mn^{4+} $(3\,\mathrm{d}^3, \mathrm{t}_{2g}^3 \mathrm{e}_g{}^0)$, while one e_g state is occupied in case of $Mn^{3+}(3\,\mathrm{d}^4, \mathrm{t}_{2g}^3 \mathrm{e}_g{}^1)$.[46] Due to the instability of the latter state, the degeneracy of the energy levels is further lifted by the Jahn Teller distortion of the MnO_6 octahedra so that the Mn ions experience a tetragonal crystal field.[49] The influence of epitaxial strain on these energy levels will be addressed in the subsequent chapter on the magnetic anisotropy in LSMO thin films.

The magnetism in manganites is dictated by the (indirect) exchange interactions between the Mn ions, mediated by oxygen ions.[49] In case of strontium doped lanthanum manganite, these interactions are dominated by the double exchange, which was originally proposed by Zener[150,151] and explains the ferromagnetic ordering in mixed valence manganites.[46,150,151] In the double exchange model, the electron of the Mn^{3+} e_g orbital hops to the oxygen *2p*-orbital and simultaneously an electron from the oxygen *2p*-orbital hops to the unoccupied e_g orbital of Mn^{4+} (only) when the Mn spins are aligned parallel.[151]

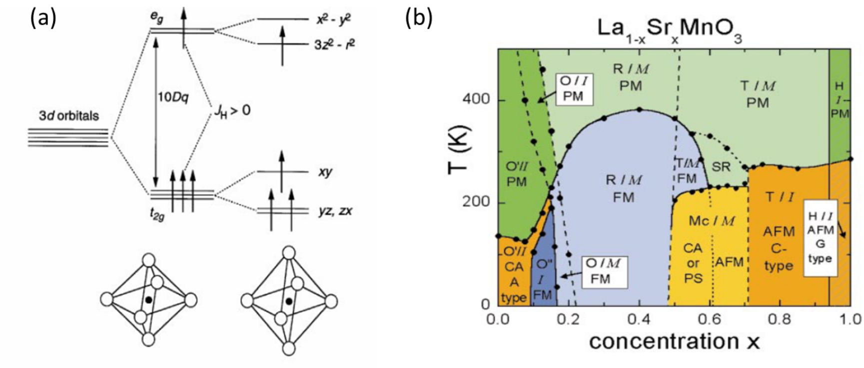

Figure 2.12: (a) Crystal-field splitting of five-fold degenerate atomic *3d* levels into lower t_{2g}(triply degenerate) and higher e_g (doubly degenerate) levels. Jahn-Teller distortion of MnO_6 octahedron further lifts each degeneracy. Figure adapted from Ref. [143]. (b) Phase diagram of $La_{1-x}Sr_xMnO_3$ for the complete concentration regime. The crystal structures (Jahn-Teller distorted orthorhombic: O', orthorhombic: O, orbital-ordered orthorhombic: O", rhombohedral: R, tetragonal: T, monoclinic: Mc, and hexagonal: H) are indicated as well as the magnetic structures [paramagnetic: PM (green), shortrange order (SR), canted (CA), A-type antiferromagnetic structure: AFM (yellow), ferromagnetic: FM (blue), phase separated (PS), and AFM C-type structure] and the electronic state [insulating: I (dark), metallic: M (light)]. Figure (a) reprinted from Journal of Magnetism and Magnetic Materials **200** (1999), Y. Tokura, Y. Tomioka: Colossal magnetoresistive manganites, p. 1-23, Copyright (1999), with permission from Elsevier. Figure (b) reprinted from Ref. [152], with permission from J. Hemberger, A. Krimmel, T. Kurz, H.-A. Krug von Nidda, V. Yu. Ivanov, A. A. Mukhin, A. M. Balbashov,and A. Loidl, Physical Review B **66**, 094410 (2002), Copyright 2002 by the American Physical Society.

In case of strong Hund's coupling, the generalization of the double exchange model by Anderson and Hasegawa[8] showed that the absolute magnitude of the effective hopping is proportional to $\cos\theta/2$. Here, the angle θ is between the orientation of neighboring spins and is therefore maximized for parallel alignment ($\theta = 0$).[143,155] In that way, the electron hopping process leads to the lifting of the otherwise energetic degeneracy of the $Mn^{3+}-O^{2-}-Mn^{4+}$ and

---

[8] A quantummechanical description of the DE mechanism was developed by Kubo and Ohata.[153,154]

$Mn^{4+}-O^{2-}-Mn^{3+}$ bond configurations[46] and the energetic lowering for ferromagnetic alignment of neighboring Mn spins.[155]

Another important exchange mechanism in manganites is the so-called superexchange interaction between manganese ions of identical valence states. Described by the Goodenough-Kanamori rules,[156–158] the interaction between Mn^{4+} ions, mediated by an oxygen ion, is antiferromagnetic. In case of Mn^{3+}-O-Mn^{3+}, the superexchange interaction can be antiferromagnetic for 180° or ferromagnetic for 90° angle between the Mn *3d* orbitals.[156–158]
The competition between the different exchange mechanisms leads to the rich magnetic phase diagram of LSMO as function of strontium concentration,[46] shown in Fig. 2.12 (b). Single crystals of $La_{1-x}Sr_xMnO_3$ are ferromagnetic at low temperatures for strontium concentrations between 0.1 and about 0.5, which is approximately the regime where LSMO is also metallic.[152] The maximum transition temperature and a half-metallic state was observed for $x = 1/3$, which is the compound of main interest for this thesis. For further information on the charge-ordered or orbital-ordered states of $La_{1-x}Sr_xMnO_3$, the reader is referred to one of the review articles.[46,49,143]
Due to the strong quenching of the orbital contribution to the magnetic moment,[159] the total magnetic moment of LSMO is governed by the spin moment of the Mn ions. Following Hund's rule, the Mn^{3+} ions with electronic configuration $3\,d^4, t_{2g}^3 e_g^{\ 1}$ with $S = 2$ have a magnetic moment of 4 μ_B and Mn^{4+} ($3\,d^3, t_{2g}^3 e_g^{\ 0}$ with $S = 3/2$) of 3 μ_B.[46]

The Jahn Teller distortions and the double exchange mechanism lead to the strong coupling of lattice, charge, and spin degree of freedom in $La_{1-x}Sr_xMnO_3$.[46] For a strontium concentration around 1/3, a transition from the ferromagnetic-metallic to paramagnetic-insulating state is observed as function of temperature,[46] which can be explained in a simplified picture by the dominance of the double exchange mechanism. In mixed valence LSMO in the ferromagnetic, metallic state, the t_{2g} electrons are considered as localized, while the electrons of the e_g states are delocalized and determine the electronic transport.[46] The relation between the ferromagnetic alignment of Mn spins and the metallic properties was initially proposed already by Zener within the double exchange mechanism.[151] Is the Mn-O bond-length increased, or the Mn-O-Mn bond angle deviating from 180°, the hopping integral of e_g electrons between Mn ions and therefore the electron bandwidth will be reduced. This leads to an increase of the resistivity.[143] Thus, the bandwidth and the band filling can be tuned by the strontium concentration in LSMO.[143]

Below the ferromagnetic transition temperature T_c, the resistivity can then be described reasonably by $\rho \approx \rho_0 + aT^2$.[46] Upon increasing temperature, thermal fluctuations and the corresponding scattering of conduction electrons and disordered spins cause the increase of resistivity.[143] Above T_c, additionally local lattice distortions due to hopping electrons (Jahn-Teller polarons)[46] and magnetic disorder induced localization of charge carriers[160] are mechanisms proposed to explain the insulating behavior. Here, the realignment of the Mn spins and therefore the increase of the hopping probability can be realized by the application of an external magnetic field, which is at the core of the (simplified) explanation for the occurrence of the collosal magnetoresistance (CMR) in mixed valence manganites. The CMR is maximized around T_C, reaching values of about 50 % in $La_{2/3}Sr_{1/3}MnO_3$ films,[47] whereas it is strongly reduced at low temperatures due to the reduced influence of the external magnetic field when the DE mediated ferromagnetic order is strong even in zero field.[46]

$La_{2/3}Sr_{1/3}MnO_3$ is a half metal with almost 100 % spin polarization due to the strong Hund's coupling exceeding the electron bandwidth.[46,143,154,161]

The ordinary Hall constant in LSMO single crystals has a positive sign with a weak dependence on stoichiometry when $0.18 \leq x \leq 0.5$.[161,162] Due to the discrepancy between the calculated charge carrier density of the ordinary Hall constant in a single-band model and the carrier concentration theoretically expected for the specific LSMO composition, the ordinary Hall effect needs to be described in a multiband-model.[161,163]

A negative anomalous Hall (AHE) constant with increasing absolute magnitude upon increasing temperature up to T_c was observed in LSMO single crystals.[162] The AHE was related to the intrinsic mechanism due to the Berry phase that is picked up by the conduction electrons, which need to follow the local spin texture (due to the strong Hund's coupling in LSMO).[154,164] Here, Ye *et al.* attributed the acquired Berry phase to the hopping of carriers in a nontrivial spin background in CMR manganites.[164]

LSMO thin films

Due to the strong dependence of the magnetic and electronic properties on the Mn-O-Mn angle as well as the Mn-O bond length, strain engineering by heteroepitaxial growth is an efficient way to tailor the properties of LSMO thin films. The lattice mismatch $\delta = (a_{\text{substrate}} - a_{\text{film}})/a_{\text{substrate}}$ between the in-plane lattice parameter of the substrate $a_{\text{substrate}}$ and of the bulk value of the film a_{film} causes the adjustment of the film lattice parameters.[46] Since the unit cell volume has to stay constant in first approximation, the shortening (elongation) of the in-plane lattice parameters causes the elongation (shortening) of the out-of-plane lattice parameter in case of compressive (tensile) strain. For LSMO thin films, this epitaxial strain leads to the compression or elongation of the MnO_6 octahedra and therefore to a tetragonal crystal field that splits the degeneracy of the e_g levels in the $3z^2 - r^2$ and $x^2 - y^2$ orbitals, as schematically shown in Fig. 2.13.[165] This causes the preferential occupation of one of the states depending on the induced epitaxial strain.[166]

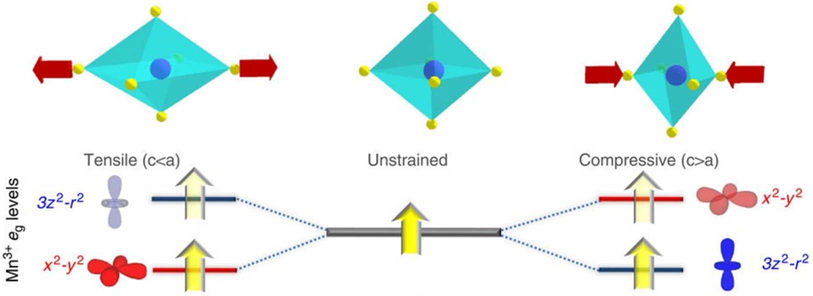

Figure 2.13: Top panel: Scheme of the influence of the epitaxial strain on the MnO_6 octahedral distortions; bottom panel: Effect of the strain-induced distortions on the e_g levels of Mn^{3+} ions. Figure adapted from Ref. [165]. Subfigure reproduced with permission from Springer Nature: Nature Communications, **3**, 1189 (2012), Surface symmetry-breaking and strain effects on orbital occupancy in transition metal perovskite epitaxial films, D. Pesquera, G. Herranz, A. Barla, E. Pellegrin, F. Bondino, E. Magnano, F. Sánchez, Copyright (2012).

X-ray linear dichroism studies of LSMO thin films confirmed experimentally the preferential electronic occupation of the $3z^2 - r^2$ over the $x^2 - y^2$ state in case of compressively strained films, while tensile strain[9] favors the occupation of the $x^2 - y^2$.[165,168,169]

The preferential $3z^2 - r^2$ occupancy leads to a ferromagnetic coupling of spins in neighboring Mn ions along the z-axis and thus favors perpendicular magnetic anisotropy.[170,171]

---

[9] Additional symmetry breaking at free surfaces or interfaces was observed in ultrathin LSMO films that lead to the occupation of the out-of-plane $3z^2 - r^2$ orbital even in unstrained or tensile strained ultrathin films.[165,167]

In addition to the compression or elongation of the MnO_6 octahedra, the lattice parameter accommodation in LSMO is realized by rotation and tilting of the octahedra.[46]

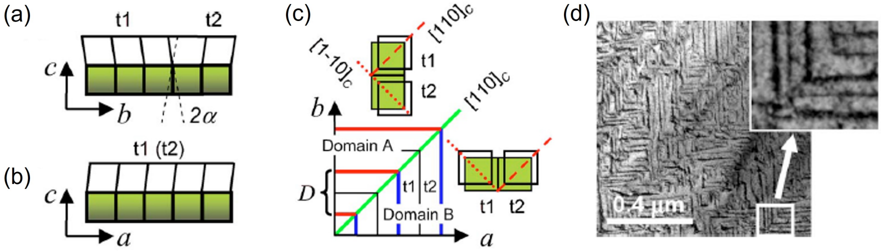

Figure 2.14: $La_{0.7}Sr_{0.3}MnO_3$ thin film deposited on LSAT(100). Schematic side views along [100] (a) and [010] (b) of a twinned domain in real space. In (c), the in-plane domain structure shows stripes along [100] (domain A) and along [010] (domain B), and the insets show twinning of the structure by tilting the pseudocubic (100) or $(1\bar{1}0)$ plane. (d) TEM plane-view images of an $La_{0.7}Sr_{0.3}MnO_3$ thin film deposited on LSAT(100). Figures adapted from Ref. [172]. Subfigures reproduced from S. W. Jin, G. Y. Gao, Z. Huang, Z. Z. Yin, X. Zheng, and W. Wu, Shear-strain- induced low symmetry phase and domain order in epitaxial $La_{0.7}Sr_{0.3}MnO_3$ thin films, Applied Physics Letters **92**, 261901 (2008), with the permission of AIP publishing.

When bulk rhombohedral LSMO is epitaxially grown on cubic substrates, such as on $SrTiO_3(100)$ or $(LaAlO_3)_{0.3}(Sr_2TaAlO_6)_{0.7}(100)$ (LSAT), the film experiences lattice-mismatch induced normal biaxial strain as well as elastic shear strain.[173,174] This angle-mismatch induced shear strain is typically relaxed by structural domain formation.[146,172–177] In contrast to the lattice-mismatch induced strain that relaxes often only in thick films of LSMO,[176] the structural domain formation was observed already in the thin film limit of 2.5 nm in case of $La_{0.7}Sr_{0.3}MnO_3$ on $SrTiO_3$.[175] The existence of these structural domains in thin films of LSMO was observed by XRD studies, (orientation contrast scanning) electron microscopy, or transmission electron microscopy.[146,172,174,175,177–180] An example of such structural domain formation in an $La_{0.7}Sr_{0.3}MnO_3$ thin film, which was deposited on LSAT(100),[172] is presented in Fig. 2.14. Viewed along [100], the domains tilt their (010) planes by an angle α, oppositely to each other (see Fig. 2.14 (a)).[172] Furthermore, they tilt their (100) planes by α in the side view along [010] (see Fig. 2.14 (b)).[172] This then leads to the formation of the twinned stripe (t_1 and

t_2) and the resulting in-plane domain structure that has perpendicular stripes, sketched in Fig. 2.14 (c), which was observed by TEM plane-view images (cf. Fig. 2.14 (d)).[172]

The details of the substrate morphology, such as the substrate miscut and miscut direction, determine the characteristics of the structural domains.[177,181] While cubic substrates with a small miscut angle were found to allow the formation of four possible domain variants for the rhombohedral LSMO,[182] vicinal cubic substrates with larger miscut allow only 2-variant LSMO domains.[181,183] It was shown by Boscker *et al.* that periodic twinning is dominant for 2-variant films, with the out-of-plane modulations parallel to the step edges so that the structural domain walls were observed perpendicular to the step edges.[183]
In contrast, terrace step-edge induced long-range structural modulations,[146] often with periodic microtwinning, were seen in 4-variant films,[183] attributed to the preferred initial nucleation at step edges.[183] Two types of domains oriented along the [100] and [010] cubic axes were seen aligned perpendicularly to each other. Especially in case of biaxial (isotropic) lattice-mismatch-induced epitaxial strain, unidirectional structural domains or modulations in LSMO impact on the orbital occupancy of the Mn ions and thus strongly influence the magnetic properties, such as the magnetic anisotropy or transition temperature.[177,181,184]

Further interface effects that can alter the material properties of LSMO thin films are inversion symmetry breaking[185] and charge transfer at the interfaces with the layers with which the LSMO layers are epitaxially stacked.[186] Additionally, the magnetic anisotropy can be tailored by the control of the oxygen octahedral rotation at interfaces of LSMO and perovskites exhibiting strong spin-orbit coupling.[12]
In the framework of this thesis, the focus is on Ru-substituted $La_{0.67}Sr_{0.33}MnO_3$ thin films deposited on LSAT(100). Thus, the substrate-induced compressive strain of the order of 0.2 % for zero ruthenium substitution is small. The magnetic anisotropy of undoped LSMO films depends strongly and nontrivially on temperature and film thickness, as studied in detail by S.K. Chaluvadi.[149] Weak uniaxial in-plane anisotropy was observed in 50 nm thick films at room temperature, while biaxial combined with uniaxial anisotropy was seen in 25 nm, and strong uniaxial in-plane anisotropy was found in 12 nm thick LSMO films.[149] The competition of several contributions to the total magnetic

anisotropy, which all depend individually on strain and film thickness, was considered as origin of the nontrivial thickness dependence.[149] At low film thicknesses, the uniaxial anisotropy was attributed to step-surface induced anisotropy or to octahedral rotations, whereas the biaxial anisotropy contribution was related to strain-induced anisotropy.[149] At higher and intermediate thicknesses, the biaxial contribution was related to the magnetocrystalline anisotropy and the uniaxial contribution was attributed to the orthorhombicity of LSMO.[149]

Due to the small compressive strain imposed by the LSAT substrate, also a small out-of-plane canting of the magnetization was observed.[149]

Ruthenium substituted $\mathbf{La_{0.67-0.7}Sr_{0.33-0.3}Mn_{1-x}Ru_xO_3}$

When the Mn ions are partially substituted by ruthenium, the lattice parameters of the distorted perovskite structure are modified due to the distinct ionic radii of the ruthenium and manganese ions. Ruthenium substitution of manganese (up to 60 %[187,188]) causes an increase of the unit cell volume due to the larger ionic radius of Ru,[188,189] but does not lead to a deviation from the structure of the parent compound LSMO.[187,189]

Furthermore, it strongly impacts on the double exchange mechanism in LSMO due to the modification of the Mn^{3+}-O-Mn^{4+} arrangement.[188] However, in contrast to the strong reduction of the ferromagnetic transition temperature by the B-site substitution with Al^{3+} or Fe^{3+}, ruthenium doping of $La_{0.67-0.7}Sr_{0.33-0.3}Mn_{1-x}Ru_xO_3$ up to 15 % was found to lead only to a moderate decrease[10] of T_c.[187,188,191] This difference was attributed to the more delocalized electrons of 4*d* ruthenium so that Ru-O-Mn exchange was expected, stabilizing the magnetic ordering instead of the disordering behavior that was typically observed for other B-site substitutes.[190,191] Indeed, x-ray photoelectron spectroscopy studies revealed the existence of mixed valence[11] of Ru^{4+} and Ru^{3+} that proposes the interplay of Ru^{3+}/Ru^{4+}- Mn^{3+}/Mn^{4+} pairs.[187,188,191]

The observed reduction of the saturation magnetization was attributed to antiferromagnetic superexchange between manganese and ruthenium.[188,190]

---

[10] A moderate increase of T_c was observed upon 5% Ru substitution in $La_{0.6}Sr_{0.4}MnO_3$ thin films on $SrTiO_3$.[190]

[11] Additional Ru^{5+} valence was proposed in the high doping regime above 50 % Ru substitution.[188]

The spin moment of $La_{0.7}Sr_{0.3}Mn_{1-x}Ru_xO_3$ in the low doping regime (x $\leq$ 0.5) is given by:[188]

$$\mu_S(x \leq 0.5) = [4(0.7-0.7x) - 3(0.7x) + 3(0.3-3x) + 2(0.3x)]\mu_B \qquad (2.24)$$

Indeed, x-ray absorption spectroscopy combined with x-ray circular dichroism studies of 50 nm 5 % Ru-doped $La_{0.6}Sr_{0.4}MnO_3$ thin films, deposited on $SrTiO_3$, showed that the directions of the spins of Mn and Ru are opposite.[192] The orbital contribution to the total magnetic moment was found to be negligible for Mn, but finite (and parallel to the spin moment) for Ru.[192]

Caused by the partial occupancy of the degenerated t_{2g} orbitals by ruthenium electrons and significant spin-orbit coupling, strong single ion anisotropy of Ru was proposed.[190] This single ion anisotropy was later suggested as the origin of the out-of-plane tilting of the magnetic easy axis observed in compressively strained $La_{0.7}Sr_{0.3}MnO_3$ thin films upon the replacement of 10 % Mn by Ru.[193]

Up to 15 % ruthenium substitution, $La_{0.7}Sr_{0.3}Mn_{1-x}Ru_xO_3$ films still show metallic behavior, which turns semiconducting in the higher substitution regime.[188] The metal-to-insulator transition temperature, consistently larger than T_c,[188] is reduced and the resistivity is increased upon the increase of ruthenium. This was attributed to reduced hole carrier density induced by Ru^{4+} that acts as electron donors.[194] In addition, a second metal-to-insulator transition was observed at low temperatures for larger ruthenium doping in polycrystalline $La_{0.67}Sr_{0.33}Mn_{1-y}Ru_yMnO_3$ samples.[189]

References

[1] C. Kittel: *Introduction to Solid State Physics*, 8th ed. (Wiley John & Sons, New York, Nov. 2004).

[2] M. T. Johnson, P. J. H. Bloemen, F. J. A. den Broeder, and J. J. de Vries: *Magnetic anisotropy in metallic multilayers*, Reports on Progress in Physics **59**, 1409–1458 (1996).

[3] R. Gross and A. Marx: *Festkörperphysik*, 3rd ed. (de Gruyter, Berlin/Boston, Jan. 2018).

[4] P. Bruno: Physical origins and theoretical models of magnetic anisotropy, *Ferienkurse des Forschungszentrums Jülich* (Forschungszentrum Jülich, 1993) Chap. 24, 1–28.

[5] H. J. G. Draaisma and W. J. M. de Jonge: *Surface and volume anisotropy from dipole-dipole interactions in ultrathin ferromagnetic films*, Journal of Applied Physics **64**, 3610–3613 (1988).

[6] D. S. Chuang, C. A. Ballentine, and R. C. O'Handley: *Surface and step magnetic anisotropy*, Physical Review B **49**, 15084–15095 (1994).

[7] L. Néel: *Anisotropie magnétique superficielle et surstructures d'orientation*, J. Phys. Radium **15**, 225–239 (1954).

[8] U. Gradmann: *Magnetic surface anisotropies*, Journal of Magnetism and Magnetic Materials **54-57**, 733–736 (1986).

[9] M. Mathews, F. M. Postma, J. C. Lodder, R. Jansen, G. Rijnders, and D. H. A. Blank: *Step-induced uniaxial magnetic anisotropy of $La_{0.67}Sr_{0.33}MnO_3$ thin films*, Applied Physics Letters **87**, 242507 (2005).

[10] R. Arias and D. L. Mills: *Theory of roughness-induced anisotropy in ferromagnetic films: The dipolar mechanism*, Physical Review B **59**, 11871–11881 (1999).

[11] A. Encinas-Oropesa and F. Nguyen Van Dau: *Origin of magnetic anisotropy in thin films deposited on step-bunched substrates*, Journal of Magnetism and Magnetic Materials **256**, 301–305 (2003).

[12] D. Yi, C. L. Flint, P. P. Balakrishnan, K. Mahalingam, B. Urwin, A. Vailionis, A. T. N'Diaye, P. Shafer, E. Arenholz, Y. Choi, K. H. Stone, J.-H. Chu, B. M. Howe, J. Liu, I. R. Fisher, and Y. Suzuki: *Tuning Perpendicular Magnetic Anisotropy by Oxygen Octahedral Rotations in $(La_{1-x}Sr_xMnO_3)/(SrIrO_3)$ Superlattices*, Physical Review Letters **119**, 077201 (2017).

[13] P. Grünberg, R. Schreiber, Y. Pang, M. B. Brodsky, and H. Sowers: *Layered Magnetic Structures: Evidence for Antiferromagnetic Coupling of Fe Layers across Cr Interlayers*, Physical Review Letters **57**, 2442 (1986).

[14] P. Bruno: *Theory of interlayer magnetic coupling*, Physical Review B **52**, 411 (1995).

[15] J. C. Slonczewski: *Conductance and exchange coupling of two ferromagnets separated by a tunneling barrier*, Physical Review B **39**, 6995 (1989).

[16] M. A. Ruderman and C. Kittel: *Indirect exchange coupling of nuclear magnetic moments by conduction electrons*, Phys. Rev. **96**, 99 (1954).

[17] T. Kasuya: *A Theory of Metallic Ferro- and Antiferromagnetism on Zener's Model*, Progress of Theoretical Physics **16**, 45–57 (1956).

[18] K. Yosida: *Magnetic Properties of Cu-Mn Alloys*, Phys. Rev. **106**, 893 (1957).

[19] P. Bruno: *Theory of intrinsic and thermally induced interlayer magnetic coupling between ferromagnetic films separated by an insulating layer*, Physical Review B **49**, 13231 (1994).

[20] D. A. Rabson, B. J. Jönsson-Åkerman, A. H. Romero, R. Escudero, C. Leighton, S. Kim, and I. K. Schuller: *Pinholes may mimic tunneling*, Journal of Applied Physics **89**, 2786–2790 (2001).

[21] J. F. Bobo, M. Piecuch, and E. Snoeck: *Complex AF coupling for Cu-Co multilayers with low copper thickness*, Journal of Magnetism and Magnetic Materials **126**, 440–442 (1993).

[22] D. B. Fulghum and R. E. Camley: *Magnetic behavior of antiferromagnetically coupled layers connected by ferromagnetic pinholes*, Physical Review B **52**, 13436 (1995).

[23] J. J. de Vries, J. Kohlhepp, F. J. A. den Broeder, R. Coehoorn, R. Jungblut, A. Reinders, and W. J. de Jonge: *Exponential Dependence of the Interlayer Exchange Coupling on the Spacer Thickness in MBE-grown Fe/SiFe/Fe Sandwiches*, Physical Review Letters **78**, 3023 (1997).

[24] J. F. Bobo, H. Kikuchi, O. Redon, E. Snoeck, M. Piecuch, and R. L. White: *Pinholes in antiferromagnetically coupled multilayers: Effects on hysteresis loops and relation to biquadratic exchange*, Physical Review B **60**, 4131 (1999).

[25] Y. Lu, R. A. Altman, A. Marley, S. A. Rishton, P. L. Trouilloud, G. Xiao, W. J. Gallagher, and S. S. Parkin: *Shape-anisotropy-controlled magnetoresistive response in magnetic tunnel junctions*, Applied Physics Letters **70**, 2610–2612 (1997).

[26] C. L. Platt, M. R. McCartney, F. T. Parker, and A. E. Berkowitz: *Magnetic interlayer coupling in ferromagnet/insulator/ferromagnet structures*, Physical Review B **61**, 9633 (2000).

[27] L. Néel: *Sur un probleme de magnetostatique relatif a des couches minces ferromagnetiques*, Comptes Rendus Hebdomadaires Des Seances De L Academie Des Sciences **255**, 1545–1550 (1962).

[28] J. Moritz, F. Garcia, J. C. Toussaint, B. Dieny, and J. P. Nozières: *Orange peel coupling in multilayers with perpendicular magnetic anisotropy: Application to (Co/Pt)-based exchange-biased spin-valves*, Europhysics Letters **65**, 123 (2004).

[29] B. Rodmacq, V. Baltz, and B. Dieny: *Macroscopic probing of domain configurations in interacting bilayers with perpendicular magnetic anisotropy*, Physical Review B **73**, 092405 (2006).

[30] V. Baltz, A. Marty, B. Rodmacq, and B. Dieny: *Magnetic domain replication in interacting bilayers with out-of-plane anisotropy: Application to Co/Pt multilayers*, Physical Review B **75**, 014406 (2007).

[31] S. M. Mohseni, R. K. Dumas, Y. Fang, J. W. Lau, S. R. Sani, J. Persson, and J. Åkerman: *Temperature-dependent interlayer coupling in Ni/Co perpendicular pseudo-spin-valve structures*, Physical Review B **84**, 174432 (2011).

[32] K.-S. Moon, R. E. Fontana Jr., and S. S. Parkin: *Exchange-biased magnetic tunnel junctions: Dependence of offset field on junction width*, Applied Physics Letters **74**, 3690–3692 (1999).

[33] A. V. Davydenko, E. V. Pustovalo, A. V. Ognev, A. G. Kozlov, L. A. Chetbotkevich, and X. F. Han: *Néel coupling in Co/Cu/Co stripes with unidirectional interface roughness*, Journal of Magnetism and Magnetic Materials **377**, 334–342 (2015).

[34] X. Li, I. Lindfors-Vrejoiu, M. Ziese, A. Gloter, and P. A. van Aken: *Impact of interfacial coupling of oxygen octahedra on ferromagnetic order in* $La_{0.7}Sr_{0.3}MnO_3/SrTiO_3$ *heterostructures*, Scientific Reports **7**, 40068 (2017).

[35] B. D. Schrag, A. Anguelouch, G. Xiao, P. Trouilloud, Y. Lu, W. J. Gallagher, and S. S. Parkin: *Magnetization reversal and interlayer coupling in magnetic tunneling junctions*, Journal of Applied Physics **87**, 4682–4684 (2000).

[36] L. E. Nistor: "Magnetic tunnel junctions with perpendicular magnetization: Anisotropy, magnetoresistance, magnetic coupling and spin transfer torque switching", PhD Thesis (Universite de Grenoble, 2011).

[37] S. Wiebel, J.-P. Jamet, N. Vernier, A. Mougin, J. Ferŕe, V. Baltz, B. Rodmacq, and B. Dieny: *Domain decoration in dipolar coupled ferromagnetic stacks with perpendicular anisotropy*, Applied Physics Letters **86**, 142502 (2005).

[38] H. W. Fuller and D. L. Sullivan: *Magnetostatic interactions between thin magnetic films*, Journal of Applied Physics **33**, 1063–1064 (1962).

[39] L. Thomas, M. G. Samant, and S. S. Parkin: *Domain-wall induced coupling between ferromagnetic layers*, Physical Review Letters **84**, 1816 (2000).

[40] W. S. Lew, S. P. Li, L. Lopez-Diaz, D. C. Hatton, and J. A. Bland: *Mirror Domain Structures Induced by Interlayer Magnetic Wall Coupling*, Physical Review Letters **90**, 217201 (2003).

[41] J. Vogel, W. Kuch, R. Hertel, J. Camarero, K. Fukumoto, F. Romanens, S. Pizzini, M. Bonfim, F. Petroff, A. Fontaine, and J. Kirschner: *Influence of domain wall interactions on nanosecond switching in magnetic tunnel junctions*, Physical Review B **72**, 220402(R) (2005).

[42] T. Hauet, C. M. Günther, B. Pfau, M. E. Schabes, J.-U. Thiele, R. L. Rick, P. Fischer, S. Eisebitt, and O. Hellwig: *Direct observation of field and temperature induced domain replication in dipolar coupled perpendicular anisotropy films*, Physical Review B **77**, 184421 (2008).

[43] P. A. A. van der Heijden, P. J. H. Bloemen, J. M. Metselaar, R. M. Wolf, J. M. Gaines, J. T. W. M. van Eemeren, P. van der Zaag, and W. J. M. de Jonge: *Interlayer coupling between Fe_3O_4 layers separated by an insulating nonmagnetic MgO layer*, Physical Review B **55**, 11569 (1997).

[44] A. Fert and C. Vouille, Lecture Notes of the 30th summer school on magnetic thin film systems, Title: Magnetoresistance Overview: AMR, GMR, TMR, CMR, Schriften des Forschungszentrum Jülich, Materie und Material, Band 2, 1999.

[45] M. Kohler: *Theorie der magnetischen Widerstandseffekte in Metallen*, Annalen der Physik **441**, 18–38 (1950).

[46] A.-M. Haghiri-Gosnet and J.-P. Renard: *CMR manganites: physics, thin films and devices*, J. Phys. D: Appl. Phys. **36**, R127 (2003).

[47] Z. Liao, M. Huijben, G. Koster, and G. Rijnders: *Uniaxial magnetic anisotropy induced low field anomalous anisotropic magnetoresistance in manganite thin films*, APL Materials **2**, 096112 (2014).

[48] Y. Suzuki, Y. Wu, J. Yu, U. Ruediger, A. D. Kent, T. K. Nath, and C. B. Eom: *Domain structure and magnetotransport in epitaxial colossal magnetoresistance thin films*, Journal of Applied Physics **87**, 6746–6748 (2000).

[49] K. Dörr: *Ferromagnetic manganites: spin-polarized conduction versus competing interactions*, Journal of Physics D: Applied Physics **39**, R125–R150 (2006).

[50] W. Thomson: *XIX. On the electro-dynamic qualities of metals: Effects of magnetization on the electric conductivity of nickel and of iron*, Proceedings of the Royal Society of London **8**, 546–550 (1857).

[51] P. Perna, D. Maccariello, F. Ajejas, R. Guerrero, L. Méchin, S. Flament, J. Santamaria, R. Miranda, and J. Camarero: *Engineering Large Anisotropic Magnetoresistance in $La_{0.7}Sr_{0.3}MnO_3$ Films at Room Temperature*, Advanced Functional Materials **27**, 1700664 (2017).

[52] J. Velev, R. F. Sabirianov, S. S. Jaswal, and E. Y. Tsymbal: *Ballistic anisotropic magnetoresistance*, Physical Review Letters **94**, 127203 (2005).

[53] R. P. van Gorkom, A. Brataas, and G. E. W. Bauer: *Negative domain wall resistance in ferromagnets*, Physical Review Letters **83**, 4401 (1999).

[54] G. Tatara and H. Fukuyama: *Resistivity due to a domain wall in ferromagnetic metal*, Physical Review Letters **78**, 3773 (1997).

[55] L. Klein, Y. Kats, A. F. Marshall, J. W. Reiner, T. H. Geballe, M. R. Beasley, and A. Kapitulnik: *Domain Wall Resistivity in* $SrRuO_3$, Physical Review Letters **84**, 6090–6093 (2000).

[56] A. D. Kent, J. Yu, U. Rüdiger, and S. S. P. Parkin: *Domain wall resistivity in epitaxial thin film microstructures*, Journal of Physics: Condensed Matter **13**, R461–R488 (2001).

[57] M. Viret, Y. Samson, P. Warin, A. Marty, F. Ott, E. Søndergård, O. Klein, and C. Fermon: *Anisotropy of domain wall resistance*, Physical Review Letters **85**, 3962 (2000).

[58] G. G. Cabrera and L. M. Falicov: *Theory of the Residual Resistivity of Bloch Walls. II. Inclusion of Diamagnetic Effects*, physica status solidi (b) **62**, 217–222 (1974).

[59] P. M. Levy and S. Zhang: *Resistivity due to Domain Wall Scattering*, Physical Review Letters **79**, 5110–5113 (1997).

[60] U. Rüdiger, J. Yu, L. Thomas, S. S. P. Parkin, and A. D. Kent: *Magnetoresistance, micromagnetism, and domain-wall scattering in epitaxial hcp Co films*, Physical Review B **59**, 11914–11918 (1999).

[61] J. Wang, S. Wu, J. Ma, L. Xie, C. Wang, I. A. Malik, Y. Zhang, K. Xia, C.-W. Nan, and J. Zhang: *Nanoscale control of stripe-ordered magnetic domain walls by vertical spin transfer torque in* $La_{0.67}Sr_{0.33}MnO_3$ *film*, Applied Physics Letters **112**, 072408 (2018).

[62] L. Berger: *Low-field magnetoresistance and domain drag in ferromagnets*, Journal of Applied Physics **49**, 2156–2161 (1978).

[63] E. M. Pugh and N. Rostoker: *Hall Effect in Ferromagnetic Materials*, Reviews of Modern Physics **25**, 151 (1953).

[64] E. H. Hall: *On a new action of the magnet on electric currents*, American Journal of Mathematics **2**, 287–292 (1879).

[65] N. Manca, D. J. Groenendijk, I. Pallecchi, C. Autieri, L. M. K. Tang, F. Telesio, G. Mattoni, A. McCollam, S. Picozzi, and A. D. Caviglia: *Balanced electron-hole transport in spin-orbit semimetal* $SrIrO_3$ *heterostructures*, Physical Review B **97**, 081105(R) (2018).

[66] N. Nagaosa, J. Sinova, S. Onoda, A. H. MacDonald, and N. P. Ong: *Anomalous Hall effect*, Reviews of Modern Physics **82**, 1539 (2010).

[67] J. Smit: *The spontaneous Hall effect in ferromagnetics I*, Physica **21**, 877–887 (1955).

[68] L. Berger: *Side-Jump Mechanism for the Hall Effect of Ferromagnets*, Physical Review B **2**, 4559 (1970).

[69] Y. Shiomi: *Anomalous and topological Hall effect in itinerant magnets*, 1st ed. (Springer Japan, Tokyo, 2013).

[70] A. Crépieux and P. Bruno: *Theory of the anomalous Hall effect from the Kubo formula and the Dirac equation*, Physical Review B **64**, 014416 (2001).

[71] R. Karplus and J. M. Luttinger: *Hall effect in ferromagnetics*, Phys. Rev. **95**, 1154 (1954).

[72] G. Koster, L. Klein, W. Siemons, G. Rijnders, J. S. Dodge, C.-B. Eom, D. H. A. Blank, and M. R. Beasley: *Structure, physical properties, and applications of* $SrRuO_3$ *thin films*, Review of Modern Physics **84**, 253 (2012).

[73] I. Kézsmárki, S. Bordács, P. Milde, E. Neuber, L. M. Eng, J. S. White, H. M. Rønnow, C. D. Dewhurst, M. Mochizuki, K. Yanai, H. Nakamura, D. Ehlers, V. Tsurkan, and A. Loidl: *Néel-type skyrmion lattice with confined orientation in the polar magnetic semiconductor* GaV_4S_8, Nature Materials **14**, 1116–1122 (2015).

[74] C. Pfleiderer and A. Rosch: *Single skyrmions spotted*, Nature **465**, 880–881 (2010).

[75] K. Evershor-Sitte, Lecture notes of the 48th IFF spring school on topological matter, Title: Emergent electrodynamics in magnetic systems with a focus on magnetic skyrmions, Schriften des Forschungszentrum Jülich, Reihe Schlüsseltechnologien, Band/Volume 139, 2017.

[76] G. Metalidis and P. Bruno: *Topological Hall effect studied in simple models*, Physical Review B **74**, 045327 (2006).

[77] M. V. Berry: *Quantal phase factors accompanying adiabatic changes*, Proceedings of the Royal Society of London. Series A, Mathematical and Physical Sciences **392**, 45–57 (1984).

[78] P. Bruno, V. K. Dugaev, and M. Taillefumier: *Topological Hall Effect and Berry Phase in Magnetic Nanostructures*, Physical Review Letters **93**, 096806 (2004).

[79] M. B. A. Jalil and S. G. Tan: *Robustness of topological Hall effect of nontrivial spin textures*, Scientific Reports **4**, 5123 (2014).

[80] A. Neubauer, C. Pfleiderer, B. Binz, A. Rosch, R. Ritz, P. G. Niklowitz, and P. Böni: *Topological Hall Effect in the A Phase of MnSi*, Physical Review Letters **102**, 186602 (2009).

[81] J. Matsuno, N. Ogawa, K. Yasuda, F. Kagawa, W. Koshibae, N. Nagaosa, Y. Tokura, and M. Kawasaki: *Interface-driven topological Hall effect in* $SrRuO_3$ - $SrIrO_3$ *bilayer*, Science Advances **2**, e1600304 (2016).

[82] X. Z. Yu, Y. Onose, N. Kanazawa, J. H. Park, J. H. Han, Y. Matsui, N. Nagaosa, and Y. Tokura: *Real-space observation of a two-dimensional skyrmion crystal*, Nature **465**, 901–904 (2010).

[83] K. von Bergmann, A. Kubetzka, O. Pietzsch, and R. Wiesendanger: *Interface-induced chiral domain walls, spin spirals and skyrmions revealed by spin-polarized scanning tunneling microscopy*, Journal of Physics: Condensed Matter **26**, 394002 (2014).

[84] B. F. Miao, L. Sun, Y. W. Wu, X. D. Tao, X. Xiong, Y. Wen, R. X. Cao, P. Wang, D. Wu, Q. F. Zhan, B. You, J. Du, R. W. Li, and H. F. Ding: *Experimental realization of two-dimensional artificial skyrmion crystals at room temperature*, Physical Review B **90**, 174411 (2014).

[85] P. Milde, D. Köhler, J. Seidel, L. M. Eng, A. Bauer, A. Chacon, J. Kindervater, S. Mühlbauer, C. Pfleiderer, S. Buhrandt, C. Schütte, and A. Rosch: *Unwinding of a skyrmion lattice by magnetic monopoles*, Science **340**, 1076–1080 (2013).

[86] C. W. Jones, P. D. Battle, P. Lightfoot, and W. T. A. Harrison: *The structure of* $SrRuO_3$ *by time-of-flight neutron powder diffraction*, Acta Crystallographica Section C **45**, 365–367 (1989).

[87] F. Bern, M. Ziese, K. Dörr, A. Herklotz, and I. Vrejoiu: *Hall effect of tetragonal and orthorhombic* $SrRuO_3$ *films*, physica status solidi (RRL) **7**, 204–206 (2013).

[88] F. Bern, M. Ziese, A. Setzer, E. Pippel, D. Hesse, and I. Vrejoiu: *Structural, magnetic and electrical properties of* $SrRuO_3$ *films and* $SrRuO_3$ */*$SrTiO_3$ *superlattices*, Journal of Physics Condensed Matter **25**, 496003 (2013).

[89] J. Xia, W. Siemons, G. Koster, M. R. Beasley, and A. Kapitulnik: *Critical thickness for itinerant ferromagnetism in ultrathin films of* $SrRuO_3$, Physical Review B **79**, 140407(R) (2009).

[90] L. Klein, J. S. Dodge, C. H. Ahn, G. J. Snyder, T. H. Geballe, M. R. Beasley, and A. Kapitulnik: *Anomalous Spin Scattering Effects in the Badly Metallic Itinerant Ferromagnet* $SrRuO_3$, Physical Review Letters **77**, 2774 (1996).

[91] S. C. Gausepohl, M. Lee, R. A. Rao, and C. B. Eom: *Hall-effect sign reversal in* $CaRuO_3$ *and* $SrRuO_3$ *thin films*, Physical Review B **54**, 8996 (1996).

[92] M. Izumi, K. Nakazawa, Y. Bando, Y. Yoneda, and H. Terauchi: *Magnetotransport of* $SrRuO_3$ *Thin Film on* $SrTiO_3$ *(001)*, Journal of the Physical Society of Japan **66**, 3893–3900 (1997).

[93] Z. Fang, N. Nagaosa, K. S. Takahashi, A. Asamitsu, R. Mathieu, T. Ogasawara, H. Yamada, M. Kawasaki, Y. Tokura, and K. Terakura: *The Anomalous Hall Effect and Magnetic Monopoles in Momentum Space*, Science **302**, 92–95 (2003).

[94] R. Mathieu, A. Asamitsu, H. Yamada, K. S. Takahashi, M. Kawasaki, Z. Fang, N. Nagaosa, and Y. Tokura: *Scaling of the Anomalous Hall Effect in* $Sr_{1-x}Ca_xRuO_3$, Physical Review Letters **93**, 016602 (2004).

[95] M. Ziese and I. Vrejoiu: *Anomalous and planar Hall effect of orthorhombic and tetragonal* $SrRuO_3$ *layers*, Physical Review B **84**, 104413 (2011).

[96] H. Mizuno, K. T. Yamada, D. Kan, T. Moriyama, Y. Shimakawa, and T. Ono: *Electric-field-induced modulation of the anomalous Hall effect in a heterostructured itinerant ferromagnet* $SrRuO_3$, Physical Review B **96**, 214422 (2017).

[97] D. Roy, N. Haham, J. W. Reiner, E. Shimshoni, and L. Klein: *Intermixing of ordinary and anomalous Hall effect in* $SrRuO_3$, Physical Review B **92**, 235101 (2015).

[98] R. Mathieu, C. U. Jung, H. Yamada, A. Asamitsu, M. Kawasaki, and Y. Tokura: *Determination of the intrinsic anomalous Hall effect of* $SrRuO_3$, Physical Review B **72**, 064436 (2005).

[99] M. Schultz, J. W. Reiner, and L. Klein: *The extraordinary Hall effect of* $SrRuO_3$ *in the ultrathin limit*, Journal of Applied Physics **105**, 07E906 (2009).

[100] N. Haham, Y. Shperber, M. Schultz, N. Naftalis, E. Shimshoni, J. W. Reiner, and L. Klein: *Scaling of the anomalous Hall effect in* $SrRuO_3$, Physical Review B **84**, 174439 (2011).

[101] Y. Kats, I. Genish, L. Klein, J. W. Reiner, and M. R. Beasley: *Testing the Berry phase model for extraordinary Hall effect in* $SrRuO_3$, Physical Review B **70**, 180407(R) (2004).

[102] Y. Chen, D. L. Bergman, and A. A. Burkov: *Weyl fermions and the anomalous Hall effect in metallic ferromagnets*, Physical Review B **88**, 125110 (2013).

[103] S. Itoh, Y. Endoh, T. Yokoo, S. Ibuka, J.-G. Park, Y. Kaneko, K. S. Takahashi, Y. Tokura, and N. Nagaosa: *Weyl fermions and spin dynamics of metallic ferromagnet* $SrRuO_3$, Nature Communications **7**, 11788 (2016).

[104] D. Zheng, Y.-W. Fang, S. Zhang, P. Li, Y. Wen, B. Fang, X. He, Y. Li, C. Zhang, W. Tong, W. Mi, H. Bai, H. N. Alshareef, Z. Q. Qiu, and X. Zhang: *Berry Phase Engineering in* $SrRuO_3/SrIrO_3/SrTiO_3$ *Superlattices Induced by Band Structure Reconstruction*, ACS Nano **15**, 5086–5095 (2021).

[105] B. Sohn, E. Lee, S. Y. Park, W. Kyung, J. Hwang, J. D. Denlinger, M. Kim, D. Kim, B. Kim, H. Ryu, S. Huh, J. S. Oh, J. K. Jung, D. Oh, Y. Kim, M. Han, T. W. Noh, B.-J. Yang, and C. Kim: *Sign-tunable anomalous Hall effect induced by two-dimensional symmetry-protected nodal structures in ferromagnetic perovskite thin films*, Nature Materials **20**, 1643–1649 (2021).

[106] R. Shimano, Y. Ikebe, K. S. Takahashi, M. Kawasaki, N. Nagaosa, and Y. Tokura: *Terahertz Faraday rotation induced by an anomalous Hall effect in the itinerant ferromagnet* $SrRuO_3$, EPL (Europhysics Letters) **95**, 17002 (2011).

[107] K. Takiguchi, Y. K. Wakabayashi, H. Irie, Y. Krockenberger, T. Otsuka, H. Sawada, S. A. Nikolaev, H. Das, M. Tanaka, Y. Taniyasu, and H. Yamamoto: *Quantum transport evidence of Weyl fermions in an epitaxial ferromagnetic oxide*, Nature Communications **11**, 4969 (2020).

[108] L. Wu, F. Wen, Y. Fu, J. H. Wilson, X. Liu, Y. Zhang, D. M. Vasiukov, M. S. Kareev, J. H. Pixley, and J. Chakhalian: *Berry phase manipulation in ultrathin* $SrRuO_3$ *films*, Physical Review B **102**, 220406(R) (2020).

[109] D. J. Groenendijk, C. Autieri, T. C. van Thiel, W. Brzezicki, J. R. Hortensius, D. Afanasiev, N. Gauquelin, P. Barone, K. H. W. van den Bos, S. van Aert, J. Verbeeck, A. Filippetti, S. Picozzi, M. Cuoco, and A. D. Caviglia: *Berry phase engineering at oxide interfaces*, Physical Review Research **2**, 023404 (2020).

[110] Y. Ohuchi, J. Matsuno, N. Ogawa, Y. Kozuka, M. Uchida, Y. Tokura, and M. Kawasaki: *Electric-field control of anomalous and topological Hall effects in oxide bilayer thin films*, Nature Communications **9**, 213 (2018).

[111] D. Kan and Y. Shimakawa: *Defect-Induced Anomalous Transverse Resistivity in an Itinerant Ferromagnetic Oxide*, physica status solidi (b) **255**, 1800175 (2018).

[112] C. Wang, C.-H. Chang, A. Herklotz, C. Chen, F. Ganss, U. Kentsch, D. Chen, X. Gao, Y.-J. Zeng, O. Hellwig, M. Helm, S. Gemming, Y.-H. Chu, and S. Zhou: *Topological Hall Effect in Single Thick* $SrRuO_3$ *Layers Induced by Defect Engineering*, Advanced Electronic Materials **6**, 2000184 (2020).

[113] P. Zhang, A. Das, E. Barts, M. Azhar, L. Si, K. Held, M. Mostovoy, and T. Banerjee: *Robust skyrmion-bubble textures in $SrRuO_3$ thin films stabilized by magnetic anisotropy*, Physical Review Research **2**, 032026(R) (2020).

[114] Z. Li, S. Shen, Z. Tian, K. Hwangbo, M. Wang, Y. Wang, F. M. Bartram, L. He, Y. Lyu, Y. Dong, G. Wan, H. Li, N. Lu, J. Zang, H. Zhou, E. Arenholz, Q. He, L. Yang, W. Luo, and P. Yu: *Reversible manipulation of the magnetic state in $SrRuO_3$ through electric-field controlled proton evolution*, Nature Communications **11**, 184 (2020).

[115] H. Huang, S.-J. Lee, B. Kim, B. Sohn, C. Kim, C.-C. Kao, and J.-S. Lee: *Detection of the Chiral Spin Structure in Ferromagnetic $SrRuO_3$ Thin Film*, ACS Applied Materials & Interfaces **12**, 37757–37763 (2020).

[116] D. Kan, T. Moriyama, K. Kobayashi, and Y. Shimakawa: *Alternative to the topological interpretation of the transverse resistivity anomalies in $SrRuO_3$*, Physical Review B **98**, 180408(R) (2018).

[117] D. Kan, K. Kobayashi, and Y. Shimakawa: *Electric field induced modulation of transverse resistivity anomalies in ultrathin $SrRuO_3$ epitaxial films*, Physical Review B **101**, 144405 (2020).

[118] D. Kan, T. Moriyama, and Y. Shimakawa: *Field-sweep-rate and time dependence of transverse resistivity anomalies in ultrathin $SrRuO_3$ films*, Physical Review B **101**, 014448 (2020).

[119] G. Kimbell, P. M. Sass, B. Woltjes, E. K. Ko, T. W. Noh, W. Wu, and J. W. A. Robinson: *Two-channel anomalous Hall effect in $SrRuO_3$*, Physical Review Materials **4**, 054414 (2020).

[120] L. Miao, N. J. Schreiber, H. P. Nair, B. H. Goodge, S. Jiang, J. P. Ruf, Y. Lee, M. Fu, B. Tsang, Y. Li, C. Zeledon, J. Shan, K. F. Mak, L. F. Kourkoutis, D. G. Schlom, and K. M. Shen: *Strain relaxation induced transverse resistivity anomalies in $SrRuO_3$ thin films*, Physical Review B **102**, 064406 (2020).

[121] Y. Gu, Y.-W. Wei, K. Xu, H. Zhang, F. Wang, F. Li, M. S. Saleem, C.-Z. Chang, J. Sun, C. Song, J. Feng, X. Zhong, W. Liu, Z. Zhang, J. Zhu, and F. Pan: *Interfacial oxygen-octahedral-tilting-driven electrically tunable topological Hall effect in ultrathin $SrRuO_3$ films*, Journal of Physics D: Applied Physics **52**, 404001 (2019).

[122] B. Sohn, B. Kim, J. W. Choi, S. H. Chang, J. H. Han, and C. Kim: *Hump-like structure in Hall signal from ultra-thin $SrRuO_3$ films without inhomogeneous anomalous Hall effect*, Current Applied Physics **20**, 186–190 (2020).

[123] B. Sohn, B. Kim, S. Y. Park, H. Y. Choi, J. Y. Moon, T. Choi, Y. J. Choi, H. Zhou, J. W. Choi, A. Bombardi, D. G. Porter, S. H. Chang, J. H. Han, and C. Kim: *Stable humplike Hall effect and noncoplanar spin textures in* $SrRuO_3$ *ultrathin films*, Physical Review Research **3**, 023232 (2021).

[124] B. Pang, L. Zhang, Y. B. Chen, J. Zhou, S. Yao, S. Zhang, and Y. Chen: *Spin-Glass-Like Behavior and Topological Hall Effect in* $SrRuO_3/SrIrO_3$ *Superlattices for Oxide Spintronics Applications*, ACS Applied Materials and Interfaces **9**, 3201–3207 (2017).

[125] K.-Y. Meng, A. S. Ahmed, M. Baćani, A.-O. Mandru, X. Zhao, N. Bagués, B. D. Esser, J. Flores, D. W. McComb, H. J. Hug, and F. Yang: *Observation of Nanoscale Skyrmions in* $SrIrO_3$ / $SrRuO_3$ *Bilayers*, Nano Letters **19**, 3169–3175 (2019).

[126] L. Yang, L. Wysocki, J. Schöpf, L. Jin, A. Kovács, F. Gunkel, R. Dittmann, P. H. M. van Loosdrecht, and I. Lindfors-Vrejoiu: *Origin of the hump anomalies in the Hall resistance loops of ultrathin* $SrRuO_3$/ $SrIrO_3$ *multilayers*, Physical Review Materials **5**, 014403 (2021).

[127] S. Esser, J. Wu, S. Esser, R. Gruhl, A. Jesche, V. Roddatis, V. Moshnyaga, R. Pentcheva, and P. Gegenwart: *Angular dependence of Hall effect and magnetoresistance in* $SrRuO_3$-$SrIrO_3$ *heterostructures*, Physical Review B **103**, 214430 (2021).

[128] Q. Qin, L. Liu, W. Lin, X. Shu, Q. Xie, Z. Lim, C. Li, S. He, G. M. Chow, and J. Chen: *Emergence of Topological Hall Effect in a* $SrRuO_3$ *Single Layer*, Advanced Materials **31**, 1807008 (2019).

[129] A. Gerber: *Interpretation of experimental evidence of the topological Hall effect*, Physical Review B **98**, 214440 (2018).

[130] L. Wysocki, L. Yang, F. Gunkel, R. Dittmann, P. H. M. van Loosdrecht, and I. Lindfors-Vrejoiu: *Validity of magnetotransport detection of skyrmions in epitaxial* $SrRuO_3$ *heterostructures*, Phys. Rev. Materials **4**, 054402 (2020).

[131] T. C. van Thiel, D. J. Groenendijk, and A. D. Caviglia: *Extraordinary Hall balance in ultrathin* $SrRuO_3$ *bilayers*, Journal of Physics: Materials **3**, 025005 (2020).

[132] G. Malsch, D. Ivaneyko, P. Milde, L. Wysocki, L. Yang, P. H. M. van Loosdrecht, I. Lindfors-Vrejoiu, and L. M. Eng: *Correlating the Nanoscale Structural, Magnetic, and Magneto-Transport Properties in* $SrRuO_3$*-Based Perovskite Thin Films: Implications for Oxide Skyrmion Devices*, ACS Applied Nano Materials **3**, 1182–1190 (2020).

[133] L. Wang, Q. Feng, H. G. Lee, E. K. Ko, Q. Lu, and T. W. Noh: *Controllable Thickness Inhomogeneity and Berry Curvature Engineering of Anomalous Hall Effect in* $SrRuO_3$ *Ultrathin Films*, Nano Letters **20**, 2468–2477 (2020).

[134] G. Kim, K. Son, Y. E. Suyolcu, L. Miao, N. J. Schreiber, H. P. Nair, D. Putzky, M. Minola, G. Christiani, P. A. van Aken, K. M. Shen, D. G. Schlom, G. Logvenov, and B. Keimer: *Inhomogeneous ferromagnetism mimics signatures of the topological Hall effect in* $SrRuO_3$ *films*, Physical Review Materials **4**, 104410 (2020).

[135] M. Ziese, L. Jin, and I. Lindfors-Vrejoiu: *Unconventional anomalous Hall effect driven by oxygen-octahedra-tailoring of the* $SrRuO_3$ *structure*, Journal of Physics: Materials **2**, 034008 (2019).

[136] Z. Y. Ren, F. Shao, P. F. Liu, M. X. Wang, J. K. Chen, K. K. Meng, X. G. Xu, J. Miao, and Y. Jiang: *Nonvolatile Ferroelectric Field Control of the Anomalous Hall Effect in* $BiFeO_3$*-* $SrRuO_3$ *Bilayer*, Physical Review Applied **13**, 024044 (2020).

[137] E. Skoropata, A. R. Mazza, A. Herklotz, J. M. Ok, G. Eres, M. Brahlek, T. R. Charlton, H. N. Lee, and T. Z. Ward: *Post-synthesis control of Berry phase driven magnetotransport in* $SrRuO_3$ *films*, Physical Review B **103**, 085121 (2021).

[138] J. Lu, L. Si, Q. Zhang, C. Tian, X. Liu, C. Song, S. Dong, J. Wang, S. Cheng, L. Qu, K. Zhang, Y. Shi, H. Huang, T. Zhu, W. Mi, Z. Zhong, L. Gu, K. Held, L. Wang, and J. Zhang: *Defect-Engineered Dzyaloshinskii–Moriya Interaction and Electric-Field-Switchable Topological Spin Texture in* $SrRuO_3$, Advanced Materials **33**, 2102525 (2021).

[139] L. Wang, Q. Feng, Y. Kim, R. Kim, K. H. Lee, S. D. Pollard, Y. J. Shin, H. Zhou, W. Peng, D. Lee, W. Meng, H. Yang, J. H. Han, M. Kim, Q. Lu, and T. W. Noh: *Ferroelectrically tunable magnetic skyrmions in ultrathin oxide heterostructures*, Nature Materials **17**, 1087–1094 (2018).

[140] S. D. Seddon, D. E. Dogaru, S. J. R. Holt, D. Rusu, J. J. P. Peters, A. M. Sanchez, and M. Alexe: *Real-space observation of ferroelectrically induced magnetic spin crystal in* $SrRuO_3$, Nature Communications **12**, 2007 (2021).

[141] W. Wang, M. W. Daniels, Z. Liao, Y. Zhao, J. Wang, G. Koster, G. Rijnders, C.-Z. Chang, D. Xiao, and W. Wu: *Spin chirality fluctuation in two-dimensional ferromagnets with perpendicular magnetic anisotropy*, Nature Materials **18**, 1054–1059 (2019).

[142] V. M. Goldschmidt: *Die Gesetze der Krystallochemie*, Naturwissenschaften **14**, 477–485 (1926).

[143] Y. Tokura and Y. Tomioka: *Colossal magnetoresistive manganites*, Journal of Magnetism and Magnetic Materials **200**, 1–23 (1999).

[144] A. Urushibara, Y. Moritomo, T. Arima, A. Asamitsu, G. Kido, and Y. Tokura: *Insulator-metal transition and giant magnetoresistance in* $La_{1-x}Sr_xMnO_3$, Physical Review B **51**, 14103 (1995).

[145] A. Asamitsu, Y. Moritomo, Y. Tomioka, T. Arima, and Y. Tokura: *A structural phase transition induced by an external magnetic field*, Nature **373**, 407–409 (1995).

[146] A. Vailionis, H. Boschker, W. Siemons, E. P. Houwman, D. H. A. Blank, G. Rijnders, and G. Koster: *Misfit strain accommodation in epitaxial* ABO_3 *perovskites: Lattice rotations and lattice modulations*, Physical Review B **83**, 064101 (2011).

[147] P. G. Radaelli, G. Iannone, M. Marezio, H. Y. Hwang, S.-W. Cheong, J. D. Jorgensen, and D. N. Argyriou: *Structural effects on the magnetic and transport properties of perovskite* $A_{1-x}A^{'}_x\mathrm{MnO_3}$ *(*$x = 0.25$, *0.30)*, Physical Review B **56**, 8265 (1997).

[148] J.-M. Moreau, C. Michel, R. Gerson, and W. J. James: *Atomic displacement relationship to rhombohedral deformation in some perovskite-type compounds*, Acta Crystallographica Section B **26**, 1425–1428 (1970).

[149] S. K. Chaluvadi: “Influence of the epitaxial strain on magnetic anisotropy in LSMO thin films for spintronics applications”, PhD thesis (Normandie Universite, 2017).

[150] C. Zener: *Interaction between the d shells in the transition metals*, Phys. Rev. **81**, 440 (1951).

[151] C. Zener and R. R. Heikes: *Exchange interactions*, Rev. Mod. Phys. **25**, 191 (1953).

[152] J. Hemberger, A. Krimmel, T. Kurz, H.-A. Krug von Nidda, V. Y. Ivanov, A. A. Mukhin, A. M. Balbashov, and A. Loidl: *Structural, magnetic, and electrical properties of single-crystalline* $La_{1-x}Sr_xMnO_3$ $(0.4 < x < 0.85)$, Physical Review B **66**, 094410 (2002).

[153] K. Kubo and N. Ohata: *A Quantum Theory of Double Exchange*, Journal of the Physical Society of Japan **33**, 21–32 (1972).

[154] M. B. Salamon and M. Jaime: *The physics of manganites: structure and transport*, Rev. Mod. Phys. **73**, 583 (2001).

[155] P. W. Anderson and H. Hasegawa: *Considerations on double exchange*, Phys. Rev. **100**, 675 (1955).

[156] J. B. Goodenough: *Theory of the Role of Covalence in the Perovskite-Type Manganites [La, M(II)]* MnO_3, Phys. Rev. **100**, 564 (1955).

[157] J. B. Goodenough: *An interpretation of the magnetic properties of the perovskite-type mixed crystals* $La_{1-x}Sr_xCoO_{3-\lambda}$, Journal of Physics and Chemistry of Solids **6**, 287–297 (1958).

[158] J. Kanamori: *Superexchange interaction and symmetry properties of electron orbitals*, Journal of Physics and Chemistry of Solids **10**, 87–98 (1959).

[159] S. Maekawa, T. Toyama, S. Barnes, S. Ishihara, W. Koshibae, and G. Khaliullin: *Physics of Transition Metal Oxides*, 1st ed. (Springer Verlag, Berlin, Heidelberg, 2004).

[160] M. Viret, L. Ranno, and J. M. D. Coey: *Magnetic localization in mixed-valence manganites*, Physical Review B **55**, 8067 (1997).

[161] N. G. Bebin, R. I. Zainullina, and V. V. Ustinov: *Colossal magnetoresistance manganites*, Phys.-Usp. **61**, 719–738 (2018).

[162] A. Asamitsu and Y. Tokura: *Hall effect in* $La_{1-x}Sr_xMnO_3$, Physical Review B **58**, 47–50 (1998).

[163] I. M. Dildar, C. Beekman, X. He, and J. Aarts: *Hall effect measurements on strained and unstrained thin films of* $La_{0.7}Ca_{0.3}MnO_3$ *and* $La_{0.7}Sr_{0.3}MnO_3$, Physical Review B **85**, 205103 (2012).

[164] J. Ye, Y. B. Kim, A. J. Millis, B. I. Shraiman, P. Majumdar, and Z. Tssanovic: *Berry Phase Theory of the Anomalous Hall Effect: Application to Colossal Magnetoresistance Manganites*, Physical Review Letters **83**, 3737 (1999).

[165] D. Pesquera, G. Herranz, A. Barla, E. Pellegrin, F. Bondino, E. Magnano, F. Sánchez, and J. Foncuberta: *Surface symmetry-breaking and strain effects on orbital occupancy in transition metal perovskite epitaxial films*, Nature Communications **3**, 1189 (2012).

[166] J. Pilo, M. Pruneda, and N. Bristowe: *Structural and magnetic phase diagram of epitaxial* $La_{0.7}Sr_{0.3}MnO_3$ *from first principles*, Electronic Structure **3**, 024001 (2021).

[167] A. Tebano, C. Aruta, S. Sanna, P. G. Medaglia, G. Balestrino, A. A. Sidorenko, R. De Renzi, G. Ghiringhelli, L. Braicovich, V. Bisogni, and N. B. Brookes: *Evidence of Orbital Reconstruction at Interfaces in Ultrathin* $La_{0.67}Sr_{0.33}MnO_3$ *Films*, Physical Review Letters **100**, 137401 (2008).

[168] A. Tebano, C. Aruta, P. G. Medaglia, F. Tozzi, G. Balestrino, A. A. Sidorenko, G. Allodi, R. De Renzi, G. Ghiringhelli, C. Dallera, L. Braicovich, and N. B.

Brookes: *Strain-induced phase separation in* $La_{0.7}Sr_{0.3}MnO_3$ *thin films*, Physical Review B **74**, 245116 (2006).

[169] M. Huijben, L. W. Martin, Y.-H. Chu, M. B. Holcomb, P. Yu, G. Rijnders, D. H. A. Blank, and R. Ramesh: *Critical thickness and orbital ordering in ultrathin* $La_{0.7}Sr_{0.3}MnO_3$ *films*, Physical Review B **78**, 094413 (2008).

[170] C. Song, X. Li, L. Shen, B. Cui, X. Xu, G. Yu, M. Liu, S. Meng, and K. Wu: *Emergent perpendicular magnetic anisotropy at the interface of an oxide heterostructure*, Physical Review B **104**, 115162 (2021).

[171] Z. Xiao, F. Zhang, M. A. Farrukh, R. Wang, G. Zhou, Z. Quan, and X. Xu: *Perpendicular magnetic anisotropy in compressive strained* $La_{0.67}Sr_{0.33}MnO_3$ *films*, Journal of Materials Science **54**, 9017–9024 (2019).

[172] S. W. Jin, G. Y. Gao, Z. Huang, Z. Z. Yin, X. Zheng, and W. Wu: *Shear-strain-induced low symmetry phase and domain ordering in epitaxial* $La_{0.7}Sr_{0.3}MnO_3$ *thin films*, Applied Physics Letters **92**, 261901 (2008).

[173] N. Farag, M. Bobeth, W. Pompe, A. E. Romanov, and J. S. Speck: *Modeling of twinning in epitaxial (001)-oriented* $La_{0.67}Sr_{0.33}MnO_3$ *thin films*, Journal of Applied Physics **97**, 113516 (2005).

[174] T. F. Zhou, G. Li, X. G. Li, S. W. Jin, and W. B. Wu: *Self-generated in-plane superlattice in relaxed epitaxial* $La_{0.67}Sr_{0.33}MnO_3$ *films*, Applied Physics Letters **90**, 042512 (2007).

[175] J. Santiso, L. Balcells, Z. Konstantinovic, J. Roqueta, P. Ferrer, A. Pomar, B. Martínez, and F. Sandiumenge: *Thickness evolution of the twin structure and shear strain in LSMO films*, CrystEngComm **15**, 3908–3918 (2013).

[176] F. Pailloux, R. Lyonnet, J.-L. Maurice, and J.-P. Contour: *Twinning and lattice distortions in the epitaxy of* $La_{0.67}Sr_{0.33}MnO_3$ *thin films on (001)* $SrTiO_3$, Applied Surface Science **177**, 263–267 (2001).

[177] D. Lan, P. Chen, C. Liu, X. Wu, P. Yang, X. Yu, J. Ding, J. Chen, and G. M. Chow: *Interfacial control of domain structure and magnetic anisotropy in* $La_{0.67}Sr_{0.33}MnO_3$ *manganite heterostructures*, Physical Review B **104**, 125423 (2021).

[178] U. Gebhardt, N. V. Kasper, A. Vigliante, P. Wochner, H. Dosch, F. S. Razavi, and H.-U. Habermeier: *Formation and Thickness Evolution of Periodic Twin Domains in Manganite Films Grown on* $SrTiO_3$ *(001) Substrates*, Physical Review Letters **98**, 096101 (2007).

[179] J.-L. Maurice, F. Pailloux, A. Barthélémy, A. Rocher, O. Durand, R. Lyonnet, and J.-P. Contour: *Strain and magnetism in* $(La_{0.7}Sr_{0.3})MnO_3$ *very thin films epitaxially grown on* $SrTiO_3$, Applied Surface Science **188**, 176–181 (2002).

[180] O. I. Lebedev, G. Van Tendeloo, S. Amelinckx, H. L. Ju, and K. M. Krishnan: *High-resolution electron microscopy study of strained epitaxial* $La_{0.7}Sr_{0.3}MnO_3$ *thin films*, Philosophical Magazine A **80**, 673–691 (2000).

[181] B. Paudel, B. Zhang, Y. Sharma, K. T. Kang, H. Nakotte, H. Wang, and A. Chen: *Anisotropic domains and antiferrodistortive-transition controlled magnetization in epitaxial manganite films on vicinal* $SrTiO_3$ *substrates*, Applied Physics Letters **117**, 081903 (2020).

[182] S. K. Streiffer, C. B. Parker, A. E. Romanov, M. J. Lefevre, L. Zhao, J. S. Speck, W. Pompe, C. M. Foster, and G. R. Bai: *Domain patterns in epitaxial rhombohedral ferroelectric films. I. Geometry and experiments*, Journal of Applied Physics **83**, 2742–2753 (1998).

[183] J. E. Boschker, Å. F. Monsen, M. Nord, R. Mathieu, J. K. Grepstad, R. Holmestad, E. Wahlström, and T. Tybell: *In-plane structural order of domain engineered* $La_{0.7}Sr_{0.3}MnO_3$ *thin films*, Philosophical Magazine **93**, 1549–1562 (2013).

[184] B. Paudel, K. T. Kang, Y. Sharma, H. Nakotte, D. Yarotski, and A. Chen: *Symmetry mismatch controlled ferroelastic domain ordering and the functional properties of manganite films on cubic miscut substrates*, Phys. Chem. Chem. Phys. **23**, 16623–16628 (2021).

[185] Y. Li, L. Zhang, Q. Zhang, C. Li, T. Yang, Y. Deng, L. Gu, and D. Wu: *Emergent Topological Hall Effect in* $La_{0.7}Sr_{0.3}MnO_3/SrIrO_3$ *Heterostructures*, ACS Applied Materials & Interfaces **11**, 21268–21274 (2019).

[186] B. Zhang, L. Wu, J. Zheng, P. Yang, X. Yu, J. Ding, S. M. Heald, R. A. Rosenberg, T. V. Venkatesan, J. Chen, C.-J. Sun, Y. Zhu, and G. M. Chow: *Control of magnetic anisotropy by orbital hybridization with charge transfer in* $(La_{0.67}Sr_{0.33}MnO_3)_n/(SrTiO_3)n$ *superlattice*, NPG Asia Materials **10**, 931–942 (2018).

[187] S. S. Manoharan, H. L. Ju, and K. M. Krishnan: *Unusual substitutional properties of Ru in the* $La_{0.7}Sr_{0.3}Mn_{1-x}Ru_xO_3$ *system*, Journal of Applied Physics **83**, 7183–7185 (1998).

[188] L. M. Wang, J.-H. Lai, J.-I. Wu, Y.-K. Kuo, and C. L. Chang: *Effects of Ru substitution for Mn on* $La_{0.7}Sr_{0.3}MnO_3$ *perovskites*, Journal of Applied Physics **102**, 023915 (2007).

[189] D. Bhargava, T. M. Tank, A. Bodhaye, and S. P. Sanyal: *Transport and Magneto-Transport Properties of Ru Doped* $Ln_{0.67}Sr_{0.33}MnO_3$ *(Ln = La, Pr, and Nd)*, Transactions of the Indian Institute of Metals **65**, 443–447 (2012).

[190] H. Yamada, M. Kawasaki, and Y. Tokura: *Ru-doped* $La_{0.6}Sr_{0.4}MnO_3$ *thin films as a coercivity tunable electrode for magnetic tunnel junctions*, Applied Physics Letters **86**, 192505 (2005).

[191] K. M. Krishnan and H. L. Ju: *Role of stoichiometry and structure in colossal magnetoresistive* $La_{1-x}Sr_xMn_{1-y}Ru_yO_{3\delta}$, Physical Review B **60**, 14793 (1999).

[192] T. Harano, G. Shibata, K. Ishigami, Y. Takashashi, V. K. Verma, V. R. Singh, T. Kadono, A. Fujimori, Y. Takeda, T. Okane, Y. Saitoh, H. Yamagami, T. Koide, H. Yamada, A. Sawa, M. Kawasaki, Y. Tokura, and A. Tanaka: *Role of doped Ru in coercivity-enhanced* $La_{0.6}Sr_{0.4}MnO_3$ *thin film studied by x-ray magnetic circular dichroism*, Applied Physics Letters **102**, 222404 (2013).

[193] M. Nakamura, D. Morikawa, X. Yu, F. Kagawa, T.-h. Arima, Y. Tokura, and M. Kawasaki: *Emergence of Topological Hall Effect in Half-Metallic Manganite Thin Films by Tuning Perpendicular Magnetic Anisotropy*, Journal of the Physical Society of Japan **87**, 074704 (2018).

[194] K. Shigematsu, A. Chikamatsu, Y. Hirose, T. Fukumura, and T. Hasegawa: *Enhanced coercivity of half-metallic* $La_{0.7}Sr_{0.3}MnO_3$ *by Ru substitution under in-plane uniaxial strain*, Journal of Applied Physics **111**, 07B102 (2012).

Chapter 3

Sample deposition and experimental methods

Contents

The aim of this chapter is to present the basic principles of pulsed-laser deposition, the technique used to deposit all the heterostructures investigated in the course of this dissertation. Subsequently, the characterization techniques which were most important for these studies are described. Additionally, the general concepts of the data analysis are shown.

3.1 Pulsed-laser deposition

Pulsed lasers have been used for the thin film deposition soon after their development in the 1960's.[1–3] However, pulsed-laser deposition (PLD) became prominent with the successful growth of high T_c superconductors in the late 1980's.[1–4] Nowadays, PLD is a versatile technique, frequently utilized to grow multicomponent thin films and superlattices.

The principle of pulsed-laser deposition is sketched in Fig. 3.1 (a). Initially, the photon energy, provided by the pulsed-laser, is absorbed by the target material and transformed into electronic excitation[1,3] so that the material gets vaporized rapidly within hundreds of picoseconds.[3] In order to achieve congruent ablation of multielemental materials, independent of the individual vapor pressures, only a small volume of the target needs to absorb high energy densities.[2] This is typically realized by the usage of high-energy (ultraviolet) laser pulses with short (pulse) duration.[2,3]

The vaporized cloud absorbs the energy of the remaining incident laser pulse, which typically has a duration of tens of nanoseconds.[1,3] This leads to further ionization of the plasma plume that consists of electrons, ions, and neutral species[1] with high kinetic energies in a range between a few and hundreds of electron volts.[3]

The forward-directed plasma plume propagates towards the substrate surface.[2] Its shape and the kinetic energies of its constituents are influenced by the interactions between the plasma species among themselves and with the background gas molecules.[1,2] The background gas not only reduces the kinetic energies of the plasma particles, but can also create molecular species which are sometimes beneficial for the growth of particular materials.[2] On the substrate surface, condensation of the plasma takes place and initializes the film growth. The supersaturation in the plasma plume favors the two-dimensional film growth.[2] Additionally, the heating of the substrate enables the diffusion of the arriving adatoms until they stick at energetically favorable positions.[1] At these sites, typically their atomic coordination number is enhanced, which is fulfilled for instance at terrace steps or existing islands.[1] Pulsed-laser deposition has as an advantage that most (condensed matter) materials can be grown, and even metastable phases can be stabilized due to the deposition out of (thermal and chemical) equilibrium.[1–3] Further great advantages are the preserved stoichiometry and the capability to control the growth mode and rates, related to the usage of high-energy laser pulses with short pulse duration.[1–3]

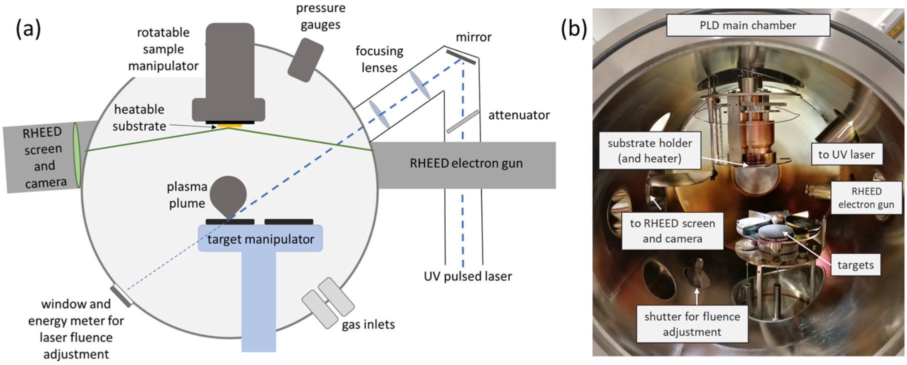

Figure 3.1: (a) Schematic of the pulsed-laser deposition set-up. (b) Inside-view photograph of the main chamber of the pulsed-laser deposition set-up, manufactured by *SURFACE*. The individual components are labeled accordingly.

The low complexity of the set-up, the installation of the laser as energy source outside of the evacuated chamber, and the possibility to keep the targets at room temperature, lead to the great flexibility in the geometrical design of PLD systems.[1–3] Additionally, the capability to tune the size and shape of the plasma plume by the control of the laser spot size and background pressure in a broad range, as well as the suitable kinetic energy of the plasma constituents, which disfavors bulk displacement but favors surface diffusion, are desirable.[3] On the other hand, the grown films are affected by unavoidable impurities in the target and can be influenced by larger particles that are ejected from the ceramic targets.[3] Therefore, one important point is to use ceramic targets of high purity and high density, which is not always possible. This is for instance the case for $SrIrO_3$ targets, which often have rather low density. Moreover, thin film inhomogeneities can be induced by inhomogeneous ion- or energy distribution within the plasma plume.[3] Furthermore, large discrepancies between the vapor pressures of the individual elements can lead to off-stoichiometry of the deposited thin film.[2,3]

The influence of these drawbacks can be minimized by the proper adjustment of the deposition parameters, for instance by tuning of the laser properties, such as the laser fluence and pulse repetition rate, by the optimization of the substrate heating, gas pressure, or the usage of over-stoichiometric targets to compensate potential losses of volatile elements. This emphasizes the requirement for the optimization of the growth parameters for every material, with fine tuning for the utilized vicinal substrates that determine the diffusion and sticking characteristics.

Within the framework of this thesis, two different pulsed-laser deposition set-ups were used. The first set of samples was grown in the system of Prof. Regina Dittmann's group at the Forschungszentrum Jülich. The PLD system, produced by *Twente Solid State Technology (TSST) B.V., The Netherlands* is equipped with a krypton fluorine (KrF) excimer laser producing nanosecond laser pulses with fluences between 1 J/cm^2 and 3.2 J/cm^2.[5]

The second set of samples was deposited in the PLD set-up at the University of Cologne, which was provided by the company *SURFACE & SURFACE systems+technology GmbH & Co. KG*. Here, the growth processes are done in the main vacuum chamber presented in Fig. 3.1 (b), which can be evacuated to a base pressure of the order of 10^{-7} mbar within a few hours by the usage of a turbopump (Pfeiffer HiPace300) and a membrane pump that operates as backpump. Oxygen or nitrogen can be used as background gas. The pressure is measured by the combination of two pressure gauges (CCR and PKR gauge, both produced by *Pfeiffer Vacuum Technology AG*). A KrF excimer laser (produced by *Coherent, Inc.*) delivers nanoseconds-laser pulses of 248 nm with a repetition rate between 1 and 10 Hz and pulse energy up to 800 mJ. Through the stepless rotation of an attenuator that is placed in the laser beam path in front of the main chamber entrance, the laser fluences can be varied up to 4.8 J cm^{-2} in case of minimum realizable spot size and 700 mJ energy.[6] The adjustment of the laser fluence is automized. Based on the preset values of spot size, the transmission of the window, and the measured laser energy, the software automatically calculates the laser fluence for the current position of the attenuator. By rotating the attenuator, the transmitted laser energy is varied until the requested laser fluence is achieved. The laser energy is measured outside of the chamber when the target carousel is rotated so that the laser can pass in between two target sites of the target carousel.

In contrast to the *TSST* set-up where both substrate and targets are mounted vertically, the *SURFACE* system is equipped with a horizontally installed target carousel and substrate manipulator, as shown in Fig. 3.1. The target carousel offers the possibility to install four targets of up to 50 mm diameter simultaneously. During the deposition, the target is moved in a toggling manner to ablate the target surface as homogenously as possible.

The substrate is mounted on a heater with silver paste to ensure good thermal contact. Substrate temperatures up to 1000 °C can be achieved.[6] The temperature is measured with a thermocouple. The distance between target and substrate can be varied, but was typically set to about 6 cm for the growth of the heterostructures studied here.

The system is equipped with a high-pressure RHEED system that enables *in situ* growth monitoring in pressures up to 0.5 mbar. The reflected and diffracted electron beam is visualized by a phosphorus screen and recorded by a CCD camera.[6]

The whole deposition process is computer-controlled with the ability to select the laser properties (fluence, repetition rate, number of pulses), the type and pressure of the background gas, the substrate temperature, and the details of the target movement.

3.1.1 Reflection high-energy electron diffraction

The growth mode as well as the surface crystallinity of the deposited films can be monitored *in situ* by reflection high-energy electron diffraction (RHEED). As displayed in Fig. 3.2 (a), a high-energy electron beam (typically monoenergetic between 10-50 keV[2]) is focused onto the sample surface in grazing incidence (0.1° to 5°[2]). The electrons are diffracted by the sample surface and the diffracted beam is then visualized by the interaction with a phosphorus screen. Due to the low angle of incidence, the electrons mainly interact with the top atomic layers at the sample surface.[2] Thus, the monitored diffraction pattern delivers information on the lattice and roughness of the topmost atomic layers.

RHEED spots are generated if the difference between the wavevectors of the diffracted ($\boldsymbol{k_d}$) and the incident electron beam ($\boldsymbol{k_0}$) is equal to the reciprocal lattice vector ($\boldsymbol{G}$). In case of elastic scattering, $|\boldsymbol{k_0}|$ is equal to $|\boldsymbol{k_d}|$. Multiple, inelastic scattering events can lead to Kikuchi lines, which are observed as curved lines in the RHEED pattern.[2,7]

However, deviations from an atomically flat surface, such as surface roughness, lead to the broadening of the diffraction spots or the appearance of so called transmission spots in case of three-dimensional islands.[2,7] Thus, the RHEED pattern can be used as (qualitative) measure of the sample surface roughness and crystallinity.[7]

The temporal evolution of the intensity of the RHEED spots, in particular of the specularly reflected spot, yields insight into the growth mode. In case of layer-by-layer growth, oscillations are observed in the time dependence of

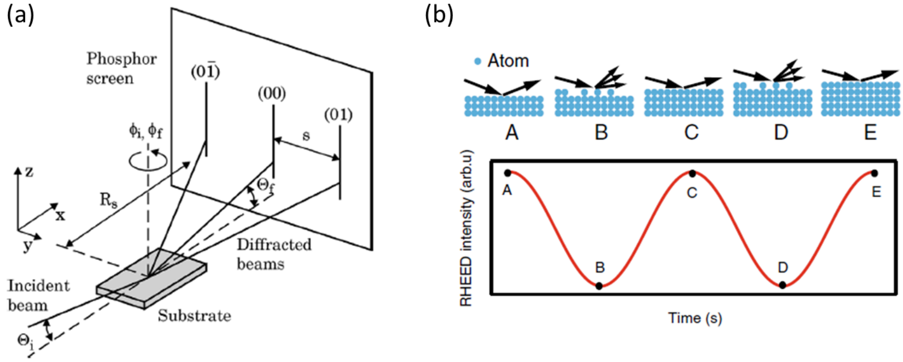

Figure 3.2: (a) Scheme of the RHEED geometry. Θ_{I} (Θ_{F}) and Φ_{I} (Φ_{F}) are the angles of incidence and azimutal angles of the incident (diffracted) beam. S is the distance between the diffraction spots (or streaks) and R_{s} the distance between the substrate and the phosphorus screen. (b) Sketch of the correlation between surface coverage and RHEED spot intensity under the assumption of ideal layer-by-layer growth. Figure (a) reproduced from Ref. [2], with permission from Robert Eason, Pulsed Laser Deposition of Thin films: Applications-LED growth of functional materials (2007) ©2007 by John Wiley & Sons, Inc. Figure (b) adapted from Ref. [8] (published under a Creative Commons Attribution 4.0 International License, ©2018, H. Y. Sun, Z. W. Mao, T. W. Zhang, L. Han, T. T. Zhang, X. B. Cai, X. Guo, Y. F. Li, Y. P. Zang, W. Guo, J. H. Song, D. X. Ji, C.Y. Gu, C. Tang, Z. B. Gu, N. Wang, Y. Zhu, D. G. Schlom, Y. F. Nie, and X. Q. Pan, Chemically specific termination control of oxide interfaces via layer-by-layer mean inner potential engineering, Nature Communications **9**, 2965 (2018), doi: 10.1038/s41467-018-04903-4).

the specular-reflection spot intensity, whose period correlates to the growth of one monolayer.[7,8] As sketched in Fig. 3.2 (b), the intensity of the (specular) RHEED spot is maximum for an atomically flat surface.[1,7,8] During the layer growth, the surface is partially covered by two-dimensional islands that act as scattering centers so that the intensity of the specular beam is reduced.[7,8] If the surface is half covered, the surface roughness is maximum within this simple model and the RHEED intensity therefore minimum.[7,8] With further increasing surface coverage, the number of scattering centers decreases again, which leads to an intensity increase.[7,8] In case of a perfect layer-by-layer growth, the initial intensity is recovered after the completion of one monolayer.[1] This oscillatory behavior of the RHEED intensity enables the thickness determination of materials that grow in the layer-by-layer mode.

3.1.2 Substrate preparation

In the framework of this thesis, the perovskite oxides $SrTiO_3$ and $(LaAlO_3)_{0.3}(Sr_2TaAlO_6)_{0.7}$ (LSAT) are used as substrates. In case of the $SrTiO_3$(100) substrates, atomically flat, TiO_2-terminated surfaces with step edges of one-unit-cell step height can be achieved by wet etching in buffered hydrofluoric acid,[9] subsequent cleaning, and annealing in 950 °C-1000 °C for 1-2 hours. The well-established wet-etching and cleaning procedure was performed on our substrates by René Borowski at the Research Centre Jülich.

In contrast, the optimal treatment of LSAT(100) substrates that creates atomically flat surfaces, is under debate.[10–14] While Ohnishi *et al.* reported the creation of flat terraces with 0.4 nm step-height and B-site termination with 91 % surface coverage by annealing at 1300 °C in air,[12] the formation of SrO mounds were observed after annealing in air at elevated temperatures of about 1100 °C by Ngai *et al.*[10] Other researchers reported optimized results for annealing at 1050 °C in continuous oxygen flow.[14] Thus, various annealing procedures were tested within the framework of this thesis.

The LSAT substrates in (100) orientation were delivered by *CrysTec GmbH Kristalltechnologie*, unless otherwise stated.

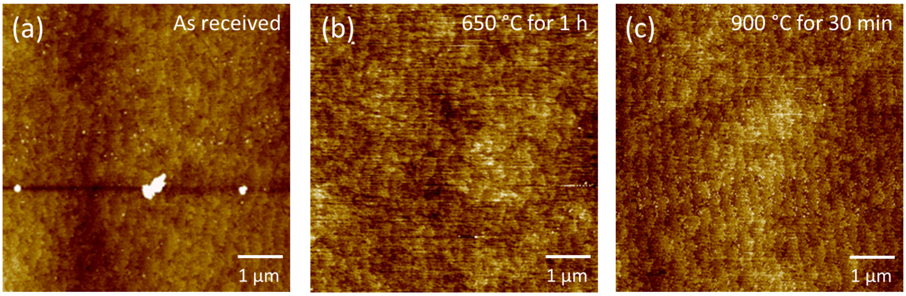

Figure 3.3: AFM surface scans (5 µm x 5 µm) of the as-received LSAT(100) substrate (a), and after annealing in 1×10^{-6} mbar at 650 °C (b) and 900 °C (c).

Since the annealing in our furnace cannot be carried out under continuous gas flow, the first annealing processes were performed under defined conditions in oxygen-reduced atmosphere in the PLD chamber. For this purpose, the substrates were glued on the substrate holder with silver paste. The chamber was evacuated and the annealing was performed at a pressure of 1×10^{-6} mbar with a heating rate of 10 °C/min to 15 °C/min. After keeping the substrates for 60 min at 650 °C (Fig. 3.3 (b)) or for 30 min at 900 °C (Fig. 3.3 (c)), the substrates were cooled down in vacuum with 10 °C/min. Shown in Fig. 3.3 is the comparison of the atomic force microscopy (AFM) scans of an as-received substrate (after cutting and cleaning in isopropanol) in (a) and the surface morphology after different (non-consecutive) annealing procedures ((b) - (c)). The surface of the as-received substrate exhibits terrace-step morphology with disordered step edges. As presented in Fig. 3.3 (b) and (c), even the annealing at 900 °C did not enable the formation of well defined terraces. Thus, it can be concluded that annealing temperatures larger than 900 °C are required in order to thermally activate the surface reconstruction and form well-defined terraces.

In order to avoid the formation of SrO clusters on the surface, which typically takes place at elevated temperatures, the procedure proposed by Ngai *et al.* was tested.[10] In this work, the LSAT substrate was placed between two sapphire plates and an $LaAlO_3$ (LAO) substrate was put on top of the sapphire plates above the LSAT substrate surface. The increase of the La vapor pressure in this configuration was proposed to suppress the creation of SrO mounds even at 1300 °C, which is sufficient to enable the formation of well ordered terrace steps.[10] This procedure was modified by placing the LSAT substrate with a thickness of 0.5 mm in between two 1 mm thick LAO substrates and covering it by another LAO substrate. As shown in Fig. 3.4 (b), the annealing of the LSAT substrates (the as-received AFM images shown in Fig. 3.4 (a)) at 1150 °C enabled the formation of step-and-terrace structure, but also of three-dimensional clusters. Furthermore, also spherical mounds were formed, despite the surrounding with LAO crystals. By testing lower annealing temperatures, a trade-off between the formation of terraces and low densities of mounds was found to be at about 1075 °C to 1100 °C (cf. Fig. 3.4 (c)-(d)).

However, substrate-to-substrate variations, with differences between different substrate batches, were observed. Thus, every LSAT substrate used in this study was investigated by atomic force microscopy before the deposition in order to ensure that the density of mounds was small.

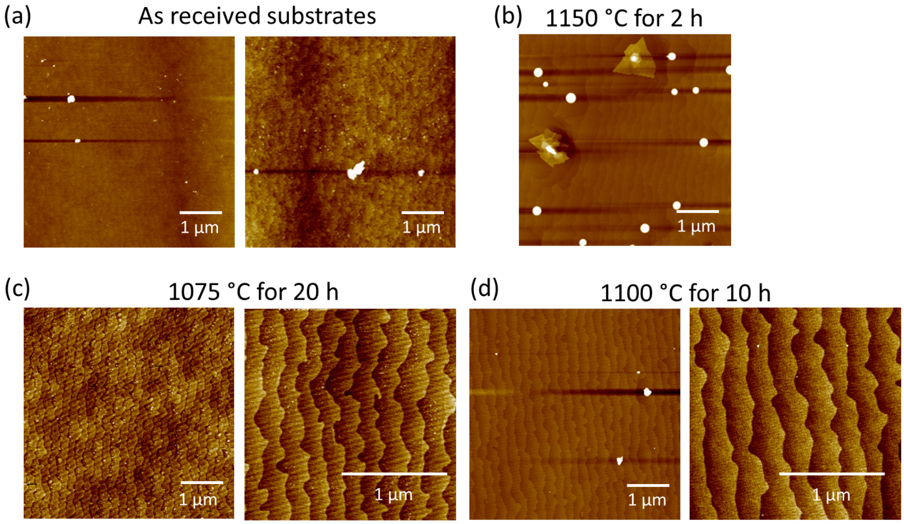

Figure 3.4: AFM surface scans (5 µm x 5 µm) of two as-received LSAT(100) substrates (a) and after annealing with an $LaAlO_3$ surrounding ((b)-(d)). The left substrate of (a) was annealed at 1150 °C for 2 h in air (b). (c) AFM images of a substrate that was annealed at 1075 °C for 20 h in air. The right substrate of (a) was annealed at 1100 °C for 10 h in air (d). (2 µm x 2 µm) AFM scans of the annealed substrates are presented in the right images of (c) and (d), respectively.

3.2 Thin film characterization methods

After the deposition, the heterostructures were characterized by several techniques. The most relevant ones will be presented subsequently. The topography of the samples was studied by atomic force microscopy. The magnetotransport measurements were mainly acquired with a custom-built set-up, which allowed additionally the simultaneous measurement of the magneto-optical Kerr effect in polar geometry. The magnetic properties were investigated by SQUID magnetometry, first order reversal curve investigations, and magnetic force microscopy.

3.2.1 Atomic force microscopy

Invented by G. Binnig, C.F. Quate, and Ch. Gerber,[17] atomic force microscopy (AFM) belongs to the class of scanning probe microscopy. The basic principle of AFM, which is frequently used to determine the topography of thin films and substrates, is sketched in Fig. 3.5.

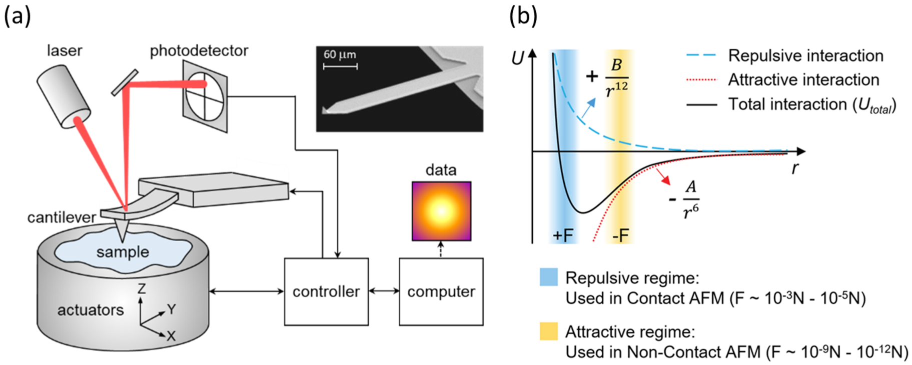

Figure 3.5: (a) Basic operation principle of atomic force microscopy; reproduced from Ref. [15] (©2022 NanoAndMore GmbH). (b) Sketch of the Lennard-Jones potential as function of the tip-sample distance. The operation regimes of the contact and non-contact mode are marked with blue and yellow, respectively. Figure reproduced from Ref. [16] (©2022 Park Systems)

The AFM probe consists of a cantilever with a sharp tip that is mounted at the movable cantilever end. When the probe laterally scans over the sample surface, the morphology-induced changes of the interatomic forces between the sample and tip will lead either to static deflection, or dynamic changes of the oscillation characteristics of the cantilever, depending on the utilized measurement mode.[16] The changes are recorded with the help of a laser beam, which is reflected from the backside of the cantilever and detected by a position-dependent (four-quadrant) photodetector.[15]

The AFM images presented throughout this thesis were acquired either in the contact- or non-contact mode. These correspond to distinct sample-tip distances and thus to different regimes of the tip-sample interactions, which are typically described by the Lennard-Jones potential.[16] The AFM measurements are performed in the repulsive regime in case of the contact-mode, while the non-contact mode is acquired at larger tip-sample distances in the attractive interaction regime (compare 3.5 (b)).[16]

In the non-contact regime, the cantilever oscillates at (or close to) its resonance frequency f_0, which is proportional to the squareroot of the effective spring constant k_0, according to Hook's law.[16,18] The changes of the surface topography then lead to variations of the sample-tip forces and therefore to alteration of the effective spring constant.[16] This affects the oscillation amplitude, oscillation frequency, or the phase.[16] Typically, the oscillation amplitude is kept constant by a feedback loop during the scan in the non-contact regime.[16] The topography-related variation of the distance between tip and sample induces a change of the oscillation amplitude that is detected by the photodetector and used for the feedback loop, which moves the z (piezo-)scanner to keep the distance constant. From the z scanner movement, the sample topography at each measured (x,y) point is calculated.[16]

3.2.2 Magnetic force microscopy

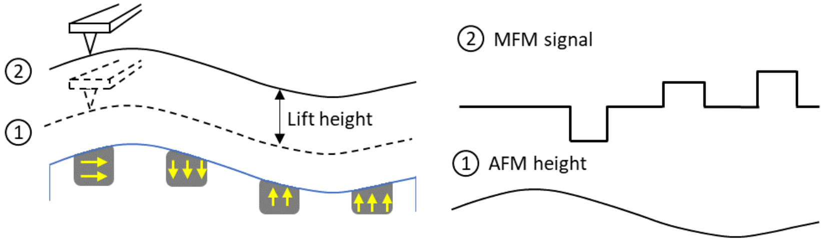

Figure 3.6: The schematic of the ‘Dual Pass’ technique that is used for MFM on an exemplary sample structure containing multiple areas with different magnetizations. The topography signal (1) is obtained in the first pass scan close to the sample and the MFM signals amplitude and phase (2), which capture the relative strength and orientation of the magnetization, respectively, is obtained in the second scan. Figure adapted from Ref. [19].

Magnetic force microscopy (MFM) is a scanning probe technique that is used to map the magnetic domain pattern[20] with spatial resolution down to 10 nm.[21] The basic measurement principle is based on conventional atomic force microscopy, with a magnetic tip on a cantilever, which interacts with the magnetic stray field of the sample surface.[20] Typically, the tip is magnetized along its axis in z-direction.

The tip-sample interactions lead to a frequency shift of the cantilever oscillation Δf[1]. If the sample-tip-distance is constant, the damping of the cantilever-oscillation is constant during the image scan, and the tip-sample distance is large with respect to the oscillation amplitude, then Δf is approximately proportional to the resonance frequency f_0 and the force gradient:

---

[1] Commercially available MFM often determine the change of the amplitude and phase of the cantilever (compare for instance Ref. [19]).

$\Delta f \approx -(f_0/(2k)(\partial F_z/\partial z)$,[22,23] where k is the spring constant of the cantilever. If the magnetic tip is approximated by a point dipole, the magnetic force between tip and sample is given by $\boldsymbol{F} = \mu_0(\boldsymbol{m}\cdot\bigtriangledown)\boldsymbol{H}$, where $\boldsymbol{H}$ is the stray field of the sample and $\boldsymbol{m}$ the magnetic moment of the tip. Thus, the magnetic contrast in MFM studies corresponds to the (out-of-plane) component of the magnetic stray field of the sample surface.[23] However, MFM measurements typically yield qualitative understanding rather than the real magnetization distribution, which can only be calculated under certain conditions.[22] By the usage of the dual-pass technique, the long range magnetic interactions can be separated from the short-range van der Waals interactions, acting between the tip and the sample surface atoms.[19,24] As indicated in Fig. 3.6, the topography of the sample is recorded during the first scan by conventional AFM. For the second scan, the tip is lifted by a few nanometers and moves along the same (x,y) line, following the topography in constant height mode.[19] During the second scan, the short-range van der Waals interactions can be neglected.[24]

3.2.3 SQUID magnetometry

The magnetization measurements presented in the course of this dissertation were carried out with the commercially available superconducting quantum interference device (SQUID) magnetometer MPMS-XL (*Quantum Design Inc*). It offers the possibility to measure the magnetic moment by applying a maximum of 7 T in a temperature range between 2 K and 400 K.[25] However, since the thin films are mounted in plastic straws, the maximum achievable temperature is limited by their deformation temperature to 350 K.

In order to detect the magnetic moment of a specimen, the straw with the mounted sample is moved through a pick-up coil that is shaped as second-order gradiometer, which efficiently cancels external constant magnetic fields and magnetic field gradients.[27] The pick-up coil is part of a superconducting closed circuit, the so-called flux transformer, which is shown in Fig. 3.7.[26,28] To conserve the total flux in the superconducting circuit, the sample movement through the pick-up coil and the corresponding change of the magnetic flux induces a (persistent) current in the flux transformer.[28,29] Due to the inductive coupling with the SQUID loop, this current generates a change of the magnetic flux in the SQUID loop that scales with the sample-induced magnetic flux change[28] and is transformed into a voltage by the (radio frequency-biased)

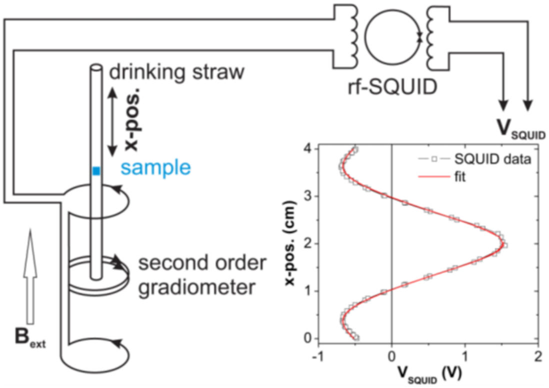

Figure 3.7: Schematic set-up of a SQUID magnetometer with 2^{nd} order gradiometer. The inset shows the SQUID response versus sample position (x-pos.). Figure reproduced from Ref. [26]: M. Buchner, K. Höfler, B. Henne, V. Ney, and A. Ney, Tutorial: Basic principles, limits of detection, and pitfalls of highly sensitive SQUID magnetometry for nanomagnetism and spintronics, Journal of Applied Physics **124**, 161101 (1018), with the permission of AIP publishing.

sensor.[30,31] The SQUID response voltage is recorded as a function of the sample position during the scan and fitted by the approximation for a magnetic point dipole that moves in the center of the pick-up coil.[26] The magnetic moment of the sample is then determined from the fitting parameters.[25,26] According to Ref. [32], the SQUID response function, depending on the sample position z, is fitted by the function $f(z)$:

$$f(z) = X(1) + X(2)\cdot z + X(3)\cdot\left(\frac{2}{(R^2+(z+X(4))^2)^{3/2}} - \frac{1}{(R^2+(\Lambda+(z+X(4)))^2)^{3/2}} - \frac{1}{(R^2+(-\Lambda+(z+X(4)))^2)^{3/2}}\right) \tag{3.1}$$

with the longitudinal coil separation Λ and the longitudinal coil radius R. While the fit parameter $X(1)$ is a constant voltage offset, $X(2)$ describes the linear electronic SQUID drift during the data aquisition process.[32] Parameter $X(4)$ corresponds to the sample shift with respect to the magnet axis.[32]

The magnetic moment of the sample is then calculated from the fit parameter $X(3)$ by the multiplication with a device-specific factor D_s, a correction factor C, and a scan-dependent factor S: [2]

$$m_{textsample} = X(3) \cdot D_s \cdot C \cdot S \tag{3.2}$$

Subtraction of magnetic impurities contribution

Since SQUID magnetometry senses every magnetic contribution that has a spatial extension smaller than the scan length, not only the magnetic signal of the sample, but also of the substrate, magnetic impurites on the sample as well as contributions from imperfect sample mounting are detected.[26,31,33,34] Furthermore, artifacts can arise from the remanent magnetic field, finite sample size, and off-centered mounting of the sample.[31,34] As investigated in detail by Garcia and Sawicki *et al.*, magnetic impurities can be introduced during many steps of the sample preparation.[33,34]

To avoid additional contributions, nonmagnetic tweezers are used during every sample handling step. The avoidance of magnetic contributions introduced by inhomogeneous sample environment on the sample holder is achieved by the mounting without additional glue for the out-of-plane orientation. Therefore, the sample is cut precisely to 4 mm x 4 mm and clamped between the walls of the plastic straw. For the in-plane measurements, the sample is glued with conventional double-sided scotch tape on a plastic sheet, both exceeding the scan length of the measurements so that additional magnetic responses due to the mounting are minimized. In order to reduce errors in the fitting procedure of the point-dipole approximation,[26] the sample size of 4 mm x 4 mm is also used for the in-plane measurements.

Despite the precautions, the intrinsic substrate contribution as well as additional paramagnetic and ferromagnetic contributions are still observed in the magnetization measurements (compare Fig. 3.8). Due to the ratio of the volumes of substrate and ultrathin film, the measured total magnetic signal is often even dominated by the magnetic signal of the substrate. Thus, the knowledge of the temperature and magnetic field dependence of magnetic background contributions is required in order to extract the sample response correctly.

The purely diamagnetic contribution, mainly originating from the substrate, is

---

[2] For further details on the device- and scan-specific parameters, the reader is referred to Ref. [32].

subtracted by linear fitting in the high magnetic field range for all the samples shown throughout this dissertation.

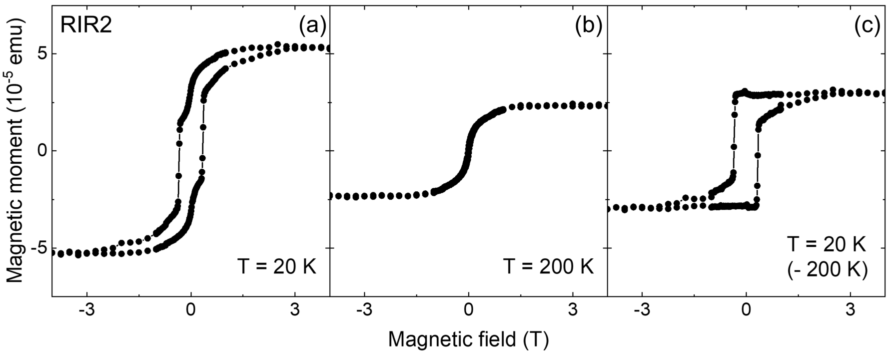

Figure 3.8: Magnetic field dependent magnetization measurements of the $SrRuO_3$-based heterostructure RIR2, corrected for the diamagnetic substrate contribution. (a) Magnetic hysteresis loop at 20 K. (b) Magnetization hysteresis loop at 200 K, above the transition temperature of the $SrRuO_3$ layers . (c) Magnetic hysteresis loop of RIR2 at 10 K after subtraction of the diamagnetic contribution and the 200 K data, shown in (b).

One source of magnetic impurities is introduced during the sample cutting with a (Ni-coated) diamond wire.[34,35] To reduce the amount of Ni contamination, the thin films were spincoated with PMMA before the cutting and cleaned with acetone and isopropanol afterwards. In case of the LSAT substrates, for which no chemical etching was necessary, the substrates were cut manually to suitable size, cleaned, and annealed afterwards, or directly ordered in 4 x 4 mm^2 from *CrysTec GmbH*. Nonetheless, the contribution due to magnetic impurities, visible in the sample hysteresis loop shown exemplarily for the $SrRuO_3$-based heterostructure RIR2 in Fig. 3.8 (a), needs to be subtracted. If such artifical contributions are not subtracted, the magnetic moment in saturation could be overestimated or the coercive field evaluation could be influenced. Since the transition temperature of Ni is at about 700 K[36] and therefore far above T_c of the heterostructures under study, the magnetic moment and the coercive fields are assumed to be constant in the temperature range between 3 K and 350 K. Thus, by measuring above the transition temperature of the ferromagnetic layers of the samples, the magnetic response of the background can be determined, as shown in Fig. 3.8. The subtraction of this measurement (Fig. 3.8 (b)) from the low temperature hysteresis loop yields a good estimation of the

sample response, as presented in Fig. 3.8 (c). However, also this correction is imperfect, as small peak-like features persist at small magnetic field values, most likely related to small temperature dependent variations of the real and estimated coercive fields of the magnetic impurity contributions.
The temperature dependent magnetic measurements, shown in the scope of this dissertation, were also background corrected.

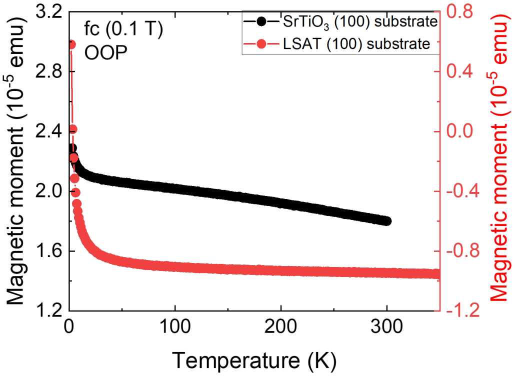

Figure 3.9: Temperature dependent magnetic moment of the two perovskite substrates $SrTiO_3$ and $(LaAlO_3)_{0.3}(Sr_2TaAlO_6)_{0.7}$.

The temperature dependence of the magnetic moment of $SrTiO_3$(100) and LSAT(100) substrates, treated as the other samples of the study, i.e. cut with the same wire saw, glued on the PLD sample holder and clamped in a plastic straw, are shown in Fig. 3.9. While the overall magnetic moment of the $SrTiO_3$ substrate is positive during the fc measurement in presence of 0.1 T, indicating the presence of ferromagnetic or paramagnetic impurities, the LSAT substrate has an overall negative magnetic moment. This indicates that the latter substrate is dominated by the intrinsic diamagnetic substrate response and that the cutting and cleaning before the annealing did not introduce large impurity densities.
The presented (scaled) fc m(T) measurements were subtracted from the measured m(T) data in order to extract the sample response. Here, the variation of the substrate volume, which might be different for the substrates used for the background measurement and those of the individual samples, is taken into account by scaling the magnetic moment of the background m(T) curve to the magnetic moment calculated from the susceptibility, extracted from the high

magnetic field fit of the magnetic hysteresis loop at high temperatures. This background correction helped to reduce the initial decrease of the magnetic moment at low temperatures, which originates from the substrate and has been attributed to magnetic impurities that occupy lattice sites in common diamagnetic substrates.[37]

3.2.4 First order reversal curve studies

In the framework of this dissertation, selected heterostructures were investigated not only by major magnetization hysteresis loops, but also by first order reversal curve studies (FORC). With FORC investigations, single magnetization reversal processes that take place in a sample can be disentangled and the distributions of the coercive fields and internal interaction fields can be accessed, which is typically unfeasible in the case of conventional major loop magnetometry.[38–45]

This makes FORC a versatile technique to study magnetic multi-component systems,[41,43,46] such as magnetic heterostructures,[43] magnetic microstructures,[41] or magnetic mineral composites.[46]

Developed by Mayergoyz,[47] FORC is considered as experimental approach to estimate the Preisach distribution under certain conditions.[38,39,47] In the Preisach model, the magnetic hysteresis of a system is described by the superposition (see Fig. 3.10 (b)) of so called hysterons.[48] Each hysteron (see Fig. 3.10 (a)), which is a rectangular defined by the switching fields H_{up} and H_{down}, corresponds to a single, sharp (irreversible) magnetization reversal process. As schematically presented in Fig. 3.10 (a), the hysteron can be described equivalently by the coercive field H_{c} and the interaction field H_{u}. The mapping of the hysteron characteristics onto the H_{c}-H_{u}-plane then yields the Preisach distribution (cf. Fig. 3.10 (c)).[48]

According to Mayergoyz, first order reversal curves can be used to experimentally approach the Preisach distribution, if two criteria[3] are fulfilled:[47]

- Wiping out property:
  All minor loops, measured between the reversal points H_{min} and H_{max} (with $H_{\mathrm{min}} < H_{\mathrm{max}}$) are independent of the details of the magnetic field sweep for $H_{\mathrm{min}} < H < H_{\mathrm{max}}$ and close after one cycle.

---

[3] The two criteria are formulated following Ref. [45].

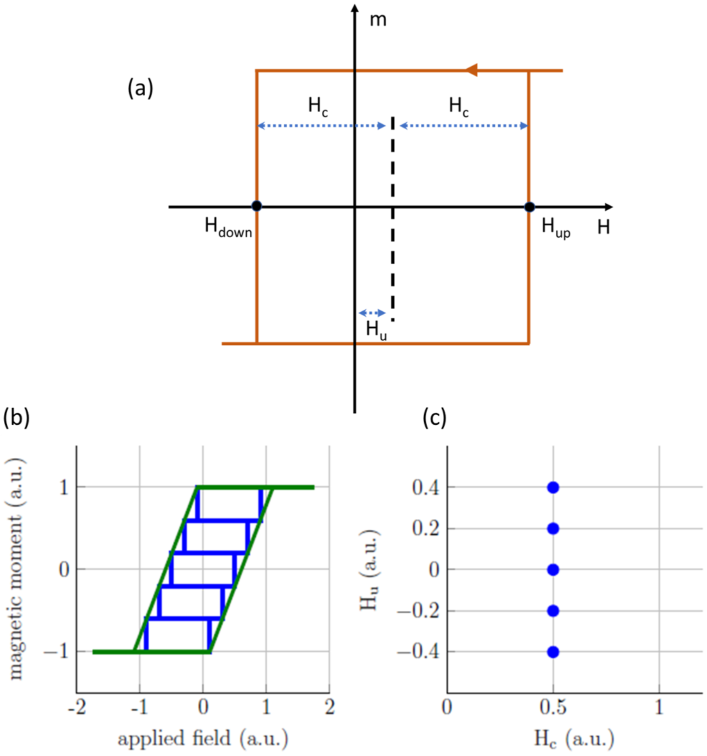

Figure 3.10: (a) Scheme of a hysteron, as introduced by Preisach. H_{up} and H_{down} are the magnetic fields where the magnetization is switched. H_{u} is the interaction field and H_{c} is the coercive field. (b) Fictitious magnetic hysteresis loop (green), approximated by 5 hysterons (blue). The individual hysterons have different interaction fields, but identical coercive field. The corresponding Preisach distribution in the H_{c}-H_{u}-plane is shown in (c). Figure (a) inspired from Ref. [39]. Figures (b) and (c) are reproduced from Ref. [45].

- Congruency property:

  All minor hysteresis loops that correspond to the same minimum applied field H_{min} and maximum applied field H_{max} are geometrically congruent.

Since these two conditions are rarely fulfilled in real systems,[38] the interpretation of FORC diagrams can be difficult and hence they are often considered as qualitative *fingerprint of the magnetic properties.*[41,42] However, Pike *et al.* proposed to use FORC as an experimental technique independent of the Preisach-like interpretation.[49] Several studies have shown that FORC densities can help to gain a deeper understanding of a system and yield quantative information, instead of being a mere fingerprint.[38,41,42]

In order to obtain the FORC-density map, a set of first order curves (cf. Fig. 3.11 (b)) is measured with set-ups capable to study the magnetization or quantities proportional to the magnetization, such as SQUID magnetometry[42] or magneto-optical Kerr effect investigations.[43]

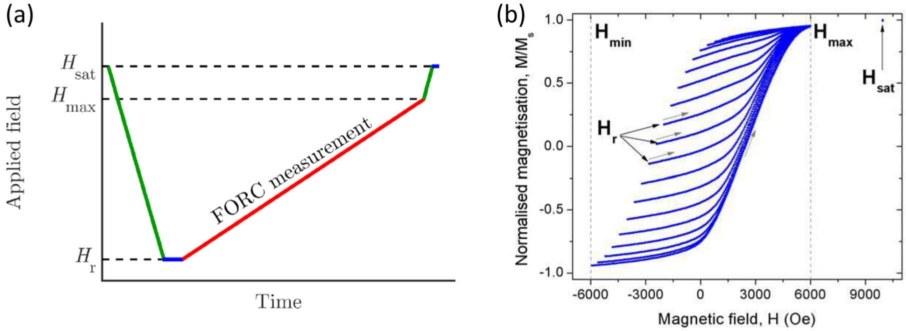

Figure 3.11: (a) Schematics of the applied magnetic field as function of time for a single first order reversal curve measurement. (b) Example of a set of first order reversal curves of a CoFe nanowire array. Figure (a) reprinted with permission from Ref. [42]: S. E. Ilse, F. Groß, G. Schütz, J. Gräfe, and E. Goering, Understanding the interaction of soft and hard magnetic components in NdFeB with first-order reversal curves, Physical Review B **103**, 024425 (2021), Copyright 2021 by the American Physical Society. Figure (b) reproduced from Ref. [39] (distributed under the terms of the Creative COmmons Attribution- NonCommercial-ShareAlike-3.0 License, ©2010 Fanny Béron, Louis-Philippe Carignan, David Ménard, and Arthur Yelon.

Each first order reversal curve is a minor loop that is characterized by its reversal field H_{r}.[43] The measurement procedure with a SQUID magnetometer, sketched in Fig. 3.11 (a) and following Ref. [39, 42, 45], starts by saturating the sample in H_{sat}. Subsequently, the magnetic field H_{r} (with $H_{\text{r}} < H_{\text{sat}}$) is applied to reverse the sample´s magnetization partially. Then, the first order reversal curve is measured by sweeping the external magnetic field H from H_{r} to H_{max}. For the next minor loop, the sample is again saturated in H_{sat}.

The FORC density[4] is then obtained by calculating the mixed second derivative of the measured magnetic moment surface:[38]

$$\rho_{\text{FORC}}(H, H_r) = -\frac{1}{2}\frac{\partial^2 m(H, H_r)}{\partial H \partial H_r} \tag{3.3}$$

---

[4] For further details on the numeric data analysis, the reader is referred to Ref. [40, 42, 44, 45].

To describe the FORC density as function of the interaction field H_u and the coercive field H_c, the H- and H_r-axes are transformed:

$$H_c = \frac{1}{2}(H - H_r), \qquad H_u = \frac{1}{2}(H + H_r) \tag{3.4}$$

It was recently shown that FORC studies are furthermore capable to detect the type of magnetic coupling in heterogeneous systems.[41] In presence of magnetic coupling, the magnetic switching field of a magnetic subsystem depends on the magnetization of the other subsystems, which violates the congruency property.[41] According to Ref. [41], this leads to the generation of an interaction peak pair, whose shape gives insight whether the coupling is ferromagnetic or antiferromagnetic.

3.2.5 Magneto-optical Kerr effect measurements

The magneto-optical Kerr effect (MOKE), discovered by Kerr in 1878,[50] describes the phenomenon that linearly polarized light gets elliptically polarized with a rotation of the polarization plane upon reflection at the surface of a magnetized medium (in polar and longitudinal geometry).[51–53] The change of the polarization state is described by the (wavelength dependent) complex Kerr angle $\widetilde{\Theta_\mathrm{K}} = \Theta_\mathrm{K} + i\eta_\mathrm{K}$. The geometric definition of the Kerr rotation angle Θ_K and the ellipticity angle η_K is indicated in Fig. 3.12. The ellipticity $\epsilon_\mathrm{K} = \tan \eta_\mathrm{K}$ is determined by the ratio of the long and short axes a, b of the ellipse and is usually defined as $\epsilon_\mathrm{K} = b/a$,[52] whereas Θ_K is the angle between the major axis and the axis of polarization of the incident wave.

The magneto-optical Kerr effect originates from the difference of the refractive indices of left-circularly polarized (LCP) and right-circularly polarized (RCP) light for the reflection at the surface of a magnetized crystal.[51] Linearly polarized light can always be written as the combination of left-circularly polarized and right-circularly polarized waves with equal amplitudes.[52]

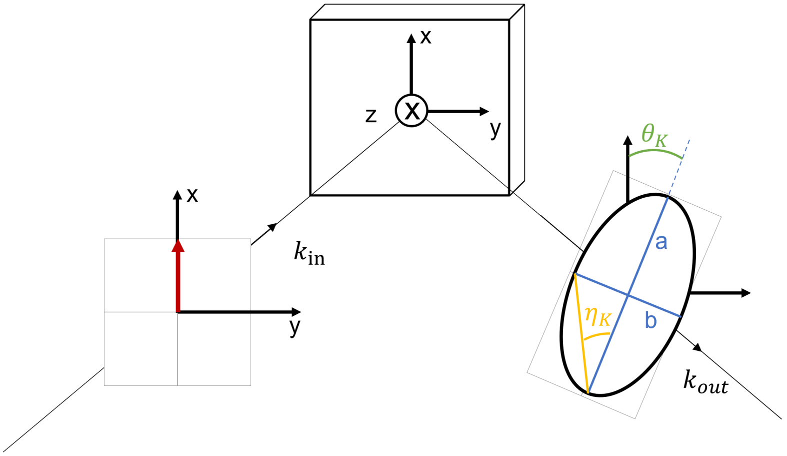

Figure 3.12: Scheme of the change of the polarization state of linearly polarized light upon reflection at the surface of a magnetized solid. The incident light wave, propagating along z-direction, is linearly polarized with the polarization (red) along the x-direction. Upon reflection at the surface of the sample, magnetized along z-direction by a magnetic field, the light gets elliptically polarized. The polarization plane is rotated by Θ_K with respect to the polarization vector of the incident wave. The ellipticity ϵ_K is defined by the ratio of the ellipse axes b and a. Figure inspired from Ref. [54].

To derive the relation between the complex Kerr rotation $\widetilde{\Theta_{\mathrm{K}}}$ and the optical properties of a solid, the dielectric tensor is considered. In case of a sample with cubic symmetry that is magnetized in crystallographic z-direction and the light propagation along z-direction (polar geometry), the optical dielectric tensor $\tilde{\epsilon}$ is given by:

$$\tilde{\epsilon} = \begin{pmatrix} \epsilon_{xx} & \epsilon_{xy} & 0 \\ -\epsilon_{xy} & \epsilon_{xx} & 0 \\ 0 & 0 & \epsilon_{xx} \end{pmatrix} \qquad \tilde{\epsilon_c} = \begin{pmatrix} \epsilon_{xx} - i\epsilon_{xy} & 0 & 0 \\ 0 & \epsilon_{xx} + i\epsilon_{xy} & 0 \\ 0 & 0 & \epsilon_{xx} \end{pmatrix} \tag{3.5}$$

The off-diagonal elements of $\tilde{\epsilon}$ that cause the difference of the refractive indices for LCP and RCP waves, are only non-zero when time-reversal symmetry is broken, i.e. in presence of an external magnetic field or finite magnetization.[52] $\tilde{\epsilon_c}$ represents the diagonalized form of $\tilde{\epsilon}$ with spherical basis. The eigenvalues $\tilde{n}_{\pm} = \sqrt{\epsilon_{xx} \pm i\epsilon_{xy}}$ are the complex refractive indices.

Following Ref. [52, 55–57], the polarization variable ζ describes the ratio of left and right circular polarization components of the reflected wave ($E_{\text{out},+}$ and $E_{\text{out,-}}$) and can be expressed in terms of the incoming light polarization components $E_{\text{in},\pm}$ and the complex reflection coefficient $\tilde{\rho_{\pm}}$:

$$\zeta = \frac{E_{\text{out},+}}{E_{\text{out,-}}} = \frac{E_{\text{in},+}\tilde{\rho_+}}{E_{\text{in,-}}\tilde{\rho_-}} = \frac{\tilde{\rho_+}}{\tilde{\rho_-}} \tag{3.6}$$

The Fresnel equation for reflection at normal incidence is given by

$$\tilde{\rho_{\pm}} = \frac{\tilde{n}_{\pm} - 1}{\tilde{n}_{\pm} + 1} \tag{3.7}$$

Since $\epsilon_{xy} \ll \epsilon_{xx}$, Equation (3.6) can be written as:

$$\zeta = \frac{2i\epsilon_{xy}}{\sqrt{\epsilon_{xx}}(\epsilon_{xx} - 1)} + 1 \tag{3.8}$$

This polarization variable corresponds geometrically to[55,56]

$$\zeta = e^{2i\Theta_K} \frac{1 - \tan \eta_K}{1 + \tan \eta_K} \approx 1 + 2(i\Theta_k - \eta_K) \tag{3.9}$$

The approximation is valid for small Θ_K, ϵ_K. The comparison of Equations (3.8) and (3.9) then yields the connection of the complex Kerr rotation angle and the elements of the dielectric tensor:

$$\Theta_K + i\eta_K = \frac{\epsilon_{xy}}{\sqrt{\epsilon_{xx}}(\epsilon_{xx} - 1)} \tag{3.10}$$

Phenomenologically, the origin of the magneto-optical Kerr can be understood by the classical description of the interaction of light and electrons in a solid.[58] The electric field of the electromagnetic wave that is propagating through matter will move the electrons. LCP light will generate left circular motion and RCP light will cause right circular motion of the electrons. Only in presence of the Lorentz force due to an external magnetic field, the radii of the circular motion will differ for LCP and RCP which then leads to different dielectric constants for RCP and LCP.[58] Quantum mechanically, the Kerr effect is determined by the exchange splitting and scales with spin-orbit coupling.[51,52] It was experimentally observed and theoretically shown by perturbation theory that the Kerr constants are (in first order) proportional to the sample magnetization.[51,58]

In case of magnetic multilayers, the total Kerr effect Θ_K^{tot} is the sum of the contributions originating from the Kerr response of the individual magnetic layers θ_i:[54]$\Theta_K^{\text{tot}} = \sum_i \theta_i$. In case of thin films, the ratio of the penetration depth and film thickness requires the consideration of additional internal reflections or reflections at the substrate-sample-interface.[54,59]

Due to its proportionality to the magnetization, the Kerr rotation angle is an important measurable in the scope of this dissertation.

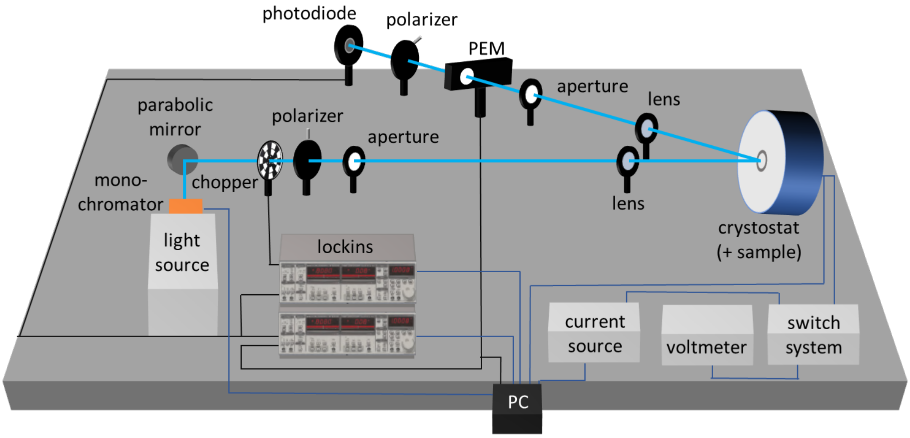

Figure 3.13: Scheme of the polar magneto-optical Kerr effect measurement set-up utilized in the framework of this dissertation. The optical set-up was upgraded by Jörg Schöpf so that p-MOKE and magnetotransport can be measured simultaneously. Figure inspired from Ref. [55, 56, 59].

Sketched in Fig. 3.13 is the experimental set-up used to study the Kerr rotation angle in polar geometry (p-MOKE). The propagation vector is slightly tilted (5 deg[56]) with respect to the surface normal of the sample, which can be magnetized by the application of a magnetic field perpendicular to the thin film surface.

In order to determine the change of the light polarization state due to the reflection at a magnetized sample, the light intensity is measured as a function of the polarization state. The simultaneous detection of the Kerr rotation angle and the ellipticity can be achieved with high accuracy by usage of the double modulation technique and lock-in amplifiers.

Depending on the sample requirements, either a 450 W xenon lamp, or a 491 nm laser are used as light source for the p-MOKE experiments. As shown in Fig.

3.13, a monochromator installed behind the xenon lamp is utilized in order to select a specific light wavelength from the achievable range between 350 and 1500 nm.[56] After light collimation by a parabolic mirror, an optical chopper, operating at 680 Hz, modulates the light. Subsequently, the light gets linearly polarized by the first polarizer, which consists of a Glan-Taylor prism. The sample is installed in a cryostat (*MagnetoStatMo Oxford*) that allows the application of magnetic fields up to 5 T perpendicular to the thin film surface.[56] Measurements can be performed in a temperature range between 300 K and 8 K.[56] The focusing of the light is achieved by biconvex lenses in front of the crystotat before and after the reflection at the sample surface. As indicated in Fig. 3.13, the reflected laser light is furthermore modulated by a photoelastic modulator (PEM). The PEM (*Hinds Instruments*) consists of a transparent crystal, often fused silica, which is periodically deformed by a piezoelectric element. This induces periodically stress birefringence and therefore modulates the polarization state of the light with 50 kHz and 100 kHz (2nd harmonic). Then, the light passes through a second polarizer, the analyzer. At the detector (a silicon photodiode) the light intensity is measured and decomposed by 2 lock-in amplifiers into its 680 Hz component, corresponding to I_{DC}, the 50 kHz ($I_{1\mathrm{f}}$), and 100 kHz ($I_{2\mathrm{f}}$) components. The Kerr rotation Θ_{Kerr} and ellipticity ϵ_{Kerr} are then calculated from:[56]

$$\epsilon_{\mathrm{Kerr}} = \frac{1}{C_1}\frac{I_{1\mathrm{f}}}{I_{\mathrm{DC}}} \qquad \Theta_{\mathrm{Kerr}} = \frac{1}{C_2}\frac{I_{2\mathrm{f}}}{I_{\mathrm{DC}}} \tag{3.11}$$

with calibration factors C_1 and C_2 that are generally wavelength-dependent. C_2 can be easily determined by the change of the first polarizer from the angle ϕ_0 to ϕ_i. In the small angle regime, C_2 is then given by the slope of the linear function fitted to the determined data points of $(I_{2\mathrm{f}}/I_{\mathrm{DC}})(\phi)$. Since the setup was originally designed by Dr. Rolf Versteeg and Simon Schäfer,[55,56] and upgraded by an electric-transport-measurement system by Jörg Schöpf, the reader is referred to the respective theses for further details on the derivation of Equation (3.11) and the determination of C_1.[55,56,59]

3.2.6 Transport measurements in van der Pauw geometry

The thin films characterized in the scope of this dissertation were investigated by (magneto-)transport investigations in the van der Pauw geometry, which allows the determination of the resistivity and Hall effect of arbitrarily shaped samples without the need for the knowledge of the exact current distribution.[60]

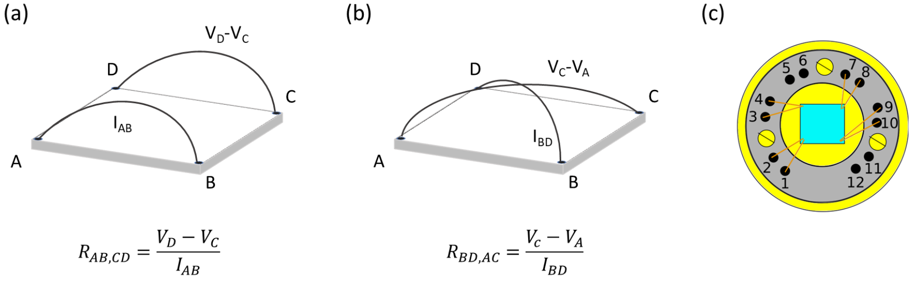

Figure 3.14: General idea of the measurement principle of magnetotransport investigations in van der Pauw geometry (a) and (b). Exemplarily shown in (a) is the definition of $R_{\mathrm{AB,CD}}$ and the definition of $R_{\mathrm{BD,AC}}$ (for Hall studies) is presented in (b). (c) Sketch of the sample holder and respective electrical wiring for the set-up presented in Fig. 3.13. The sample is drawn as blue square, the wiring for Hall measurements in van der Pauw geometry are shown in orange. Figure (c) reprinted from Ref. [59].

If the isotropic[5] and singly connected sample is homogeneously thick and the four point-like contacts situated arbitrarily on the samples' circumference, the resistivity ρ is calculated from:[60]

$$\exp\left(-\frac{\pi d R_{\mathrm{AB,CD}}}{\rho}\right) + \exp\left(-\frac{\pi d R_{\mathrm{BC,DA}}}{\rho}\right) = 1 \qquad (3.12)$$

d is the thickness of the sample. The resistance $R_{\mathrm{AB,CD}}$ denotes the quotient of the potential difference V_D-V_C, measured between contacts D and C, and the current I_{AB} that is flowing through contacts A and B (cf. Fig. 3.14 (a)).[60] $R_{\mathrm{BC,DA}}$ is defined accordingly by the voltage difference V_A-V_D per current I_{BC}. The Equation (3.12) can be solved numerically.[61] As shown by van der Pauw, the resistivity ρ is given by:

$$\rho = \frac{\pi d}{\ln 2} \frac{R_{\mathrm{AB,CD}} + R_{\mathrm{BC,DA}}}{2} f\left(\frac{R_{\mathrm{AB,CD}}}{R_{\mathrm{BC,DA}}}\right) \qquad (3.13)$$

---

[5] An example of the extension of the van der Pauw method for anisotropic samples is presented in Chapter 8.

with the correction factor f, which is given by the solution of:

$$\frac{R_{\mathrm{AB,CD}} - R_{\mathrm{BC,DA}}}{R_{\mathrm{AB,CD}} + R_{\mathrm{BC,DA}}} = f \operatorname{arccos}\left(\frac{\exp\left(\ln 2/f\right)}{2}\right) \tag{3.14}$$

Experimental artifacts impacting on the resistivity can arise from (charge carrier) inhomogeneities[62] or improper contact placement at finite distance from the circumference.[60] It was furthermore demonstrated by van der Pauw that the transversal Hall voltage can be determined in van der Pauw geometry by the measurement of the resistance $R_{\mathrm{BD,AC}}$, as presented in Fig. 3.14 (b). In the low field limit, the application of a magnetic field perpendicular to the thin film surface causes the change of the resistance $R_{\mathrm{BD,AC}}$ (measured in absence of a magnetic field) by $\Delta R_{\mathrm{BD,AC}}$.[60] However, in sizable magnetic fields H along the surface normal, contributions originating from the longitudinal magnetoresistance will contribute additionally to the Hall coefficient R_H.[63] Since the longitudinal magnetoresistance is an even function of the magnetic field, wheras the transversal Hall is an odd function, this contribution can be subracted by calculating (half of) the difference of the measurements of $R_{\mathrm{BD,AC}}$ in $+H$ and $-H$ magnetic field directions.[63] According to Spal,[64] Sample,[65] and Levy *et al.*,[63] the interchange of current and voltage electrodes is equivalent to the inversion of the magnetic field direction. Thus, the Hall resistance was calculated in the scope of this dissertation by:[59]

$$R_{Hall} = \frac{1}{2}\left(R_{\mathrm{BD,AC}}(H) - R_{\mathrm{AC,BD}}(H)\right) \tag{3.15}$$

with the definitions of $R_{\mathrm{BD,AC}}$ (and $R_{\mathrm{AC,BD}}$) as sketched in Fig. 3.14 (b). Most of the electric studies were performed with the set-up presented in Fig. 3.13, due to the capability to aquire the electric resistance and magneto-optical Kerr rotation angle under as identical conditions as possible, such as temperature, magnetic field, and sweep rate.

The permutation of the voltage and current electrodes was realized by the sample mounting on the holder presented in Fig. 3.14 (c) and a software-controlled switch system which periodically switched[6] between the measurement of $R_{\mathrm{BD,AC}}$ and $R_{\mathrm{AC,BD}}$.[59]

---

[6] The time delay between the two measurements of $R_{\mathrm{BD,AC}}$ and $R_{\mathrm{AC,BD}}$ leads to differences in the applied magnetic field, which is depending on the sweep rate. According to Ref. [59], the difference is about 13 mT for a sweep rate of 0.5 T/min.

When magnetic fields larger than 5 T were required, the transport measurements were performed in a PPMS (*Quantum Design Inc.*). Two measurement bridges with interchanged voltage and current electrodes were connected so that the sample was contacted with two copper wires per contact.

References

[1] H. M. Christen and G. Eres: *Recent advances in pulsed-laser deposition of complex oxides*, Journal of Physics: Condensed Matter **20**, 264005 (2008).

[2] R. Eason: *Pulsed laser deposition of thin films: Applications-LED growth of functional materials* (John Wiley & Sons, Hoboken, 2007).

[3] P. R. Willmott and J. R. Huber: *Pulsed laser vaporization and deposition*, Rev. Mod. Phys. **72**, 315 (2000).

[4] D. Dijkkamp, T. Venkatesan, X. D. Wu, S. A. Shaheen, N. Jisrawi, Y. H. Min-Lee, W. L. McLean, and M. Croft: *Preparation of Y-Ba-Cu oxide superconductor thin films using pulsed laser evaporation from high T_c bulk material*, Applied Physics Letters **51**, 619–621 (1987).

[5] F. Gunkel: "The role of defects at functional interfaces between polar and non-polar perovskite oxides", Rheinisch-Westfälisch Technische Hochschule Aachen, PhD thesis (Apr. 2013).

[6] Application note pulsed-laser deposition set up (SURFACE & SURFACE systems+technology GmbH & Co. KG), print-out, 2019.

[7] S. Hasegawa: Reflection high-energy electron diffraction, *Characterization of materials* (John Wiley & Sons, Ltd, 2012), 1925–1938.

[8] H. Y. Sun, Z. W. Mao, T. W. Zhang, L. Han, T. T. Zhang, X. B. Cai, X. Guo, Y. F. Li, Y. P. Zang, W. Guo, J. H. Song, D. X. Ji, C. Y. Gu, C. Tang, Z. B. Gu, N. Wang, Y. Zhu, D. G. Schlom, Y. F. Nie, and X. Q. Pan: *Chemically specific termination control of oxide interfaces via layer-by-layer mean inner potential engineering*, Nature Communications **9**, 2965 (2018).

[9] G. Koster, B. L. Kropman, G. J. H. M. Rijnders, D. H. A. Blank, and H. Rogalla: *Quasi-ideal strontium titanate crystal surfaces through formation of strontium hydroxide*, Applied Physics Letters **73**, 2920–2922 (1998).

[10] J. H. Ngai, T. C. Schwendemann, A. E. Walker, Y. Segal, F. J. Walker, E. I. Altman, and C. H. Ahn: *Achieving A-site termination on $La_{0.18}Sr_{0.82}Al_{0.59}Ta_{0.41}O_3$ substrates*, Advanced Materials **22**, 2945–2948 (2010).

[11] A. Biswas, C.-H. Yang, R. Ramesh, and Y. H. Jeong: *Atomically flat single terminated oxide substrate surfaces*, Progress in Surface Science **92**, 117–141 (2017).

[12] T. Ohnishi, K. Takahashi, M. Nakamura, M. Kawasaki, M. Yoshimoto, and H. Koinuma: *A-site layer terminated perovskite substrate:* $NdGaO_3$, Applied Physics Letters **74**, 2531–2533 (1999).

[13] H. Li, L. Salamanca-Riba, R. Ramesh, and J. H. Scott: *Ordering in* $(La, Sr)(Al, Ta)O_3$ *substrates*, Journal of Materials Research **18**, 1698–1704 (2003).

[14] P. Brinks: "Highly anisotropic transport properties at interfaces of oxides", Master thesis, University of Twente (May 2010).

[15] `https://afm.oxinst.com/outreach/atomic-force-microscopy`, last accessed: 03/04/22.

[16] Application note Parksystems AFM, `https://www.parksystems.com/index.php/park-spm-modes/91-standard-imaging-mode/217-true-non-contact-mode`, last accessed:03/04/22.

[17] S. Morita, F. J. Giessibl, E. Meyer, and R. Wiesendanger: *Noncontact Atomic Force Microscopy*, Vol. 3 (Springer, Berlin/Heidelberg, 2015).

[18] Application note Nanoandmore, `https://www.nanoandmore.com/what-is-atomic-force-microscopy`, last accessed:02/04/22.

[19] Application note Parksystems MFM, `https://www.parksystems.com/images/spmmodes/standard/ModeNote_MFM_Park_Systems.pdf`, last accessed:03/04/22.

[20] D. Rugar, H. J. Mamin, P. Guethner, S. E. Lambert, J. E. Stern, I. McFadyen, and T. Yogi: *Magnetic force microscopy: General principles and application to longitudinal recording media*, Journal of Applied Physics **68**, 1169–1183 (1990).

[21] M. R. Freeman and B. C. Choi: *Advances in magnetic microscopy*, Science **294**, 1484–1488 (2001).

[22] H. J. Hug, B. Stiefel, P. J. A. van Schendel, A. Moser, R. Hofer, S. Martin, H.-J. Güntherodt, S. Porthun, L. Abelmann, J. C. Lodder, G. Bochi, and R. C. O'Handley: *Quantitative magnetic force microscopy on perpendicularly magnetized samples*, Journal of Applied Physics **83**, 5609–5620 (1998).

[23] M. Liebmann, A. Schwarz, U. Kaiser, R. Wiesendanger, D.-W. Kim, and T.-W. Noh: *Magnetization reversal of a structurally disordered manganite thin film with perpendicular anisotropy*, Physical Review B **71**, 104431 (2005).

[24] O. Kazakova, R. Puttock, C. Barton, H. Corte-León, M. Jaafar, V. Neu, and A. Asenjo: *Frontiers of magnetic force microscopy*, Journal of Applied Physics **125**, 060901 (2019).

[25] MPMS User manual, print-out.

[26] M. Buchner, K. Höfler, B. Henne, V. Ney, and A. Ney: *Tutorial: Basic principles, limits of detection, and pitfalls of highly sensitive SQUID magnetometry for nanomagnetism and spintronics*, Journal of Applied Physics **124**, 161101 (2018).

[27] G. J. van Nieuwenhuyzen and V. J. de Waal: *Second order gradiometer and dc squid integrated on a planar substrate*, Applied Physics Letters **46**, 439–441 (1985).

[28] A. Zieba: *Image and sample geometry effects in SQUID magnetometers*, Review of Scientific Instruments **64**, 3357–3375 (1993).

[29] R. L. Fagaly: *Superconducting quantum interference device instruments and applications*, Review of Scientific Instruments **77**, 101101 (2006).

[30] M. McElfresh: *Fundamentals of magnetism and magnetic measurements featuring Quantum Design´s Magnetic Property Measurements System* (Quantum Design, 1994).

[31] P. Stamenov and J. M. D. Coey: *Sample size, position, and structure effects on magnetization measurements using second-order gradiometer pickup coils*, Review of Scientific Instruments **77**, 015106 (2006).

[32] MPMS Application Note 1014-213: Subtracting the Sample Holder Background from Dilute Samples, 2002.

[33] M. A. Garcia, E. Fernandez Pinel, J. de la Venta, A. Quesada, V. Bouzas, J. F. Fernández, J. J. Romero, M. S. Martín González, and J. L. Costa-Krämer: *Sources of experimental errors in the observation of nanoscale magnetism*, Journal of Applied Physics **105**, 013925 (2009).

[34] M. Sawicki, W. Stefanowicz, and A. Ney: *Sensitive SQUID magnetometry for studying nanomagnetism*, Semiconductor Science and Technology **26**, 064006 (2011).

[35] `https://www.diamondwiretec.com`, last accessed: 03/04/22.

[36] L. Néel: *Propriétés magnétiques du nickel pur à proximité du point de curie*, J. Phys. Radium **6**, 27–34 (1935).

[37] M. Khalid, A. Setzer, M. Ziese, P. Esquinazi, D. Spemann, A. Pöppl, and E. Goering: *Ubiquity of ferromagnetic signals in common diamagnetic oxide crystals*, Physical Review B **81**, 214414 (2010).

[38] C.-I. Dobrotă and A. Stancu: *What does a first-order reversal curve diagram really mean? A study case: Array of ferromagnetic nanowires*, Journal of Applied Physics **113**, 043928 (2013).

[39] F. Béron, L.-P. Carignan, D. Ménard, and A. Yelon: Extracting individual properties from global behaviour: first-order reversal curve method applied to magnetic nanowire arrays, *Electrodeposited nanowires and their applications*, edited by N. Lupu (IntechOpen, Rijeka, 2010) Chap. 7.

[40] F. Groß, J. C. Martínez-García, S. E. Ilse, G. Schütz, E. Goering, M. Rivas, and J. Gräfe: *GFORC: A graphics processing unit accelerated first-order reversal-curve calculator*, Journal of Applied Physics **126**, 163901 (2019).

[41] F. Groß, S. E. Ilse, G. Schütz, J. Gräfe, and E. Goering: *Interpreting first-order reversal curves beyond the Preisach model: An experimental permalloy microarray investigation*, Physical Review B **99**, 064401 (2019).

[42] S. E. Ilse, F. Groß, G. Schütz, J. Gräfe, and E. Goering: *Understanding the interaction of soft and hard magnetic components in NdFeB with first-order reversal curves*, Phys. Rev. B **103**, 024425 (2021).

[43] J. Gräfe, M. Schmidt, P. Audehm, G. Schütz, and E. Goering: *Application of magneto-optical Kerr effect to first-order reversal curve measurements*, Review of Scientific Instruments **85**, 023901 (2014).

[44] J. Gräfe, F. Groß, S. E. Ilse, D. B. Boltje, S. Muralidhar, and E. J. Goering: *LeXtender: a software package for advanced MOKE acquisition and analysis*, Measurement Science and Technology **32**, 067002 (2021).

[45] S. E. Ilse: "Using FORC to understand the microstructure-micromagnetism relationship in supermagnets", Master thesis (Max Planck Institut für Intelligente Systeme und Universität Stuttgart, Nov. 2017).

[46] T. A. Berndt, L. Chang, S. Wang, and S. Badejo: *Time-Asymmetric FORC Diagrams: A New Protocol for Visualizing Thermal Fluctuations and Distinguishing Magnetic Mineral Mixtures*, Geochemistry, Geophysics, Geosystems **19**, 3056–3070 (2018).

[47] I. D. Mayergoyz: *Mathematical models of hysteresis*, Phys. Rev. Lett. **56**, 1518 (1986).

[48] F. Preisach: *Über die magnetische Nachwirkung*, Zeitschrift für Physik **94**, 277–302 (1935).

[49] C. R. Pike, A. P. Roberts, and K. L. Verosub: *Characterizing interactions in fine magnetic particle systems using first order reversal curves*, Journal of Applied Physics **85**, 6660–6667 (1999).

[50] J. Kerr: *XLIII. On rotation of the plane of polarization by reflection from the pole of a magnet*, The London, Edinburgh, and Dublin Philosophical Magazine and Journal of Science **3**, 321–343 (1877).

[51] P. N. Argyres: *Theory of the Faraday and Kerr Effects in Ferromagnetics*, Phys. Rev. **97**, 334 (1955).

[52] P. Oppeneer: Magneto-Optical Kerr Spectra, *Handbook of magnetic materials* (Elsevier, Amsterdam, Jan. 2001), 229–422.

[53] T. Haider: *A Review of Magneto-Optic Effects and Its Application*, International Journal of Electromagnetics and Applications **7**, 17–24 (2017).

[54] J. Hamrle: “Magneto-optical determination of the in-depth magnetization profile in magnetic multilayers”, PhD thesis (Université Paris Sud- Paris XI, June 2003).

[55] S. Schäfer: “Construction of a polarization spectrometer and observation of the skyrmion phase in the magneto-electric insulator Cu_2OSeO_3”, Master thesis, University of Cologne (May 2015).

[56] R. B. Versteeg: “Optically probed order and dynamics in the chiral cluster magnet Cu_2OSeO_3”, University of Cologne, PhD thesis (May 2019).

[57] R. Mirzaaghayev: “Magneto-optical studies of $SrRuO_3$ thin film heterostructures”, Master thesis, University of Bonn (Sept. 2018).

[58] Z. Q. Qiu and S. D. Bader: *Surface magneto-optic Kerr effect*, Review of Scientific Instruments **71**, 1243–1255 (2000).

[59] J. Schöpf: “Design of a setup for simultaneous magneto-transport and magneto-optical effects of ferromagnetic thin film heterostructures”, Master thesis, University of Cologne (Nov. 2019).

[60] L. J. van der Pauw: *A method of measuring specific resistivity and Hall effect of discs of arbitrary shape*, Philips Research Reports **13**, 1–9 (1958).

[61] W. L. V. Price: *Electric potential and current distribution in a rectangular sample of anisotropic material with application to the measurement of the principal resistivities by an extension of van der Pauw’s method*, Solid-State Electronics **16**, 753–762 (1973).

[62] O. Bierwagen, T. Ive, C. G. Van de Walle, and J. S. Speck: *Causes of incorrect carrier-type identification in van der Pauw–Hall measurements*, Applied Physics Letters **93**, 242108 (2008).

[63] M. Levy and M. P. Sarachik: *Measurement of the Hall coefficient using van der Pauw method without magnetic field reversal*, Review of Scientific Instruments **60**, 1342–1343 (1989).

[64] R. Spal: *A new dc method of measuring the magnetoconductivity tensor of anisotropic crystals*, Journal of Applied Physics **51**, 4221–4225 (1980).

[65] H. H. Sample, W. J. Bruno, S. B. Sample, and E. K. Sichel: *Reverse-field reciprocity for conducting specimens in magnetic fields*, Journal of Applied Physics **61**, 1079–1084 (1987).

Part II

Design and investigation of epitaxial heterostructures with (different thickness) $SrRuO_3$ layers

Chapter 4

Correlating the nanoscale structural, magnetic, and magnetotransport properties in $SrRuO_3$-based perovskite heterostructures

Contents

This chapter is based on the paper:
Gerald Malsch, Dmytro Ivaneyko, Peter Milde, Lena Wysocki, Lin Yang, Paul H. M. van Loosdrecht, Ionela Lindfors-Vrejoiu, and Lukas M. Eng, *Correlating the Nanoscale Structural, Magnetic and Magneto-Transport Properties in $SrRuO_3$-Based Perovskite Thin Films: Implications for Oxide Skyrmion Devices*, ACS Applied Nano Materials **3**, 1182-1190 (2020) (named as Ref. [1]). The figures are reprinted or adapted as indicated in the figure captions.

4.1 Introduction

Magnetic skyrmions and their potential application for instance in new data storage devices[2,3] or for reservoir computing,[4] caused enormous research activity within the last decade. The 4*d* transition metal oxide $SrRuO_3$, which is ferromagnetic down to a few unit cells when it is deposited on $SrTiO_3$(100) substrates,[5] is considered as a promising material in the prospect of skyrmions in epitaxial oxide heterostructures. Its strong magnetocrystalline anisotropy can be tuned to favor perpendicular magnetic anisotropy, for instance by the growth on $SrTiO_3$(100) substrates.[5]

During the last years, unconventional features in the Hall resistance loops mimicking a topological Hall effect (THE) were observed in bilayers of $SrRuO_3$ and the strong spin-orbit coupled $SrIrO_3$.[6–8] Due to the breaking of the inversion symmetry at the interface and the strong spin-orbit coupling of the 5*d* $SrIrO_3$, the generation of an interfacial Dzyaloshinskii-Moriya interaction (DMI) was proposed to stabilize noncollinear magnetic textures, such as skyrmions in $SrRuO_3$ layers of 4 - 6 monolayers (MLs) thickness.[6] In magnetic force microscopy investigations of such a 5 MLs $SrRuO_3$/2 MLs $SrIrO_3$ bilayer, round magnetic domains were interpreted as magnetic skyrmions.[6]

However, hump-like anomalies were also observed in ultrathin bare $SrRuO_3$ films when it was deposited under non-optimal conditions.[9,10] An alternative interpretation of the origin of the THE-like features that was proposed is the existence of multiple conduction channels of the anomalous Hall effect due to disorder,[11] off-stoichiometry,[9] interfacial modifications,[12] or spatial inhomogeneities.[13,14] This debate about the origin of the peculiar features appearing in the Hall resistance loops emphasizes that the conclusion of the presence of magnetic skyrmions based only on transverse transport measurements can be faulty and highlights the importance of definite experimental proof by magnetic imaging for instance.

In order to shed light on the origin of the hump-like features in ultrathin $SrRuO_3$ layers interfaced with 2 MLs $SrIrO_3$, the morphology and magnetic domain formation of a 4 MLs $SrRuO_3$ / 2 MLs $SrIrO_3$ / 2 MLs $SrZrO_3$ trilayer (4RIZ) was investigated within the framework of this study. Hall measurements were correlated with microscopic studies of the magnetization reversal, aiming to unravel the origin of THE-like features observed in the Hall resistance hysteresis loops for the trilayer 4RIZ. A bare $SrRuO_3$ thin film of identical thickness was investigated as reference sample. In case of the studied 4 MLs

$SrRuO_3$ / 2 MLs $SrIrO_3$ / 2 MLs $SrZrO_3$ trilayer, nanoscale thickness variations, which led to local variations of the switching field as well as modifications of the anomalous Hall constant in the nominally 4 MLs thick $SrRuO_3$ layer, can explain the observation of THE-like features without the existence of magnetic skyrmions. The results highlight that hump-like anomalies that resemble a topological Hall effect can be observed without the formation of magnetic skyrmions and thus the observation of such features should not be used as validation of a skyrmionic phase.

4.2 Sample deposition

Since the hump-like features were seen by Matsuno *et al.* in their study of $SrRuO_3$/$SrIrO_3$-bilayers only for $SrRuO_3$ layer thicknesses between 4 and 6 MLs,[6] the focus of this study was on the investigation of a trilayer composed of 4 MLs $SrRuO_3$ interfaced with 2 MLs $SrIrO_3$, as presented in Fig. 4.1(b). The bilayer was capped by 2 MLs of the large band gap insulating oxide $SrZrO_3$ in order to protect the moisture sensitive $SrIrO_3$ from degradation.[15]

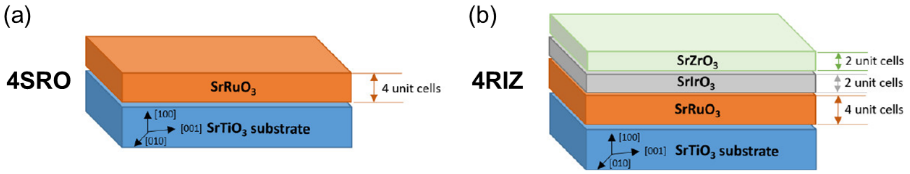

Figure 4.1: Schematic sample design of the 4 MLs bare $SrRuO_3$ film (a) and the $SrRuO_3$/ $SrIrO_3$/ $SrZrO_3$ trilayer 4RIZ (b), both deposited on $SrTiO_3$(100) substrates. Figure adapted from Ref. [1]. Adapted with permission from G. Malsch, D. Ivaneyko, P. Milde, L. Wysocki, L. Yang, P. H. M. van Loosdrecht, I. Lindfors-Vrejoiu, L. M. Eng, ACS Appl. Nano Mater. 2020, **3**, 2, 1182–1190, Copyright 2020 American Chemical Society.

The second sample under study is a bare $SrRuO_3$ thin film of the same (4 MLs) thickness, labeled 4SRO (see Fig. 4.1 (a)).

The cubic $SrTiO_3$(100) substrates used for the sample fabrication, exhibiting a miscut angle of 0.1 deg, were etched in NH_4F-buffered HF and subsequently annealed at 1000 °C for 2 h in ambient conditions. This treatment ensured a uniform step-terrace morphology with terrace width between 200 nm to 450 nm and TiO_2-termination on a large scale.

Both samples were deposited by pulsed-laser deposition with a KrF excimer laser from stoichiometric $SrRuO_3$, $SrIrO_3$, and $SrZrO_3$ targets. The deposition took place in 0.133 mbar O_2 atmosphere with the substrate heated to 650 °C. A laser fluence of $2\,J\,cm^{-2}$ was used for all layers, while the laser repetition rate was set to 1 Hz to 2 Hz for the $SrIrO_3$ and $SrZrO_3$ layers and to 5 Hz for the $SrRuO_3$ layers.

In order to monitor the growth mode, to control the individual layer thickness, and to achieve an initial understanding of the crystal structure of the films after the growth, *in situ* high-energy electron diffraction (RHEED) was utilized in high-oxygen pressure. Depicted in red in Fig. 4.2 ((a) and (b)) are the integrated intensities of the specular spots of the RHEED patterns as function of time. Additionally plotted in purple and blue in Fig. 4.2 (a) are the integrated intensities of the 1st order diffraction spots of the RHEED pattern of the bare $SrRuO_3$ thin film. The observation of oscillations in the time-dependent RHEED intensity for the deposition of the $SrIrO_3$ and $SrZrO_3$ layers indicate the layer-by-layer growth and enabled to control the layer thickness to be 2 monolayers each. In contrast, the $SrRuO_3$ layers, both the bare thin film and the $SrRuO_3$ layer of the heterostructure, grew in step-flow mode, indicated by the almost time-independent, high RHEED intensity.[16] As often recognized for $SrRuO_3$ films deposited on TiO_2-terminated $SrTiO_3$ substrates, the intensity exhibits an initial deep oscillation, which typically corresponds to the growth of 1.5 monolayers.[16] From this time period, the $SrRuO_3$ layer thickness was estimated to be 4 monolayers for the bare $SrRuO_3$ thin film as well as the $SrRuO_3$ layer of the trilayer 4RIZ.

The RHEED pattern acquired *in situ* after the deposition of the 4 MLs $SrRuO_3$ layer (see Fig. 4.2 (c)) shows the smooth deposition, pseudomorphic to the $SrTiO_3(100)$ substrate. Also after cooling in 200 mbar O_2 atmosphere to 150 °C, no additional reflections are observed, indicating that the $SrRuO_3$ is still above the transition to the orthorhombic crystal structure (see Fig. 4.2 (d)). In contrast, as shown in Fig. 4.2 (e), the RHEED pattern of a 150 MLs thick bare $SrRuO_3$ film after deposition on $SrTiO_3$ and cooling to 120 °C shows the existence of additional reflections, which can be attributed to the orthorhombic distortion of the crystal structure.

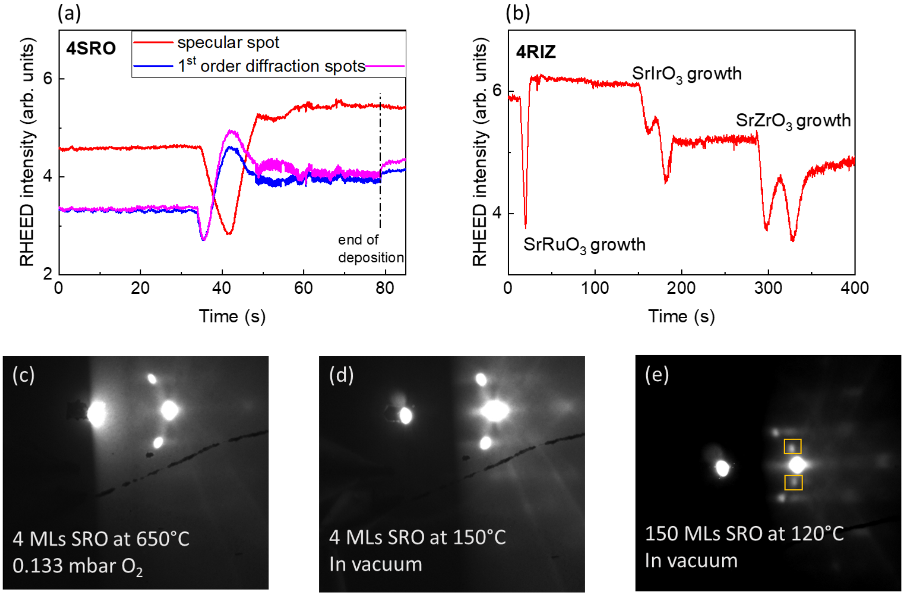

Figure 4.2: Integrated RHEED intensity plotted as function of time for the deposition of the bare $SrRuO_3$ film 4SRO (a) and the trilayer 4RIZ (b). The integrated RHEED intensity of the specular spots are drawn in red. The purple and blue plot correspond to 1st order diffraction spots in (a). *In situ* RHEED pattern after the deposition of 4 MLs $SrRuO_3$, taken under growth conditions (c), and after cooling the sample to 150 °C in 200 mbar and subsequent evacuation of the growth chamber (d). Depicted in (e) is the RHEED pattern of a 150 MLs thick bare $SrRuO_3$ layer after cooling to 120 °C. Marked by yellow boxes are additional reflections that originate from the orthorhombic crystal structure of this thick $SrRuO_3$ film. Figures adapted from Ref. [1]. Adapted with permission from G. Malsch, D. Ivaneyko, P. Milde, L. Wysocki, L. Yang, P. H. M. van Loosdrecht, I. Lindfors-Vrejoiu, L. M. Eng, ACS Appl. Nano Mater. 2020, **3**, 2, 1182–1190, Copyright 2020 American Chemical Society.

4.3 Magneto-optical Kerr effect and Hall investigations

Macroscopic magnetization measurements, by means of polar magneto-optical Kerr effect (MOKE), and Hall measurements were performed for both samples, the bare $SrRuO_3$ thin film 4SRO and the trilayer 4RIZ. The Hall investigations were acquired in van der Pauw geometry, as described in Chapter 3.2.6. The magnetic field was applied perpendicular to the film surface and a driving current of 100 µA was applied for all the Hall measurements shown here.

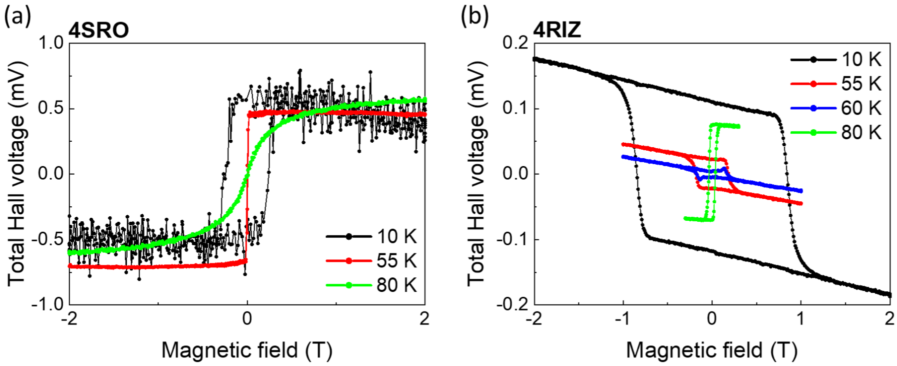

Figure 4.3: Total Hall voltage hysteresis loops for the 4 MLs bare $SrRuO_3$ layer (a) and the $SrRuO_3$/ $SrIrO_3$/ $SrZrO_3$ trilayer 4RIZ (b) at representative temperatures. The magnetic field was applied perpendicular to the film surface. Sample 4SRO is paramagnetic at 80 K, while heterostructure 4RIZ still exhibits an open Hall voltage hysteresis loop indicating ferromagnetic order. Figures adapted from Ref. [1]. Adapted with permission from G. Malsch, D. Ivaneyko, P. Milde, L. Wysocki, L. Yang, P. H. M. van Loosdrecht, I. Lindfors-Vrejoiu, L. M. Eng, ACS Appl. Nano Mater. 2020, **3**, 2, 1182–1190, Copyright 2020 American Chemical Society.

Depicted in Fig. 4.3 are the Hall voltage hysteresis loops of the bare 4SRO thin film (a) and the trilayer 4RIZ (b) at selected temperatures, e.g. at which magnetic force microscopy investigations were performed. The total Hall voltage is directly proportional to the total Hall resistivity ρ_{xy}, which is the sum of the ordinary Hall resistivity ρ_{OHE} and the anomalous Hall resistivity ρ_{AHE}. In the strong magnetic field range, where magnetic saturation of the sample is assumed, the total Hall voltage is therefore determined by the magnetic field dependence of the ordinary Hall effect.

The comparison of the magnetic field dependence of the total Hall voltages shows that the interfacing of the 4 MLs thick $SrRuO_3$ layer with 2 MLs of the strong spin-orbit coupled $SrIrO_3$ and the additional capping with 2 MLs $SrZrO_3$ has a strong impact on the magnetotransport and the magnetic properties of the $SrRuO_3$ layer, as it will be discussed later. While the total Hall voltage of trilayer 4RIZ has a negative slope in high magnetic fields, indicating electron-dominated transport (see Fig. 4.3 (b)), the total Hall voltage of the 4 MLs $SrRuO_3$ thin film is almost constant as a function of magnetic field in this range. Such strong variations of the charge carrier densities are a first indication of the impact of the interfacial environment of the $SrRuO_3$ layers on the band structure and thus on the magnetotransport properties of the samples.

Due to the proportionality of the anomalous Hall effect (AHE) to the out-of-plane component of the magnetization,[17] the Hall hysteresis loops yield initial insight into the macroscopic magnetic properties of the samples under study. The Hall loop of the bare 4SRO film has an s-shape at 80 K, which indicates that the sample is already in its paramagnetic state,[18] whereas the 4 MLs $SrRuO_3$ layer of trilayer 4RIZ is still in its ferromagnetic phase, according to the open hysteresis loop.[19]

The anomalous Hall constant R_A of the bare 4SRO thin film is positive within the entire ferromagnetic phase, as depicted in Fig. 4.3 (a). In contrast, R_A of heterostructure 4RIZ is negative below 60 K and changes its sign to positive values at about 70 K. Also these differences in the anomalous Hall effect properties can be a sign of band structure modifications of the $SrRuO_3$ layer due to the capping with 2 MLs $SrIrO_3$/2 MLs $SrZrO_3$, since it was seen that the anomalous Hall effect in $SrRuO_3$ is dominated by the intrinsic contribution.[13,20] This intrinsic contribution is dictated by the Berry curvature of the conduction bands.[21] Due to the existence of several Weyl nodes close to the Fermi level yielding large contributions to the Berry curvature, the anomalous Hall effect in $SrRuO_3$ is sensitive to modifications of the band structure,[21] for instance by the stoichiometry,[9] the film thickness,[22] interfacial interactions,[12] or the crystal structure.[18]

In the present case, the band structure variations of the two samples under study might originate from different crystal structures of the $SrRuO_3$ layers.[23] The nonmonotonous temperature dependence of the AHE, including the sign change from negative to positive, observed for the trilayer 4RIZ, is consistent with the stabilization of an orthorhombic crystal structure of the $SrRuO_3$ layer.[21,23] The capping of $SrRuO_3$ with orthorhombic $SrIrO_3$ and $SrZrO_3$ layers, which exhibit large tilting angles of the oxygen octahedra, could support the stabilization of the RuO_6 tilt angles bringing them closer to the bulk values of orthorhombic $SrRuO_3$. Such modification of oxygen octahedral rotation by the interfacing with capping layers was found to be efficient in ultrathin $SrRuO_3$ films.[24,25] When the $SrRuO_3$ layer, deposited on an orthorhombic $DyScO_3$(100) substrate, was for instance capped with cubic $SrTiO_3$, the tilts of the RuO_6 octahedra were suppressed, which stabilized tetragonal structure and influenced the ferromagnetic transition temperature.[25]

The positive AHE down to 10 K in case of the uncapped 4 MLs $SrRuO_3$ thin film however might be an indication of a tetragonal crystal structure.[18,23] This ultrathin $SrRuO_3$ film has its top interface with vacuum and was deposited on a cubic $SrTiO_3$ substrate, which most likely leads to the suppression of the oxygen octahedra tilts. Recent high-resolution x-ray diffraction investigations of a 3 unit cell thick $SrRuO_3$ film, deposited on Nb-doped $SrTiO_3$(100) substrates, indeed confirm the strong suppression of the octahedra tilts, although the film is still not tetragonal.[26]

Only for the heterostructure 4RIZ, when the 4 MLs thick $SrRuO_3$ layer was capped by 2 MLs $SrIrO_3$/2 MLs $SrZrO_3$, the Hall voltage loops (cf. Fig. 4.3 (b)) possess additional hump-like features in the temperature range close to the AHE sign change. In order to elucidate the origin of these unconventional features, which were not observed in case of the bare $SrRuO_3$ thin film, the Hall measurements of the trilayer 4RIZ were compared to polar magneto-optical Kerr effect measurements (see Fig. 4.4).

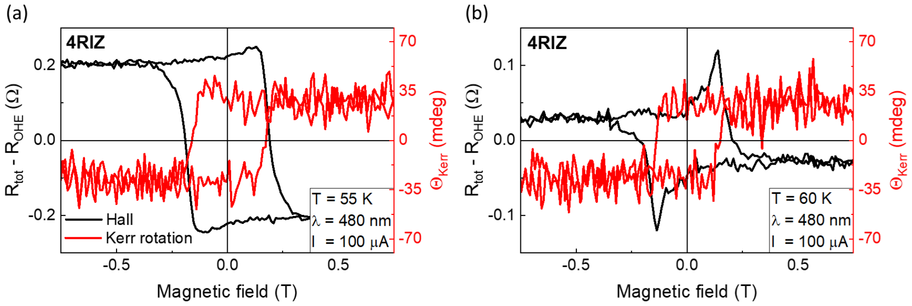

Figure 4.4: Hall resistance after subtraction of the ordinary Hall resistance (R_{tot}- R_{OHE} (black)) and Kerr rotation angle (red) hysteresis loops of the $SrRuO_3$/$SrIrO_3$/$SrZrO_3$ trilayer 4RIZ at 55 K (a) and 60 K (b), close to the sign change temperature of the AHE constant. Figure reprinted with permission from G. Malsch, D. Ivaneyko, P. Milde, L. Wysocki, L. Yang, P. H. M. van Loosdrecht, I. Lindfors-Vrejoiu, L. M. Eng, ACS Appl. Nano Mater. 2020, **3**, 2, 1182–1190, Copyright 2020 American Chemical Society.

Both quantities, Kerr rotation angle Θ_{Kerr} and Hall voltage, were measured simultaneously with a home-built set-up ensuring identical conditions for the magnetic field, its sweep rate, and the sample temperature (cf. Chapter 3). Due to the proportionality of the Kerr rotation angle (in polar geometry) to the out-of-plane component of the sample magnetization, the MOKE investigations are interpreted as magnetic hysteresis loops with the magnetic field applied perpendicular to the sample surface. The Hall resistance R_{tot} - R_{OHE}, plotted in black in Fig. 4.4, was calculated under the assumption that the measured Hall voltage is determined by the metallic properties of the $SrRuO_3$ layer, whereas the top $SrIrO_3/SrZrO_3$ layers are insulating. The ordinary Hall resistance R_{OHE} was subtracted by linear fitting in the high magnetic field range where the magnetic $SrRuO_3$ layer is in its saturated state.

In contrast to the Hall resistance loop, the shape of the MOKE hysteresis loops of the trilayer 4RIZ is squarish at 55 K (Fig. 4.4 (a)) and 60 K (Fig. 4.4 (b)). Θ_{Kerr} in remanence is approximately equal to Θ_{Kerr} in saturation, which resembles the magnetization reversal of a hard ferromagnet when the magnetic field is applied close to the easy axis.

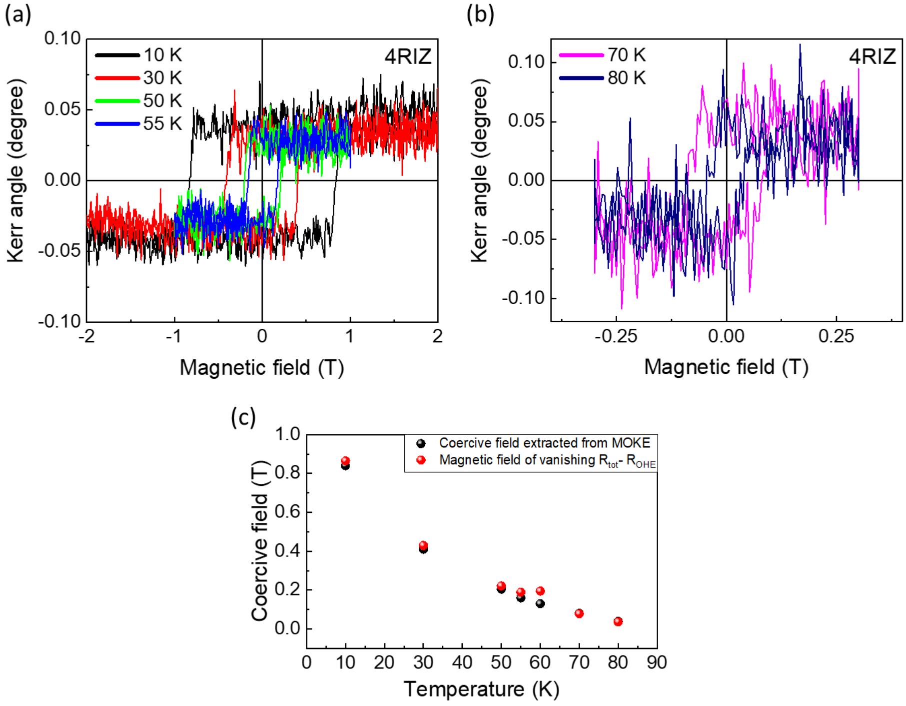

Figure 4.5: Polar MOKE hysteresis loops of the trilayer 4RIZ at 10 - 55 K (a) and at 70, 80 K (b). The coercive fields extracted from the MOKE hysteresis loops (black) and the magnetic field where [R_{tot} - R_{OHE}] vanishes (red) are plotted as a function of temperature in (c). Figures (a) and (b) reprinted with permission from G. Malsch, D. Ivaneyko, P. Milde, L. Wysocki, L. Yang, P. H. M. van Loosdrecht, I. Lindfors-Vrejoiu, L. M. Eng, ACS Appl. Nano Mater. 2020, **3**, 2, 1182–1190, Copyright 2020 American Chemical Society.

As shown in Fig. 4.5 (a) and (b), squarish MOKE hysteresis loops were observed throughout the ferromagnetic phase with the transition temperature close to 90 K. Thus, no indications of the existence of a nontrivial magnetic phase, such as a skyrmionic phase, were identified by the polar MOKE study of the trilayer 4RIZ.

Furthermore, the coercive fields of the MOKE hysteresis loops and the field where R_{tot} - R_{OHE} vanishes differ significantly only in the region close to the AHE sign change temperature, where hump-like features were observed (see Fig. 4.5 (c)). In contrast, the coercive fields of the MOKE loops are in good agreement with the field of the vanishing Hall resistance R_{tot} - R_{OHE} below 50 K and above 70 K, where hump-like features were absent in the Hall loops, as plotted in Fig. 4.5 (c).
The understanding of the magnetic properties on the microscopic length scale, such as the details of the domain nucleation, might be helpful to elucidate the origin of the discrepancies between the MOKE and Hall measurements of the trilayer 4RIZ. The existence of skyrmions for instance would lead to an additional (topological) Hall effect that impacts on the shape of the total measured Hall hysteresis loop. Magnetic force microscopy is a versatile tool to image the out-of-plane component of the magnetic stray field and was shown to be capable to image the fingerprint of skyrmions, which appear as bubble-like domains in MFM.[27]

4.4 Low-temperature scanning force microscopy and magnetic force microscopy study

In order to understand the magnetization reversal processes on the microscale, low temperature noncontact scanning force microscopy (nc-SFM) and magnetic force microscopy were performed. The measurements were conducted in ultrahigh vacuum (pressure less than 2×10^{-10} mbar). The MFM investigations were performed in the two-path mode, in which the topography of the thin film was acquired in the first scan. During the second scan, the tip was retracted by 20 nm to sense only the long-range magnetic forces.[28] The frequency shift Δf of the cantilever oscillation, whose amplitude was constantly 10 nm, was taken for the topographic and magnetic feedback control in the SFM and MFM measurements. SSS-QMFMR-type probes, coated with a magnetically hard material and having a mechanical quality factor of minimum 1.45×10^5, were therefore utilized for SFM as well as MFM scanning. For the study presented here, the tip magnetization changed its direction at 22 mT at 55 K and at 60 mT at 10 K and aligned its magnetization parallel to the external magnetic field.

Subsequently, the Hall effect loops and the (polar) Kerr rotation loops will be correlated with the local scale structure by nc-SFM, and with the magnetic characterization on the nanoscale by MFM in the temperature range between 10 K and 80 K.

4.4.1 Nanoscale real-space analysis of the topography of a bare $SrRuO_3$ thin film and a $SrRuO_3$-based trilayer

Presented in Fig. 4.6 are the nc-SFM images of the 4 MLs bare $SrRuO_3$ film (a) and the 4RIZ trilayer (b). The step-and-terrace morphology of the vicinal $SrTiO_3(100)$ substrate, with terrace width of 200 nm to 450 nm and step height of 0.39 nm, is preserved for both samples, confirming the pseudomorphic epitaxial growth. However, over- and undergrown areas were observed in both samples. For these areas of the 4SRO film, marked by white arrows in Fig. 4.6 (a), the $SrRuO_3$ layer thickness is 5 MLs or 3 MLs, respectively. The over- and undergrown areas are marked by pink and blue in the cross section taken along the white dotted line in Fig. 4.6 (c), and in a pseudo-3D view in Fig. 4.6 (e). Over- and undergrowth of the nominally 4 MLs thick $SrRuO_3$ layer most likely originate from local variations of the termination of the $SrTiO_3$ substrate. The $SrTiO_3$ substrates were etched in buffered HF for 2.5 min to achieve TiO_2 surface termination. However, it is likely that residual SrO islands remained, located typically at the $SrTiO_3$ terrace steps. Due to the reduced deposition rate of $SrRuO_3$ on SrO-terminated $SrTiO_3$ surfaces,[29] trenches form in the topography of the sample that mark the positions of the substrate step edges. The step edges of the $SrRuO_3$ film do not terminate exactly at straight terrace edges due to the stochastic nature of the deposition process. This then leads to the observed over- and undergrowth.

In case of the trilayer 4RIZ, the local thickness variations of the $SrRuO_3$ layer are expected to cause further areas of under- and overgrowth in the nominally 2 MLs thick $SrIrO_3$ and 2 MLs $SrZrO_3$ layers. Indeed, the topography image of trilayer 4RIZ (see Fig. 4.6 (b)) has a more disturbed step-terrace-like structure with dips of almost step-height depth as well as mounds of nanometer height

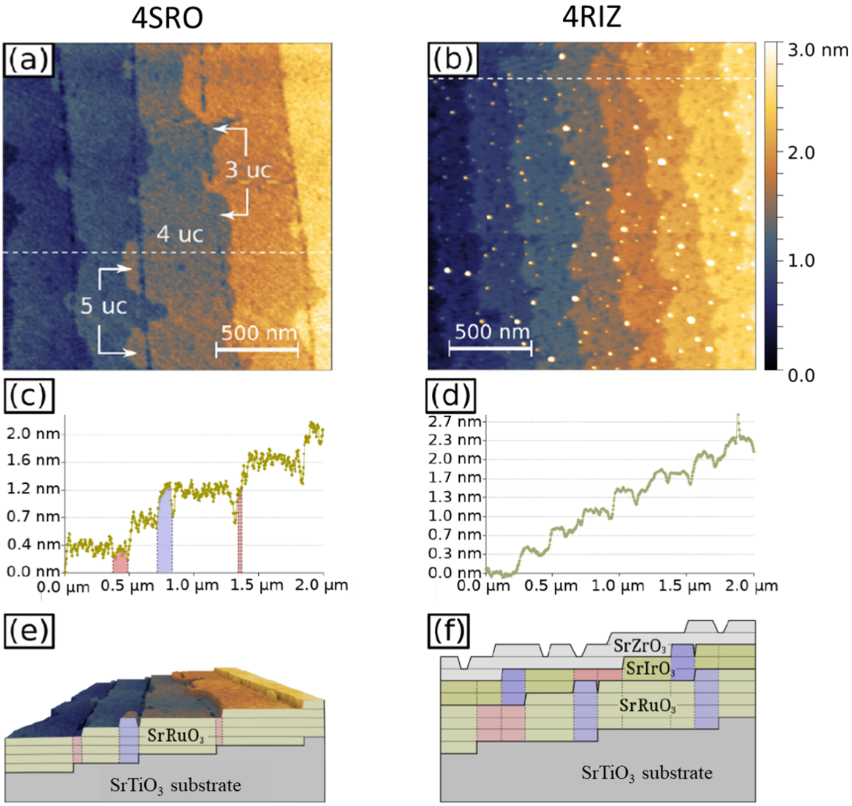

Figure 4.6: Topographic nc-SFM scans of the bare 4 MLs thick $SrRuO_3$ film 4SRO (a) and the 4RIZ trilayer (b). Marked with white arrows in (a) are undergrown (3 MLs) and overgrown (5 MLs) areas. Line profiles taken perpendicular to the topographic terraces along the white lines are plotted in (c) for the 4SRO film and for the 4RIZ trilayer in (d). (e) Pseudo-3D topographic image of the 4SRO thin film with the over- and undergrown areas schematically marked by blue and pink, respectively. (f) Schematic illustration of possible under- and overgrown areas for the trilayer 4RIZ. Figure adapted from Ref. [1]. Adapted with permission from G. Malsch, D. Ivaneyko, P. Milde, L. Wysocki, L. Yang, P. H. M. van Loosdrecht, I. Lindfors-Vrejoiu, L. M. Eng, ACS Appl. Nano Mater. 2020, **3**, 2, 1182–1190, Copyright 2020 American Chemical Society.

(see also Fig. 4.6 (d)). As schematically displayed in Fig. 4.6 (f), the local thickness variations of the bottom $SrRuO_3$ layer can be continued in various possibilities by the top $SrIrO_3$ and $SrZrO_3$ layers, which disables the determination of the local $SrRuO_3$ layer thickness for the trilayer 4RIZ.

However, the preserved step-and-terrace structure that emphasizes the pseudomorphic growth of $SrRuO_3$ enables the prediction of the approximate orientation of the magnetic easy axis of the bare 4 MLs $SrRuO_3$ layer. Generally, the magnetic anisotropy of $SrRuO_3$ films is depending on the epitaxial strain, temperature, and the film thickness.[5,30,31] The angle between the film normal and the magnetic easy axis of a 4 MLs $SrRuO_3$ thin film deposited on vicinal $SrTiO_3$ substrates was 14° at 0.4 K and therefore mainly favors out-of-plane magnetization orientation.[5]

Thus, the magnetic easy axis of the bare $SrRuO_3$ layer (4SRO) and most likely also of the trilayer (4RIZ) is close to the thin film normal, which is preferable for magnetic force microscopy due to the maximization of the out-of-plane stray field component in presence of magnetic domains.

4.4.2 Magnetic force microscopy of the $SrRuO_3$-based trilayer

Displayed in Fig. 4.7 is a representative set of magnetic force microscopy images of the trilayer 4RIZ, acquired at 55 K, the temperature at which hump-like features were recorded in the Hall resistance loops. The sample was saturated in 2 T and the magnetic field was then sweeped to -2 T for the images Fig. 4.7 (a) - (e). The MFM images during the backward sweep are shown in Fig. 4.7 (f) - (k). During the forward magnetic field sweep, the trilayer stayed in its saturated state, without domains of reversed orientation, down to the remanent state at zero magnetic field. This is consistent with the macroscopic MOKE study (see Fig. 4.5), where the Kerr rotation angle in remanence is equal to Θ_{Kerr} in saturation. It is additionally in agreement with previous reports on ultrathin $SrRuO_3$ thin films.[5]

Even in the saturated state, weak variations of the magnetic contrast are still observed along the terraces, which are parallel to the y-direction in our images (see Fig. 4.7 (a)). These contrast variations originate most likely from the thickness-variation-induced differences in the magnetic susceptibility impacting on the measured MFM signal.

Small initial domains of reversed orientation nucleate at around -100 mT (see Fig. 4.7 (a)-(b)), which grow abruptly in size upon the increase of magnetic field, as displayed in Fig. 4.7 (c) - (e). At -240 mT (e), the trilayer magnetization is almost fully switched. Only isolated domains that were still pinned get annihilated in magnetic fields larger than -300 mT.

During the magnetization reversal, domains with sharp domain walls in y-direction, parallel to the topographic terraces, are present (see Fig. 4.7 (d) and (j)), which is a sign that the domain growth is affected by the step-and-terrace topography of the sample.

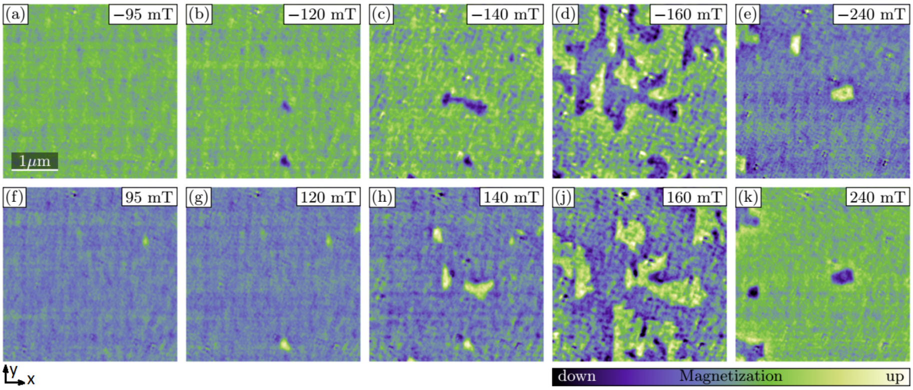

Figure 4.7: Magnetic force microscopy scans of the 4RIZ trilayer at 55 K, where THE-like features were observed in the Hall resistance loops. The color code corresponds to the out-of-plane component of the magnetization aligned in +z (green) or -z (blue) orientation. The domain formation during the sweep from positive to negative magnetic fields is displayed in (a) - (e) and the backward loop in (f) - (k). The magnetic features observed show lateral sizes of micrometers, extending over several terraces. Figure reprinted with permission from G. Malsch, D. Ivaneyko, P. Milde, L. Wysocki, L. Yang, P. H. M. van Loosdrecht, I. Lindfors-Vrejoiu, L. M. Eng, ACS Appl. Nano Mater. 2020, **3**, 2, 1182–1190, Copyright 2020 American Chemical Society.

Nevertheless, the domain growth is not dominated by the substrate terraces, since the magnetic domains of micrometer lateral size are expanded over several terraces.

The comparison of the forward and backward sweep shows strong pinning effects for regions of initial magnetic nucleation as well as for areas that remain oriented opposite to the external magnetic field direction even in large magnetic fields (cf. Fig. 4.7 (b) and (g) as well as (e) and (k)).

While features mimicking a topological Hall effect were observed at 55 K in this trilayer, no hints of a skyrmionic phase could be observed with MFM.

In the magnetic field range between 0 T and ±130 mT, where the hump-like features appeared for the Hall resistance loop, the sample is still mainly saturated according to both the MFM, and macroscopic MOKE measurements. The magnetic field range in which the THE-like features were observed is much broader than the region in which the magnetization mainly switches, based on the polar MOKE and MFM studies of trilayer 4RIZ. Thus, bubble domains formed during the magnetization switching likely cannot account for the hump-like anomalies in the Hall resistance loop. The initial or pinned domains are isolated regions of irregular shape and do not resemble the shape of a skyrmion or magnetic bubble (compare for instance Ref. [32]).

These pinning effects were also observed at low temperatures, exemplarily displayed in Fig. 4.8 at 10 K. Highlighted in red is a hammerhead-shaped magnetic domain that formed reproducibly in successive sweeps from negative to positive magnetic fields and stayed strongly pinned up to 1 T.

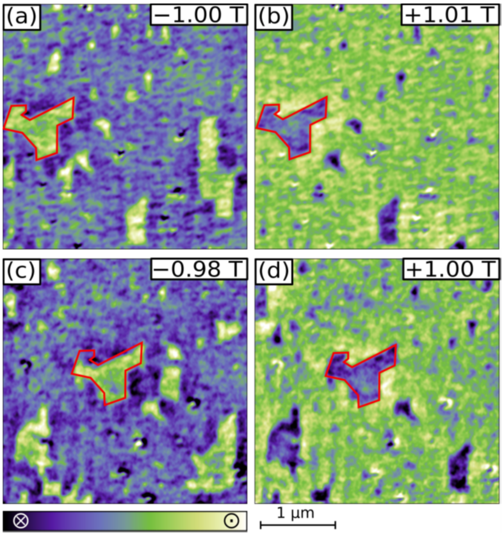

Figure 4.8: MFM of the trilayer 4RIZ at 10 K during successive sweeps from negative to positive magnetic fields. Shown in (c) and (d) are MFM images acquired under the same conditions as (a) and (b), but three days later. The color code corresponds to the magnetization component aligned in positive (green) and negative (blue) z-direction. Figures reprinted with permission from G. Malsch, D. Ivaneyko, P. Milde, L. Wysocki, L. Yang, P. H. M. van Loosdrecht, I. Lindfors-Vrejoiu, L. M. Eng, ACS Appl. Nano Mater. 2020, **3**, 2, 1182–1190, Copyright 2020 American Chemical Society.

4.4.3 Magnetic force microscopy of a bare $SrRuO_3$ film

To achieve a deeper understanding of the domain formation in the 4 MLs $SrRuO_3$ thin film, magnetic force microscopy investigations were also performed on the reference sample 4SRO. The MFM images were again taken during the magnetic field sweep from 2 T to -2 T (see Fig. 4.9 (a) - (e)) and back to 2 T (Fig. 4.9 (f) - (k)).

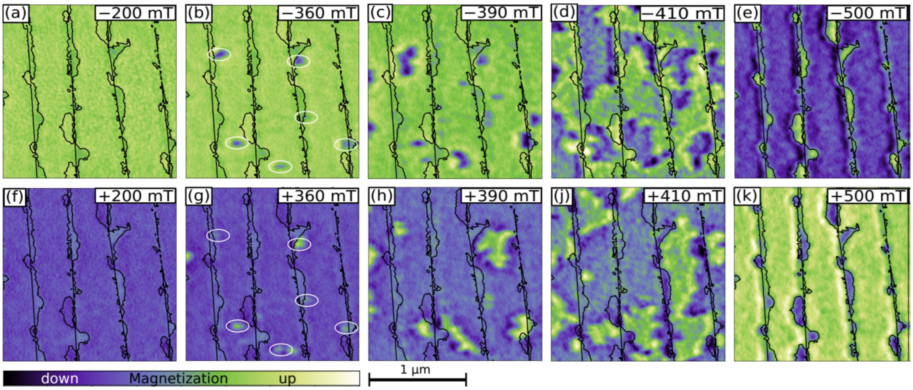

Figure 4.9: Magnetic force microscopy scans of the bare 4SRO film at 10 K. Shown in (a)-(e) is the domain formation during the forward sweep from positive to negative magnetic fields and the backward loop in (f)- (k). The color code corresponds to the out-of-plane component of the magnetization aligned in +z (green) or -z (blue) orientation. Magnetic nuclei are marked in white in (b) and (g). The magnetic tip changes its magnetization at ∓ 60 mT. Figures reprinted with permission from G. Malsch, D. Ivaneyko, P. Milde, L. Wysocki, L. Yang, P. H. M. van Loosdrecht, I. Lindfors-Vrejoiu, L. M. Eng, ACS Appl. Nano Mater. 2020, **3**, 2, 1182–1190, Copyright 2020 American Chemical Society.

Also the bare $SrRuO_3$ film is saturated in 2 T and no initial nucleation domains of reversed orientation are observed up to -200 mT. Weak variations of the magnetic contrast are again visible (see Fig. 4.9 (a)) although the sample is saturated, which most likely originate from different magnetic susceptibilities of the areas with 3 - 5 MLs thickness. Round magnetic domains of reversed orientation, smaller than 100 nm, nucleate at -360 mT (see dark blue areas in Fig. 4.9 (b)). Further decrease of the magnetic field leads to the appearance of more domains and to the expansion of the already existing magnetic domains (see Fig. 4.9 (c) and (d)). At -500 mT, the thin film is almost saturated with the magnetization aligned along the external magnetic field. Only a few domains are still pinned up to $-1\,\mathrm{T}$, which are observed in areas where topographic islands due to thickness variations are visible (as indicated by the black lines).

Memory effects are also observed in case of the bare 4SRO film, when MFM scans during the forward and backward sweep are compared. As presented in Fig. 4.9 (b) and (g), the initial magnetic nuclei form at the same positions, mostly at step edges of the sample topography (topographic features are highlighted by black lines). This indicates that the nucleation of reversed domains preferentially starts at step edges or other topographic defects. Due to the round shape and the small lateral extension, the initial magnetic nuclei formed in the bare 4SRO have similarities to isolated magnetic bubbles or skyrmions, as seen for instance in metallic Pt/Co/Ir multilayers.[32] However, these magnetic domains of round shape were observed in our MFM investigations only in the bare 4SRO thin film at 10 K, where no unconventional features were observed in the Hall resistance loop that would correlate with a topological Hall effect contribution. The small round bubbles are most likely trivial magnetic nucleation domains.

Representative images of the MFM study of the bare 4SRO thin film at 55 K are displayed in Fig. 4.10 (a) - (d).

In accordance with the Hall resistance measurements of the bare 4SRO thin film, the nucleation of reversed domains at 55 K starts at smaller magnetic fields of about $-12\,\mathrm{mT}$. Also the coercive field is strongly reduced upon temperature increase. In contrast to the 10 K data, the domain nucleation and growth are determined by the topographic terraces, since all domains extend over the width of the individual terraces and grow parallel to the terraces. The steps of one unit cell (0.39 nm) height seem to hinder the propagation of domain walls. Interestingly, the domain walls form almost perpendicularly (cf. the red lines in Fig. 4.10 (a), (b), and (d)) to the step edges[1]. The red lines mark the domain walls that appear reproducibly during forward and backward sweep at the same positions (see Fig. 4.10 (a) and (d)), indicating that the domain growth is stopped at the same pinning sites. At $-32\,\mathrm{mT}$, the magnetization of the thin film is mainly aligned along the direction of the external magnetic field (see Fig. 4.10 (c)).

---

[1] The correlation of local switching fields to structural, orthorhombic twin domains could explain this domain formation, as it was observed in $SrRuO_3$ thin films that were deposited on vicinal $SrTiO_3$ substrates of various miscut direction.[33]

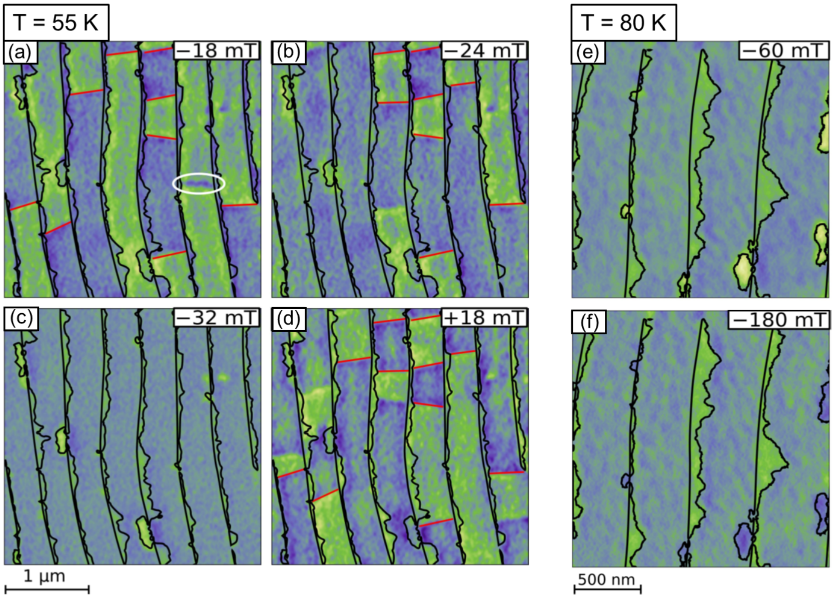

Figure 4.10: Magnetic force microscopy images of the bare 4SRO film at 55 K ((a) - (d)). The selected images present the domain formation sweeping the magnetic field from 2 T to −2 T in (a) - (c). (d) was acquired after sweeping back to positive magnetic field at 18 mT. Marked in black are topographic contour lines. Red lines highlight domain boundaries reappearing in the MFM scans at respective positive and negative magnetic fields. Presented in (e) and (f) are MFM scans at 80 K at −60 mT (e) and −180 mT (f). Only overgrown areas still show magnetization reversal (f). Figures adapted from Ref. [1]. Adapted with permission from G. Malsch, D. Ivaneyko, P. Milde, L. Wysocki, L. Yang, P. H. M. van Loosdrecht, I. Lindfors-Vrejoiu, L. M. Eng, ACS Appl. Nano Mater. 2020, **3**, 2, 1182–1190, Copyright 2020 American Chemical Society.

The MFM study did not reveal any round or unusual domains during the magnetization switching of the bare 4SRO film at 55 K.
As expected from the s-shaped Hall loop of the bare 4SRO film, the major part of the nominally 4 MLs thick $SrRuO_3$ is in the paramagnetic state at 80 K. Only the overgrown 5 MLs thick areas, indicated by black lines in Fig. 4.10 (e) and (f), are ferromagnetic so that magnetization switching behavior was observed by MFM.

In Fig. 4.11 is shown a two-dimensional map of the local switching fields for the bare 4SRO film at 10 K (a) and 55 K (b). The local switching fields were determined by the performance of a full hysteresis loop at every point of the 512 pixel x 512 pixel image and the subsequent application of Otsu's method.[34]

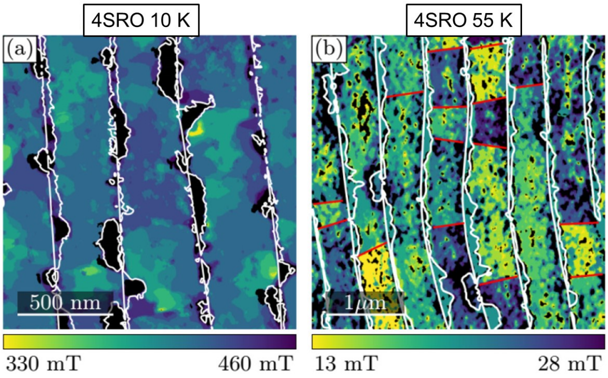

Figure 4.11: Map of the local switching fields of the 4SRO film at 10 K (a) and 55 K (b). The color code describes the local switching fields as indicated by the bars below the maps. Black areas do not reverse magnetization within the drawn magnetic field ranges of 330 mT to 460 mT at 10 K and 13 mT to 28 mT at 55 K. Figures reprinted with permission from G. Malsch, D. Ivaneyko, P. Milde, L. Wysocki, L. Yang, P. H. M. van Loosdrecht, I. Lindfors-Vrejoiu, L. M. Eng, ACS Appl. Nano Mater. 2020, **3**, 2, 1182–1190, Copyright 2020 American Chemical Society.

In case of a perfect hard ferromagnet (defect-free, homogeneous, and without topographic influence on the switching behavior) with the magnetic field applied along the easy axis, the map in Fig. 4.11 would be of uniform color, because the magnetization would reverse its orientation as a single domain. As shown in Fig. 4.11, the 4SRO bare film exhibits however strong local variations of the switching fields. Most areas reverse the magnetization orientation within 330 mT to 460 mT (±130 mT) at 10 K and between 13 mT to 28 mT (±15 mT) at 55 K. The black areas do not switch within the shown magnetic field ranges. In agreement with Fig. 4.9, the domains grow along and perpendicular to the topographic step edges at 10 K, since large domains are of uniform contrast indicating identical or similar local switching fields. However, the greenish areas in Fig. 4.11 (a) , which represent small local switching fields, are preferably observed close to step edges. This influence of the topography on the domain formation and growth is more pronounced at 55 K (see Fig. 4.11 (b)). Overall, the switching field map confirmed the observation from the individual MFM images of Fig. 4.10 that the domains nucleation and expansion is depending on the topography. The initial domain size is limited by the terrace width and the domains grow along the terraces subsequently.

Similar local variations of the switching field are also observed in the 4RIZ trilayer, as presented in Fig. 4.12 at 10 K (a) and 55 K (b).

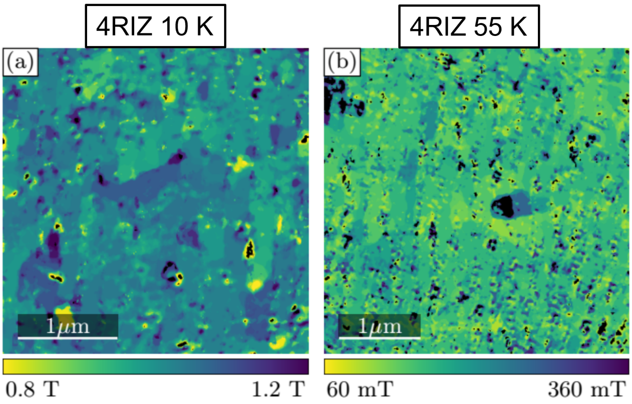

Figure 4.12: Map of the local switching fields of the 4RIZ trilayer at 10 K (a) and 55 K (b). Black areas do not switch its magnetization orientation within the shown magnetic field ranges. Figures reprinted with permission from G. Malsch, D. Ivaneyko, P. Milde, L. Wysocki, L. Yang, P. H. M. van Loosdrecht, I. Lindfors-Vrejoiu, L. M. Eng, ACS Appl. Nano Mater. 2020, **3**, 2, 1182–1190, Copyright 2020 American Chemical Society.

This distribution of the local switching fields of the $SrRuO_3$ layer, which is most likely also related to thickness inhomogeneities in the $SrRuO_3$ film, will impact on the macroscopic magnetotransport properties of the trilayer. Due to the dominance of the intrinsic contribution, the anomalous Hall effect of $SrRuO_3$ is sensitive to band structure modifications, such as thickness variations.[9,21,22] Thus, the observed local thickness variations likely cause differences of the anomalous Hall constant. Combined with the local distribution of switching fields, this might generate hump-like features in the Hall resistance in the temperature region of the sign change of the anomalous Hall constant of the whole trilayer.

4.4.4 Magnetization characteristics

Polar magneto-optical Kerr effect hysteresis loops of the bare 4 MLs $SrRuO_3$ thin film at low temperature are displayed in Fig. 4.13 (a). Like in case of the trilayer 4RIZ, the hysteresis loops are squarish, which is consistent with the microscopic MFM study that showed that the magnetization reversal takes place in a narrow magnetic field range. In case of the MOKE study, the sample signal was too weak above 20 K to separate it from the background contributions of the cryostat window.[2] Summarized in Fig. 4.13 are the switching fields of the bare 4SRO film and the trilayer 4RIZ as function of temperature. The coercive fields determined by macroscopic MOKE measurements of the bare 4SRO film (plotted in Fig. 4.13 (a)) are smaller than the switching fields extracted locally by MFM for the 4 MLs thick areas (green).

Discrepancies might originate from differences in the magnetic field sweep rates, which become probably relevant in case of the bare 4SRO film due to the small field range in which the magnetization reversal takes place. While the MFM investigations were performed in stabilized field, the magnetic field was continuously varied during the performance of the MOKE hysteresis loops. Additionally, it is impossible with the used MOKE set-up to distinguish the areas with 4 MLs and 5 MLs thickness and the local switching fields, as it was realized by MFM. This emphasizes the importance of nanoscale magnetization techniques such as MFM due to the sensitivity on the nanoscale, which is invisible to macroscopic experiments such as MOKE.

While the enhancement of the transition temperature for the overgrown 5 MLs thick areas (compared to the 4 MLs areas) is consistent with literature on bare $SrRuO_3$ thin films,[5] the increase of the switching fields for the 5 MLs thick areas appears counterintuitive firstly, due to the usually observed decrease of the coercive field for increasing $SrRuO_3$ layer thickness.[5]

However, since the overgrown areas were found mainly at step edges, local pinning effects might play a role in this enlargement of the local switching fields.

In case of the trilayer 4RIZ, the coercive fields determined by MOKE, drawn in red in Fig. 4.13 (b), and extracted from the MFM images,[34] plotted in orange, are in reasonable agreement.

---

[2] The thin film is placed inside of a cryostat during the MOKE investigations. The optical cryostat window, made of fused silica, generates a finite polar Kerr rotation angle, which is proportional to the external magnetic field and needs to be subtracted from the raw data in order to extract the sample response.

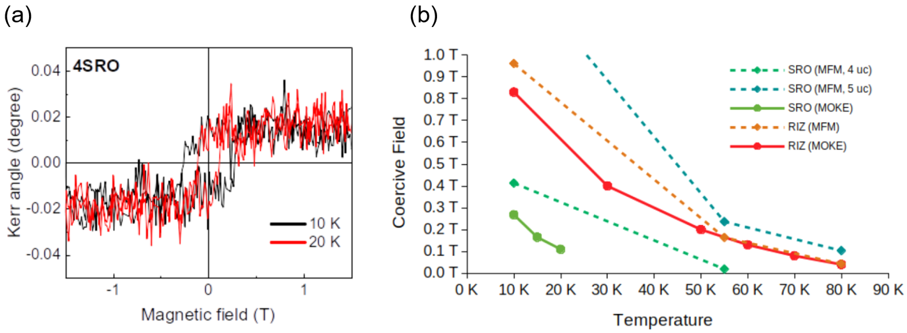

Figure 4.13: (a) Polar MOKE hysteresis loop of 4SRO at 10 K (black) and 20 K (red). (b) Magnetization switching fields of the trilayer 4RIZ and the bare 4SRO film as function of temperature, determined from MOKE (solid lines) and MFM (dashed lines). Figures adapted from Ref. [1]. Adapted with permission from G. Malsch, D. Ivaneyko, P. Milde, L. Wysocki, L. Yang, P. H. M. van Loosdrecht, I. Lindfors-Vrejoiu, L. M. Eng, ACS Appl. Nano Mater. 2020, **3**, 2, 1182–1190, Copyright 2020 American Chemical Society.

The impact of the interfacial environment on the magnetic properties of the $SrRuO_3$ layer becomes visible for instance by the increase of the transition temperature by the capping with 2 MLs $SrIrO_3$ / 2 MLs $SrZrO_3$. The enhancement of the ferromagnetic temperature to about 90 K was observed in the MOKE, Hall, and MFM studies. It is likely related to capping-induced changes of the RuO_6 octahedra tilts, which was found to be relevant for the transition temperature in $SrRuO_3$ thin films.[25]

4.5 Conclusion

The combined study of Hall resistance, magnetic force microscopy and polar MOKE measurements, probing the magnetization on the micrometer- and macroscopic scale, yield consistent, strong indications that the peculiar THE-like features in the Hall resistance loops of our $SrRuO_3$ / $SrIrO_3$ / $SrZrO_3$ trilayer do not originate from skyrmions. In the temperature and magnetic field range where hump-like anomalies in the Hall effect were observed, no domains resembling the shape of magnetic skyrmions were identified by MFM. In contrast, according to the magnetic domain formation, the trilayer remained in its saturated state in the magnetic field range where the peculiar features were already present. On the other hand, the nc-SFM investigations showed that local inhomogeneities of the $SrRuO_3$ layer thickness led to spatial variations of the magnetic switching fields. Due to the sensitivity of the anomalous Hall effect in $SrRuO_3$ on the details of the electronic band structure, which itself is strongly depending on the layer thickness, crystal structure, stoichiometry, or interfacial modifications, these thickness inhomogeneities are expected to cause local variations of the anomalous Hall effect of $SrRuO_3$.[9,11,22] Moreover, band structure modifications at the $SrRuO_3$/ $SrIrO_3$ interface or local variations of the stoichiometry were recently demonstrated to impact on the AHE magnitude and sign.[9,12] In the model of multiple AHE conduction channels, such local inhomogeneities of the anomalous Hall constant and the observed distribution of switching fields are most likely responsible for the peculiar anomalies in the Hall resistance loops of the investigated $SrRuO_3$-based trilayer. The study further highlights that the conclusion of the existence of skyrmions based only on Hall resistance hysteresis loops can be faulty.

Acknowledgement and own contribution

This chapter summarized results that have been published in the manuscript G. Malsch *et al.*, ACS Appl. Nano Materials **3**, 1182-1190 (2020). The atomic and magnetic force microscopy investigations, the corresponding analysis and presented figures were performed by Gerald Malsch, Dr. Dmytro Ivaneyko and Dr. Peter Milde. The MOKE and Hall measurements were performed by Lin Yang. I grew the studied samples, performed the analyses of the MOKE and Hall measurements, and wrote the part describing these in the paper.

References

[1] G. Malsch, D. Ivaneyko, P. Milde, L. Wysocki, L. Yang, P. H. M. van Loosdrecht, I. Lindfors-Vrejoiu, and L. M. Eng: *Correlating the Nanoscale Structural, Magnetic, and Magneto-Transport Properties in $SrRuO_3$-Based Perovskite Thin Films: Implications for Oxide Skyrmion Devices*, ACS Applied Nano Materials **3**, 1182–1190 (2020).

[2] A. Fert, V. Cros, and J. Sampaio: *Skyrmions on the track*, Nature Nanotechnology **8**, 152–156 (2013).

[3] R. Tomasello, E. Martinez, R. Zivieri, L. Torres, M. Carpentieri, and G. Finocchio: *A strategy for the design of skyrmion racetrack memories*, Scientific Reports **4**, 6784 (2014).

[4] G. Bourianoff, D. Pinna, M. Sitte, and K. Everschor-Sitte: *Potential implementation of reservoir computing models based on magnetic skyrmions*, AIP Advances **8**, 055602 (2018).

[5] J. Xia, W. Siemons, G. Koster, M. R. Beasley, and A. Kapitulnik: *Critical thickness for itinerant ferromagnetism in ultrathin films of* $SrRuO_3$, Physical Review B **79**, 140407(R) (2009).

[6] J. Matsuno, N. Ogawa, K. Yasuda, F. Kagawa, W. Koshibae, N. Nagaosa, Y. Tokura, and M. Kawasaki: *Interface-driven topological Hall effect in* $SrRuO_3$ *-* $SrIrO_3$ *bilayer*, Science Advances **2**, e1600304 (2016).

[7] Y. Ohuchi, J. Matsuno, N. Ogawa, Y. Kozuka, M. Uchida, Y. Tokura, and M. Kawasaki: *Electric-field control of anomalous and topological Hall effects in oxide bilayer thin films*, Nature Communications **9**, 213 (2018).

[8] K.-Y. Meng, A. S. Ahmed, M. Baćani, A.-O. Mandru, X. Zhao, N. Bagués, B. D. Esser, J. Flores, D. W. McComb, H. J. Hug, and F. Yang: *Observation of Nanoscale Skyrmions in* $SrIrO_3$ */* $SrRuO_3$ *Bilayers*, Nano Letters **19**, 3169–3175 (2019).

[9] D. Kan and Y. Shimakawa: *Defect-Induced Anomalous Transverse Resistivity in an Itinerant Ferromagnetic Oxide*, physica status solidi (b) **255**, 1800175 (2018).

[10] Q. Qin, L. Liu, W. Lin, X. Shu, Q. Xie, Z. Lim, C. Li, S. He, G. M. Chow, and J. Chen: *Emergence of Topological Hall Effect in a* $SrRuO_3$ *Single Layer*, Advanced Materials **31**, 1807008 (2019).

[11] L. Wu, F. Wen, Y. Fu, J. H. Wilson, X. Liu, Y. Zhang, D. M. Vasiukov, M. S. Kareev, J. H. Pixley, and J. Chakhalian: *Berry phase manipulation in ultrathin* $SrRuO_3$ *films*, Physical Review B **102**, 220406(R) (2020).

[12] D. J. Groenendijk, C. Autieri, T. C. van Thiel, W. Brzezicki, J. R. Hortensius, D. Afanasiev, N. Gauquelin, P. Barone, K. H. W. van den Bos, S. van Aert, J. Verbeeck, A. Filippetti, S. Picozzi, M. Cuoco, and A. D. Caviglia: *Berry phase engineering at oxide interfaces*, Physical Review Research **2**, 023404 (2020).

[13] D. Kan, T. Moriyama, K. Kobayashi, and Y. Shimakawa: *Alternative to the topological interpretation of the transverse resistivity anomalies in* $SrRuO_3$, Physical Review B **98**, 180408(R) (2018).

[14] L. Wang, Q. Feng, H. G. Lee, E. K. Ko, Q. Lu, and T. W. Noh: *Controllable Thickness Inhomogeneity and Berry Curvature Engineering of Anomalous Hall Effect in* $SrRuO_3$ *Ultrathin Films*, Nano Letters **20**, 2468–2477 (2020).

[15] D. J. Groenendijk, N. Manca, G. Mattoni, L. Kootstra, S. Gariglio, Y. Huang, E. van Heumen, and A. D. Caviglia: *Epitaxial growth and thermodynamic stability of $SrIrO_3/SrTiO_3$ heterostructures*, Applied Physics Letters **109**, 041906 (2016).

[16] J. Choi, C. B. Eom, G. Rijnders, H. Rogalla, and D. H. A. Blank: *Growth mode transition from layer by layer to step flow during the growth of heteroepitaxial $SrRuO_3$ on (001) $SrTiO_3$*, Applied Physics Letters **79**, 1447–1449 (2001).

[17] E. M. Pugh and N. Rostoker: *Hall Effect in Ferromagnetic Materials*, Reviews of Modern Physics **25**, 151 (1953).

[18] F. Bern, M. Ziese, A. Setzer, E. Pippel, D. Hesse, and I. Vrejoiu: *Structural, magnetic and electrical properties of $SrRuO_3$ films and $SrRuO_3$ /$SrTiO_3$ superlattices*, Journal of Physics Condensed Matter **25**, 496003 (2013).

[19] S. Shimizu, K. S. Takahashi, M. Kubota, M. Kawasaki, Y. Tokura, and Y. Iwasa: *Gate tuning of anomalous Hall effect in ferromagnetic metal $SrRuO_3$*, Applied Physics Letters **105**, 163509 (2014).

[20] N. Nagaosa, J. Sinova, S. Onoda, A. H. MacDonald, and N. P. Ong: *Anomalous Hall effect*, Reviews of Modern Physics **82**, 1539 (2010).

[21] Z. Fang, N. Nagaosa, K. S. Takahashi, A. Asamitsu, R. Mathieu, T. Ogasawara, H. Yamada, M. Kawasaki, Y. Tokura, and K. Terakura: *The Anomalous Hall Effect and Magnetic Monopoles in Momentum Space*, Science **302**, 92–95 (2003).

[22] N. Haham, Y. Shperber, M. Schultz, N. Naftalis, E. Shimshoni, J. W. Reiner, and L. Klein: *Scaling of the anomalous Hall effect in $SrRuO_3$*, Physical Review B **84**, 174439 (2011).

[23] M. Ziese and I. Vrejoiu: *Anomalous and planar Hall effect of orthorhombic and tetragonal $SrRuO_3$ layers*, Physical Review B **84**, 104413 (2011).

[24] D. Kan, R. Aso, R. Sato, M. Haruta, H. Kurata, and Y. Shimakawa: *Tuning magnetic anisotropy by interfacially engineering the oxygen coordination environment in a transition metal oxide*, Nature Materials **15**, 432–437 (2016).

[25] S. Thomas, B. Kuiper, J. Hu, J. Smit, Z. Liao, Z. Zhong, G. Rijnders, A. Vailionis, R. Wu, G. Koster, and J. Xia: *Localized Control of Curie Temperature in Perovskite Oxide Film by Capping-Layer-Induced Octahedral Distortion*, Physical Review Letters **119**, 177203 (2017).

[26] X. Zhang, A. N. Penn, L. Wysocki, Z. Zhang, P. H. M. van Loosdrecht, L. Kornblum, J. M. LeBeau, I. Lindfors-Vrejoiu, and D. P. Kumah: *Thickness*

and temperature dependence of the atomic-scale structure of $SrRuO_3$ *thin films*, APL Materials **10**, 051107 (2022).

[27] P. Milde, D. Köhler, J. Seidel, L. M. Eng, A. Bauer, A. Chacon, J. Kindervater, S. Mühlbauer, C. Pfleiderer, S. Buhrandt, C. Schütte, and A. Rosch: *Unwinding of a skyrmion lattice by magnetic monopoles*, Science **340**, 1076–1080 (2013).

[28] O. Kazakova, R. Puttock, C. Barton, H. Corte-León, M. Jaafar, V. Neu, and A. Asenjo: *Frontiers of magnetic force microscopy*, Journal of Applied Physics **125**, 060901 (2019).

[29] R. Bachelet, F. Sánchez, J. Santiso, C. Munuera, C. Ocal, and J. Fontcuberta: *Self-Assembly of* $SrTiO_3$*(001) Chemical-Terminations: A Route for Oxide-Nanostructure Fabrication by Selective Growth*, Chemistry of Materials **21**, 2494–2498 (2009).

[30] Q. Gan, R. A. Rao, C. B. Eom, L. Wu, and F. Tsui: *Lattice distortion and uniaxial magnetic anisotropy in single domain epitaxial (110) films of* $SrRuO_3$, Journal of Applied Physics **85**, 5297–5299 (1999).

[31] M. Ziese, I. Vrejoiu, and D. Hesse: *Structural symmetry and magnetocrystalline anisotropy of* $SrRuO_3$ *films on* $SrTiO_3$, Physical Review B **81**, 184418 (2010).

[32] C. Moreau-Luchaire, C. Moutafis, N. Reyren, J. Sampaio, C. A. Vaz, N. Van Horne, K. Bouzehouane, K. Garcia, C. Deranlot, P. Warnicke, P. Wohlhüter, J. M. George, M. Weigand, J. Raabe, V. Cros, and A. Fert: *Additive interfacial chiral interaction in multilayers for stabilization of small individual skyrmions at room temperature*, Nature Nanotechnology **11**, 444–448 (2016).

[33] W. Wang, L. Li, J. Liu, B. Chen, Y. Ji, J. Wang, G. Cheng, Y. Lu, G. Rijnders, G. Koster, W. Wu, and Z. Liao: *Magnetic domain engineering in* $SrRuO_3$ *thin films*, npj Quantum Materials **5**, 73 (2020).

[34] N. Otsu: *A threshold selection method from gray-level histograms*, IEEE Transactions on Systems, Man, and Cybernetics **9**, 62–66 (1979).

Chapter 5

Magnetic interlayer coupling between ferromagnetic $SrRuO_3$ layers through a $SrIrO_3$ spacer

Contents

The main part of this chapter is published in the manuscript:
Lena Wysocki, Sven Erik Ilse, Lin Yang, Eberhard Goering, Felix Gunkel, Regina Dittmann, Paul H. M. van Loosdrecht, Ionela Lindfors-Vrejoiu, *Magnetic interlayer coupling between ferromagnetic $SrRuO_3$ layers through a $SrIrO_3$ spacer*, Journal of Applied Physics **131**, 133902 (2022) (named as Ref. [1]). Figures and text are reproduced or adapted as indicated from Ref. [1], with the permission of AIP Publishing.

5.1 Introduction

If skyrmions can form in a magnetic multilayer, their ferromagnetic coupling across the stack has to be achieved, as it was realized in metallic superlattices.[2–4] Although several studies focused on the discussion of the origin of unconventional features in the magnetotransport of $SrRuO_3/SrIrO_3$ heterostructures and the existence of topologically non-trivial textures in $SrRuO_3$ thin films is still under debate,[5–16] the interlayer coupling in $SrRuO_3$-based multilayers was only little investigated. Experimental studies of the magnetic interlayer coupling between $SrRuO_3$ layers were performed only in multilayers with spacers that are not expected to induce interfacial Dzyaloshinskii-Moriya interaction (DMI), such as $LaNiO_3$ or $SrTiO_3$.[17,18] Yang *et al.* achieved strong ferromagnetic coupling of the $SrRuO_3$ layers by introducing a 4 monolayers[1] (MLs) thick metallic $LaNiO_3$ spacer, while weak ferromagnetic coupling was observed for the separation of the $SrRuO_3$ layers by 2 MLs of $LaNiO_3$.[17] Insulating $SrTiO_3$ spacers, 1 nm to 2.5 nm thick, were found to result also in weak coupling or in magnetic decoupling of two epitaxial $SrRuO_3$ layers in the study by Herranz *et al.*[18] In a previous study (Ref. [19]), the interlayer coupling between $SrRuO_3$ layers separated by an asymmetric spacer of the strong spin-orbit coupling oxide $SrIrO_3$ and the large band gap insulator $SrZrO_3$ was addressed. Weak ferromagnetic coupling was observed with enhanced coupling strength upon the reduction of the total spacer thickness from 1.6 nm to 0.8 nm.[19] However, for $SrRuO_3/SrIrO_3$ multilayers with 2 MLs thick $SrIrO_3$ (about 0.8 nm), where the $SrIrO_3$ is discussed to induce interfacial DMI,[5,10,20,21] there are only theoretical calculations and no experimental data, which predict that ferromagnetic coupling between the $SrRuO_3$ layers is more favorable than an antiferromagnetic type of coupling.[20]

This study addresses the magnetic interlayer coupling in $SrRuO_3$-$SrIrO_3$ multilayers experimentally. Here the magnetic interlayer coupling was investigated for heterostructures in which the $SrRuO_3$ layers were separated by $SrIrO_3$ spacers with various thickness, by means of superconducting quantum interference device (SQUID) magnetometry (full and minor hysteresis loops) and first order reversal curve measurements (FORC). The FORC method has proven to provide valuable information in many different systems that is inaccessible for

---

[1] 1 ML is about 0.4 nm thick for all the perovskites under discussion here and represents the dimensions of a pseudocubic cell.

conventional magnetometry measurements. For example, microstructural information without actual lateral resolution in microstructured and model magnetic systems,[22–25] information about coercive and interaction field distribution in permanent hard magnetic systems,[26–28] as well as interaction strength and interaction type between different magnetic components in systems[22,28] can be achieved. The performance of minor hysteresis loops and FORC measurements enabled to quantify the sign and strength of the magnetic interlayer coupling between the $SrRuO_3$ layers for various $SrIrO_3$ spacer thicknesses. For the heterostructure with only 2 MLs $SrIrO_3$ spacer, the minor loops showed a small positive shift with respect to the major hysteresis loops above 30 K, indicating that the coupling turned weakly antiferromagnetic. However, the estimated coupling strength of about $-7\,\mu\mathrm{J\,m^{-2}}$ at 40 K led to the conclusion that the two $SrRuO_3$ layers switch their magnetization almost independently. In its bulk form and thick films, the spacer material $SrIrO_3$ is a paramagnetic semimetal with a Fermi surface that consists of electron- and holelike pockets.[29] The transition to an insulating state can be induced in $SrIrO_3$ thin films by the reduction of the film thickness in the ultrathin limit[29–31] and by tailoring of epitaxial strain.[32,33] Manca *et al.* reported the (semi-)metal-to-insulator transition to take place in $SrIrO_3$ films between 3 and 4 MLs.[31] A resistivity increase was observed upon temperature enhancement in these $SrIrO_3$ layers of minimum 4 MLs thickness that indicated the metallic properties.[31] In contrast, a 20 nm thick $SrIrO_3$ film showed only weakly temperature-dependent resistivity in the study by Gruenewald *et al.*[34] In this study, it was therefore expected that the 2 MLs $SrIrO_3$ spacer is insulating and might undergo a transition from the insulating to the (semi-)metallic state, upon thickness increase. In case of a transition to the semimetallic state with clear temperature dependent resisitivity, the influence of the $SrIrO_3$ electronic transport properties on the interlayer coupling could be adressed, in addition to the commonly observed thickness dependence of the interlayer coupling mediated by exchange or magnetostatic interactions. It turned out that the coupling strength did not increase upon the increase of the spacer thickness to 12 MLs and the two $SrRuO_3$ layers stayed decoupled. Resistivity investigations of $SrIrO_3$ reference films show that they are semimetallic with very weakly temperature-dependent behavior. Thus $SrIrO_3$ layers may be unsuitable as spacers for achieving a strong magnetic coupling between ferromagnetic $SrRuO_3$ and other oxide layers ought to be considered for realizing this.

5.2 Sample design and experimental methods

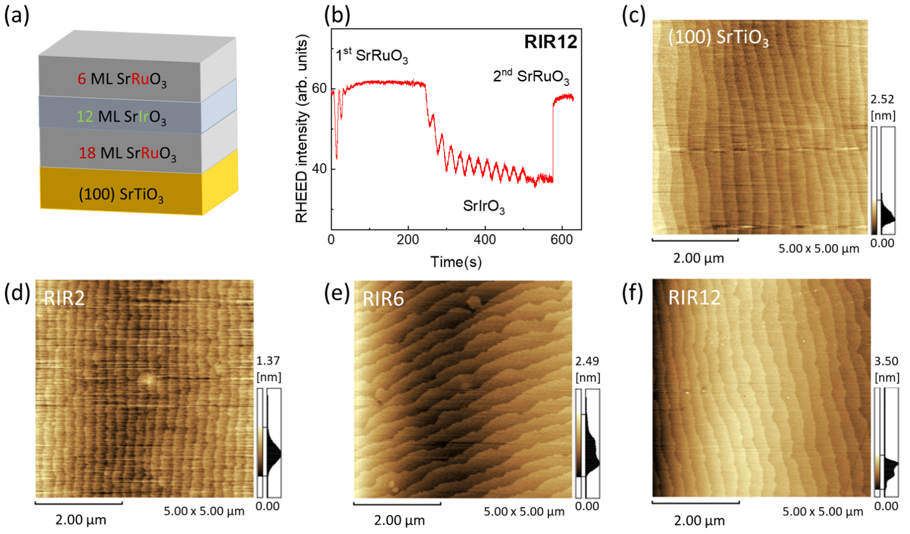

Figure 5.1: (a) Scheme of the heterostructures under study, exemplarily drawn for heterostructure RIR12, with 12 MLs $SrIrO_3$ spacer. (b) Integrated RHEED intensity plotted as function of deposition time of the heterostructure RIR12. Atomic force microscopy images (5 µm x 5 µm) of one $SrTiO_3$ (100) substrate after etching and annealing (c), and AFM images of the heterostructures RIR2 (d), RIR6 (e), and RIR12 (f). Adapted from Ref. [1], with the permission of AIP Publishing.

For investigating the type and strength of the magnetic coupling of the ferromagnetic $SrRuO_3$ layers, a set of heterostructures with two ferromagnetic $SrRuO_3$ layers of distinct thicknesses was designed. To make use of the thickness dependence of the coercive field H_c and ferromagnetic transition temperature T_c of $SrRuO_3$ thin films,[35] each multilayer was composed of two separated $SrRuO_3$ layers with 6 MLs and 18 MLs thickness. The 18 MLs thick $SrRuO_3$ layer was deposited directly on the $SrTiO_3$ (100) substrate, while the top 6 MLs $SrRuO_3$ layer was grown on top of the spacer layer, as illustrated in the scheme of the heterostructure design in Fig. 5.1 (a). A $SrIrO_3$ spacer separates the two ferromagnetic layers. The heterostructure with 2 MLs $SrIrO_3$ spacer is named RIR2, the one with 6 MLs $SrIrO_3$ spacer RIR6, and the multilayer with 12 MLs $SrIrO_3$ is labeled RIR12. In case of decoupled or only weakly coupled layers, the magnetic hysteresis loop of such heterostructures shows a two-step switching behavior due to the different temperature dependencies of the coercive fields of the two $SrRuO_3$ layers. This allows to assess the magnetic interlayer coupling.

For the heterostructure RIR2, the top $SrRuO_3$ layer is additionally capped by a 2 MLs $SrIrO_3$ layer. This capping layer was added so that the 6 MLs $SrRuO_3$ layer has the same boundary conditions on both interfaces, as this kind of unit was employed by Yang *et al.* in the study of symmetric $SrRuO_3$/$SrIrO_3$ multilayers in a recent work.[8] The capping layer of the RIR2 heterostructure is not expected to play an active role in the magnetic interlayer coupling studied here, for which only the spacer layer between the two magnetic layers has high relevance.

The heterostructures were fabricated by pulsed-laser deposition (PLD), using the TSST set-up (cf. Chapter 3). The multilayers were grown on TiO_2-terminated $SrTiO_3$ (100) substrates, which had been prepared as described in Chapter 3. During the growth, the deposition temperature was 650°C, the oxygen pressure was kept at 0.133 mbar and the laser fluence was set to about 2 J/cm^2. 5 Hz repetition rate was used for the $SrRuO_3$ and 1 Hz for $SrIrO_3$. In order to ensure a smooth epitaxial growth for enhanced thicknesses of the $SrIrO_3$ spacer, the deposition temperature was increased for the heterostructure RIR12 to 700°C. Employing *in situ* high-energy electron diffraction (RHEED) enabled the precise control of the $SrIrO_3$ layer thickness, which grew in a layer-by-layer mode (see Fig. 5.1 (b)). The $SrRuO_3$ layers grew in step-flow mode which has been proven to result in smooth thin films.[36] Atomic force microscopy (AFM) investigations, presented in Fig. 5.1 (d) - (f), confirmed the smooth topography of the heterostructure surfaces maintaining the stepped terrace structure of the $SrTiO_3$ (100) substrates with uniform terrace width and one unit cell step height, which indicates the pseudomorphic, crystalline growth. The investigation of the surface topography by AFM did not show any etch pits on the substrates before deposition, or deep holes in the heterostructures with $SrIrO_3$ spacers of 2, 6, or 12 MLs thickness.

The magnetic interlayer coupling was investigated by a combination of conventional SQUID magnetometry (temperature-dependent and magnetic-field-dependent magnetic moment measurements) and FORC investigations. The study was complemented by polar magneto-optical Kerr effect (p-MOKE) and Hall voltage measurements for selected samples. All Hall measurements were performed in the van der Pauw geometry with our home-built set-up.

SQUID magnetometry was performed with a SQUID magnetometer (MPMS-XL, Quantum Design inc.). In order to extract the magnetic response of the ferromagnetic $SrRuO_3$ layers, the linear contribution of the diamagnetic $SrTiO_3$ substrate was subtracted by linear fitting in the high magnetic field range. Furthermore, the nonlinear magnetic moment measured above the Curie temperature of the $SrRuO_3$ layers was subtracted to correct the additional background response originating from magnetic impurities introduced most likely during the required sample cutting (see Chapter 3 for further details).

The FORC measurements were performed with a SQUID magnetometer (MPMS 3 , Quantum Design inc.). Processing of raw data was done with LeXtender,[37] and the FORC densities were calculated using the gFORC algorithm.[38] For the FORC study[2], a set of minor loops with various reversal fields was performed. Before each minor loop, the sample was saturated in a positive magnetic field of 5 T. Then the external magnetic field was decreased to the required reversal field H_r. The first order reversal curve was determined by measuring the magnetic moment when the magnetic field was increased from H_r to saturation in positive magnetic fields.[22,27,38] This procedure was repeated with step-like decreasing of the reversal field until the reversal field reached negative saturation. The FORC density was calculated by the mixed second derivative of the magnetic moment surface:

$$\rho(H, H_r) = -\frac{1}{2}\frac{\partial^2 m(H, H_r)}{\partial H \partial H_r} \tag{5.1}$$

The FORC density was then transformed on the axes of the coercive field H_c and the interaction field H_u via:

$$H_u = \frac{1}{2}(H + H_r); \quad H_c = \frac{1}{2}(H - H_r) \tag{5.2}$$

From the FORC-density, plotted as function of the interaction field and the coercive field, the sign of the magnetic interlayer coupling can be assessed, as described in more detail in Chapter 3.

---

[2] For further details on the FORC measurement procedure, please see Chapter 3.2.4.

5.3 Magnetometry study of a heterostructure with 2 MLs SrIrO$_3$ spacer

Summarized in Fig. 5.2 (a) and (b) are major and minor magnetic hysteresis loops for the heterostructure RIR2 (2 MLs SrIrO$_3$/ 6 MLs SrRuO$_3$ / 2 MLs SrIrO$_3$/ 18 MLs SrRuO$_3$ on SrTiO$_3$(100), at representative temperatures of 10 K and 80 K.

The magnetization of the heterostructure RIR2 reverses its orientation in a two-step reversal process indicating at best a weak coupling of the two SrRuO$_3$ layers. Since the 18 MLs thick SrRuO$_3$ layer has a larger magnetic moment than the thinner SrRuO$_3$ layer, it can be concluded that the thicker layer is the magnetically softer layer at 10 K. At elevated temperatures[3], such as 80 K, the thinner 6 MLs SrRuO$_3$ layer is magnetically softer and switches at smaller magnetic fields than the 18 MLs SrRuO$_3$ layer, as it has been shown already in our previous study on similar SrRuO$_3$-based heterostructures.[19]

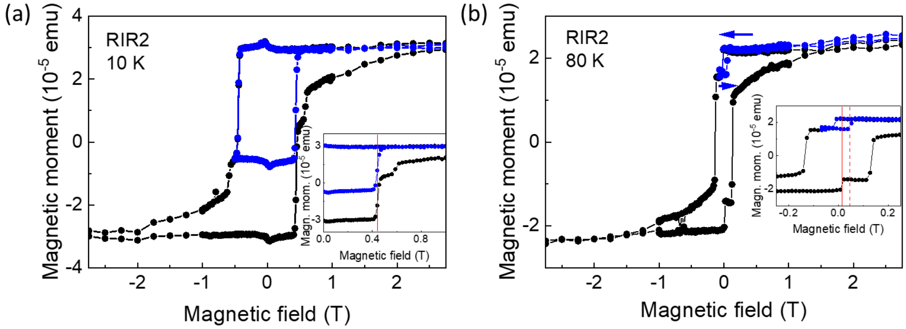

Figure 5.2: (a) Major (black) and minor (blue) magnetic hysteresis loops for the heterostructure RIR2 with 2 MLs SrIrO$_3$ spacer at 10 K (a) and 80 K (b). The magnetic field was applied perpendicular to the thin film surface. The minor loops were carried out between 5 T and -0.5 T (a), and -0.07 T (b). The minor loop at 10 K (a) does not show a measurable shift. At 80 K (b), the switching field (during the backward sweep) of the minor loop (red dashed line) is shifted by $+30$ mT with respect to the reversal field of the magnetically softer layer during the major loop (solid red line) (b). Subfigures reproduced from L. Wysocki, S. E. Ilse, L. Yang, E. Goering, F.Gunkel, R. Dittmann, P. H. M. van Loosdrecht, I. Lindfors-Vrejoiu, Journal of Applied Physics **131**, 133902 (2022), with the permission of AIP Publishing.

---

[3] The temperature dependence of the switching fields of the two ferromagnetic layers of this particular heterostructure RIR2 is shown in Fig. 5.3 (a).

In addition to the sharp two-step magnetization reversal, the magnetic hysteresis loops possess a tail in the high magnetic field range, which can be related most likely to strongly pinned domains in the bottom $SrRuO_3$ layer deposited directly on the $SrTiO_3$ (100) substrate.[39]

The minor loop of heterostructure RIR2, plotted in blue in Fig. 5.2 (a), did not show a measurable shift with respect to the major hysteresis loop at 10 K, showing that the two $SrRuO_3$ layers of the heterostructure are indeed magnetically decoupled. In contrast, the minor loop of the heterostructure RIR2 is shifted by +30 mT to higher magnetic fields at 80 K (cf. inset in Fig. 5.2 (b)). Such a shift of the minor loop to larger magnetic field, compared to the full loop, can be an indication for antiferromagnetic coupling of the two $SrRuO_3$ layers (see for instance Ref. [40–42]). As indicated by the red lines in Fig. 5.2 (b), the switching field of the magnetically softer layer increased by + 30 mT with respect to the major loop.

Presented in Fig. 5.3 is the detailed temperature dependence of the switching fields and the calculated coupling strengths. 40 K is the lowest temperature of the current study at which a positive minor loop shift was observed. The full and minor magnetic hysteresis loops of heterostructure RIR2 at 40 K are shown in Fig. 5.3 (a). The minor loop (blue) is shifted by +30 mT with respect to the full loop (black). Displayed in Fig. 5.3 (b) are the switching fields of the two $SrRuO_3$ layers of heterostructure RIR2 as a function of temperature. The two $SrRuO_3$ layers of the heterostructure have the same switching field at 20 K. Below 20 K, the bottom 18 MLs $SrRuO_3$ switches at smaller magnetic fields than the 6 MLs top $SrRuO_3$, while they behave *vice versa* above 20 K. Plotted with open triangles are the switching fields of the minor loops at the respective temperatures. The minor loop shift is zero below 20 K, when the bottom, 18 MLs thick $SrRuO_3$ is magnetically softer than the 6 MLs thin $SrRuO_3$ layer. When the thinner layer switches at smaller magnetic fields than the thicker $SrRuO_3$ layer, the minor loop is shifted by 30 mT to elevated fields at all investigated temperatures below the Curie temperature of the thin layer at 110 K (compare the m(T) measurement in Fig. 5.3 (c)).

According to the calculation proposed by van der Heijden *et al.*, the magnetic coupling strength is directly proportional to the difference of the switching fields of the magnetically softer layer of the major loop and the minor loop:[40]

$$J_C = \mu_0 \Delta H_{\text{shift}} M_{\text{soft,rev}} t_{\text{soft,rev}} = \mu_0 (H_{\text{major}} - H_{\text{minor}}) M_{\text{soft,rev}} t_{\text{soft,rev}} \quad (5.3)$$

with the minor loop shift $\Delta H_{\mathrm{shift}}$. $t_{\mathrm{soft,rev}}$ and $M_{\mathrm{soft,rev}}$ are the thickness and the magnetization of the magnetically softer layer, respectively.

As shown in Fig. 5.3 (c) for heterostructure RIR2, the minor loop shift is almost temperature independent between 40 K and 100 K, when the 6 MLs top $SrRuO_3$ layer is the magnetically softer layer of the heterostructure. Thus, the coupling strength, which is directly proportional to the magnetization of the magnetically softer layer,[40] decreases for increasing temperature above 40 K, following the temperature dependence of the magnetization of the thinner $SrRuO_3$ layer.

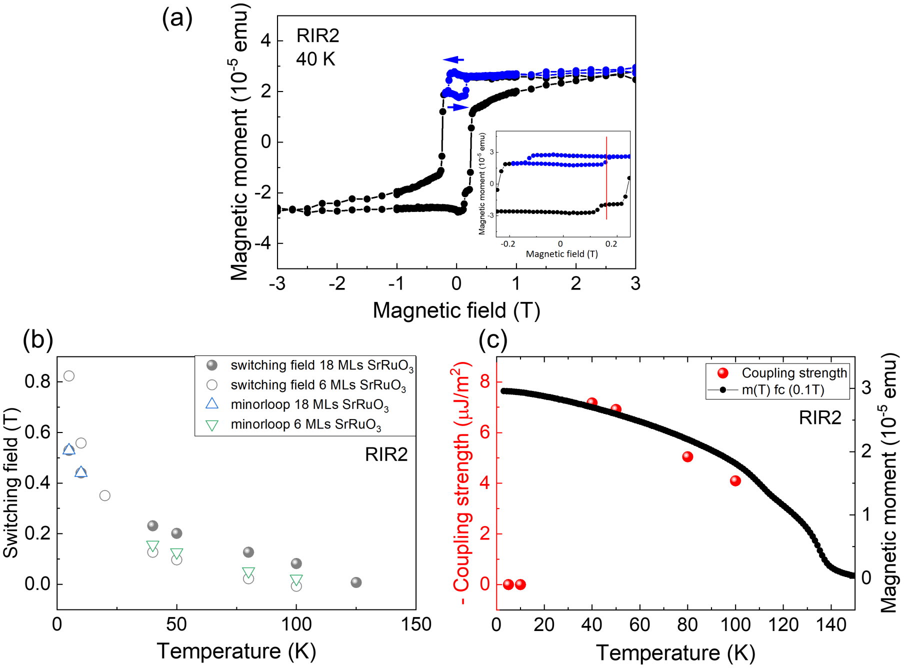

Figure 5.3: (a) Full and minor magnetic hysteresis loops of heterostructure RIR2 at 40 K. Shown in the inset is the magnetic field range in which the shift of the minor loop reversal field to elevated magnetic fields is highlighted. (b) Temperature dependence of the switching fields of the two $SrRuO_3$ layers of heterostructure RIR2, determined from the major hysteresis loops (circles) and from the minor loops (open triangles). (c) Temperature dependence of the calculated coupling strength (red) and the magnetic moment during warming in 0.1 T after field cooling (in 0.1 T). Reproduced from L. Wysocki, S. E. Ilse, L. Yang, E. Goering, F.Gunkel, R. Dittmann, P. H. M. van Loosdrecht, I. Lindfors-Vrejoiu, Journal of Applied Physics **131**, 133902 (2022), with the permission of AIP Publishing.

The temperature dependence of the magnetic moment of the heterostructure RIR2 is shown in Fig. 5.3 (c) for comparison.
The estimated coupling strength is $-5\,\mu\mathrm{J\,m^{-2}}$ at 80 K, increasing to $-7\,\mu\mathrm{J\,m^{-2}}$ at 40 K. This coupling strength is very weak. In a previous study on asymmetric $SrIrO_3/SrZrO_3$ spacers, weak ferromagnetic coupling on the order of $35\,\mu\mathrm{J\,m^{-2}}$ was observed for a 1 ML $SrIrO_3$/ 1 MLs $SrZrO_3$ spacer (about 0.8 nm total spacer thickness).[19] For 2 MLs thick $LaNiO_3$ spacers between $SrRuO_3$ layers, a coupling strength of $106\,\mu\mathrm{J\,m^{-2}}$ at 10 K was reported.[17]

The change of the magnetic interlayer coupling from decoupling below 20 K to very weak antiferromagnetic coupling above 40 K seems to be correlated to the change of the magnetically softer and harder layer of the heterostructure (cf. Fig. 5.3 (b)). When the 18 MLs thick bottom $SrRuO_3$ layer is the magnetically harder layer of the heterostructure, no shift of the minor loop is observed. Only in the temperature range where the 6 MLs thick top $SrRuO_3$ layer has smaller coercive fields, the small shift of the minor loop, indicating weak antiferromagnetic coupling, is seen.
A similar temperature dependence, namely decoupling at low temperatures and strong coupling at higher temperatures, has been observed in Ni/Co pseudo-spin-valve structures in which the Ni/Co multilayers of different repetition numbers, separated by 4.6 nm Cu, were strongly coupled via magnetic dipolar coupling.[43] Mohseni *et al.* attributed this dependence and the decoupling at low temperatures to the increase of the difference of the coercive fields of the magnetically softer and harder layers at low temperatures so that the stray fields of the magnetically harder layer were insufficient to initiate the reversal of the magnetically softer layer.[43]
Maybe also in the present case, the coupling at low temperatures, where the difference between the coercive fields is about two times larger than above 30 K, is too weak to initiate the switching in the magnetically harder
(18 MLs thick) layer.
On the other hand, assuming that the coupling strength was also on the order of a few $\mu\mathrm{J\,m^{-2}}$ at low temperature, the expected shift of the minor loop would be smaller by a factor of 5 - 6.5, since the thicker $SrRuO_3$ is the magnetically softer one at low temperature. However, a minor loop shift of 6 mT is close to the detection limit of our experimental set-ups and therefore experimentally challenging to observe.

To confirm the sign and order of magnitude of the minor loop shifts, determined from the magnetometry measurements, polar magneto-optical Kerr rotation measurements were performed with our home-built set-up based on the well-established double modulation technique with light from a Xe-lamp.

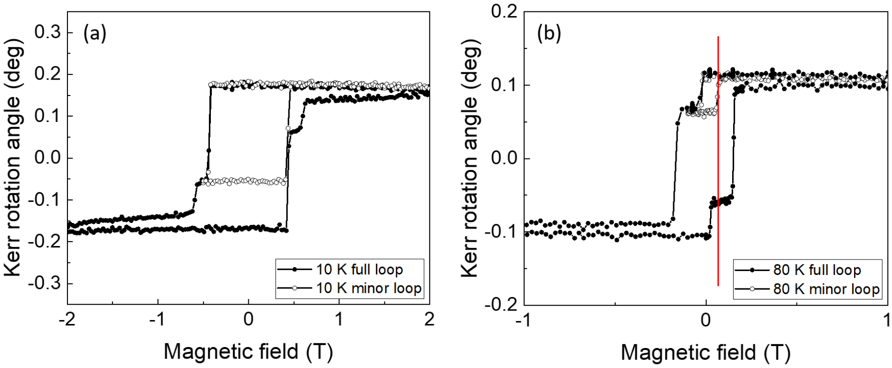

Figure 5.4: Magneto-optical Kerr rotation measurements of heterostructure RIR2 at 10 K (a) and 80 K (b), measured with incoherent light of 540 nm. Drawn with full symbols are the major hysteresis loops; the open symbols are the minor loops. The minor loop at 80 K, measured between 2.5 T and -0.1 T is shifted by + 38 mT with respect to the full loop. Reproduced from L. Wysocki, S. E. Ilse, L. Yang, E. Goering, F.Gunkel, R. Dittmann, P. H. M. van Loosdrecht, I. Lindfors-Vrejoiu, Journal of Applied Physics **131**, 133902 (2022), with the permission of AIP Publishing.

The Kerr rotation angle, determined in the polar MOKE geometry, scales linearly with the perpendicular component of the magnetization, but is not influenced by magnetic impurities at the backsides or on the edges of the sample for our measurements in reflection geometry and therefore a useful probe of the qualitative interlayer coupling. In agreement with our results from the SQUID investigations, the minor loop at 10 K (Fig. 5.4 (a)) is not shifted within the magnetic field accuracy, while the minor loop at 80 K is also shifted by +38 mT (Fig. 5.4 (b)).

To further study the magnetic interlayer coupling in the heterostructure RIR2, FORC measurements were performed at 10 K (Fig. 5.5) and 80 K (Fig. 5.6). Presented in Fig. 5.5 (a) is the set of minor loops of heterostructure RIR2 at 10 K. All minor loops were corrected by the subtraction of the diamagnetic contribution originating from the $SrTiO_3$ substrate. The soft magnetic contribution visible in the minor loops at small magnetic fields is related to magnetic impurities, often introduced during the sample cutting process, as mentioned earlier.

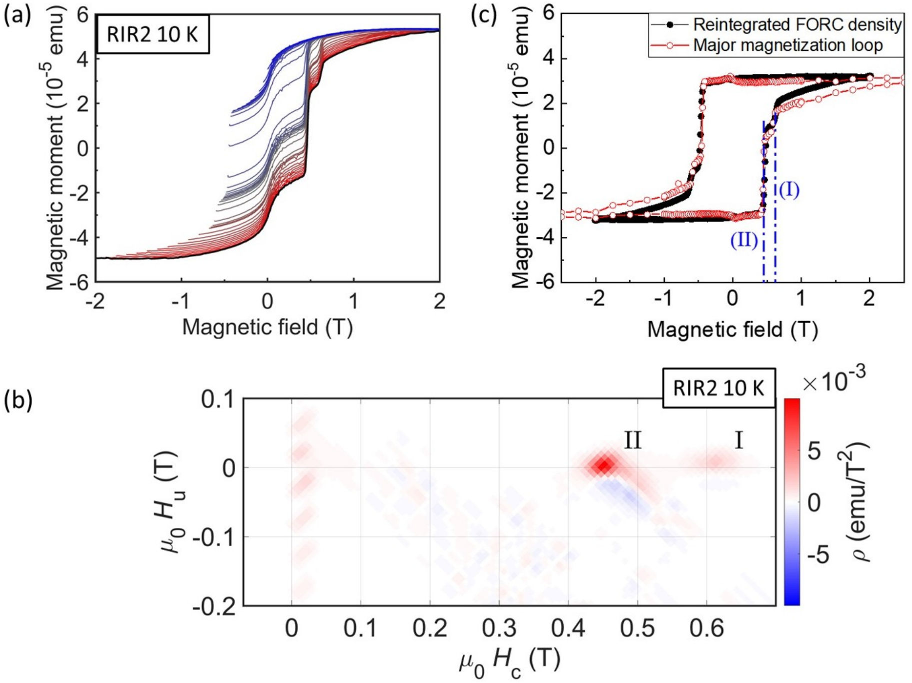

Figure 5.5: First order reversal curve study of the heterostructure RIR2 at 10 K. The magnetic field was applied perpendicular to the heterostructure surface. The measured minor loops, corrected for the diamagnetic contribution originating from the substrate, are presented in (a). The color of the respective minor loops changes from red to blue for increasing reversal fields. The FORC density ρ plotted as function of the coercive field H_c and the interaction field H_u at the corresponding temperatures is shown in (b). Positive FORC density peaks are plotted in red, negative ones in blue. Features (I) and (II) correspond to the magnetization switching of the 6 MLs (I) and 18 MLs $SrRuO_3$ (II) layer, respectively. Shown in (c) is the comparison of the major magnetization loop (red), corrected by the subtraction of the diamagnetic substrate and magnetic impurity contribution (see Chapter 3), and the reintegrated FORC density (black) after removal of the soft magnetic contribution of the reversible ridge between -0.05 T $< \mu_0 H_c <$ 0.1 T and -1.5 T$< \mu_0 H_u <$ 1.5 T. The dashed blue lines in (c) indicate the magnetic fields of the center positions of the peaks (I) and (II) of the FORC density. Reproduced from L. Wysocki, S. E. Ilse, L. Yang, E. Goering, F.Gunkel, R. Dittmann, P. H. M. van Loosdrecht, I. Lindfors-Vrejoiu, Journal of Applied Physics **131**, 133902 (2022), with the permission of AIP Publishing.

Additionally, the expected two step-reversal of the heterostructure magnetization is observed in the minor loops that started close to negative saturation. From these minor loops, the FORC density was calculated according to equation (5.1) and is shown in Fig. 5.5 (b). Three general features are present in the FORC density at 10 K. The positive peaks (I) and (II) correspond to the reversal of the two ferromagnetic SrRuO$_3$ layers. The intensity of the peaks is proportional to the magnetization of the respective layer. Hence, the more intense peak (II) is related to the switching of the 18 MLs bottom SrRuO$_3$ layer and (I) to the 6 MLs thin SrRuO$_3$ layer. The positions of the center of the peaks at 620 mT (I) and 450 mT (II) are in good agreement with the switching fields determined from the major magnetization hysteresis loops (see Fig. 5.3 (b)). The FORC investigations of heterostructure RIR2 do not show any hints of the coupling of the two ferromagnetic SrRuO$_3$ layers at 10 K. The additional feature located at tiny magnetic field values is the reversible ridge, which is dominated by magnetically soft, reversible contributions originating mainly from magnetic impurities. In case of the SQUID hysteresis loop (Fig. 5.2), these contributions were removed by subtraction of the hysteresis loop measured above the transition temperature of the SrRuO$_3$ layers and therefore related to high T_c magnetic impurities. To confirm that the reversible ridge is dominated by the contribution of these magnetic impurities, the FORC density presented in Fig. 5.5 (b) was reintegrated with the exclusion of the contribution between -0.05 T $< \mu_0 H_c <$ 0.1 T and -1.5 T$< \mu_0 H_u <$ 1.5 T. Such integration of the FORC density was possible, because features (I) and (II), originating from the magnetization reversal of the layers, were sufficiently separated from the reversible ridge. The integration yielded half of the hysteresis loop from -2 T to 2 T and was mirrored at both x- and y-axis in order to reconstruct the full hysteresis loop. Plotted in Fig. 5.5 (c) is the comparison of the reconstructed hysteresis loop of the FORC study (black) and the conventional major magnetization loop (red), which has been corrected for the magnetic impurity contribution. Both hysteresis loops are overall in good agreement and the switching fields of the two SrRuO$_3$ layers are identical for both techniques within a few mT. However, the major SQUID and the reconstructed hysteresis loops possess small differences of the shape of the tail that is observed in high magnetic fields. The deviations might be related to small reversible contributions of the sample magnetization reversal that contribute slightly to the reversible ridge and are thus not considered for the reconstruction of the hysteresis loop from the FORC density. Nonetheless, the overall agreement of both hysteresis loops supports the expectation that the reversible ridge is dominated by uncorrelated magnetic impurities that do not influence the switching fields of the magnetic SrRuO$_3$ layers of the heterostructure. This shows that the reintegration of the FORC density without the reversal ridge can be used in this case to obtain a hysteresis loop where the contribution of the soft magnetic impurity is removed, without the need of an additional measurement above the transition temperature of $SrRuO_3$.

The FORC study of heterostructure RIR2 at 80 K is summarized in Fig. 5.6.

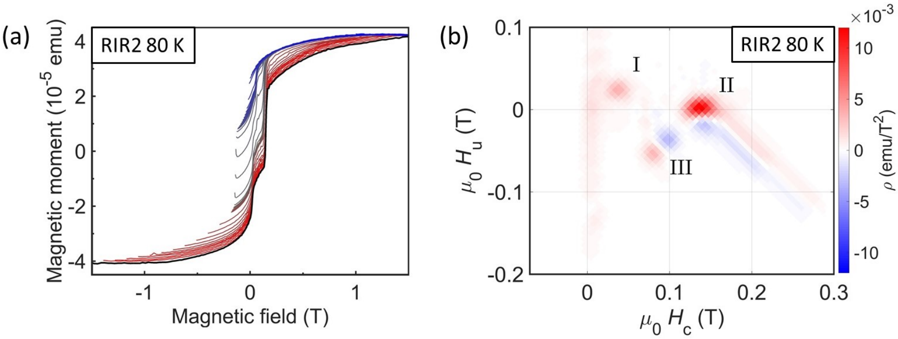

Figure 5.6: FORC study of the heterotructure RIR2 at 80 K with the magnetic field applied perpendicular to the heterostructure surface. The measured minor loops, corrected for the diamagnetic contribution originating from the substrate, are shown in (a). The color of the respective minor loops changes from red to blue for increasing reversal fields. The FORC density ρ is plotted in (b) as a function of the coercive field H_c and the interaction field H_u. Positive FORC density peaks are shown in red, negative ones in blue. Features (I) and (II) correspond to the magnetization switching of the 6 MLs (I) and 18 MLs $SrRuO_3$ (II) layer, respectively. The additional peak pair (III) at 80 K is the interaction peak indicating antiferromagnetic coupling. The additional feature located along $H_c = 0$ T is the reversible ridge. Reproduced from L. Wysocki, S. E. Ilse, L. Yang, E. Goering, F.Gunkel, R. Dittmann, P. H. M. van Loosdrecht, I. Lindfors-Vrejoiu, Journal of Applied Physics **131**, 133902 (2022), with the permission of AIP Publishing.

Also the minor loops measured at 80 K, presented in Fig. 5.6 (a), show a two-step magnetization reversal. At 80 K, the 6 MLs thin $SrRuO_3$ layer switches at smaller magnetic fields than the 18 MLs thick bottom $SrRuO_3$ layer. In the FORC density, shown in Fig. 5.6 (b), feature (I) corresponds again to the reversal of the 6 MLs $SrRuO_3$, while feature (II) originates from the magnetization switching of the 18 MLs thick $SrRuO_3$ layer. In contrast to the FORC density map at 10 K, an additional positive-negative-peak pair (structure (III)) is present at finite interaction field (see Fig. 5.6 (b)) at 80 K. According to previous FORC studies on well defined systems of coupled microarrays and on NdFeB samples with components with different coercivities, such additional positive-negative-peak pairs are characteristic for magnetic coupling

between two different magnetic sites and denominated as the so-called "interaction peak".[22,27] The relative position of the positive and negative part of the interaction peak with respect to each other yields information about the nature of the coupling. As shown in Ref. [22], the coupling is antiparallel if the negative FORC density part of the interaction peak is at higher coercive and interaction fields than the positive part of the interaction peak and parallel if it is *vice versa*. According to this, the interaction peak in Fig. 5.6 (b) shows that the $SrRuO_3$ layers in sample RIR2 are coupled antiparallel, which confirms our observation from the conventional SQUID magnetometry. If exchange bias between a ferromagnet and an antiferromagnet was present, this would lead most likely to a positive peak in the FORC density which is elongated,[44] rather than a positive-negative peak pair.
The FORC density of a $SrRuO_3$-based heterostructure in which the ferromagnetic layers are coupled weakly ferromagnetically is presented in Fig. 5.8 in section 5.6. In this heterostructure RIZR1, the two $SrRuO_3$ layers were weakly ferromagnetically coupled through a spacer of 1 ML $SrIrO_3$ and 1 ML $SrZrO_3$. The FORC density, plotted in Fig. 5.8 (c), also shows two positive peaks related to the magnetization reversal of the magnetization of the two $SrRuO_3$ layers. The observed interaction peak shows the positive FORC density at higher coercive and interaction field than the negative peak, which indicates the ferromagnetic coupling between the $SrRuO_3$ layers.[22]

Generally, the coupling of two ferromagnetic layers separated by a nonmagnetic insulator can originate from different mechanisms, such as the direct coupling via pinholes,[45] magnetostatic Néel's coupling due to correlated surface roughness,[46,47] due to shape-induced magnetic poles,[48] or induced by the coupling of magnetic domain walls.[49–52] Another coupling mechanism is the magnetic exchange coupling by tunneling of spin-polarized electrons through the insulating barrier.[41,53,54]
The coupling via pinholes, which are often present in heterostructures with ultrathin spacers, would lead to trivial ferromagnetic coupling[45,55] between the $SrRuO_3$ layers and thus cannot explain the minor loop shift to higher magnetic fields for sample RIR2. On the other hand, it needs to be emphasized that the coupling of the two $SrRuO_3$ layers separated by 2 MLs $SrIrO_3$ was found to be very sensitive to the existence of (pin-)holes in the heterostructure. As presented in Fig. 5.11 in Section 5.6, a second heterostructure where holes of nanometer depth were observed by atomic force microscopy showed weak

ferromagnetic coupling. In contrast, atomic force microscopy did not show the existence of holes in any of the heterostructures RIR2, RIR6, RIR12 so that it can be concluded that the density of pinholes connecting the two $SrRuO_3$ layers is most likely small for these samples. The weak antiferromagnetic coupling was observed only in heterostructure RIR2 with 2 MLs $SrIrO_3$ spacer and with a small density of holes seen by AFM.

In addition, magnetostatic and interlayer exchange coupling can lead to magnetic coupling of the $SrRuO_3$ layers. Antiferromagnetic coupling between ferromagnetic layers separated by nonmagnetic, insulating spacers has been previously related to exchange coupling,[41] described by the Slonczweski spin-current model[53] or the quantum interference model developed by Bruno.[54] However, the observed decrease of the coupling strength J_C (calculated with equation (5.3)) with increasing temperature observed for heterostructure RIR2 cannot be explained within the model of quantum interference effects, which predicts an increase for increasing temperatures in case of insulating spacers.[54] The prediction of the temperature-induced increase of the magnitude of the coupling strength is based on approximations that are only valid for temperatures below $T = \hbar k_F / 2 k_B m D$.[54] In case of heterostructure RIR2, with 0.8 nm thick $SrIrO_3$ spacer, this corresponds to temperatures on the order of 365 K (for Fermi velocities of about $7.6 \cdot 10^4$ m/s[56]) which confirms that the approximations should be valid for the temperature range that was studied here. However, due to the dependence of the electronic transport properties of $SrIrO_3$ on the details of the interfacial environment and the thickness, the Fermi wavevector for the $SrIrO_3$ layers of heterostructure RIR2 probably differs from the reported values of bare $SrIrO_3$ thin films.

Néel's theory of the magnetostatic coupling due to magnetic surface charges induced by correlated surface roughness was extended by Moritz *et al.* to magnetic multilayers with perpendicular magnetic anisotropy.[47] Depending on the strength of the magnetic anisotropy constant, the magnetostatic orange-peel coupling has been found to be ferromagnetic for a weak perpendicular anisotropy constant and antiferromagnetic for strong perpendicular magnetic anisotropy.[47] $SrRuO_3$ thin films deposited on $SrTiO_3(100)$ typically have a large magnetic anisotropy with the magnetic easy axis close to the $[110]_{\text{orthorh.}}$ direction[57] so that the orange-peel coupling would be expected to favor antiferromagnetic coupling between the layers. The heterostructures under study were all deposited on $SrTiO_3$ (100) substrates with a step-and-terrace structure of 0.4 nm height and 250-300 nm width that most likely led to unidirectional interface roughness.[58] However, the orange-peel coupling fields[59] expected for the substrate induced roughness would be too small to explain the observed weak antiferromagnetic coupling.

One possible coupling mechanism of magnetostatic origin, which is qualitatively consistent with the observed temperature- and spacer-thickness dependence of the antiferromagnetic interlayer coupling, might be the model of domain replication in the hard layer via magnetostatic interactions, as proposed by Nistor.[60] When the magnetic field required to reverse the magnetization of the soft layer during the minor loops is close to the nucleation field of the hard layer, inversed domains in the soft layer will generate stray fields that can induce so-called replicated domains in the hard layer, acting as negative bias field during the second half of the minor loop.[60,61] However, it cannot be proven that the domain replication mechanism is the only explanation for the coupling observed for the 2 MLs $SrIrO_3$ spacer.

5.4 Influence of the $SrIrO_3$ spacer thickness on the interlayer coupling

The possibility of a (semi-)metal-to-insulator transition that was reported by Manca *et al.* to take place between 3 and 4 MLs in bare $SrIrO_3$ thin films[31] motivated the growth of the two heterostructures RIR6 and RIR12, with $SrIrO_3$ spacers that are considerably thicker than 4 MLs (6 MLs spacer for RIR6 and 12 MLs for RIR12). If such spacer thickness increase led to a significant change of the $SrIrO_3$ electronic transport properties, a major impact on the interlayer exchange coupling would be expected, as it was achieved in $SrRuO_3$-based heterostructures separated by $LaNiO_3$ spacers.[17] Presented in Fig. 5.7 (a) and (b) are the full and minor magnetic hysteresis loops of heterostructure RIR6 (6 MLs $SrIrO_3$ spacer) at 50 K and 80 K, acquired by SQUID magnetometry. The major hysteresis loops of the heterostructure RIR6 show a two-step reversal of the magnetization, similar to heterostructure RIR2. At 50 K, the switching at 0.1 T originates from the magnetization reversal of the 6 MLs $SrRuO_3$ layer, while the step at 0.25 T is related to the switching of the 18 MLs $SrRuO_3$ layer, which is the magnetically harder layer at 50 K. Such two-step switching process indicates again the decoupling or weak magnetic interlayer coupling. To determine the interlayer coupling strength, the reversal fields of the minor

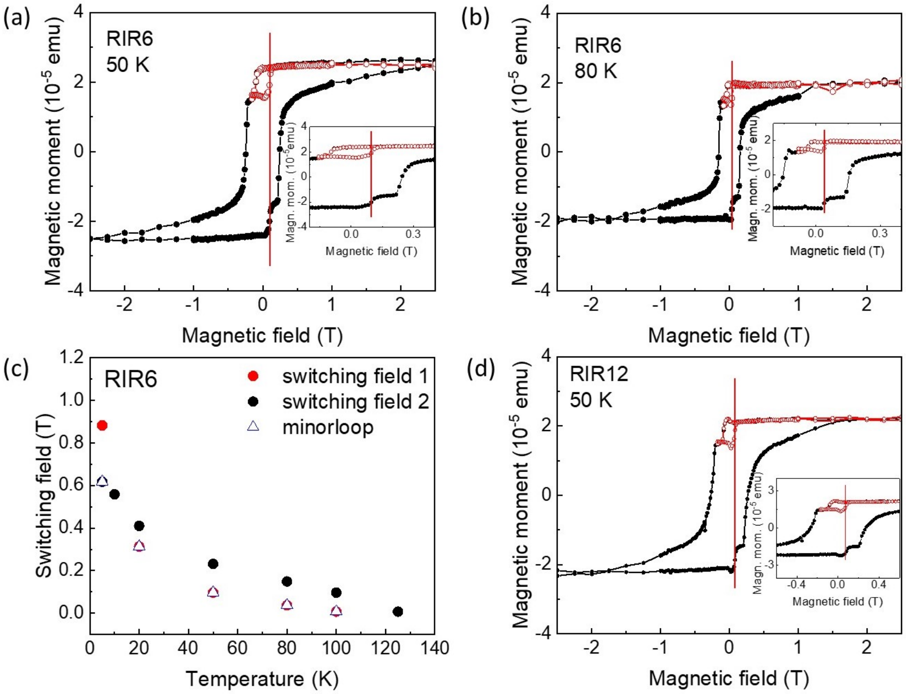

Figure 5.7: Full and minor hysteresis loops of the magnetic moment of heterostructure RIR6 with 6 MLs $SrIrO_3$ spacer at 50 K (a) and 80 K (b). (c) Temperature dependence of the switching fields of the two $SrRuO_3$ layers with 18 MLs (switching field 2) and 6 MLs (switching field 1) thickness, and the switching fields determined from minor loops experiments for the heterostructure RIR6. (d) Major and minor hysteresis loops of the magnetic moment of heterostructure RIR12 with 12 MLs $SrIrO_3$ spacer at 50 K. The magnetic field was applied perpendicular to the surfaces of the heterostructures. Reproduced from L. Wysocki, S. E. Ilse, L. Yang, E. Goering, F.Gunkel, R. Dittmann, P. H. M. van Loosdrecht, I. Lindfors-Vrejoiu, Journal of Applied Physics **131**, 133902 (2022), with the permission of AIP Publishing.

loop were compared to the switching behavior of the magnetically softer layer during the full loop. As highlighted in the inset of Fig. 5.7 (a), the minor loop switching field is equal to the switching field of the major loop. This shows that the minor loop shift and therefore the coupling strength is zero (see Section 5.6 for further details on the calculation). The two $SrRuO_3$ layers are fully decoupled by 6 MLs $SrIrO_3$ at 50 K. Also at 80 K, where a weak antiferromagnetic coupling was observed for heterostructure RIR2, the minor loop is not shifted in case of heterostructure RIR6 (see inset of Fig. 5.7 (b)). As shown in Fig. 5.7 (c), such equality of the switching fields of minor loop (drawn as blue triangles) and major loop (full symbols) was observed at all temperatures investigated for heterostructure RIR6. The absence of a measurable minor loop shift shows that the 6 MLs $SrIrO_3$ spacer decouples the two ferromagnetic $SrRuO_3$ layers fully at all temperatures.

Even further thickness increase of the $SrIrO_3$ spacer to 12 MLs was still insufficient to couple the two $SrRuO_3$ layers of heterostructure RIR12 considerably. As shown by the loop measurements at 50 K in Fig. 5.7 (d), the magnetic hysteresis is consistent with a two step-reversal of the magnetization. The minor loop is not shifted within the magnetic field accuracy indicating the decoupling of the two ferromagnetic layers. The decoupling of the $SrRuO_3$ layers was confirmed by a magnetotransport study of heterostructure RIR12, presented in Section 5.6.

The decoupling of the ferromagnetic $SrRuO_3$ layers, observed in a broad temperature range and consistently for the heterostructures RIR6 and RIR12 with spacer thicknesses above the limit for which a (semi-)metal-to-insulator transition was reported, indicates that a $SrIrO_3$ spacer may not be a suitable choice for enabling an exchange mediated coupling in these heterostructures. In contrast to $LaNiO_3$ spacer layers,[17] the semimetallic $SrIrO_3$ layers may not permit the strong ferromagnetic coupling of $SrRuO_3$ layers, which would be relevant in the context of skyrmion formation in $SrRuO_3$-$SrIrO_3$ multilayers.[8,20] The $SrIrO_3$ resistivity was investigated by reference thin film measurements, presented in Section 5.6, because the details of the $SrIrO_3$ spacer resistivity could not be assessed directly for our heterostructures when the $SrIrO_3$ was sandwiched between the metallic $SrRuO_3$ layers. The resistivities of these 6 MLs and 12 MLs $SrIrO_3$ reference thin films showed a very weak temperature dependence with a small resistivity increase for decreasing temperature, as it was also observed in 20 nm $SrIrO_3$ deposited on $SrTiO_3$,[34] or when sandwiched between $LaMnO_3$.[62] Based on the observed semimetallic behavior of the 6 MLs and 12 MLs bare $SrIrO_3$ thin films, also the $SrIrO_3$ spacers of the heterostructures likely did not become metallic.

5.5 Conclusion

The magnetic interlayer coupling between ferromagnetic $SrRuO_3$ epitaxial layers separated by the strong spin-orbit coupling $SrIrO_3$ was investigated by the combination of conventional SQUID magnetometry and FORC measurements. The minor loops of the heterostructure with 2 MLs $SrIrO_3$ spacer showed a small shift to higher magnetic fields above 30 K, indicating very weak antiferromagnetic coupling of about $-7\,\mu J\,m^{-2}$. The minor loop of a second heterostructure with 2 MLs $SrIrO_3$ spacer, which exhibited nanometer-deep holes in the surface topography, showed only weak ferromagnetic coupling. The increase of the $SrIrO_3$ layer thickness above the thickness for which a metal-to-insulator transition was reported for bare $SrIrO_3$ layers did not lead to an increase of the coupling, but to rather fully decoupled layers. This is most likely related to the electronic properties of the $SrIrO_3$ spacer, which, unlike $LaNiO_3$ spacers,[17] does not enable the ferromagnetic coupling of $SrRuO_3$ layers. The magnetic decoupling of the $SrRuO_3$ by $SrIrO_3$ spacers is undesirable in the context of skyrmion formation. Without ferromagnetic coupling between the magnetic layers, skyrmions forming in the $SrRuO_3$ layers cannot be coupled through multilayer stacks. As $SrIrO_3$ layers turned out to be unsuitable as spacers for achieving a strong magnetic coupling, other oxide layers ought to be considered for realizing this end.

The study further highlights the scientific relevance of first order reversal curve investigations for the study of magnetic interlayer coupling, being capable to detect weak coupling interactions as well as to determine whether the coupling is antiferromagnetic or ferromagnetic. Additionally, FORC measurements have the advantage that a correction for the contribution of magnetic impurities is not necessary, because the peaks representing the various magnetization reversal steps are well separated in the FORC density maps. Additionally, it was shown that reintegrating the FORC density without the reversible ridge can be an alternative method to correct a sample´s hysteresis loop for a soft magnetic impurity.

5.6 Supportive investigations

First order reversal curve study of heterostructure RIZR1 showing weak ferromagnetic coupling of the $SrRuO_3$ layers

The major and minor hysteresis loops, determined by SQUID magnetometry of heterostructure RIZR1 are shown exemplarily at 10 K in Fig. 5.8 (a). Similar to heterostructure RIR2, also this heterostructure is composed of two $SrRuO_3$ layers of 18 MLs and 6 MLs thickness. They are separated and capped by 1 ML $SrIrO_3$ / 1 ML $SrZrO_3$. As highlighted in the inset of Fig. 5.8 (a), the minor loop is shifted by about 30 mT to smaller magnetic fields indicating a weak ferromagnetic coupling on the order of 35 µJ m^{-2}, as is has been demonstrated in a previous study.[19] In order to confirm the relation of the interaction peak with the type of magnetic coupling, FORC studies were also performed at 10 K for the heterostructure RIZR1 with heterogeneous spacer of 1 ML $SrIrO_3$/ 1 ML $SrZrO_3$. Depicted in Fig. 5.8 (b) are the individual minor loops of the first order reversal curve study at 10 K. Only the diamagnetic contribution originating from the $SrTiO_3$ substrate has been corrected by linear fitting in the high magnetic field range where the sample is in its saturated state.

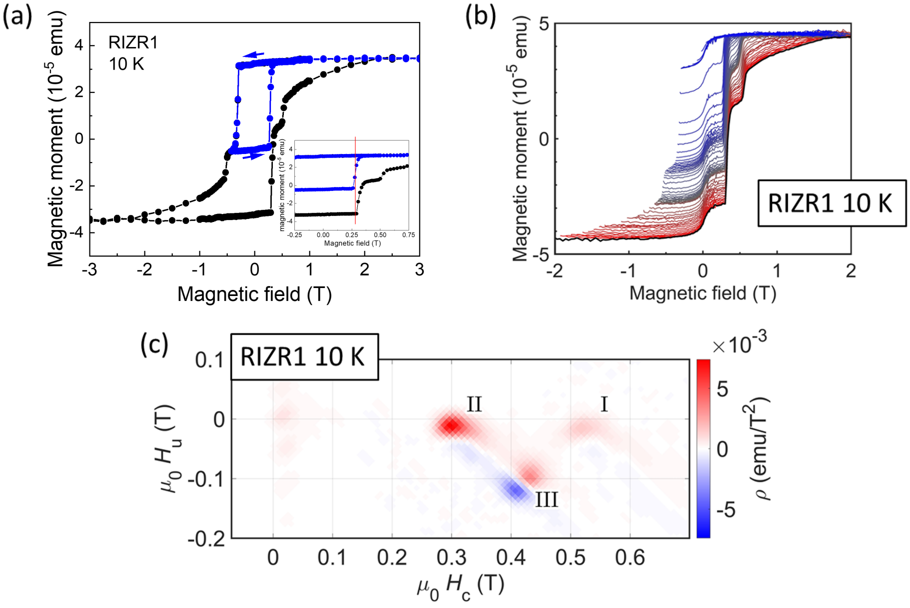

Figure 5.8: (a) Major (black) and minor (blue) magnetic hysteresis loops of heterostructure RIZR1 at 10 K, measured with conventional SQUID magnetometry. This heterostructure has 1 ML $SrIrO_3$ and 1 ML $SrZrO_3$ as spacer and capping layers. (b) Minor loops of heterostructure RIZR1 measured at 10 K. The color of the respective minor loops changes from red to blue for increasing reversal fields. (c) FORC density ρ plotted as a function of the coercive field H_c and the interaction field H_u for the heterostructure RIZR1 at 10 K. Positive FORC density peaks are shown in red, negative ones in blue. Features (I) and (II) correspond to the magnetization switching of the 6 MLs (I) and 18 MLs $SrRuO_3$ (II) layer, respectively. (III) is the interaction peak indicating ferromagnetic coupling. Reproduced from L. Wysocki, S. E. Ilse, L. Yang, E. Goering, F.Gunkel, R. Dittmann, P. H. M. van Loosdrecht, I. Lindfors-Vrejoiu, Journal of Applied Physics **131**, 133902 (2022), with the permission of AIP Publishing.

The soft magnetic contribution is related to magnetic impurities introduced during the sample cutting and handling. The FORC density at 10 K is plotted in Fig. 5.8 (c) as function of the interaction field H_u and the coercive field H_c. Similar to heterostructure RIR2 with 2 MLs $SrIrO_3$ spacer, a reversible ridge was observed at small magnetic field values, which is related to purely reversible magnetization switching. Due to the relative intensity of the peaks, the more intense peak (II) can be related to the switching field of the 18 MLs thick $SrRuO_3$ layer. Feature (I) corresponds to the irreversible switching of the 6 MLs $SrRuO_3$ layer of the heterostructure. In accordance with the global SQUID magnetometry shown in (a), the 6 MLs $SrRuO_3$ is the magnetically harder layer at 10 K. An additional positive-negative-peak pair is present in the FORC density with the orientation opposite to the one observed for heterostructure RIR2. While the orientation of feature (III) in Fig. 5.6 indicated antiferromagnetic coupling for heterostructure RIR2, the reversed orientation of feature (III) in Fig. 5.8 supports the observation of ferromagnetic coupling at 10 K in heterostructure RIZR1.

Magnetotransport investigations of heterostructure RIR12 with 12 MLs $SrIrO_3$ spacer

As described in detail in Chapter 3, all SQUID magnetometry measurements of this study have been corrected by subtraction of the magnetic hysteresis loop at 200 K, above the Curie temperature of the $SrRuO_3$ layers of the heterostructures. However, this correction leads to artifacts, such like the small peaklike features close to zero field at low temperatures (cf. Fig. 5.9).

In order to confirm that this correction does not lead to misinterpretations of the main physical properties of the heterostructures, Hall measurements were performed for sample RIR12, the heterostructure with the thickest $SrIrO_3$ spacer of this study.

In a single domain ferromagnet, the anomalous Hall constant is directly proportional to the out-of-plane component of the magnetization.[63] As shown also by van Thiel *et al.*, the measured Hall voltage of a magnetic sample that contains several anomalous Hall conduction channels is given by the sum of the different individual contributions.[64] For heterostructure RIR12, the overall anomalous Hall voltage is then the sum of the contributions of the two $SrRuO_3$ layers with distinct thicknesses and therefore different temperature dependencies of the anomalous Hall constant.

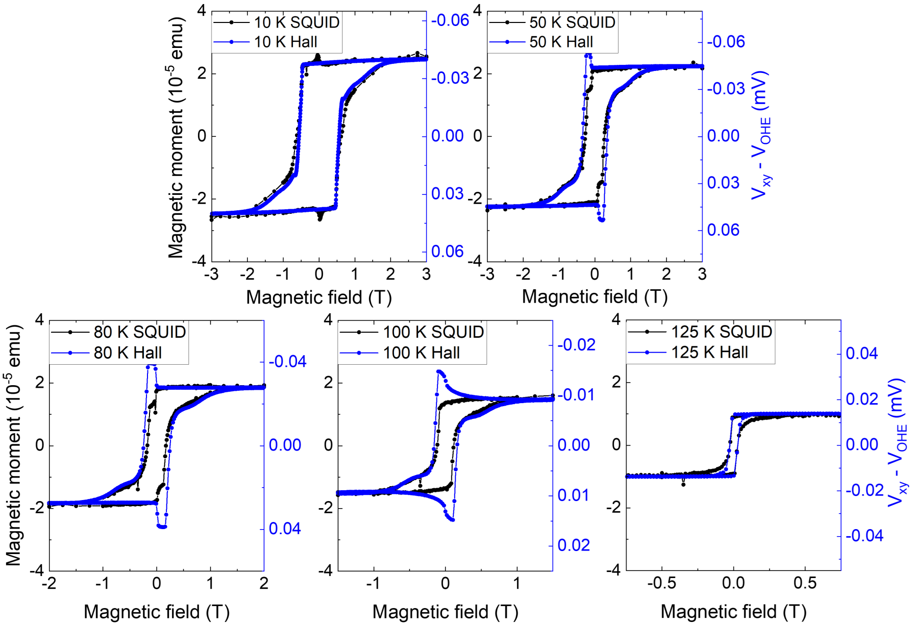

Figure 5.9: Comparison of the magnetic hysteresis loops determined by SQUID magnetometry (black) and the Hall voltage (blue), corrected for the ordinary Hall contribution, as function of applied magnetic field for heterostructure RIR12 with 12 MLs $SrIrO_3$ spacer. To increase the comparability of the magnetic field dependencies of Hall effect and magnetization reversal, the anomalous Hall voltage was plotted from positive to negative values for 10 K, 50 K, 80 K, and 100 K. Reproduced from L. Wysocki, S. E. Ilse, L. Yang, E. Goering, F.Gunkel, R. Dittmann, P. H. M. van Loosdrecht, I. Lindfors-Vrejoiu, Journal of Applied Physics **131**, 133902 (2022), with the permission of AIP Publishing.

Depicted in Fig. 5.9 is the comparison of the magnetic hysteresis loops (black) and the Hall voltage (after subtraction of the ordinary Hall effect) of heterostructure RIR12 at several temperatures below the ferromagnetic transition temperature of the 18 MLs $SrRuO_3$ layer of the heterostructure. The observation of hump-like features between 50 K and 100 K confirms our expectation of the different temperature dependencies of the anomalous Hall constant. The anomalous Hall constant of the thin $SrRuO_3$ layer is most likely positive in this temperature range, while the AHE constant of the thicker $SrRuO_3$ layer is still negative up to 100 K. Most relevant for the present study is the magnetic field range in which the two different $SrRuO_3$ layers reverse their magnetization. The comparison of the SQUID and Hall measurements confirms that the hump-like features appear in the same magnetic field range in which the magnetically softer layer reverses its magnetization and disappears when the magnetically harder layer switches its magnetization. This confirms the switching fields determined by SQUID magnetometry. At 100 K, the hump-like feature has an s-shape which is most likely related to the 6 MLs thin layer which is already in its paramagnetic phase with a still measurable contribution to the Hall voltage. At 125 K, the Hall voltage loop is mainly determined by the anomalous Hall voltage of the 18 MLs $SrRuO_3$ layer, which is still in its ferromagnetic phase, again confirming the SQUID magnetometry.

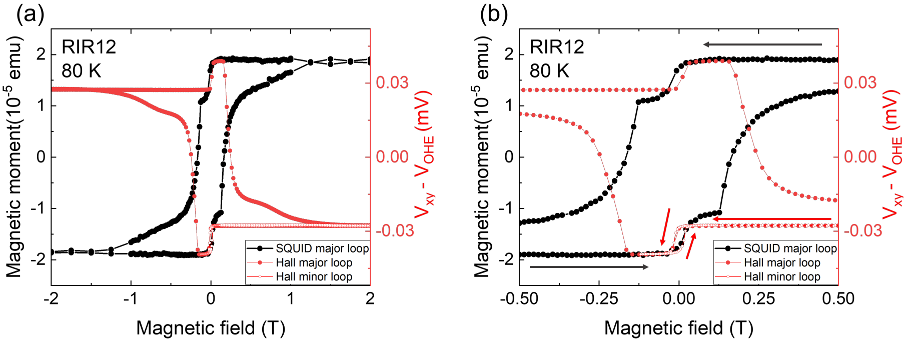

Figure 5.10: Comparison of the magnetic hysteresis loops determined by SQUID magnetometry (black) and the anomalous Hall voltage (red) as function of applied magnetic field for heterostructure RIR12 with 12 MLs $SrIrO_3$ spacer at 80 K. To increase the visibility in the magnetic field range of the minor loop switching, a zoom-in of (a) is shown in (b). Reproduced from L. Wysocki, S. E. Ilse, L. Yang, E. Goering, F. Gunkel, R. Dittmann, P. H. M. van Loosdrecht, I. Lindfors-Vrejoiu, Journal of Applied Physics **131**, 133902 (2022), with the permission of AIP Publishing.

Depicted in Fig. 5.10 are the major and minor loop hystereses of the Hall voltage, after subtraction of the ordinary Hall contribution, and compared to the major magnetic hysteresis loop (in black). As highlighted in Fig. 5.10 (b), the minor loop of the anomalous Hall voltage, which is proportional to the magnetization of the magnetically softer layer, is in good agreement with the magnetic field dependence of the major magnetic hysteresis loop for the reversal of the magnetically softer $SrRuO_3$ layer. This confirms that the minor loop is not shifted with respect to the full loop.

Minor loop investigations of a $SrRuO_3$-based heterostructure with 2 MLs $SrIrO_3$ spacer having nanometer-deep holes

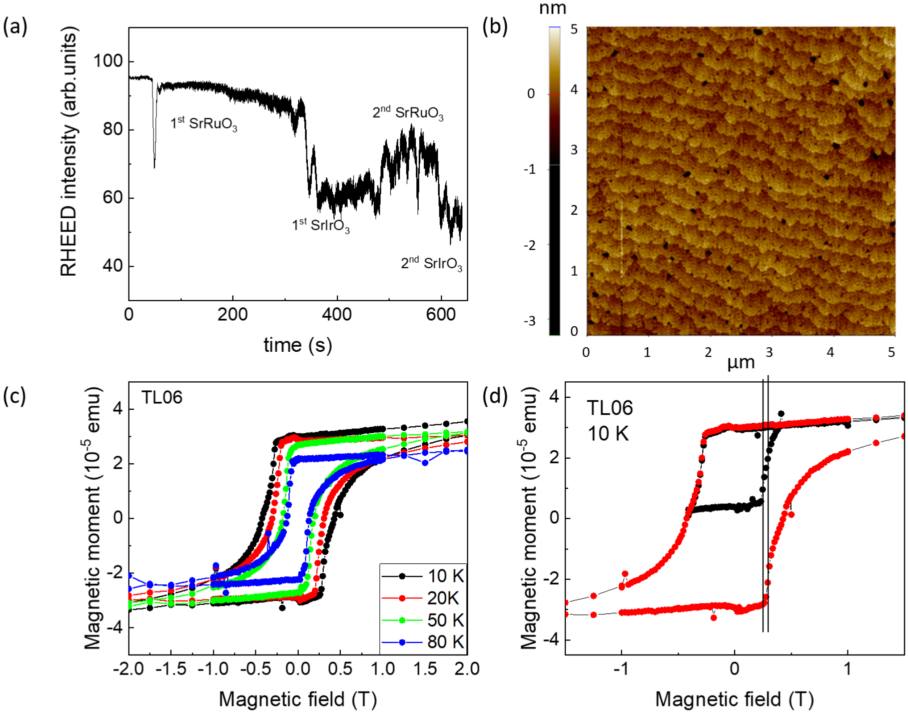

Figure 5.11: (a) Integrated RHEED intensity of the specular spot during the deposition of a second sample (TL06) with 2 MLs $SrIrO_3$ spacer and capping layer. (b) Atomic force microscopy image (5 µm x 5 µm) of the surface topography of TL06. Major (c) and minor (d) magnetic hysteresis loop measurements of the heterostructure determined by SQUID magnetometry. Reproduced from L. Wysocki, S. E. Ilse, L. Yang, E. Goering, F.Gunkel, R. Dittmann, P. H. M. van Loosdrecht, I. Lindfors-Vrejoiu, Journal of Applied Physics **131**, 133902 (2022), with the permission of AIP Publishing.

The influence of holes in the heterostructures on the magnetic interlayer coupling was investigated by the comparison of heterostructure RIR2 with a second sample with 2 MLs $SrIrO_3$ spacer where holes of minimum 1-2 nanometers depth were observed by atomic force microscopy. As shown in Fig. 5.11 by the time-dependent RHEED intensity plot, this sample also has a $SrIrO_3$ spacer and capping layer of 2 MLs thickness and two $SrRuO_3$ layers of distinct thicknesses. In contrast to the other heterostructures of the current study, this sample was deposited by our new pulsed-laser deposition set-up at the University of Cologne, manufactured by *SURFACE*. As depicted in Fig. 5.11 (b), the heterostructure surface of this sample shows the existence of nanometer-deep holes. Because there were no holes observed in the AFM investigations of the heterostructures RIR2, RIR6, or RIR12, it was expected that this heterostructure was influenced more strongly by the existence of ferromagnetic bridges by pinholes. Shown in Fig. 5.11 (c) are major hysteresis loops of this sample at various temperatures. Only at 10 K, the switching fields of the two individual $SrRuO_3$ layers are distinguishable. The performed minor loop at 10 K, drawn in Fig. 5.11 (d), shows a small negative shift of 45 mT, indicating weak ferromagnetic coupling. Thus, both samples with 2 MLs $SrIrO_3$ spacer indicate opposite sign of the coupling of the two $SrRuO_3$ layers. The difference could originate from the different densities of nanometer-deep (pin-)holes in the heterostructures, which was increased for sample TL06. Such holes are expected to lead to the formation of ferromagnetic bridges by pinholes connecting the two ferromagnetic $SrRuO_3$ layers.

Resistance measurements of bare $SrIrO_3$ thin films deposited on $SrTiO_3(100)$

Because it is sandwiched between two $SrRuO_3$ layers with much lower resistivity (about $0.5\,\mu\Omega\,\mathrm{m}$at 10 K), the resistivity of the $SrIrO_3$ spacer layers cannot be assessed easily.[31,57,65] The voltage drop measured along the whole heterostructure will therefore be dominated by the $SrRuO_3$ layers. This is confirmed by a resistance measurement of heterostructure RIR12 in comparison to a 12 MLs bare reference $SrIrO_3$ film (see Fig. 5.12). The voltage drop of this anisotropic heterostructure was measured in van der Pauw geometry as indicated in the inset in Fig. 5.12 (a). The sheet resistances of the 6 and 12 MLs bare $SrIrO_3$ thin films (shown in Fig. 5.12 (b)), deposited on $SrTiO_3$, correspond to a measured voltage drop that is almost two order of magnitudes larger than the measured voltage drop in case of the heterostructure. Thus, our following estimations of the $SrIrO_3$ spacer transport properties are based on the investigations of 6 and 12 MLs bare $SrIrO_3$ reference thin films deposited on $SrTiO_3$ (100) substrates. The sheet resistances of the 6 and 12 MLs $SrIrO_3$ thin films (see Fig. 5.12 (b)) show only a very weak temperature dependence of about 20% variation between

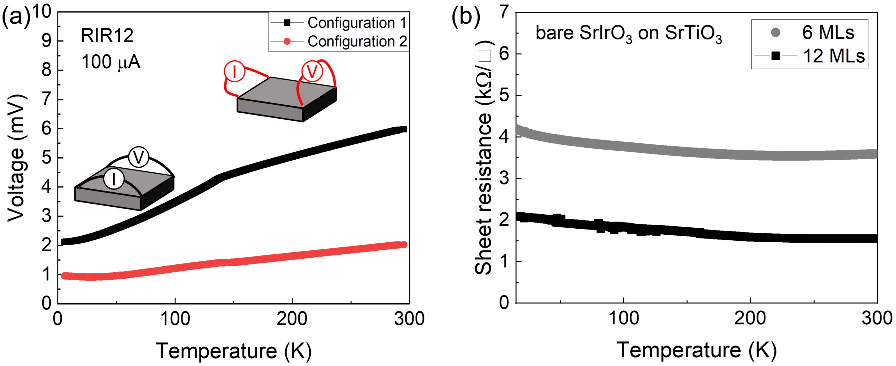

Figure 5.12: (a) Temperature dependence of the voltage measured along the edges of heterostructure RIR12 when 100 µA were applied. The two configurations that correspond to the current parallel to the two in-plane principal axes of the orthorhombic $SrRuO_3$ layers are sketched in the inset. Temperature dependence of the sheet resistance of 6 (grey) and 12 MLs (black) bare $SrIrO_3$ thin films deposited on $SrTiO_3$ (100). Reproduced from L. Wysocki, S. E. Ilse, L. Yang, E. Goering, F.Gunkel, R. Dittmann, P. H. M. van Loosdrecht, I. Lindfors-Vrejoiu, Journal of Applied Physics **131**, 133902 (2022), with the permission of AIP Publishing.

5 K and 300 K, with a small upturn for decreasing temperature. The classification of the observed transport properties of the $SrIrO_3$ reference films is not straightforward due to the variety of different experimental results of $SrIrO_3$ thin films deposited on $SrTiO_3$[30,31,34] or when $SrIrO_3$ was interfaced with dissimilar perovskite oxides.[62] A (semi-)metal-to-insulator transition, with a clear change to a positive slope of ρ(T) in the thicker films, was observed between 3 and 4 MLs thickness by Manca *et al.*[31] or below 4 MLs by Groenendijk *et al.*[30] In contrast, weakly temperature-dependent resistivity was seen in even 20 nm thick $SrIrO_3$ films by Gruenewald *et al.*,[34] or when $SrIrO_3$ was interfaced with $LaMnO_3$.[62] The latter behavior is consistent with the transport behavior of our $SrIrO_3$ thin films. Theoretical band structure calculations as well as experimental ARPES studies[29,56] showed that the Fermi surface of $SrIrO_3$ in the semimetallic state consists of electron- and holelike pockets. Thus, octahedral rotation or slight modifications of the stoichiometry were proposed to change the transport properties.[29,56] Ir deficiency, due to the volatility of IrO_x, can lead to an effective hole doping,[29] whereas oxygen vacancies can act as electron dopants.[31]

A recent (angle-resolved photoemission spectroscopy) study on (n MLs $SrIrO_3$/ 20 MLs $SrRuO_3$) heterostructures, which were deposited by molecular beam epitaxy on LSAT(100) substrates, indicates that even ultrathin (down to n=1) $SrIrO_3$ layers do not become insulating when they are interfaced with $SrRuO_3$.[66] It was shown that the $SrIrO_3$ layers are effectively hole doped due to electron transfer from $SrIrO_3$ to the $SrRuO_3$ layer, which was proposed as origin of the observed metallicity.[66] Thus, also the (2 MLs) ultrathin $SrIrO_3$ layer of our $SrIrO_3$/$SrRuO_3$ heterostructure might not be insulating. However, the $SrIrO_3$/$SrRuO_3$ heterostructures of the study by Nelson *et al.* were deposited on LSAT, which induces larger epitaxial strain than the growth on $SrTiO_3$(100) substrates. Since the epitaxial strain was shown to influence the details of the $SrRuO_3$ band structure[67] and therefore might also impact on the properties of the $SrRuO_3$/$SrIrO_3$ interface, similar investigations of $SrIrO_3$/$SrRuO_3$ heterostructures deposited on $SrTiO_3$(100) would be required to determine the conductivity of our 2 MLs thick $SrIrO_3$ layer interfaced with $SrRuO_3$.

Contributions

The samples were deposited and investigated by SQUID, MOKE, and Hall measurements by me. I made the corresponding analysis. The FORC study and analysis were performed by Sven Ilse from the Max-Planck Institute for Intelligent Systems in Stuttgart. The text of the paper was written by me with improvements from Dr. Ionela Lindfors-Vrejoiu, Prof. Dr. Paul H.M. van Loosdrecht, Sven Erik Ilse, Dr. Eberhard Goering, Dr. Felix Gunkel, Prof. Dr. Regina Dittmann, and Lin Yang. I thank Rene Borowski (Forschungszentrum Jülich, PGI-7) for treating the termination of the substrates.

References

[1] L. Wysocki, S. E. Ilse, L. Yang, E. Goering, F. Gunkel, R. Dittmann, P. H. van Loosdrecht, and I. Lindfors-Vrejoiu: *Magnetic interlayer coupling between ferromagnetic $SrRuO_3$ layers through a $SrIrO_3$ spacer*, Journal of Applied Physics **131**, 133902 (2022).

[2] A. K. Nandy, N. S. Kiselev, and S. Blügel: *Interlayer Exchange Coupling: A General Scheme Turning Chiral Magnets into Magnetic Multilayers Carrying Atomic-Scale Skyrmions*, Physical Review Letters **116**, 177202 (2016).

[3] C. Moreau-Luchaire, C. Moutafis, N. Reyren, J. Sampaio, C. A. Vaz, N. Van Horne, K. Bouzehouane, K. Garcia, C. Deranlot, P. Warnicke, P. Wohlhüter, J. M. George, M. Weigand, J. Raabe, V. Cros, and A. Fert: *Additive interfacial chiral interaction in multilayers for stabilization of small individual skyrmions at room temperature*, Nature Nanotechnology **11**, 444–448 (2016).

[4] S. D. Pollard, J. A. Garlow, J. Yu, Z. Wang, Y. Zhu, and H. Yang: *Observation of stable Néel skyrmions in cobalt/palladium multilayers with Lorentz transmission electron microscopy*, Nature Communications **8**, 14761 (2017).

[5] J. Matsuno, N. Ogawa, K. Yasuda, F. Kagawa, W. Koshibae, N. Nagaosa, Y. Tokura, and M. Kawasaki: *Interface-driven topological Hall effect in* $SrRuO_3$ *-* $SrIrO_3$ *bilayer*, Science Advances **2**, e1600304 (2016).

[6] Q. Qin, L. Liu, W. Lin, X. Shu, Q. Xie, Z. Lim, C. Li, S. He, G. M. Chow, and J. Chen: *Emergence of Topological Hall Effect in a* $SrRuO_3$ *Single Layer*, Advanced Materials **31**, 1807008 (2019).

[7] L. Wu, F. Wen, Y. Fu, J. H. Wilson, X. Liu, Y. Zhang, D. M. Vasiukov, M. S. Kareev, J. H. Pixley, and J. Chakhalian: *Berry phase manipulation in ultrathin* $\mathrm{SrRuO_3}$ *films*, Physical Review B **102**, 220406(R) (2020).

[8] L. Yang, L. Wysocki, J. Schöpf, L. Jin, A. Kovács, F. Gunkel, R. Dittmann, P. H. M. van Loosdrecht, and I. Lindfors-Vrejoiu: *Origin of the hump anomalies in the Hall resistance loops of ultrathin* $SrRuO_3$*/* $SrIrO_3$ *multilayers*, Physical Review Materials **5**, 014403 (2021).

[9] L. Wysocki, L. Yang, F. Gunkel, R. Dittmann, P. H. M. van Loosdrecht, and I. Lindfors-Vrejoiu: *Validity of magnetotransport detection of skyrmions in epitaxial* $SrRuO_3$ *heterostructures*, Phys. Rev. Materials **4**, 054402 (2020).

[10] Y. Ohuchi, J. Matsuno, N. Ogawa, Y. Kozuka, M. Uchida, Y. Tokura, and M. Kawasaki: *Electric-field control of anomalous and topological Hall effects in oxide bilayer thin films*, Nature Communications **9**, 213 (2018).

[11] K.-Y. Meng, A. S. Ahmed, M. Baćani, A.-O. Mandru, X. Zhao, N. Bagués, B. D. Esser, J. Flores, D. W. McComb, H. J. Hug, and F. Yang: *Observation of Nanoscale Skyrmions in* $SrIrO_3$ */* $SrRuO_3$ *Bilayers*, Nano Letters **19**, 3169–3175 (2019).

[12] D. J. Groenendijk, C. Autieri, T. C. van Thiel, W. Brzezicki, J. R. Hortensius, D. Afanasiev, N. Gauquelin, P. Barone, K. H. W. van den Bos, S. van Aert, J. Verbeeck, A. Filippetti, S. Picozzi, M. Cuoco, and A. D. Caviglia: *Berry phase engineering at oxide interfaces*, Physical Review Research **2**, 023404 (2020).

[13] L. Wysocki, J. Schöpf, M. Ziese, L. Yang, A. Kovács, L. Jin, R. B. Versteeg, A. Bliesener, F. Gunkel, L. Kornblum, R. Dittmann, P. H. M. van Loosdrecht, and I. Lindfors-Vrejoiu: *Electronic Inhomogeneity Influence on the Anomalous Hall Resistivity Loops of $SrRuO_3$ Epitaxially Interfaced with 5d Perovskites*, ACS Omega **5**, 5824–5833 (2020).

[14] D. Kan and Y. Shimakawa: *Defect-Induced Anomalous Transverse Resistivity in an Itinerant Ferromagnetic Oxide*, physica status solidi (b) **255**, 1800175 (2018).

[15] D. Kan, T. Moriyama, K. Kobayashi, and Y. Shimakawa: *Alternative to the topological interpretation of the transverse resistivity anomalies in $SrRuO_3$*, Physical Review B **98**, 180408(R) (2018).

[16] D. Kan, K. Kobayashi, and Y. Shimakawa: *Electric field induced modulation of transverse resistivity anomalies in ultrathin $SrRuO_3$ epitaxial films*, Physical Review B **101**, 144405 (2020).

[17] L. Yang, L. Jin, L. Wysocki, J. Schöpf, D. Jansen, B. Das, L. Kornblum, P. H. M. van Loosdrecht, and I. Lindfors-Vrejoiu: *Enhancing the ferromagnetic interlayer coupling between epitaxial $SrRuO_3$ layers*, Physical Review B **104**, 064444 (2021).

[18] G. Herranz, B. Martínez, J. Fontcuberta, F. Sánchez, M. V. García-Cuenca, C. Ferrater, and M. Varela: *$SrRuO_3$/ $SrTiO_3$/ $SrRuO_3$ heterostructures for magnetic tunnel junctions*, Journal of Applied Physics **93**, 8035–8037 (2003).

[19] L. Wysocki, R. Mirzaaghayev, M. Ziese, L. Yang, J. Schöpf, R. B. Versteeg, A. Bliesener, J. Engelmayer, A. Kovács, L. Jin, F. Gunkel, R. Dittmann, P. H. M. van Loosdrecht, and I. Lindfors-Vrejoiu: *Magnetic coupling of ferromagnetic $SrRuO_3$ epitaxial layers separated by ultrathin non-magnetic $SrZrO_3$/ $SrIrO_3$*, Applied Physics Letters **113**, 192402 (2018).

[20] S. Esser, J. Wu, S. Esser, R. Gruhl, A. Jesche, V. Roddatis, V. Moshnyaga, R. Pentcheva, and P. Gegenwart: *Angular dependence of Hall effect and magnetoresistance in $SrRuO_3$-$SrIrO_3$ heterostructures*, Physical Review B **103**, 214430 (2021).

[21] B. Pang, L. Zhang, Y. B. Chen, J. Zhou, S. Yao, S. Zhang, and Y. Chen: *Spin-Glass-Like Behavior and Topological Hall Effect in $SrRuO_3$/$SrIrO_3$ Superlattices for Oxide Spintronics Applications*, ACS Applied Materials and Interfaces **9**, 3201–3207 (2017).

[22] F. Groß, S. E. Ilse, G. Schütz, J. Gräfe, and E. Goering: *Interpreting first-order reversal curves beyond the Preisach model: An experimental permalloy microarray investigation*, Physical Review B **99**, 064401 (2019).

[23] F. Béron, L. Clime, M. Ciureanu, D. Menard, R. W. Cochrane, and A. Yelon: *First-order reversal curves diagrams of ferromagnetic soft nanowire arrays*, IEEE Transactions on Magnetics **42**, 3060–3062 (2006).

[24] J. Gräfe, M. Weigand, C. Stahl, N. Träger, M. Kopp, G. Schütz, E. J. Goering, F. Haering, P. Ziemann, and U. Wiedwald: *Combined first-order reversal curve and x-ray microscopy investigation of magnetization reversal mechanisms in hexagonal antidot lattices*, Physical Review B **93**, 014406 (2016).

[25] J. Gräfe, M. Weigand, N. Täger, G. Schütz, E. J. Goering, M. Skripnik, U. Nowak, F. Haering, P. Ziemann, and U. Wiedwald: *Geometric control of the magnetization reversal in antidot lattices with perpendicular magnetic anisotropy*, Physical Review B **93**, 104421 (2016).

[26] C.-I. Dobrotă and A. Stancu: *What does a first-order reversal curve diagram really mean? A study case: Array of ferromagnetic nanowires*, Journal of Applied Physics **113**, 043928 (2013).

[27] S. E. Ilse, F. Groß, G. Schütz, J. Gräfe, and E. Goering: *Understanding the interaction of soft and hard magnetic components in NdFeB with first-order reversal curves*, Physical Review B **103**, 024425 (2021).

[28] S. Muralidhar, J. Gräfe, Y.-C. Chen, M. Etter, G. Gregori, S. Ener, S. Sawatzki, K. Hono, O. Gutfleisch, H. Kronmüller, G. Schütz, and E. J. Goering: *Temperature-dependent first-order reversal curve measurements on unusually hard magnetic low-temperature phase of MnBi*, Physical Review B **95**, 024413 (2017).

[29] W. Guo, D. X. Ji, Z. B. Gu, J. Zhou, Y. F. Nie, and X. Q. Pan: *Engineering of octahedral rotations and electronic structure in ultrathin* $SrIrO_3$ *films*, Physical Review B **101**, 085101 (2020).

[30] D. J. Groenendijk, C. Autieri, J. Girovsky, M. C. Martinez-Velarte, N. Manca, G. Mattoni, A. M. R. V. L. Monteiro, N. Gauquelin, J. Verbeeck, A. F. Otte, M. Gabay, S. Picozzi, and A. D. Caviglia: *Spin-Orbit Semimetal* $SrIrO_3$ *in the Two-Dimensional Limit*, Physical Review Letters **119**, 256403 (2017).

[31] N. Manca, D. J. Groenendijk, I. Pallecchi, C. Autieri, L. M. K. Tang, F. Telesio, G. Mattoni, A. McCollam, S. Picozzi, and A. D. Caviglia: *Balanced electron-hole transport in spin-orbit semimetal* $SrIrO_3$ *heterostructures*, Physical Review B **97**, 081105(R) (2018).

[32] A. Biswas, K.-S. Kim, and Y. H. Jeong: *Metal insulator transitions in perovskite* $SrIrO_3$ *thin films*, Journal of Applied Physics **116**, 213704 (2014).

[33] B. Kim, P. Liu, and C. Franchini: *Dimensionality-strain phase diagram of strontium iridates*, Physical Review B **95**, 115111 (2017).

[34] J. H. Gruenewald, J. Nichols, J. Terzic, G. Cao, J. W. Brill, and S. S. A. Seo: *Compressive strain-induced metal–insulator transition in orthorhombic* $SrIrO_3$ *thin films*, Journal of Materials Research **29**, 2491–2496 (2014).

[35] J. Xia, W. Siemons, G. Koster, M. R. Beasley, and A. Kapitulnik: *Critical thickness for itinerant ferromagnetism in ultrathin films of* $SrRuO_3$, Physical Review B **79**, 140407(R) (2009).

[36] J. Choi, C. B. Eom, G. Rijnders, H. Rogalla, and D. H. A. Blank: *Growth mode transition from layer by layer to step flow during the growth of heteroepitaxial* $SrRuO_3$ *on (001)* $SrTiO_3$, Applied Physics Letters **79**, 1447–1449 (2001).

[37] J. Gräfe, F. Groß, S. E. Ilse, D. B. Boltje, S. Muralidhar, and E. J. Goering: *LeXtender: a software package for advanced MOKE acquisition and analysis*, Measurement Science and Technology **32**, 067002 (2021).

[38] F. Groß, J. C. Martínez-García, S. E. Ilse, G. Schütz, E. Goering, M. Rivas, and J. Gräfe: *GFORC: A graphics processing unit accelerated first-order reversal-curve calculator*, Journal of Applied Physics **126**, 163901 (2019).

[39] W. Wang, L. Li, J. Liu, B. Chen, Y. Ji, J. Wang, G. Cheng, Y. Lu, G. Rijnders, G. Koster, W. Wu, and Z. Liao: *Magnetic domain engineering in* $SrRuO_3$ *thin films*, npj Quantum Materials **5**, 73 (2020).

[40] P. A. A. van der Heijden, P. J. H. Bloemen, J. M. Metselaar, R. M. Wolf, J. M. Gaines, J. T. W. M. van Eemeren, P. van der Zaag, and W. J. M. de Jonge: *Interlayer coupling between* Fe_3O_4 *layers separated by an insulating nonmagnetic MgO layer*, Physical Review B **55**, 11569 (1997).

[41] J. Faure-Vincent, C. Tiusan, C. Bellouard, E. Popova, M. Hehn, F. Montaigne, and A. Schuhl: *Interlayer Magnetic Coupling Interactions of Two Ferromagnetic Layers by Spin Polarized Tunneling*, Physical Review Letters **89**, 107206 (2002).

[42] M. Matczak, B. Szymański, M. Urbaniak, M. Nowicki, H. Głowiński, P. Kuświk, M. Schmidt, J. Aleksiejew, J. Dubowik, and F. Stobiecki: *Antiferromagnetic magnetostatic coupling in Co/Au/Co films with perpendicular anisotropy*, Journal of Applied Physics **114**, 093911 (2013).

[43] S. M. Mohseni, R. K. Dumas, Y. Fang, J. W. Lau, S. R. Sani, J. Persson, and J. Åkerman: *Temperature-dependent interlayer coupling in Ni/Co perpendicular pseudo-spin-valve structures*, Physical Review B **84**, 174432 (2011).

[44] J. Gräfe, M. Schmidt, P. Audehm, G. Schütz, and E. Goering: *Application of magneto-optical Kerr effect to first-order reversal curve measurements*, Review of Scientific Instruments **85**, 023901 (2014).

[45] D. B. Fulghum and R. E. Camley: *Magnetic behavior of antiferromagnetically coupled layers connected by ferromagnetic pinholes*, Physical Review B **52**, 13436 (1995).

[46] L. Néel: *Sur un probleme de magnetostatique relatif a des couches minces ferromagnetiques*, Comptes Rendus Hebdomadaires Des Seances De L Academie Des Sciences **255**, 1545–1550 (1962).

[47] J. Moritz, F. Garcia, J. C. Toussaint, B. Dieny, and J. P. Nozières: *Orange peel coupling in multilayers with perpendicular magnetic anisotropy: Application to (Co/Pt)-based exchange-biased spin-valves*, Europhysics Letters **65**, 123 (2004).

[48] B. D. Schrag, A. Anguelouch, G. Xiao, P. Trouilloud, Y. Lu, W. J. Gallagher, and S. S. Parkin: *Magnetization reversal and interlayer coupling in magnetic tunneling junctions*, Journal of Applied Physics **87**, 4682–4684 (2000).

[49] H. W. Fuller and D. L. Sullivan: *Magnetostatic interactions between thin magnetic films*, Journal of Applied Physics **33**, 1063–1064 (1962).

[50] L. Thomas, M. G. Samant, and S. S. Parkin: *Domain-wall induced coupling between ferromagnetic layers*, Physical Review Letters **84**, 1816 (2000).

[51] C. L. Platt, M. R. McCartney, F. T. Parker, and A. E. Berkowitz: *Magnetic interlayer coupling in ferromagnet/insulator/ferromagnet structures*, Physical Review B **61**, 9633 (2000).

[52] V. Baltz, A. Marty, B. Rodmacq, and B. Dieny: *Magnetic domain replication in interacting bilayers with out-of-plane anisotropy: Application to Co/Pt multilayers*, Physical Review B **75**, 014406 (2007).

[53] J. C. Slonczewski: *Conductance and exchange coupling of two ferromagnets separated by a tunneling barrier*, Physical Review B **39**, 6995 (1989).

[54] P. Bruno: *Theory of interlayer magnetic coupling*, Physical Review B **52**, 411 (1995).

[55] J. F. Bobo, H. Kikuchi, O. Redon, E. Snoeck, M. Piecuch, and R. L. White: *Pinholes in antiferromagnetically coupled multilayers: Effects on hysteresis loops and relation to biquadratic exchange*, Physical Review B **60**, 4131 (1999).

[56] Y. F. Nie, P. D. C. King, C. H. Kim, M. Uchida, H. I. Wei, B. D. Faeth, J. P. Ruf, J. P. C. Ruff, L. Xie, X. Pan, C. J. Fennie, D. G. Schlom, and K. M. Shen: *Interplay of Spin-Orbit Interactions, Dimensionality, and Octahedral Rotations in Semimetallic* $SrIrO_3$, Physical Review Letters **114**, 016401 (2015).

[57] M. Ziese, I. Vrejoiu, and D. Hesse: *Structural symmetry and magnetocrystalline anisotropy of $SrRuO_3$ films on $SrTiO_3$*, Physical Review B **81**, 184418 (2010).

[58] A. V. Davydenko, E. V. Pustovalo, A. V. Ognev, A. G. Kozlov, L. A. Chetbotkevich, and X. F. Han: *Néel coupling in Co/Cu/Co stripes with unidirectional interface roughness*, Journal of Magnetism and Magnetic Materials **377**, 334–342 (2015).

[59] B. D. Schrag, A. Anguelouch, S. Ingvarsson, G. Xiao, Y. Lu, P. L. Trouilloud, A. Gupta, R. A. Wanner, W. J. Gallagher, P. M. Rice, and S. S. P. Parkin: *Néel "orange-peel" coupling in magnetic tunneling junction devices*, Applied Physics Letters **77**, 2373 (2000).

[60] L. E. Nistor: "Magnetic tunnel junctions with perpendicular magnetization: Anisotropy, magnetoresistance, magnetic coupling and spin transfer torque switching", PhD Thesis (Universite de Grenoble, 2011).

[61] B. Rodmacq, V. Baltz, and B. Dieny: *Macroscopic probing of domain configurations in interacting bilayers with perpendicular magnetic anisotropy*, Physical Review B **73**, 092405 (2006).

[62] E. Skoropata, J. Nichols, J. M. Ok, R. V. Chopdekar, E. S. Choi, A. Rastogi, C. Sohn, X. Gao, S. Yoon, T. Farmer, R. D. Desautels, Y. Choi, D. Haskel, J. W. Freeland, S. Okamoto, M. Brahlek, and H. N. Lee: *Interfacial tuning of chiral magnetic interactions for large topological Hall effects in $LaMnO_3/SrIrO_3$ heterostructures*, Science Advances **6**, eaaz3902 (2020).

[63] E. M. Pugh and N. Rostoker: *Hall Effect in Ferromagnetic Materials*, Reviews of Modern Physics **25**, 151 (1953).

[64] T. C. van Thiel, D. J. Groenendijk, and A. D. Caviglia: *Extraordinary Hall balance in ultrathin $SrRuO_3$ bilayers*, J. Phys.: Materials **3**, 025005 (2020).

[65] D. J. Groenendijk, N. Manca, J. D. Bruijckere, A. M. R. V. L. Monteiro, R. Gaudenzi, H. S. J. van der Zant, and A. D. Caviglia: *Anisotropic magnetoresistance in spin–orbit semimetal $SrIrO_3$*, The European Physical Journal Plus **135**, 627 (2020).

[66] J. N. Nelson, N. J. Schreiber, A. B. Georgescu, B. H. Goodge, B. D. Faeth, C. T. Parzyck, C. Zeledon, L. F. Kourkoutis, A. J. Millis, A. Georges, D. G. Schlom, and K. M. Shen: *Interfacial charge transfer and persistent metallicity of ultrathin $SrIrO_3/SrRuO_3$ heterostructures*, Science Advances **8**, eabj0481 (2022).

[67] D. Tian, Z. Liu, S. Shen, Z. Li, Y. Zhou, H. Liu, H. Chen, and P. Yu: *Manipulating Berry curvature of $SrRuO_3$ thin films via epitaxial strain*, Proceedings of the National Academy of Sciences **118**, e2101946118 (2021).

Chapter 6

Validity of magnetotransport detection of skyrmions in epitaxial $SrRuO_3$ heterostructures

Contents

The main results of this chapter are published in the manuscript:
Lena Wysocki, Lin Yang, Felix Gunkel, Regina Dittmann, Paul H. M. van Loosdrecht, and Ionela Lindfors-Vrejoiu: *Validity of magnetotransport detection of skyrmions in epitaxial $SrRuO_3$ heterostructures*, Phys. Rev. Materials **4**, 054402 (2020) (named as Ref. [1]). Figures that are reproduced or adapted are indicated in the respective captions.

6.1 Introduction

In order to prove the existence of magnetic skyrmions, real space imaging of the magnetic texture with high spatial resolution is needed. However, the real space investigations of these, typically tiny, magnetic structures are technically challenging and limited by experimental means. While magnetic force microscopy is sensitive only to the out-of-plane component of the sample's magnetic stray field and its spatial resolution is limited to typically 20 nm,[2–4] the specimen preparation required for electron holography or Lorentz transmission electron microscopy is complex.[5] Due to their sensitivity to damage by the electron or ion beam, the specimen preparation for TEM investigations of heterostructures that contain $SrRuO_3$ layers is even more challenging.

An experimentally simple technique to investigate the fingerprint of magnetic skyrmions, which is available in many laboratories, is the measurement of Hall voltage loops. In presence of magnetic skyrmions, the conduction electrons get deflected by the emergent magnetic field generated by the skyrmions.[6] This leads to the topological Hall effect, which is observed additionally to the ordinary (OHE) and anomalous Hall effect (AHE).[6]

The observation of Hall features that resemble a topological Hall effect in $SrRuO_3$-$SrIrO_3$ bilayers[2] motivated intense research activity on $SrRuO_3$ thin films and $SrRuO_3$-based heterostructures.[3,7–12] Only rarely supported by additional MFM studies,[3] similar hump-like anomalies were seen in the Hall resistivity loops of $SrRuO_3$-based thin films and were taken as proof of the existence of skyrmions.[2,3,8,9] Also the Hall resistivity hysteresis loops of ultrathin bare $SrRuO_3$ films after the post-deposition implantation of hydrogen ions[13] or the deposition in low oxygen pressure[10] showed such THE-like features. However, alternative models aiming to explain the unconventional features were proposed, disregarding the formation of skyrmions.[11,12,14–16] Within the suggested model of multiple (Hall) conduction channels, the peak-like anomalies were attributed to sample inhomogeneities and heterogenous transport.[11,12] Since the anomalous Hall effect in $SrRuO_3$ is dominated by the intrinsic contribution and hence determined by the Berry curvature of the band structure,[12,17,18] it was proposed that multiple AHE channels can be induced in $SrRuO_3$ thin films and heterostructures due to inhomogeneities within the $SrRuO_3$ films or the interfacial environment.[14–16]

In the present study, it is demonstrated that peculiar anomalies can be generated in Hall voltage hysteresis loops of $SrRuO_3$-based heterostructures in the absence of magnetic skyrmions. The investigated heterostructures are composed of two ferromagnetic, metallic $SrRuO_3$ layers of distinct thicknesses in order to generate measurably different switching fields, magnetic moments, and anomalous Hall constants. The layers with perpendicular magnetic anisotropy were magnetically basically decoupled by insulating $SrIrO_3$ and/or $SrZrO_3$ spacers (cf. Chapter 5) and electrically connected in parallel. Such heterostructure is a suitable system to investigate the phenomena of two anomalous Hall effect channels. Moreover, the study points out that the Hall effect investigations can yield misleading results and hump-like Hall features should not be considered as a proof of the formation of skyrmions.

6.2 Sample design and structural properties

The heterostructures under study are composed of two $SrRuO_3$ layers of significantly distinct thicknesses which are separated and capped by non-magnetic layers of $SrIrO_3$ or insulating $SrZrO_3$, as schematically shown in Fig. 6.1 (a). The thicknesses of the bottom and top $SrRuO_3$ layers were selected to be 18 monolayers (MLs) and 6 MLs, respectively. The thickness of the bottom $SrRuO_3$ layer is in the range where orthorhombic structure is stabilized at room temperature, but coherent structure is preserved without strain relaxation.[19] Based on previous reports on $SrRuO_3$ epitaxial thin films, both $SrRuO_3$ layers should show ferromagnetic ordering below the respective Curie temperature.[20,21] However, due to the thickness reduction, the transition temperature of the 6 MLs thick $SrRuO_3$ layer is expected to be lowered to approximately 100 K.[20,21] Furthermore, thickness-related, considerable variations of the temperature dependencies of the switching fields, magnetization[20,22] as well as of the temperature dependence of the anomalous Hall constant[21] are anticipated.

The two $SrRuO_3$ layers are separated by 2 MLs $SrIrO_3$ and/or 2 MLs $SrZrO_3$ to achieve effectively magnetic decoupling of the ferromagnetic conduction channels, which was confirmed by the FORC and SQUID magnetometry study presented in Chapter 5 and study [22].

Furthermore, only the thinner $SrRuO_3$ layer is in a range of thickness where interfacial DMI was proposed to be sufficiently strong to generate skyrmions.[2]

The substitution of $SrIrO_3$ by the large band gap insulator $SrZrO_3$ enabled the investigation of the influence of the strong spin-orbit coupling of $SrIrO_3$ at the $SrIrO_3/SrRuO_3$ interfaces.

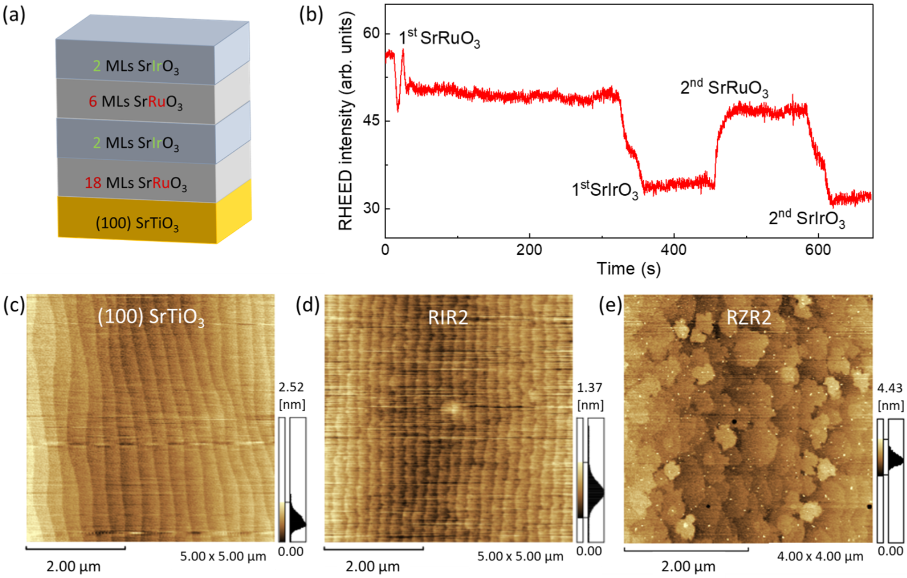

Figure 6.1: (a) Scheme of heterostructure RIR2, which is composed of a 18 MLs thick bottom $SrRuO_3$ layer and a 6 MLs thick top $SrRuO_3$ layer, separated and capped with 2 MLs thick $SrIrO_3$, deposited on $SrTiO_3$(100). (b) Time dependence of the integrated RHEED intensity of the specular spot during the deposition of the heterostructure RIR2. Atomic force microscopy images (4 - 5 µm x 4 - 5 µm) of one $SrTiO_3$(100) substrate after wet-etching and annealing (c), of the heterostructure RIR2 with 2 MLs $SrIrO_3$ spacer and capping layers (d), and of the heterostructure RZR2 with 2 MLs $SrZrO_3$ spacer and capping layers (e). Figures adapted from Ref. [1]. Adapted with permission from the American Physical Society.

While previous experiments proposed the emergence of strong interfacial DMI at the $SrIrO_3/SrRuO_3$ interface,[2] a possible DMI at the $SrZrO_3/SrRuO_3$ is expected to be negligible. In addition, a $SrIrO_3/SrRuO_3/SrIrO_3$ trilayer with 6 MLs $SrRuO_3$ was studied as a reference sample. All investigated heterostructures summarized in Table 6.1 were grown by pulsed-laser deposition on low miscut vicinal, TiO_2-terminated, single crystalline $SrTiO_3$(100) substrates. The $SrIrO_3$ and $SrZrO_3$ layers grew in a layer-by-layer growth mode, characterized by the oscillatory time trace of the integrated RHEED intensity, as exemplarily shown in Fig. 6.1 (b) for heterostructure RIR2. This enabled the precise determination of the spacer and capping layers thicknesses.

Sample name	Composition
RIR2	18 MLs SRO /2 MLs SIO / 6 MLs SRO /2 MLs SIO
RZR2	18 MLs SRO /2 MLs SZO / 6 MLs SRO /2 MLs SZO
RIZR2	18 MLs SRO /2 MLs SIO / 2 MLs SZO / 6 MLs SRO /2 MLs SIO / 2 MLs SZO
IRI	2 MLs SIO / 6 MLs SRO /2 MLs SIO

Table 6.1: Name and composition of the heterostructures under study

The $SrRuO_3$ layers of the heterostructures under study grew in the step-flow growth mode, which has been found to be preferred to generate smooth, homogeneously flat epitaxial $SrRuO_3$ layers.[23]

The surface of the heterostructures was imaged by atomic force microscopy. As shown in Fig. 6.1 (d), the surface morphology of heterostructure RIR2 is homogeneously flat and preserves the step-terrace-like structure of the $SrTiO_3$ substrate presented in Fig. 6.1 (c). The surface of the multilayer RZR2, with 2 MLs $SrZrO_3$ as spacer and capping layers, has an increased defect density (see Fig. 6.1 (e)), which is most likely related to the larger compressive strain due to the increased lattice mismatch between $SrZrO_3$ and the substrate.

6.3 Experimental methods

The Hall effect measurements were performed in the van der Pauw configuration with our home-built set-up,[24,25] which enabled the simultaneous investigation of the Hall voltage and the magneto-optical Kerr effect (MOKE) in polar geometry. For all shown Hall and polar MOKE experiments, the magnetic field was applied perpendicular to the sample surface.

The minimization of optical artifacts in the polar MOKE measurements was achieved by the individual selection of the wavelength of the incoherent light source for each heterostructure. For the MOKE study of the heterostructure RIR2, incoherent light of 540 nm wavelength was utilized and 590 nm for the sample RZR2.

In case of sample RIR2, polar MOKE measurements of a bare $SrTiO_3$ substrate were acquired and subtracted additionally in order to reduce the substrate-related background contribution.

One aim of this study was to investigate the individual contributions of the two ferromagnetic layers to the heterostructure total magnetic moment as well as to the total anomalous Hall effect. Due to the direct proportionality of the (polar) magneto-optical Kerr rotation angle to the perpendicular component of the magnetization, MOKE studies are often used to determine the magnetic properties of thin films. However, in case of multilayers with ferromagnetic layers with different properties and/or thicknesses, the proportionality constants of the different layers are expected to vary.[25]

Thus, the magnetic characteristics of the heterostructures were determined directly by SQUID magnetometry with the SQUID magnetometer MPMS-XL (Quantum Design inc.) and compared to the Hall hysteresis loops. The magnetic measurements were corrected following the procedure described in Chapter 3.

6.4 Magnetic and magnetotransport studies of a heterostructure with 2 MLs $SrIrO_3$ spacer

6.4.1 Magnetic properties

To confirm that the two $SrRuO_3$ layers of the heterostructure show indeed distinct switching fields, temperature and magnetic field dependent polar MOKE and SQUID magnetometry measurements were performed.

Since the polar Kerr rotation angle of the heterostructure is determined by the sum of the p-MOKE contributions of the two individual $SrRuO_3$ layers, which are proportional to the out-of-plane component of the magnetization of the respective $SrRuO_3$ layer, the MOKE study can indicate the existence of distinct switching fields. As depicted in Fig. 6.2, the MOKE hysteresis loops show a double-step-like switching behavior[1] in a broad temperature range below 110 K. Only at 20 K, the p-MOKE loop shows a single-step reversal due to the equality of the switching fields of the two $SrRuO_3$ layers at this particular temperature.

The observed two-step switching behavior of the MOKE hysteresis loops originates from the different temperature dependencies of the switching fields and domain nucleation fields of the basically decoupled $SrRuO_3$ layers, as it was investigated in detail in Chapter 5 of this thesis.

---

[1] Due to the imperfection of the background correction, a slight artificial curvature remains in the polar MOKE hysteresis loops at high magnetic fields.

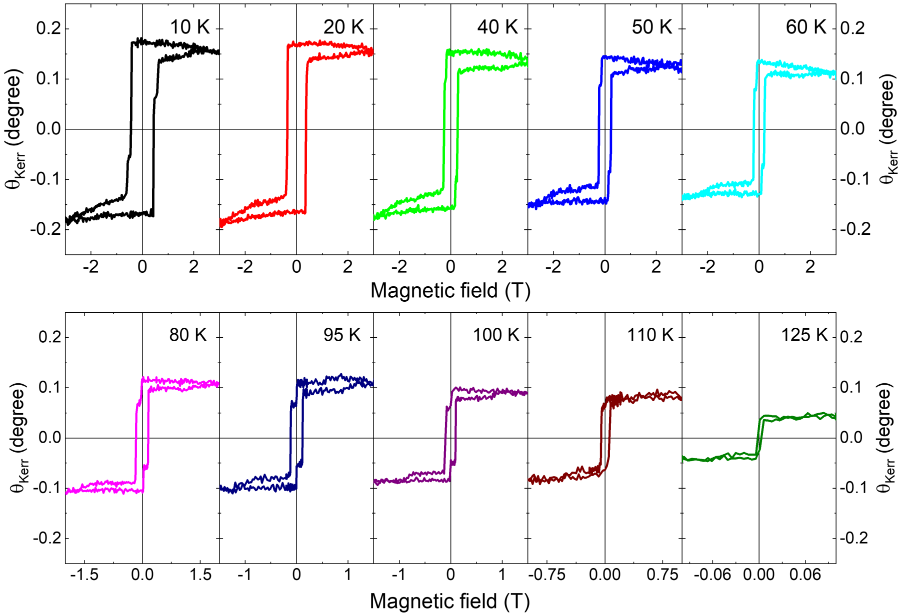

Figure 6.2: Kerr rotation angle of heterostructure RIR2 with 2 MLs $SrIrO_3$ spacer and capping layers, plotted as a function of the external magnetic field, applied perpendicular to the film surface, at selected temperatures. The measurements were performed with incoherent light of 540 nm. Reprinted figure with permission from: L. Wysocki, L. Yang, F. Gunkel, R. Dittmann, P. H. M. van Loosdrecht, and I. Lindfors-Vrejoiu, Phys. Rev. Materials **4**, 054402 (2020), Copyright (2020) by the American Physical Society.

The magnetic field dependence of the magnetic moment was confirmed by SQUID magnetometry at selected temperatures.

Exemplarily depicted in Fig. 6.3 are the hysteresis loops at 10 K (a) and 80 K (b). Due to the thickness-dependence of the magnetic moment of $SrRuO_3$ thin films, the two steps of distinct height in the magnetic hysteresis loops can be attributed to the switching of the two magnetic layers. From the relative magnitude of the magnetization in saturation it can be concluded that the 18 MLs thick layer has a smaller switching field than the 6 MLs layer at low temperatures, such as 10 K (Fig. 6.3 (a)). In contrast, the thin $SrRuO_3$ layer reverses the direction of its magnetization at smaller fields than the 18 MLs $SrRuO_3$ layer at higher temperatures (see Fig. 6.3 (b) for the measurement at 80 K).

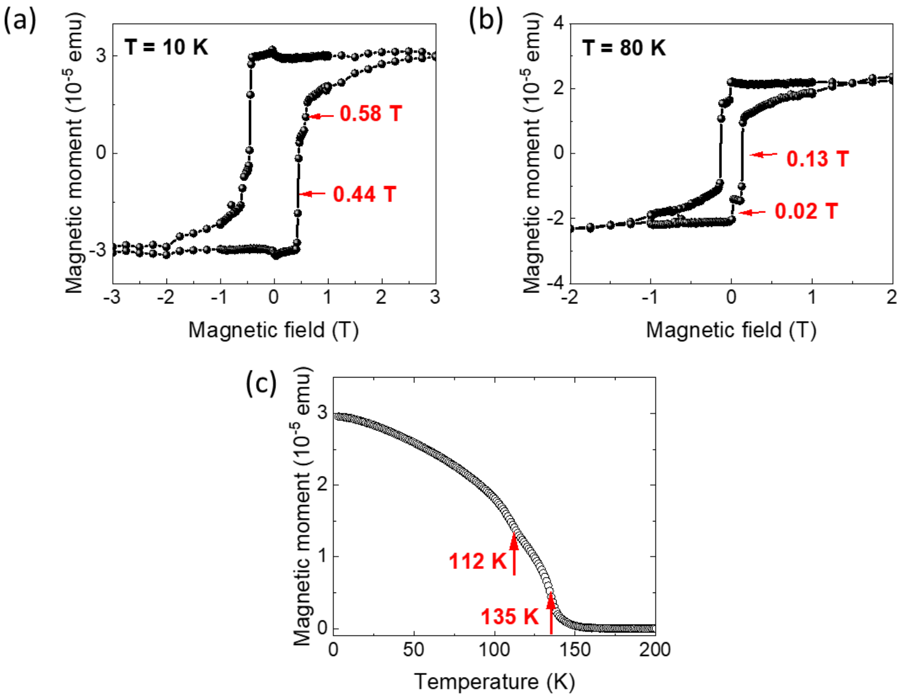

Figure 6.3: SQUID magnetometry of the heterostructure RIR2: Magnetic field dependence of the magnetic moment at 10 K (a) and 80 K (b). (c) Magnetic moment plotted as function of temperature during the warming up in presence of 0.1 T external magnetic field after field cooling (0.1 T); The transition temperatures and the switching fields of the two $SrRuO_3$ layers are highlighted in red. The magnetic field was applied perpendicular to the thin film surface. Figures adapted from Ref. [1]. Adapted with permission from the American Physical Society.

As illustrated in Fig. 6.3 (c), the temperature dependence of the magnetic moment (during warming up in 0.1 T after field cooling) shows the existence of two ferromagnetic transition temperatures. The transition at 135 K originates from the 18 MLs thick $SrRuO_3$ layer, whereas the one at T_C= 112 K is related to the 6 MLs $SrRuO_3$ layer. The difference between the two ferromagnetic transition temperatures as well as a double-step magnetization reversal indicate that the magnetic coupling of the two $SrRuO_3$ is very weak, as intensively studied in Chapter 5. Also the $SrRuO_3$ layers of the heterostructure RIZR2 are basically magnetically decoupled, as we confirmed previously.[22]

Thus, these heterostructures are suitable candidates to investigate the effect of two magnetically decoupled, but electrically (parallel) connected channels which contribute to the total anomalous Hall effect.

6.4.2 Magnetotransport

If the conducting system is composed of two channels with Hall conductances $\sigma_{\mathrm{xy}}^{\mathrm{a}}$ and $\sigma_{\mathrm{xy}}^{\mathrm{b}}$, the total Hall conductance is given by:[26]

$$\sigma_{\mathrm{xy}}^{\mathrm{tot}} = \sigma_{\mathrm{xy}}^{\mathrm{a}} + \sigma_{\mathrm{xy}}^{\mathrm{b}} \tag{6.1}$$

Since the resistivity tensor $\widehat{\rho}$ is the inverse of the conductivity tensor $\widehat{\sigma}$, under the assumption that $\rho_{\mathrm{xx}} = \rho_{\mathrm{yy}}$ and $\rho_{\mathrm{yx}} = -\rho_{\mathrm{xy}}$, the Hall resistivity ρ_{xy} can be written as:

$$\rho_{\mathrm{xy}} = \frac{-\sigma_{\mathrm{xy}}}{\sigma_{\mathrm{xx}}^2 + \sigma_{\mathrm{xy}}^2} \tag{6.2}$$

and

$$\rho_{\mathrm{xx}} = \frac{\sigma_{\mathrm{xx}}}{\sigma_{\mathrm{xx}}^2 + \sigma_{\mathrm{xy}}^2} \tag{6.3}$$

When the Hall conductivity σ_{xy} is much smaller than the longitudinal conductivity σ_{xx}, Equations (6.3) and (6.2), can be approximated as:

$$\rho_{\mathrm{xx}} \approx \frac{1}{\sigma_{\mathrm{xx}}} \tag{6.4}$$

and

$$\rho_{\mathrm{xy}} \approx \frac{\sigma_{\mathrm{xy}}}{\sigma_{\mathrm{xx}}^2} = \sigma_{\mathrm{xy}} \rho_{\mathrm{xx}}^2 \tag{6.5}$$

In a parallel circuit with the two resistances $R_{\mathrm{xx^a}}$ and $R_{\mathrm{xx^b}}$, the total resistance is given by:

$$R_{\mathrm{xx^{total}}} = \frac{R_{\mathrm{xx^a}} R_{\mathrm{xx^b}}}{R_{\mathrm{xx^a}} + R_{\mathrm{xx^b}}} \tag{6.6}$$

Combining Equations (6.1), (6.6), and (6.5) it can be shown that the total Hall voltages of two magnetically decoupled, electrically parallel connected layers sum up in this specific case.[26–29]

Depicted in Fig. 6.4 are the total Hall voltage V_{xy} hysteresis loops of the heterostructure RIR2, which were measured with the magnetic field applied parallel to the film normal. The Hall voltage loops of this multilayer possess an unconventional shape in a broad temperature range.

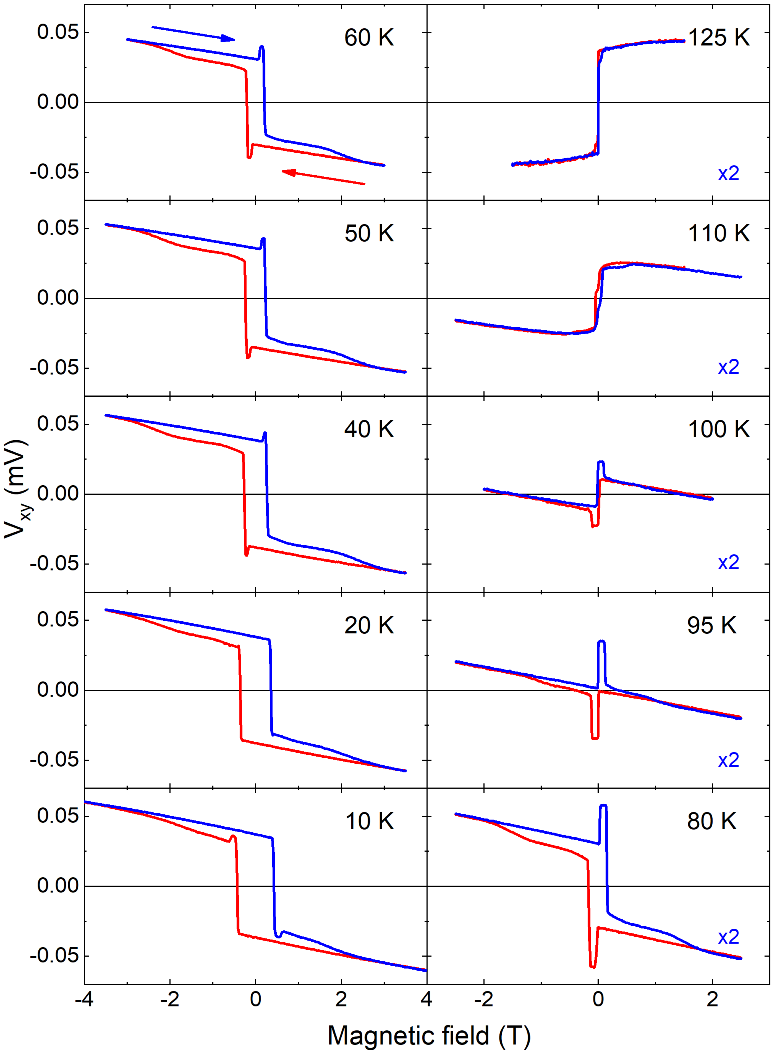

Figure 6.4: Total Hall voltage V_{xy} of the heterostructure RIR2 plotted as a function of the applied magnetic field at selected temperatures. The magnetic field was applied perpendicular to the thin film surface. The blue (red) part of the hysteresis loops was measured during the sweeping of the magnetic field from negative to positive (positive to negative) values, as indicated by the arrows in the top left panel (60 K loop). Reprinted figure with permission from: L. Wysocki, L. Yang, F. Gunkel, R. Dittmann, P. H. M. van Loosdrecht, and I. Lindfors-Vrejoiu, Phys. Rev. Materials **4**, 054402 (2020), Copyright 2020 by the American Physical Society.

Below 110 K, when both $SrRuO_3$ layers are in the ferromagnetic phase, hump-like anomalies are observed in the Hall voltage loops. These resemble the THE-like features that were seen in $SrRuO_3/SrIrO_3$ bilayers and attributed either to multiple AHE conduction channels[12] or to the formation of skyrmions.[2,3] The anomalies are peak-like between 40 K and 60 K and possess a more extended plateau-like shape between 80 K and 100 K. The Hall voltage loop at 10 K shows dips in the magnetic field range where the 18 MLs $SrRuO_3$ layer, which is the magnetically softer layer below 20 K, switches its magnetization (cf. also Fig. 6.3 (a)). To improve the comparability of the magnetic field dependence of the magnetization and the Hall voltage, the ordinary Hall voltage was subtracted by linear fitting in the high magnetic field regime for all Hall loops presented subsequently.

As displayed in Fig. 6.5, the anomalies in the Hall voltage loops build up in the magnetic field range in which the orientation of the magnetization of the ferromagnetic layer with smaller coercive field is reversed. The corresponding magnetic field range is marked by dashed green lines in Fig. 6.5.

When the thin $SrRuO_3$ layer has a lower coercive field than the 18 MLs $SrRuO_3$ layer, such as for example at 80 K (see top panel of Fig. 6.5), the anomalies have their maximum in the magnetic field range where both $SrRuO_3$ layers are magnetically saturated, but with opposite orientations. Thus, the THE-like features cannot be attributed to magnetic domains that are created during the magnetization reversal of the 6 MLs thin $SrRuO_3$ layer. This indicates that skyrmions most likely do not form in the 6 MLs $SrRuO_3$ layer, which is sandwiched between $SrIrO_3$, during the magnetic field sweep.

In contrast, the agreement of the magnetic field ranges is an indication that the THE-like anomalies are correlated with the presence of subsystems in the heterostructure which have different magnetic and magnetotransport properties, such as distinct magnitude and sign of the anomalous Hall constants as well as different switching fields.

In the absence of topologically non-trivial structures, a topological Hall effect is not expected so that the difference of the total Hall voltage V_{xy} and the ordinary Hall voltage V_{OHE} corresponds to the total anomalous Hall voltage V_{AHE} of the heterostructure. In homogeneous ferromagnets, the total anomalous Hall voltage V_{AHE} is proportional to the out-of-plane component of the overall measured sample magnetization $M_{\perp}$.[31,32] However, in case of a heterogeneous system that is composed of decoupled, distinct (magnetic) subsystems, this empirical relation needs to be modified.

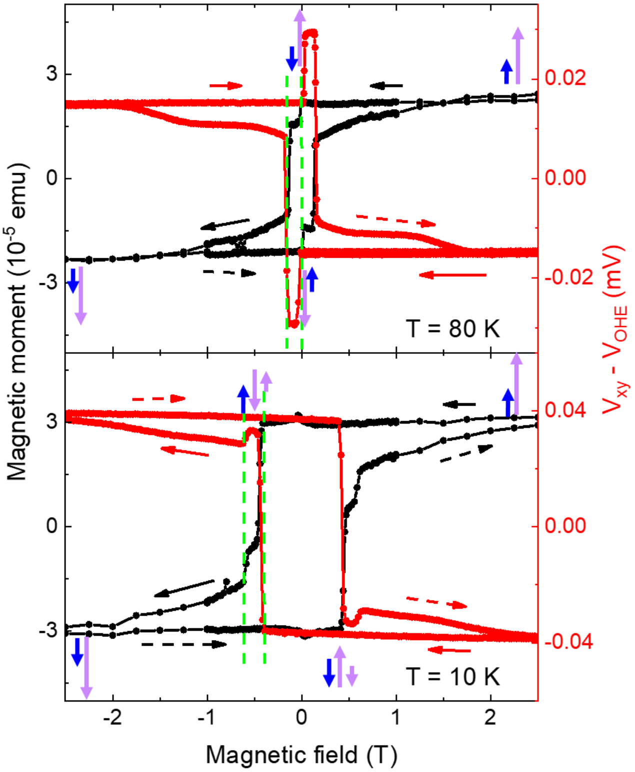

Figure 6.5: Magnetic field dependence of the magnetic moment (black) and Hall voltage loops (after subtraction of the ordinary Hall effect contribution, shown in red) of the RIR2 heterostructure at 10 K (lower panel) and at 80 K (upper panel). The magnetic hysteresis loops were acquired by SQUID magnetometry. The horizontal arrows guide the reader through the Hall voltage (red) and magnetic moment (black) hysteresis loops. Indicated by the vertical arrows are the orientations of the out-of-plane magnetization components of the 18 MLs (purple arrows) and 6 MLs (blue arrows) thick $SrRuO_3$ layers during the magnetic field sweep. The small purple arrows illustrate the tail observed in the hysteresis loops, which likely originates from pinned domains in the bottom $SrRuO_3$ layer.[30] Reprinted figure with permission from: L. Wysocki, L. Yang, F. Gunkel, R. Dittmann, P. H. M. van Loosdrecht, and I. Lindfors-Vrejoiu, Phys. Rev. Materials **4**, 054402 (2020), Copyright 2020 by the American Physical Society.

If the subsystems are electrically coupled, the measured AHE voltage is the sum of the contributions of each subsystem, which have most likely distinct temperature dependencies of the magnitude and sign of the anomalous Hall constant R_{AH}.

With the two-channels AHE model, as proposed by Zhang *et al.*[28] and Gerber,[29] the shape and the temperature range in which the hump-like anomalies are observed in the Hall voltage loops can be explained. The prerequisites of their model, which are the magnetic decoupling and the parallel electrical connection of the two ferromagnetic, metallic layers, are fulfilled in the case of the heterostructure RIR2. The magnetic decoupling was achieved by the separation of the $SrRuO_3$ layers by the $SrIrO_3$ spacer layer (cf. Chapter 5). Since signatures of both ferromagnetic layers were seen in the Hall voltage hysteresis loops, the layers have to be electrically connected, which is probably originating from the pulsed-laser deposition, in which the size of the plasma plume is larger than the lateral extension of the substrate so that material is grown also on the sample edges.

The performance of minor loop studies, as described in detail in Chapter 5, enabled to disentangle the contributions of the individual ferromagnetic $SrRuO_3$ layers to the total anomalous Hall voltage of the entire heterostructure.

Presented in Fig. 6.6 are the minor loops of the magnetic moment (black) and the Hall voltage (red), after subtraction of the ordinary Hall effect, at 10 K and 50 K.

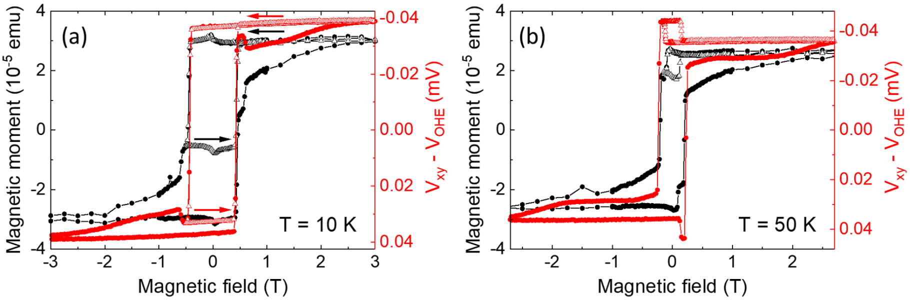

Figure 6.6: Full (solid symbols) and minor loops (open symbols) of the Hall voltage (after the subtraction of the ordinary Hall contribution, shown in red, scale inverted) and the magnetic moment (black) at 10 K (a) and 50 K (b) for the heterostructure RIR2. The magnetic field was applied perpendicular to the thin film surface. For the sake of comparison to the magnetic moment hysteresis loop, the sign of the Hall voltage values is inverted. Reprinted figure with permission from: L. Wysocki, L. Yang, F. Gunkel, R. Dittmann, P. H. M. van Loosdrecht, and I. Lindfors-Vrejoiu, Phys. Rev. Materials **4**, 054402 (2020), Copyright 2020 by the American Physical Society.

The minor loop studies shed light on the magnetization reversal behavior of the $SrRuO_3$ layer with smaller switching field and in this way also on the changes of the anomalous Hall voltage during the minor loop field sweep. At 50 K (Fig. 6.6 (b)), the 6 MLs $SrRuO_3$ is the magnetically softer layer of the heterostructure so that the minor loop represents the magnetic switching behavior of the thinner $SrRuO_3$ layer. Since the Hall voltage minor loop and the magnetic moment minor loop have the same sign[2], it can be concluded that the anomalous Hall constant of the 6 MLs thin $SrRuO_3$ layer is positive at 50 K. In contrast, the larger contribution to the total anomalous Hall voltage loop, which originates from the 18 MLs thick $SrRuO_3$ layer, is negative. Below 20 K, the 18 MLs bottom $SrRuO_3$ has smaller switching fields than the top $SrRuO_3$ layer and thus can be characterized by minor loops. As shown in Fig. 6.6 (a), the Hall voltage minor loop and therefore the anomalous Hall constant of the thicker $SrRuO_3$ layer has a negative sign also at 10 K. This indicates that the anomalous Hall constant of the 18 MLs thick $SrRuO_3$ layer has a negative sign between 50 K to 10 K, which is in good agreement with previous studies on thick $SrRuO_3$ films.[21]

In order to achieve a qualitative understanding of the anomalies seen in the Hall loops, the temperature dependencies of the individual switching fields and of the anomalous Hall voltage related to the two distinct channels will be derived subsequently. While the switching fields of the individual $SrRuO_3$ layers were given by the extrema of the magnetic field derivative of the magnetic moment, minor loop experiments were performed to determine the anomalous Hall voltages created in the two $SrRuO_3$ layers (cf. Fig. 6.6).

The procedure to extract the two anomalous Hall voltages from the minor loops is shown exemplarily in Fig. 6.7 and will be derived briefly. Since $\rho_{\mathrm{xy}} \ll \rho_{\mathrm{xx}}$ for $SrRuO_3$ thin films,[26,33] the total anomalous Hall voltage of the studied heterostructures[3] is given by the sum of the anomalous Hall voltages related to the two individual $SrRuO_3$ layers, when the electric current I_{applied} is applied to the sample. According to Pugh *et al.*, the anomalous Hall resistivity ρ_{AHE} of a homogeneous ferromagnet is proportional to the component of the magnetization that is perpendicular to the thin film surface $M_{\perp}$:[31]

$$\rho_{\mathrm{AHE}} = R_{\mathrm{AH}} M_{\perp} \tag{6.7}$$

---

[2] Please note that the scale of the Hall voltage was inverted in Fig. 6.6 for improved comparability.

[3] The validity of $\rho_{\mathrm{xy}} \ll \rho_{\mathrm{xx}}$ for our heterostructures can be also seen by the comparison of Fig. 5.12 (a) and Fig. 6.4, which indicates that V_{xy} is about two order of magnitude smaller than V_{xx} or V_{yy}.

with the anomalous Hall constant R_{AH}. Assuming that Equation (6.7) is valid for both $\mathrm{SrRuO_3}$ layers individually, the anomalous Hall resistivity and therefore the anomalous Hall voltage of the magnetically harder $\mathrm{SrRuO_3}$ layer is magnetic-field independent during the minor loop, because this layer stays saturated. The change of the anomalous Hall voltage during one minor hysteresis loop is then correlated with the contribution of the magnetically softer $\mathrm{SrRuO_3}$ layer. The anomalous Hall voltage created in the $\mathrm{SrRuO_3}$ layer with lower switching field (V_s^{AHE}) can be written as (in saturation):

$$V_s^{\mathrm{AHE}} = \frac{V_{\mathrm{sat}} - V_{\mathrm{minor}}(0\,\mathrm{T})}{2} \tag{6.8}$$

V_{sat} and $V_{\mathrm{minor}}(0T)$ are shown in Fig. 6.7 by red arrows. The anomalous Hall voltage generated in the magnetically harder $\mathrm{SrRuO_3}$ layer is then calculated by:

$$V_h^{\mathrm{AHE}} = (V_{\mathrm{sat}} - 2V_s) = V_{\mathrm{minor}}(0\,\mathrm{T}) \tag{6.9}$$

V_h^{AHE} and V_s^{AHE} correspond to the anomalous Hall voltages generated in the 6 MLs or 18 MLs $\mathrm{SrRuO_3}$ layers, depending on the switching fields at the particular temperature.

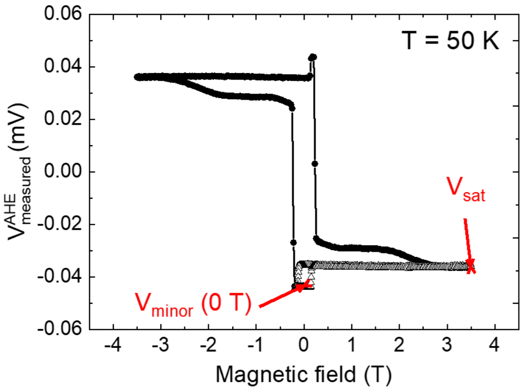

Figure 6.7: Illustration of the definition of $\mathrm{V}_{minor}(0\ \mathrm{T})$ and V_{sat} (indicated by red arrows), exemplarily shown for the full and minor loops of the anomalous Hall voltage of the RIR2 heterostructure at 50 K. Reprinted figure with permission from: L. Wysocki, L. Yang, F. Gunkel, R. Dittmann, P. H. M. van Loosdrecht, and I. Lindfors-Vrejoiu, Phys. Rev. Materials **4**, 054402 (2020), Copyright 2020 by the American Physical Society.

For the presented calculation, the tail in the hysteresis loops apparent in high magnetic fields during the resaturation is not considered.

The calculated anomalous Hall voltages generated in the 6 MLs and 18 MLs thick $SrRuO_3$ are plotted as function of temperature in Fig. 6.8 (b).

The anomalous Hall voltage of the 18 MLs thick $SrRuO_3$ layer possesses a non-monotonous temperature dependence with the change of sign from negative to positive values at 110 K, in proximity to the Curie temperature. Such behavior of the AHE is conventional for $SrRuO_3$ single crystals[17] and bare orthorhombic $SrRuO_3$ thin films of similar thickness.[21,34–37] In contrast, the anomalous Hall voltage generated in the 6 MLs thin $SrRuO_3$ layer, sandwiched between $SrIrO_3$, is positive down to 10 K. Such behavior is unusual for bare $SrRuO_3$ thin films, but was found recently in symmetric $SrIrO_3/SrRuO_3/SrIrO_3$ trilayers by Groenendijk *et al.*[12]

Within this simplified two-channels-AHE model (sketched in Fig. 6.8 (a)) that assumes the additivity of two independent anomalous Hall channels, hump-like anomalies can be generated if the AHE voltages, being proportional to the anomalous Hall constants, have opposite signs, and the switching fields of the two subsystems are different. As presented in Fig. 6.8 (b), these requirements are fulfilled between 40 K and 100 K, which is consistent with the observation of peak-like anomalies in the Hall hysteresis loops of heterostructure RIR2 (Figure 6.4). The considerably different shapes of the Hall voltage loops at 10 K and above 20 K originate from the distinct temperature dependencies of the switching fields of the two $SrRuO_3$ layers. For temperatures above 20 K, the thin $SrRuO_3$ has a lower switching field than the 18 MLs thick bottom $SrRuO_3$ layer, whereas it is the magnetically hard layer below 20 K.

At low temperatures, where the thin $SrRuO_3$ layer is the magnetically harder layer, the 18 MLs bottom $SrRuO_3$ layer starts to reverse its magnetization at smaller magnetic fields than the 6 MLs thin $SrRuO_3$. However, the thicker layer remains partially magnetized so that it is not fully reversed when the magnetization of the 6 MLs top $SrRuO_3$ layer is reversed. Such partial pinning most likely caused the tail in the hysteresis loops and was seen in previous reports on bare $SrRuO_3$ films[30] or similar $SrRuO_3$-based multilayers.[22]

The tail probably originates from strongly pinned domains in the 18 MLs bottom $SrRuO_3$ layer. Zahradník *et al.* proposed that such magnetic domain pinning in $SrRuO_3$ films can be attributed to disorder of the crystallographic orientation of $SrRuO_3$ films when they are deposited on $SrTiO_3$ substrates with low vicinal angle of 0.1 degree.[30] According to this study, the pinning can be reduced and the size of the domain nucleation increased by the epitaxial growth of $SrRuO_3$ on highly vicinal $SrTiO_3$ substrates with minimum 1° miscut angle.

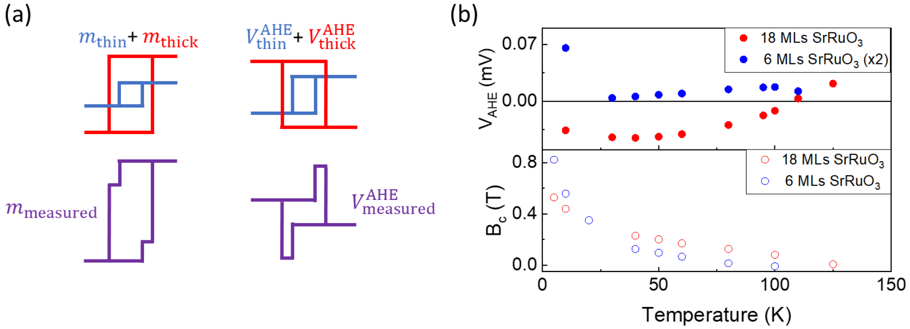

Figure 6.8: (a) Schematics of the magnetic moment and the anomalous Hall voltage hysteresis loops within the two-channels model. Temperature dependence of the AHE voltages generated in the two individual $SrRuO_3$ layers (solid circles) and the switching fields (open circles) of the 18 MLs $SrRuO_3$ layer (red) and of the 6 MLs $SrRuO_3$ layer (blue) plotted in (b). Subfigures reprinted with permission from: L. Wysocki, L. Yang, F. Gunkel, R. Dittmann, P. H. M. van Loosdrecht, and I. Lindfors-Vrejoiu, Phys. Rev. Materials **4**, 054402 (2020), Copyright 2020 by the American Physical Society.

The two-channels Hall voltage model used for the analysis is based on the assumption that the magnetization reversals are sharp and saturation of the magnetic heterostructure is achieved at the switching field of the magnetically harder layer. Thus, the contribution of pinned domains, creating the tail at magnetic fields that exceed the switching fields of the two ferromagnetic layers, is not considered within our model.

The observed behavior of the anomalous Hall constant of the 6 MLs thin $SrRuO_3$ layer of the heterostructure RIR2 is in contrast to the AHE of a reference sample that is composed of a 6 MLs $SrRuO_3$ layer sandwiched between two 2 MLs thick $SrIrO_3$ layers.

As it can be seen in Fig. 6.9, the sign of the anomalous Hall constant of the trilayer is negative at low temperatures and changes its sign close to 80 K, below the ferromagnetic phase transition at 126 K.[38]

The difference of the AHE constant of the reference sample and the thin $SrRuO_3$ layer of the sample RIR2 emphasizes the strong influence of the details of the heterostructure design on the magnetotransport properties of the $SrRuO_3$ layers.

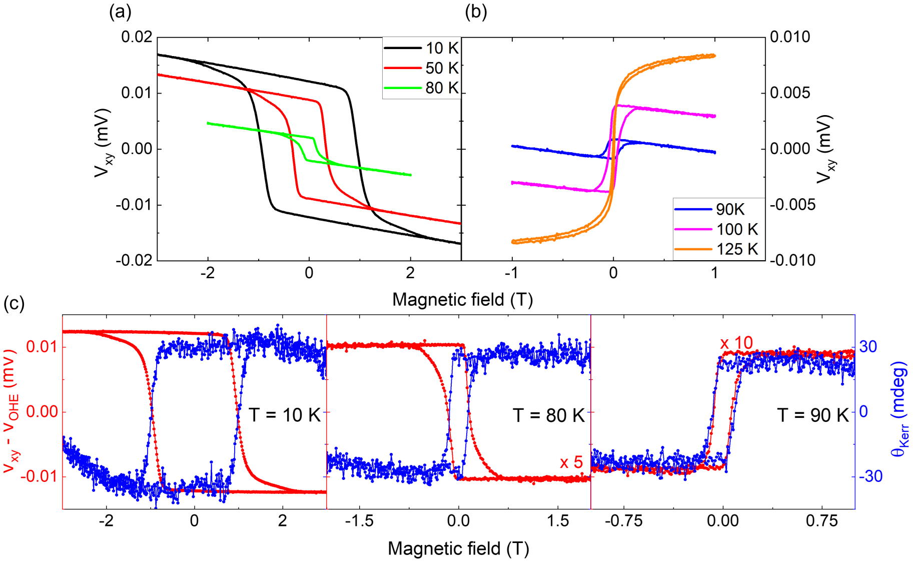

Figure 6.9: Magnetic field dependence of the total Hall voltage of a symmetric $SrIrO_3/SrRuO_3/SrIrO_3$ trilayer with 6 MLs thick $SrRuO_3$ layer and 2 MLs thick $SrIrO_3$ layers, at selected temperatures below (a) and above (b) the temperature of AHE sign change. (c) Polar Kerr rotation angle (blue) and Hall voltage (after subtraction of the ordinary Hall voltage) hysteresis loops (red) of the trilayer at three representative temperatures. To increase the visibility in (c), the Hall voltages at 80 K and 90 K are multiplied by 5 and 10, respectively. Figures reprinted with permission from: L. Wysocki, L. Yang, F. Gunkel, R. Dittmann, P. H. M. van Loosdrecht, and I. Lindfors-Vrejoiu, Phys. Rev. Materials **4**, 054402 (2020), Copyright 2020 by the American Physical Society.

To achieve a deeper insight into the impact of the interfacial environment at the $SrRuO_3$-spacer interface on the magnetic and magnetotransport properties of the whole heterostructure, the $SrIrO_3$ spacer and capping layers were substituted with the large band gap insulating oxide $SrZrO_3$.

Two-layers heterostructure with $SrZrO_3$ spacer (RZR2)

For the heterostructure RZR2, 2 MLs thick $SrZrO_3$ layers were used instead of $SrIrO_3$ as spacer and capping layer, still preserving the general sample design drawn in Fig. 6.1 (a). The comparison of the (polar) Kerr rotation angle and the Hall voltage loops, after subtraction of the ordinary Hall effect, is presented in Fig. 6.10.

Similar to heterostructure RIR2, the Kerr rotation angle θ_{Kerr}, being proportional to the magnetization component perpendicular to the thin film surface, possesses a double-step-switching below 50 K, which originates again from the existence of the two magnetically decoupled, ferromagnetic $SrRuO_3$ layers with measurable difference of the switching fields. Above 110 K, the difference between the switching fields is below the limit that is distinguishable with our MOKE measurements. In contrast to heterostructure RIR2, also the Hall voltage hysteresis loops show a double-step-reversal at low temperatures, indicating that the AHE constants of both layers are negative at low temperatures. The dominant contribution to the anomalous Hall voltage, corresponding to the 18 MLs thick $SrRuO_3$ layer with a Curie temperature of approximately 140 K, is negative below 127 K. Sharp hump-like features are observed in the Hall voltage loops only in a very narrow temperature range between 127 K and 129 K (not shown here), around the temperature of the sign change of the dominant anomalous Hall constant. This indicates that the AHE constant of the thin layer of this heterostructure is negative at low temperatures, but changes its sign in the range between 122 K and 127 K. In contrast to the thin layer of heterostructure RIR2, having a positive AHE constant down to low temperatures, the anomalous Hall constant of the 6 MLs top $SrRuO_3$ of this heterostructure, sandwiched between $SrZrO_3$, behaves like bare $SrRuO_3$ films and exhibits the AHE sign change from negative to positive values close to the ferromagnetic transition temperature.[17,37]

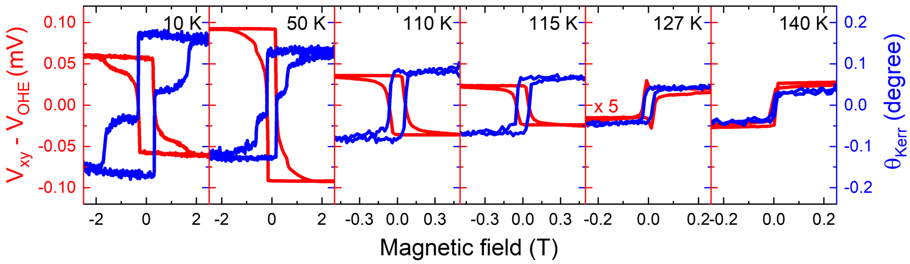

Figure 6.10: Hall voltage hysteresis loops after subtraction of the ordinary Hall contribution (red) and (polar) Kerr rotation angle loops (blue) at selected temperatures for the heterostructure RZR2 with $SrZrO_3$ spacer and capping layer. The global change of sign of the AHE from negative to positive takes place at about 127 K. The Hall voltage values at 127 K are multiplied with 5 to increase the visibility of the hump-like features. The magnetic field was applied perpendicular to the thin film surface. Reprinted figure with permission from: L. Wysocki, L. Yang, F. Gunkel, R. Dittmann, P. H. M. van Loosdrecht, and I. Lindfors-Vrejoiu, Phys. Rev. Materials **4**, 054402 (2020), Copyright 2020 by the American Physical Society.

Two-layers heterostructure with hybrid $SrIrO_3/SrZrO_3$ spacer (RIZR2)

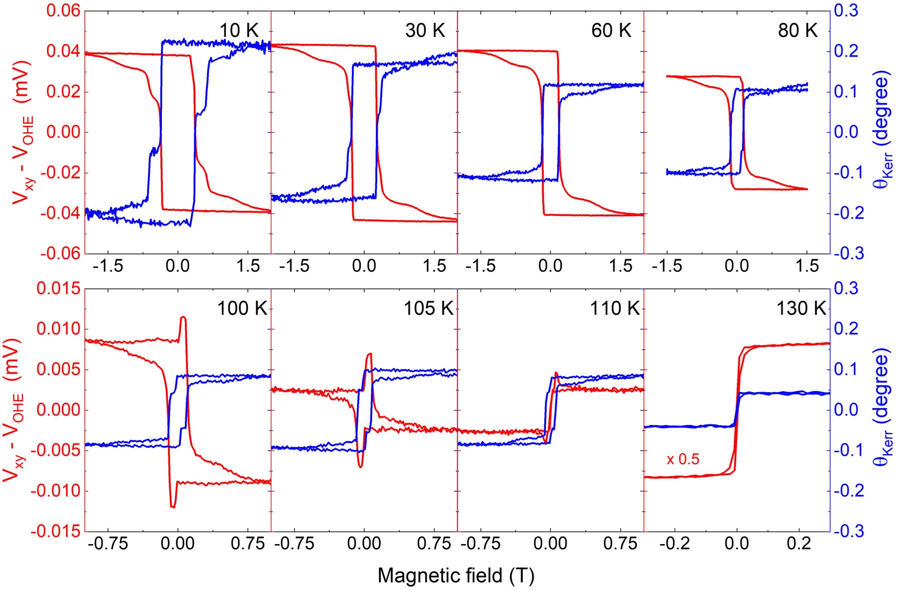

Figure 6.11: Hall voltage (after subtraction of the ordinary Hall contribution, shown in red), and (polar) Kerr rotation angle hysteresis loops (blue) of heterostructure RIZR2, the two-layer $SrRuO_3$ heterostructure with 2 MLs $SrIrO_3$/2 MLs $SrZrO_3$ spacer and capping layers. The magnetic field was applied perpendicular to the thin film surface. Reprinted figure with permission from: L. Wysocki, L. Yang, F. Gunkel, R. Dittmann, P. H. M. van Loosdrecht, and I. Lindfors-Vrejoiu, Phys. Rev. Materials **4**, 054402 (2020), Copyright 2020 by the American Physical Society.

The deposition of a $SrIrO_3/SrZrO_3$ hybrid spacer was realized for heterostructure RIZR2. This heterostructure is also composed of an 18 MLs thick bottom $SrRuO_3$ layer and a 6 MLs top $SrRuO_3$ layer, which are separated and capped by hybrid 2 MLs $SrIrO_3$ / 2 MLs $SrZrO_3$ layers. Due to the growth of such hybrid spacer and capping layers, the 6 MLs top $SrRuO_3$ layer of heterostructure RIZR2 is interfaced on one side with $SrZrO_3$ and on the other one with $SrIrO_3$. The interlayer coupling in such multilayers with asymmetric interfaces, as they were investigated in our previous study,[39] is important in the context of possible additivity of interfacial DMI. Since the inversion symmetry is broken at bottom and top interfaces of the ferromagnetic layer in the asymmetric multilayers, it might be possible that, if interfacial DMI is obtained, it might be additive, as it was achieved in metallic asymmetric multilayers, such as Pt/Co/Ir.[40]

The very weak coupling or decoupling of the two ferromagnetic layers, which was addressed in our previous publication,[22] as well as the distinct temperature dependence of the layers' switching fields is reflected by the double-step-hysteresis of the Kerr rotation angle loops, presented in Fig. 6.11 in blue. Similar to the heterostructure RIR2, the thin $SrRuO_3$ layer has a larger switching field than the bottom thick $SrRuO_3$ layer at low temperatures. For this particular heterostructure, the switching fields become equal at 60 K so that the thick $SrRuO_3$ layer is the magnetically hard layer above 60 K.

Presented in red in Fig. 6.11 is the Hall voltage after subtraction of the ordinary Hall voltage as function of the applied magnetic field. Although a two-step like behavior is seen at low temperatures, the AHE is not directly proportional to the total Kerr rotation angle of the heterostructure. Under the assumption that the existence of a skyrmion-related topological Hall effect can be disregarded[4], the presented difference of total and ordinary Hall voltage is again the total anomalous Hall voltage of the heterostructure. Within the two-channels AHE model, the two-step Hall switching behavior below 80 K is an indication that the AHE constants of both $SrRuO_3$ layers have identical (negative) signs. The dominant contribution to the anomalous Hall voltage, originating from the 18 MLs $SrRuO_3$ layer, becomes positive close to 110 K, which is decreased by almost 20 K compared to heterostructure RZR2. Hump-like features are observed only in the temperature range between 100 K and 110 K, which is most likely attributed to the AHE constant of the thin $SrRuO_3$ layer becoming positive close to 100 K.

The discussed differences in the temperature dependence of the anomalous Hall constants of both $SrRuO_3$ layers, which depend on the spacer and capping material, demonstrate the strong impact of the interfacial environment on the magnetotransport properties of the $SrRuO_3$ layers. Such effect was observed even for the 18 MLs thick bottom $SrRuO_3$ layer of the presented heterostructures. While the temperature of the AHE sign change took place at about 130 K in case of heterostructure RZR2, where the $SrRuO_3$ is interfaced with $SrZrO_3$, the temperature of the AHE sign change was reduced to 110 K for

---

[4] Due to the asymmetry of the $SrRuO_3$ interfaces, a net DMI could be generated. However, based on other studies on similar trilayers,[4] we do not consider the formation of skyrmions here.

heterostructure RIR2.

Similar impact of the $SrIrO_3/SrRuO_3$ interface on the global magnetotransport characteristics has been observed also in the study of asymmetric $SrHfO_3/SrRuO_3/SrIrO_3$ and $SrZrO_3/SrRuO_3/SrIrO_3$ multilayers.[39]

According to the current knowledge of the strong dependence of the anomalous Hall conductivity on the details of the $SrRuO_3$ band structure,[41] interfacing $SrRuO_3$ on one or both sides with distinct perovskite oxides most likely leads to modifications of the electronic band structure and in this way to changes of the anomalous Hall conductivity.

6.5 Conclusion

Due to the technical simplicity and the possibility to perform the electrical transport measurements in most modern solid state research laboratories, the possibility of examining the formation of skyrmions by magnetotransport measurements is a very attractive experimental option. However, many experimental studies lately concluded the formation of skyrmions in $SrRuO_3$ thin films and $SrRuO_3$-based heterostructures solely from the appearance of peculiar anomalies that resemble a topological Hall effect.[8–10] Other transport studies disregarded the formation of skyrmions and suggested the existence of multiple AHE channels, related to inhomogeneities of the AHE conductivity, to be the origin of the THE-like features in the Hall resistivity loops.[11,15,16]

Thus, this magnetotransport study was dedicated to $SrRuO_3$-based heterostructures, with intentional heterogeneity due to the contribution of two independent conduction channels. This was achieved by the deposition of a heterostructure with two $SrRuO_3$ layers of distinct thicknesses that were separated by epitaxial oxide spacers, such as $SrIrO_3$ and/or $SrZrO_3$. Although the thinner $SrRuO_3$ layer of the heterostructures under study was in a thickness range for which strong interfacial DMI was predicted in $SrRuO_3$-$SrIrO_3$ bilayers,[2] and consequently skyrmion formation would be expected, the investigations indicated that the observed peculiar features in the Hall loops do not correspond to a topological Hall effect.

The study demonstrated that the anomalous Hall voltage of the heterostructures with multiple $SrRuO_3$ layers is additive if the layers are electrically connected and magnetically decoupled. Furthermore, hump-like anomalies can be observed in the Hall voltage hysteresis loops when the two independent magnetic subsystems have distinct signs (and magnitudes) of the anomalous

Hall voltage as well as distinct switching fields, which was described by the two-channels Hall model. Thus, the deduction of the formation of skyrmions primarily based on THE-like anomalies in the Hall resistance loops in $SrRuO_3$ heterostructures can be faulty. The study furthermore showed the sensitivity of the anomalous Hall conductivity of $SrRuO_3$ layers on the electronic band structure due to the strong impact of the interfacial environment on the magnetotransport properties of the $SrRuO_3$ layers.

Acknowledgement and own contribution

The samples were deposited by me and Dr. Ionela Lindfors-Vrejoiu. I performed the SQUID measurements of all presented heterostructures, and the Hall and MOKE experiments of the RIR2 heterostructure. The AFM images, shown in Fig. 6.1, were taken by Dr. Andrea Bliesener. The simultaneous Hall and MOKE investigations of the heterostructures RZR2, RIZR2, and the RIZ trilayer were performed by Lin Yang. The analysis was done by me with partial support from Lin Yang for the heterostructures RZR2, RIZR2, and RIZ. The text is based on the following manuscript written mainly by me and Dr. Ionela Lindfors-Vrejoiu: *Validity of magnetotransport detection of skyrmions in epitaxial $SrRuO_3$ heterostructures*, Lena Wysocki, Lin Yang, Felix Gunkel, Regina Dittmann, Paul H. M. van Loosdrecht, and Ionela Lindfors-Vrejoiu, Phys. Rev. Materials **4**, 054402 (2020). The shown plots were adapted from this publication and its supplementary material. I thank Rene Borowski (Forschungszentrum Jülich, PGI-7) for treating the termination of the substrates and Michael Ziese (University of Leipzig) for valuable advice concerning Hall and SQUID measurements.

References

[1] L. Wysocki, L. Yang, F. Gunkel, R. Dittmann, P. H. M. van Loosdrecht, and I. Lindfors-Vrejoiu: *Validity of magnetotransport detection of skyrmions in epitaxial $SrRuO_3$ heterostructures*, Phys. Rev. Materials **4**, 054402 (2020).

[2] J. Matsuno, N. Ogawa, K. Yasuda, F. Kagawa, W. Koshibae, N. Nagaosa, Y. Tokura, and M. Kawasaki: *Interface-driven topological Hall effect in $SrRuO_3$ - $SrIrO_3$ bilayer*, Science Advances **2**, e1600304 (2016).

[3] K.-Y. Meng, A. S. Ahmed, M. Baćani, A.-O. Mandru, X. Zhao, N. Bagués, B. D. Esser, J. Flores, D. W. McComb, H. J. Hug, and F. Yang: *Observation of Nanoscale Skyrmions in SrIrO*$_3$ */ SrRuO*$_3$ *Bilayers*, Nano Letters **19**, 3169–3175 (2019).

[4] G. Malsch, D. Ivaneyko, P. Milde, L. Wysocki, L. Yang, P. H. M. van Loosdrecht, I. Lindfors-Vrejoiu, and L. M. Eng: *Correlating the Nanoscale Structural, Magnetic, and Magneto-Transport Properties in SrRuO*$_3$*-Based Perovskite Thin Films: Implications for Oxide Skyrmion Devices*, ACS Applied Nano Materials **3**, 1182–1190 (2020).

[5] M. Nakamura, D. Morikawa, X. Yu, F. Kagawa, T.-h. Arima, Y. Tokura, and M. Kawasaki: *Emergence of Topological Hall Effect in Half-Metallic Manganite Thin Films by Tuning Perpendicular Magnetic Anisotropy*, Journal of the Physical Society of Japan **87**, 074704 (2018).

[6] N. Nagaosa and Y. Tokura: *Topological properties and dynamics of magnetic skyrmions*, Nature Nanotechnology **8**, 899–911 (2013).

[7] B. Sohn, B. Kim, S. Y. Park, H. Y. Choi, J. Y. Moon, T. Choi, Y. J. Choi, T. W. Noh, H. Zhou, S. H. Chang, J. H. Han, and C. Kim: *Emergence of robust 2D skyrmions in SrRuO*$_3$ *ultrathin film without the capping layer*, arXiv:1810.01615, now published as: `https://doi.org/10.1103/PhysRevResearch.3.023232`, 2018.

[8] Y. Ohuchi, J. Matsuno, N. Ogawa, Y. Kozuka, M. Uchida, Y. Tokura, and M. Kawasaki: *Electric-field control of anomalous and topological Hall effects in oxide bilayer thin films*, Nature Communications **9**, 213 (2018).

[9] B. Pang, L. Zhang, Y. B. Chen, J. Zhou, S. Yao, S. Zhang, and Y. Chen: *Spin-Glass-Like Behavior and Topological Hall Effect in SrRuO*$_3$*/SrIrO*$_3$ *Superlattices for Oxide Spintronics Applications*, ACS Applied Materials and Interfaces **9**, 3201–3207 (2017).

[10] Q. Qin, L. Liu, W. Lin, X. Shu, Q. Xie, Z. Lim, C. Li, S. He, G. M. Chow, and J. Chen: *Emergence of Topological Hall Effect in a SrRuO*$_3$ *Single Layer*, Advanced Materials **31**, 1807008 (2019).

[11] D. Kan and Y. Shimakawa: *Defect-Induced Anomalous Transverse Resistivity in an Itinerant Ferromagnetic Oxide*, physica status solidi (b) **255**, 1800175 (2018).

[12] D. J. Groenendijk, C. Autieri, T. C. van Thiel, W. Brzezicki, J. R. Hortensius, D. Afanasiev, N. Gauquelin, P. Barone, K. H. W. van den Bos, S. van Aert, J. Verbeeck, A. Filippetti, S. Picozzi, M. Cuoco, and A. D. Caviglia: *Berry phase engineering at oxide interfaces*, Physical Review Research **2**, 023404 (2020).

[13] Z. Li, S. Shen, Z. Tian, K. Hwangbo, M. Wang, Y. Wang, F. M. Bartram, L. He, Y. Lyu, Y. Dong, G. Wan, H. Li, N. Lu, J. Zang, H. Zhou, E. Arenholz, Q. He, L. Yang, W. Luo, and P. Yu: *Reversible manipulation of the magnetic state in* $SrRuO_3$ *through electric-field controlled proton evolution*, Nature Communications **11**, 184 (2020).

[14] D. Kan, T. Moriyama, K. Kobayashi, and Y. Shimakawa: *Alternative to the topological interpretation of the transverse resistivity anomalies in* $SrRuO_3$, Physical Review B **98**, 180408(R) (2018).

[15] D. Kan, K. Kobayashi, and Y. Shimakawa: *Electric field induced modulation of transverse resistivity anomalies in ultrathin* $SrRuO_3$ *epitaxial films*, Physical Review B **101**, 144405 (2020).

[16] L. Wang, Q. Feng, H. G. Lee, E. K. Ko, Q. Lu, and T. W. Noh: *Controllable Thickness Inhomogeneity and Berry Curvature Engineering of Anomalous Hall Effect in* $SrRuO_3$ *Ultrathin Films*, Nano Letters **20**, 2468–2477 (2020).

[17] Z. Fang, N. Nagaosa, K. S. Takahashi, A. Asamitsu, R. Mathieu, T. Ogasawara, H. Yamada, M. Kawasaki, Y. Tokura, and K. Terakura: *The Anomalous Hall Effect and Magnetic Monopoles in Momentum Space*, Science **302**, 92–95 (2003).

[18] L. Wu, F. Wen, Y. Fu, J. H. Wilson, X. Liu, Y. Zhang, D. M. Vasiukov, M. S. Kareev, J. H. Pixley, and J. Chakhalian: *Berry phase manipulation in ultrathin* $SrRuO_3$ *films*, Physical Review B **102**, 220406(R) (2020).

[19] S. H. Chang, Y. J. Chang, S. Y. Jang, D. W. Jeong, C. U. Jung, Y.-J. Kim, J.-S. Chung, and T. W. Noh: *Thickness-dependent structural phase transition of strained* $SrRuO_3$ *ultrathin films: The role of octahedral tilt*, Physical Review B **84**, 104101 (2011).

[20] J. Xia, W. Siemons, G. Koster, M. R. Beasley, and A. Kapitulnik: *Critical thickness for itinerant ferromagnetism in ultrathin films of* $SrRuO_3$, Physical Review B **79**, 140407(R) (2009).

[21] N. Haham, Y. Shperber, M. Schultz, N. Naftalis, E. Shimshoni, J. W. Reiner, and L. Klein: *Scaling of the anomalous Hall effect in* $SrRuO_3$, Physical Review B **84**, 174439 (2011).

[22] L. Wysocki, R. Mirzaaghayev, M. Ziese, L. Yang, J. Schöpf, R. B. Versteeg, A. Bliesener, J. Engelmayer, A. Kovács, L. Jin, F. Gunkel, R. Dittmann, P. H. M. van Loosdrecht, and I. Lindfors-Vrejoiu: *Magnetic coupling of ferromagnetic* $SrRuO_3$ *epitaxial layers separated by ultrathin non-magnetic* $SrZrO_3$*/* $SrIrO_3$, Applied Physics Letters **113**, 192402 (2018).

[23] J. Choi, C. B. Eom, G. Rijnders, H. Rogalla, and D. H. A. Blank: *Growth mode transition from layer by layer to step flow during the growth of heteroepitaxial* $SrRuO_3$ *on (001)* $SrTiO_3$, Applied Physics Letters **79**, 1447–1449 (2001).

[24] R. Versteeg: “Optically Probed Order and Dynamics in the Chiral Cluster Magnet Cu_2OSeO_3”, Ph.D. Thesis (University of Cologne, 2019).

[25] J. Schöpf: “Design of a setup for simultaneous magneto-transport and magneto-optical effects of ferromagnetic thin film heterostructures”, Master thesis, University of Cologne (Nov. 2019).

[26] T. C. van Thiel, D. J. Groenendijk, and A. D. Caviglia: *Extraordinary Hall balance in ultrathin* $SrRuO_3$ *bilayers*, Journal of Physics: Materials **3**, 025005 (2020).

[27] S. L. Zhang, Y. Liu, L. J. Collins-McIntyre, T. Hesjedal, J. Y. Zhang, S. G. Wang, and G. H. Yu: *Extraordinary Hall balance*, Scientific Reports **3**, 2087 (2013).

[28] S. L. Zhang and T. Hesjedal: *The magneto-Hall difference and the planar extraordinary Hall balance*, AIP Advances **6**, 045019 (2016).

[29] A. Gerber: *Interpretation of experimental evidence of the topological Hall effect*, Physical Review B **98**, 214440 (2018).

[30] M. Zahradník, K. Uhlířová, T. Maroutian, G. Kurij, G. Agnus, M. Veis, and P. Lecoeur: *Magnetic domain wall motion in* $SrRuO_3$ *thin films*, Materials & Design **187**, 108390 (2020).

[31] E. M. Pugh and N. Rostoker: *Hall Effect in Ferromagnetic Materials*, Reviews of Modern Physics **25**, 151 (1953).

[32] N. Nagaosa, J. Sinova, S. Onoda, A. H. MacDonald, and N. P. Ong: *Anomalous Hall effect*, Reviews of Modern Physics **82**, 1539 (2010).

[33] G. Koster, L. Klein, W. Siemons, G. Rijnders, J. S. Dodge, C.-B. Eom, D. H. A. Blank, and M. R. Beasley: *Structure, physical properties, and applications of* $SrRuO_3$ *thin films*, Review of Modern Physics **84**, 253 (2012).

[34] M. Izumi, K. Nakazawa, Y. Bando, Y. Yoneda, and H. Terauchi: *Magnetotransport of* $SrRuO_3$ *Thin Film on* $SrTiO_3$ *(001)*, Journal of the Physical Society of Japan **66**, 3893–3900 (1997).

[35] L. Klein, J. R. Reiner, T. H. Geballe, M. R. Beasley, and A. Kapitulnik: *Extraordinary Hall effect in* $SrRuO_3$, Physical Review B **61**, R7842(R) (2000).

[36] M. Schultz, J. W. Reiner, and L. Klein: *The extraordinary Hall effect of* $SrRuO_3$ *in the ultrathin limit*, Journal of Applied Physics **105**, 07E906 (2009).

[37] M. Ziese, L. Jin, and I. Lindfors-Vrejoiu: *Unconventional anomalous Hall effect driven by oxygen-octahedra-tailoring of the SrRuO*$_3$ *structure*, Journal of Physics: Materials **2**, 034008 (2019).

[38] L. Yang, L. Wysocki, J. Schöpf, L. Jin, A. Kovács, F. Gunkel, R. Dittmann, P. H. M. van Loosdrecht, and I. Lindfors-Vrejoiu: *Origin of the hump anomalies in the Hall resistance loops of ultrathin SrRuO*$_3$*/ SrIrO*$_3$ *multilayers*, Physical Review Materials **5**, 014403 (2021).

[39] L. Wysocki, J. Schöpf, M. Ziese, L. Yang, A. Kovács, L. Jin, R. B. Versteeg, A. Bliesener, F. Gunkel, L. Kornblum, R. Dittmann, P. H. M. van Loosdrecht, and I. Lindfors-Vrejoiu: *Electronic Inhomogeneity Influence on the Anomalous Hall Resistivity Loops of SrRuO*$_3$ *Epitaxially Interfaced with 5d Perovskites*, ACS Omega **5**, 5824–5833 (2020).

[40] C. Moreau-Luchaire, C. Moutafis, N. Reyren, J. Sampaio, C. A. Vaz, N. Van Horne, K. Bouzehouane, K. Garcia, C. Deranlot, P. Warnicke, P. Wohlhüter, J. M. George, M. Weigand, J. Raabe, V. Cros, and A. Fert: *Additive interfacial chiral interaction in multilayers for stabilization of small individual skyrmions at room temperature*, Nature Nanotechnology **11**, 444–448 (2016).

[41] B. Sohn, E. Lee, S. Y. Park, W. Kyung, J. Hwang, J. D. Denlinger, M. Kim, D. Kim, B. Kim, H. Ryu, S. Huh, J. S. Oh, J. K. Jung, D. Oh, Y. Kim, M. Han, T. W. Noh, B.-J. Yang, and C. Kim: *Sign-tunable anomalous Hall effect induced by two-dimensional symmetry-protected nodal structures in ferromagnetic perovskite thin films*, Nature Materials **20**, 1643–1649 (2021).

Part III

Tailoring the magnetic anisotropy of $La_{0.67}Sr_{0.33}Mn_{1-y}Ru_yO_3$ thin films

Chapter 7

Tailoring the magnetic anisotropy of $La_{0.67}Sr_{0.33}Mn_{1-y}Ru_yO_3$ thin films by layer thickness variations

Contents

The focus of this chapter is on the magnetic study of a set of $La_{0.67}Sr_{0.33}Mn_{0.95}Ru_{0.05}O_3$ thin films, in which the influence of the film thickness on the magnetic anisotropy was investigated. In the first half of this chapter, the optimization of the deposition parameters is addressed.

7.1 Introduction and experimental methods

Strontium-substituted lanthanum manganite is a fascinating material class both from the fundamental physical, and technological point of view. Its rich electronic and magnetic phase diagram, for instance as function of temperature, strontium concentration, and epitaxial strain state, paves the way for the property tailoring by interfacial engineering, doping, and film thickness.[1] Bulk $La_{0.7}Sr_{0.3}MnO_3$ is ferromagnetic up to 350 K, possesses an exceptionally large spin polarization close to 100 %, and shows colossal magnetoresistance, making LSMO an interesting candidate for spintronic devices.[1] In this context, the control of the magnetic anisotropy, which describes the preferential alignment of the magnetic moments along a certain direction, is required.[2,3] Especially magnetic films that exhibit (uniaxial) perpendicular magnetic anisotropy can be used in stable, dense, and low power consumption devices, such as magnetoresistive random-access memories.[4–6] In comparison to in-plane magnetic anisotropy systems, the anisotropy energy is often larger, the magnetization more homogeneous, thermally more stable, and offers the possibility to maximize the information-to-cell-size ratio further.[2,4] Additionally, the control of the magnetization state in ferromagnet/heavy metal heterostructures by (spin) currents of low current densities was successfully realized.[6,7]

In the research field of skyrmionics, obtaining moderate perpendicular anisotropy in (ferro-)magnetic thin films is desirable. If the Dzyaloshinskii–Moriya interaction, generated at the interface of the magnetic thin film with a strong spin-orbit coupled layer (such as $SrIrO_3$), is of comparable strength with the Heisenberg exchange interaction in the ferromagnet and the magnetic anisotropy, nontrivial spin textures, such as magnetic skyrmions or chiral domain walls, might be stabilized.[8,9]

Epitaxial $La_{0.7}Sr_{0.3}Mn_{1\text{-}y}Ru_yO_3$ thin films have been proven to be promising candidates for the tailoring of the magnetic anisotropy by variations of the Ru/Mn ratio as well as the epitaxial strain[10] and are therefore in the focus of the subsequently presented magnetic anisotropy study. Tensile epitaxial strain (by the growth on $SrTiO_3$(100) substrates) favors in-plane magnetic anisotropy even for 10 % ruthenium substitution, while compressive strain, imposed by the deposition on LSAT(100) substrates, allows (thickness-dependent) out-of-plane canting of the magnetic moments also for 5% ruthenium substitution.

Therefore, the following study focused on the thickness dependence of the magnetic anisotropy for $La_{0.67}Sr_{0.33}Mn_{0.95}Ru_{0.05}O_3$ thin films that were deposited on LSAT(100) substrates with small miscut of about 0.1°. The magnetic properties of the thin films of 5.5 nm to 81 nm thickness were investigated by temperature and magnetic field dependent superconducting quantum interference device (SQUID) magnetometry (MPMS XL7, *Quantum Design Inc.*). The effective magnetic anisotropy showed a non-monotonic thickness dependence and varied as function of temperature. Moderate perpendicular magnetic anisotropy was seen at low temperatures for film thicknesses between 7.5 nm and 21 nm. The largest effective perpendicular magnetic anisotropy (on the order of 10^5 erg per cm^2 at 100 K) was observed in a 16 nm $La_{0.67}Sr_{0.33}Mn_{0.95}Ru_{0.05}O_3$ thin film.

7.2 Thin film deposition

7.2.1 $La_{0.7}Sr_{0.3}Mn_{1-y}Ru_yO_3$: Growth optimization

The assurance of homogenous, reproducible $La_{0.7}Sr_{0.3}Mn_{1-y}Ru_yO_3$ thin films is an important prerequisite for the consistent study of the magnetic anisotropy. As described in detail in Chapter 3, the deposition temperature, the oxygen pressure as well as the laser fluence, target-to-substrate-distance, and the laser repetition rate influence the details of the growth process in a non-trivial manner. Based on previous studies of epitaxial $La_{0.7}Sr_{0.3}MnO_3$ thin films (see for instance Ref. [11]), the $La_{0.7}Sr_{0.3}Mn_{1-y}Ru_yO_3$ thin films were deposited at 650 °C in oxygen partial pressure of 0.133 mbar. The laser repetition rate was set to 3 Hz and the target-to-substrate distance fixed at 5.9 cm. In order to reduce the formation probability of oxygen vacancies, the epitaxial films were cooled down in oxygen (partial pressure: 100 mbar) with a cooling rate of 10 °C/min. The laser fluence was in the focus of the subsequently shown deposition optimization process.

The laser fluence was varied between $2\,J\,cm^{-2}$ to $2.8\,J\,cm^{-2}$ for the deposition of a set of approximately 30 nm thick $La_{0.7}Sr_{0.3}Mn_{0.9}Ru_{0.1}O_3$ (LSMRO) films. Due to the high reproducibility of substrate surface morphology and termination, TiO_2-terminated, low miscut $SrTiO_3$(100) substrates were preferred over LSAT substrates, which were found to be prone to the formation of SrO mounds (as presented in Chapter 3). The utilized $SrTiO_3$ substrates have a terrace width of about 250 nm and one-unit-cell step height.

The *in situ* monitoring of the thin film deposition by RHEED, operating in high pressure, is depicted in Fig. 7.1 (a).

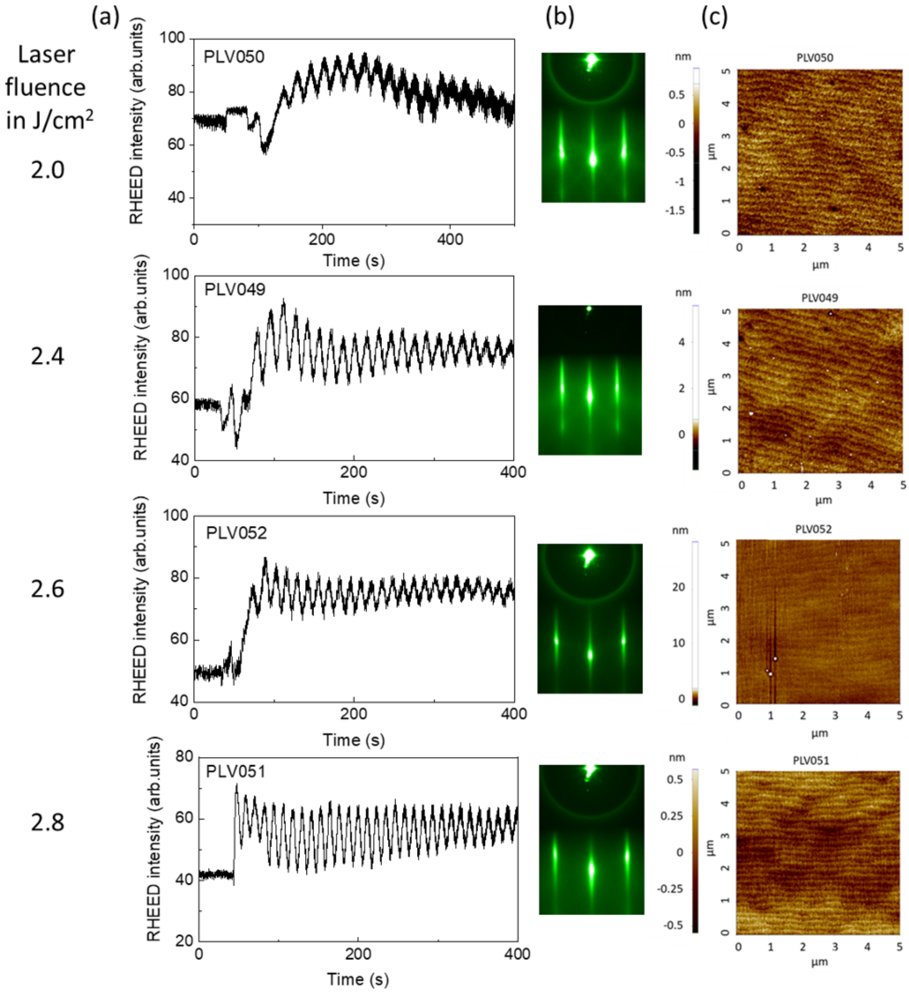

Figure 7.1: (a) Integrated RHEED intensity as function of deposition time during the initial 400 s (to 500 s) of the deposition, (b) RHEED patterns in vacuum after the cooling to about room temperature, and (c) AFM surface scans (5 µm x 5 µm) of the 30 nm $La_{0.7}Sr_{0.3}Mn_{0.9}Ru_{0.1}O_3$ films for various fluences (from top to bottom line: $2.0\,\mathrm{J\,cm^{-2}}$, $2.4\,\mathrm{J\,cm^{-2}}$, $2.6\,\mathrm{J\,cm^{-2}}$, $2.8\,\mathrm{J\,cm^{-2}}$).

As indicated by the oscillations in the time trace of the RHEED intensity, the deposition with laser fluences between $2\,\mathrm{J\,cm^{-2}}$ to $2.8\,\mathrm{J\,cm^{-2}}$ led consistently to layer-by-layer growth. The growth rate increased from about 62 pulses per unit

cell for a fluence of 2.0 J cm^{-2} to about 35 pulses per unit cell for 2.8 J cm^{-2}. Based on the knowledge of the deposition rate for each LSMRO thin film, the number of laser pulses was adjusted individually in order to keep the film thickness of about 30 nm similar.
The RHEED diffraction patterns of the thin films after the growth and cooling process to about room temperature, displayed in Fig. 7.1 (b), possess (elongated) diffraction spots. This indicates that the film surfaces are still rather flat.[12] The surface quality was confirmed by the atomic force microscopy scans presented in Fig. 7.1 (c). All thin films preserved the step-terrace-like structure imposed by the $SrTiO_3$ substrates. A few particles of maximum 10 nm height were observed for the thin films deposited with 2.6 J cm^{-2}, while some holes can be seen in the epitaxial film grown with 2.0 J cm^{-2}. However, due to the low defect density, these differences most likely originate from small substrate-to-substrate variations rather than from laser-fluence-induced differences in the thin film growth. Thus, the usage of different fluences between 2 J cm^{-2} to 2.8 J cm^{-2} did not cause significant changes of the overall surface morphology of the 30 nm $La_{0.7}Sr_{0.3}Mn_{0.9}Ru_{0.1}O_3$ thin films.

Due to the experimental difficulty to assess the stoichiometry of thin films, especially of the relevant Ru/Mn ratio, by *ex situ* EDX investigations with sufficient precision, temperature dependent SQUID magnetometry was used in order to investigate fingerprints of the stoichiometry of the $La_{0.7}Sr_{0.3}Mn_{1-y}Ru_yO_3$ thin films. The strong impact of the Ru/Mn ratio on the magnetic properties of $La_{1-x}Sr_xMn_{1-y}Ru_yO_3$ thin films, such as coercive fields, transition temperature, and magnetic anisotropy was demonstrated in previous studies.[10,13]
Displayed in Fig. 7.2 (a) - (c) are the temperature dependent magnetic moment investigations, acquired during warming up in presence of 0.1 T after field cooling in 0.1 T. The magnetic field was applied either perpendicular (OOP) or parallel to the sample surface along the sample edges (IP).
Since the contribution of the magnetic impurities was more than one order of magnitude smaller than the sample signal for this particular combination of 30 nm $La_{0.7}Sr_{0.3}Mn_{0.9}Ru_{0.1}O_3$ deposited on $SrTiO_3(100)$ substrates (compare Chapter 3), the fc measurements were only corrected by subtracting the offset above the transition temperature under the assumption that the diamagnetic contribution of the $SrTiO_3$ substrate is approximately temperature independent. All 30 nm $La_{0.7}Sr_{0.3}Mn_{0.9}Ru_{0.1}O_3$ of this study show in-plane magnetic anisotropy, due to the epitaxial tensile strain.[10]

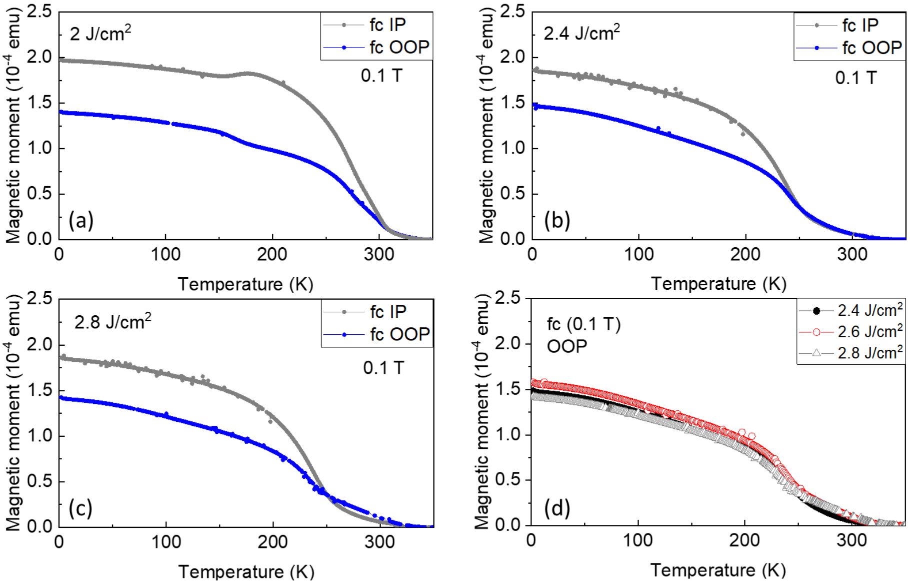

Figure 7.2: Field cooled magnetization measurements plotted as function of temperature with 0.1 T magnetic field applied parallel (grey) and perpendicular (blue) to the thin film surface for 30 nm $La_{0.7}Sr_{0.3}Mn_{0.9}Ru_{0.1}O_3$ thin films, which were deposited on $SrTiO_3(100)$ substrates with laser fluences of $2.0\,J\,cm^{-2}$ (a), $2.4\,J\,cm^{-2}$ (b), and $2.8\,J\,cm^{-2}$ (c), respectively. (d) Field cooled m(T)-curves of the $La_{0.7}Sr_{0.3}Mn_{0.9}Ru_{0.1}O_3$ films, deposited with laser fluences of $2.4\,J\,cm^{-2}$ (black), $2.6\,J\,cm^{-2}$ (red), and $2.8\,J\,cm^{-2}$ (grey) for out-of-plane magnetic field.

While the thin films deposited with laser fluences between $2.4\,J\,cm^{-2}$ to $2.8\,J\,cm^{-2}$ have comparable ferromagnetic transition temperatures around 240 K (cf. Fig. 7.2 (d))[1], the thin film grown with $2.0\,J\,cm^{-2}$ possesses an increased T_C of 273 K. Since 240 K is similar to the Curie temperatures reported for comparable (stoichiometric) $La_{0.7}Sr_{0.3}Mn_{0.9}Ru_{0.1}O_3$ films,[10] this increase of T_C might be an indication of a reduction of the Ru/Mn ratio compared to the other thin films under study.[10,13] Additionally, the temperature dependent magnetic moment curves exhibit additional structure between 150 K and 220 K, which are of opposite sign for the in-plane and out-of-plane measurement and not observed for the other Ru-substituted LSMO thin films shown here. This could be a sign either of a temperature dependent change of the magnetic anisotropy or an indication for inhomogeneities in the thin film.

Except for the lowest fluence studied ($2.0\,J\,cm^{-2}$), the chosen laser fluences did

---

[1] The Curie temperatures were extracted from the extremum of dm/dT.

not impact strongly on the (temperature) dependent magnetic characteristics of the $La_{0.7}Sr_{0.3}Mn_{0.9}Ru_{0.1}O_3$ films. As displayed in Fig. 7.2 (d), the three films that were deposited with $2.4\,\mathrm{J\,cm^{-2}}$, $2.6\,\mathrm{J\,cm^{-2}}$, and $2.8\,\mathrm{J\,cm^{-2}}$ exhibit similar transition temperature and magnetic moment at low temperatures. The magnetization of about $2.5\,\mu_B$ per uc, which was calculated exemplarily for the fc (IP) measurement of the sample deposited with $2.4\,\mathrm{J\,cm^{-2}}$ at 3 K, is comparable with values reported for similar LSMO films with 10 % ruthenium substitution that were acquired during fc measurements.[13]

Thus, the intermediate fluence of $2.4\,\mathrm{J\,cm^{-2}}$ is taken as suitable laser fluence for the deposition of $La_{0.7}Sr_{0.3}Mn_{0.9}Ru_{0.1}O_3$ on $SrTiO_3$(100) substrates.

Under the assumption that the sticking coefficients for the growth on $SrTiO_3$(100) and LSAT(100) substrates are similar and the film stoichiometry is therefore approximately independent of the utilized substrates, the optimized growth parameters were taken also for the deposition on LSAT. In order to keep the deposition parameters consistent, all $La_{1-x}Sr_xMn_{1-y}Ru_yO_3$ films of the subsequently shown study were deposited under the following conditions (unless otherwise stated):

Parameter	
Deposition Temperature	650 °C
Oxygen pressure	0.133 mbar
Laser fluence	$2.4\,\mathrm{J\,cm^{-2}}$
Laser repetition rate	3 Hz
Target-substrate distance	5.9 cm
Postannealing	In 100 mbar O_2, 10 °C/min

Table 7.1: Optimized parameters for the pulsed-laser deposition of $La_{1-x}Sr_xMn_{1-y}Ru_yO_3$ thin films.

7.2.2 Thin film deposition of $La_{0.67}Sr_{0.33}Mn_{0.95}Ru_{0.05}O_3$ thin films

To investigate the dependence of the magnetic anisotropy on the thickness of the films, a set of LSMO thin films with 5 % Ru-substitution was deposited, with thicknesses in the range from 5.5 nm to 81 nm.

The $La_{0.67}Sr_{0.33}Mn_{0.95}Ru_{0.05}O_3$ (LSMRO) thin films under study were epitaxially grown on LSAT(100) substrates by pulsed-laser deposition under the conditions summarized in Table 7.1.

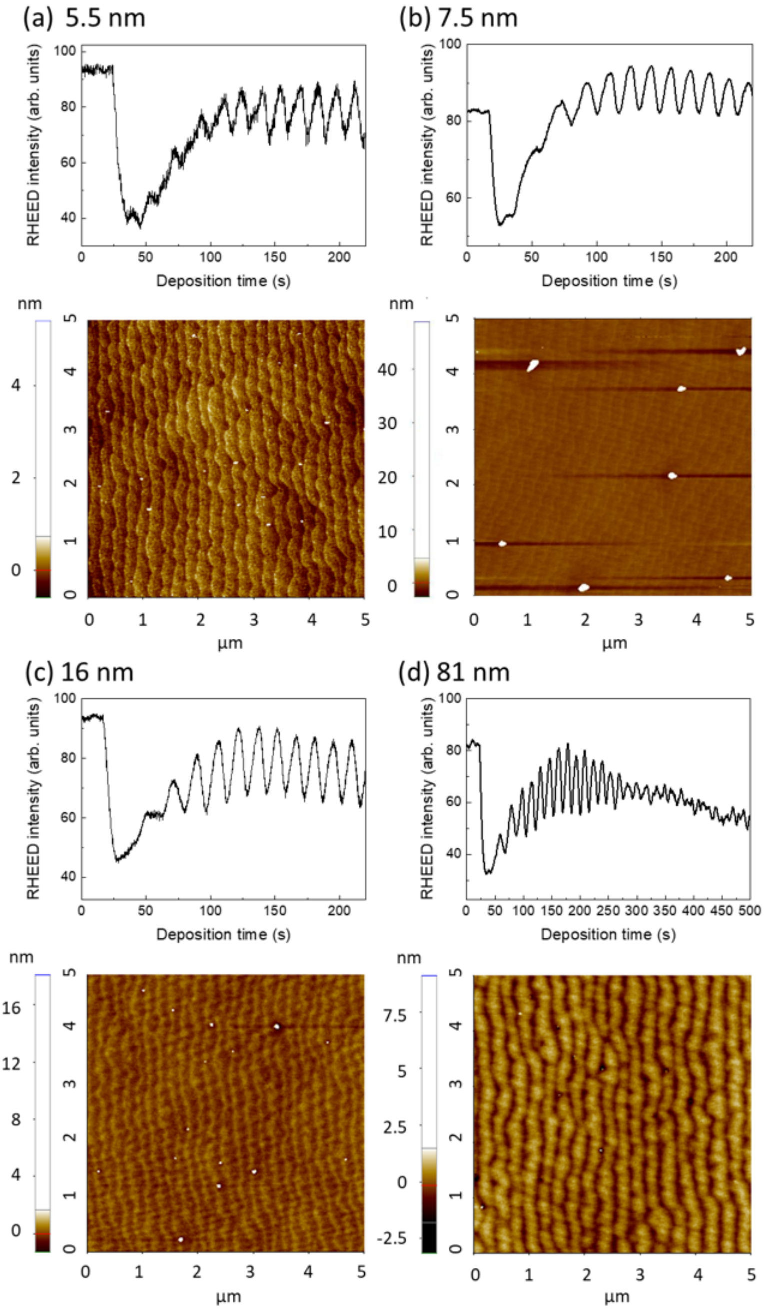

Figure 7.3: Integrated intensity of the RHEED specular spot during the initial 220 s ((a) - (c)) or 500 s (d) of the deposition of the $La_{0.67}Sr_{0.33}Mn_{0.95}Ru_{0.05}O_3$ thin films and atomic force microscopy surface scans (5 µm x 5 µm) of the thin films. Shown are exemplarily the RHEED and AFM investigations for the 5.5 nm (a), 7.5 nm (b), 16 nm (c), and the 80 nm (d) thin film.

The deposition on LSAT(100) substrates at 650 °C, which were annealed as decribed in Chapter 3, induces biaxial[2] compressive strain to the $La_{0.67}Sr_{0.33}Mn_{0.95}Ru_{0.05}O_3$ thin films.

Presented in Fig. 7.3 are the RHEED intensities of the specular spot during the initial 220 s ((a) - (c)) or 500 s (d) of the deposition as well as atomic force microscopy surface topography scans, exemplarily shown for the thinnest (a), two intermediate ((b) - (c)), and the thickest thin film (d) of this study. The Ru-substituted LSMO grew in a layer-by-layer mode, indicated by the oscillations visible in the RHEED intensity time traces, as it was also seen for the deposition of undoped $La_{0.7}Sr_{0.3}MnO_3$ on $SrTiO_3$ with step-terrace-like structure.[15,16] However, the RHEED oscillation intensity maximum increased during the initial seconds of the growth, with a change of intensity oscillation frequency. Thus, the initial oscillations were not considered for the estimation of the deposition rate.

The thickness of the individual thin films was then calculated under the assumption of fully strained films and a constant out-of-plane lattice parameter of 0.3885 nm, determined by XRD investigations of an 88 nm reference film.

The RHEED intensity does not show clear oscillations after about 16 to 20 oscillations anymore, as presented exemplarily in Fig. 7.3 (d). This could indicate a change of the growth mode, similar to the change from the layer-by-layer to steady-state growth mode that was seen to take place after 20 unit cells during the growth of $La_{0.7}Sr_{0.3}MnO_3$ on miscut $SrTiO_3$ substrates.[16] In this study, Boschker *et al.* also observed a peak in the RHEED intensity oscillation maxima[3], which they attributed to a possible conversion of the termination.[16]

Acquired by atomic force microscopy in the non-contact mode, the surface morphologies of the LSMRO films under study are summarized in the lower panels of Fig. 7.3. Up to a film thickness of 7.5 nm, the thin film surfaces are smooth, maintaining the step-and-terrace-like structure of the LSAT(100) substrates. However, the thicker films exhibit a worm-like topography aligned along the substrate terraces, which would be consistent with a possible growth mode change. The formation of islands with unit cell height was also observed in a 30 uc $La_{2/3}Sr_{1/3}MnO_3$ on miscut substrates $SrTiO_3$.[16] In order to confirm the film thicknesses estimated from the RHEED intensity oscillations during the

---

[2] Only below 150 K, LSAT possesses a small (orthorhombic) distortion from cubic symmetry.[14]

[3] Since the substrate termination is unknown for our LSAT substrates after the thermal treatment, a clear statement about the possibility of a termination conversion cannot be made here.

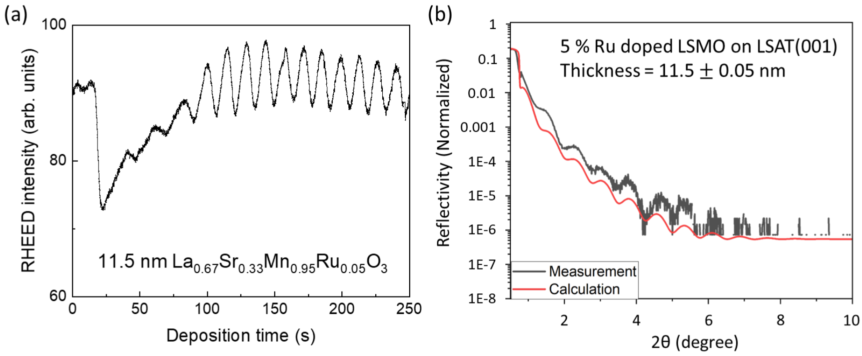

Figure 7.4: (a) RHEED intensity oscillations during the deposition of a 11.5 nm $La_{0.67}Sr_{0.33}Mn_{0.95}Ru_{0.05}O_3$ thin film. (b) X-ray reflectometry $\theta - 2\theta$ scans of the same film. The XRR measurements were performed and analysed by Brajaopal Das.

deposition (see Fig. 7.4 (a)), x-ray reflectometry measurements[4] of a reference film were performed and are shown in Fig. 7.4 (b). Plotted in black is the measured x-ray reflectivity, shown in red is the fit. The thickness of 11.5 nm, which was extracted from the data fittings, is in good agreement with the estimated thickness from the *in situ* RHEED study.

7.3 Magnetic characterization

Based on thin film studies of the parent compound $La_{0.67}Sr_{0.33}MnO_3$, which were deposited on LSAT under weak compressive strain, a non-trivial dependence of the magnetic anisotropy on thickness was expected.[17] In the study by Chaluvadi, 25 nm $La_{0.67}Sr_{0.33}MnO_3$ thin films were found to show biaxial anisotropy with the easy axes along the in-plane <110>$_c$ axes and the hard axes along in-plane <100>$_c$ (at low temperatures).[17] This biaxial contribution basically originates from the magnetocrystalline anisotropy of LSMO tight to the in-plane orientation defined by the epitaxial deposition on cubic (100) substrates.[18]

In case of the here presented study, the preferential alignment of the magnetization along <110>$_c$, compared to the in-plane <100>$_c$ axes, was tested for the two Ru-substituted LSMO films of intermediate thicknesses.

---

[4] Both studies, XRD and XRR, were performed by Brajagopal Das (Technion, Israel).

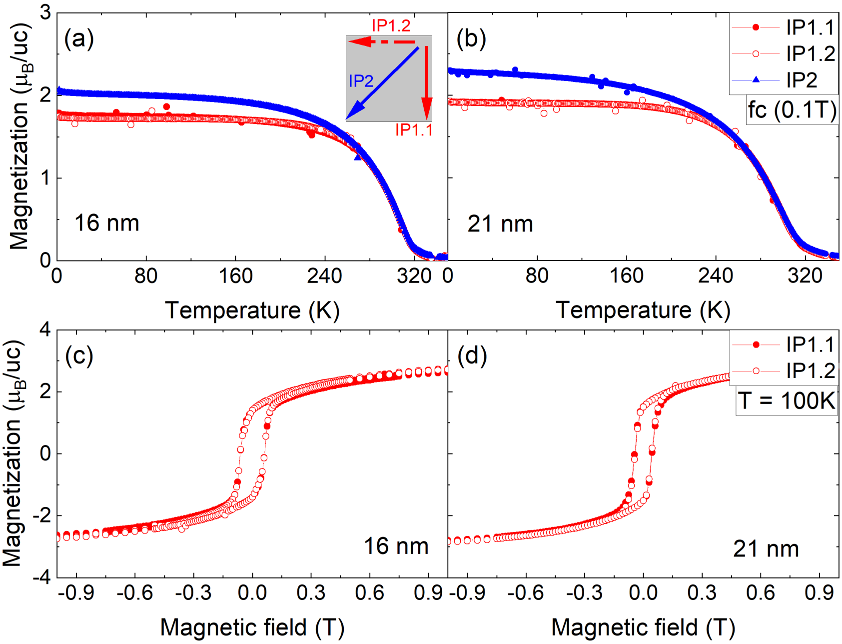

Figure 7.5: Temperature dependent (fc) magnetization measurements of the 16 nm (a) and 21 nm (b) Ru-substituted LSMO film with the magnetic field applied in the film plane along the edges of the squarish sample (red) and along the diagonal (blue). Magnetic hysteresis loops of the 16 nm (c) and 21 nm (d) Ru-substituted LSMO film with the applied magnetic field in the film plane along the two orthogonal samples edges at 100 K.

For the in-plane measurements presented in Fig. 7.5, the magnetic field was applied along two orthogonal sample edges ($[100]_c$ and $[010]_c$) and along the in-plane diagonal ($[110]_c$). As shown in Fig. 7.5 (a), the temperature-dependent magnetic moments are approximately identical throughout the entire ferromagnetic temperature range when the magnetic field is applied along $[100]_c$ or $[010]_c$ direction. In contrast, the magnetic moment is enhanced during the fc curve when the magnetic field was applied along $[110]_c$, plotted in blue. This behavior is consistent with the magnetic hysteresis loops of the two thin films at 100 K, displayed in Fig. 7.5 (c) and (d). It indicates that the magnetic easy axes in these 16 nm and 21 nm $La_{0.67}Sr_{0.33}Mn_{0.95}Ru_{0.05}O_3$ film are indeed probably also along the $<110>_c$ direction, as it was observed for the biaxial anisotropy along $<110>_c$ in 25 nm thin films of the LSMO parent compound (deposited on LSAT) at low temperatures.[17] Thus, the subsequently shown magnetic characteristics of the Ru-substituted LSMO thin films were measured for the three magnetic field directions, perpendicular to the thin film surface (OOP), in-plane parallel to the sample edges (IP1: H II sample edges) and along the in-plane diagonal (IP2; IP II sample diagonal).

All subsequently presented temperature magnetization measurements were corrected for background contributions as described in detail[5] in Chapter 3. The magnetization was calculated by normalizing the measured thin film magnetization to the unit cell volume, expressed in multiples of the Bohr magneton. Here, an out-of-plane pseudocubic lattice cell of 0.3885 nm was assumed, referring to the XRD investigations.

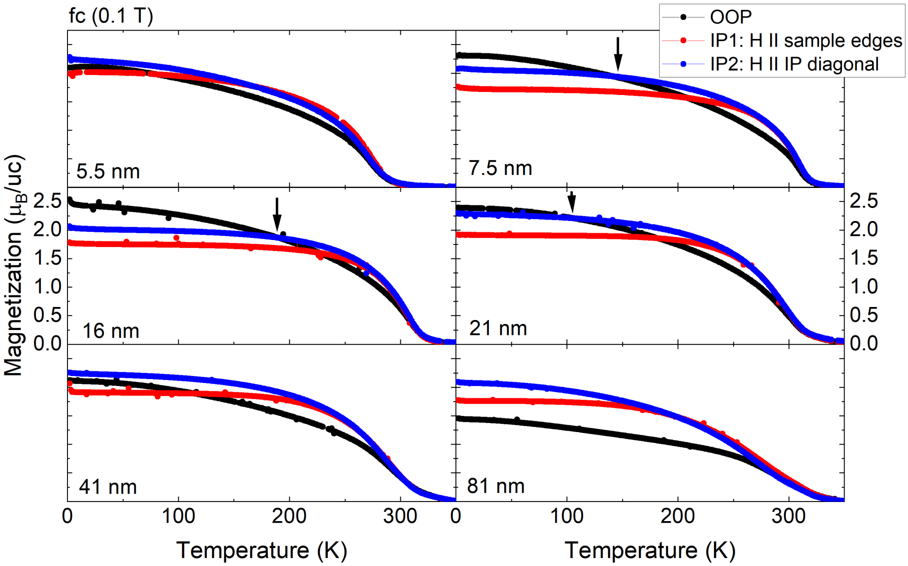

Figure 7.6: Temperature dependence of the magnetization of the $La_{0.67}Sr_{0.33}Mn_{0.95}Ru_{0.05}O_3$ thin films with thicknesses between 5.5 nm (upper left panel) and 81 nm (lower right panel), deposited on LSAT(100). The field cooled measurements with the magnetic field of 0.1 T applied perpendicular to the film surface are drawn in black. When the magnetic field was applied parallel to the film plane along one of the sample edges, the measurements are plotted with red symbols. Displayed in blue are the field cooled M(T)-curves for the magnetic field applied in-plane along the diagonal $[110]_c$ direction. Indicated by the black arrows are the temperatures at which the magnetic moments for the magnetic field applied perpendicular to the sample surface and in-plane, along $[110]_c$ direction, are identical in presence of 0.1 T.

---

[5] Since the measurements along the in-plane diagonal were performed after the resistance measurements mostly, this additional background contribution above T_c was subtracted too.

Presented in Fig. 7.6 are the temperature dependent magnetization measurements, performed during the warming process in presence of 0.1 T after cooling in 0.1 T. The applied magnetic field of 0.1 T was on the order of the coercive fields at low temperatures for most of the thin films.

In the fc-measurements in presence of 0.1 T, all $La_{0.67}Sr_{0.33}Mn_{0.95}Ru_{0.05}O_3$ films under study possess magnetic anisotropy at low temperatures. In contrast, isotropic behavior (with respect to the three orientations) is observed at higher temperatures close to (and above) the Curie temperatures. This behavior is related to the distinct temperature dependencies of the various contributions to the magnetic anisotropy, such as shape, surface, magnetocrystalline, and magnetoelastic anisotropy.

As shown in Fig. 7.6, the magnetic moment is equal to or larger when the magnetic field is applied along the sample diagonal ($[110]_c$) compared to the magnetic moment for the magnetic field applied along the sample edges ($[100]_c$ or $[010]_c$). This behavior is observed consistently at low temperatures for all $La_{0.67}Sr_{0.33}Mn_{0.95}Ru_{0.05}O_3$ between 5.5 nm and 81 nm.

However, whether the magnetization is larger for the magnetic field applied perpendicular to the thin film surface (black) or along the in-plane diagonal depends on the film thickness and temperature. Generally, favorable out-of-plane alignment (in the fc(0.1 T)-curves) is only seen at low temperature for $La_{0.67}Sr_{0.33}Mn_{0.95}Ru_{0.05}O_3$ films with thicknesses between 7.5 nm and 21 nm. Highlighted by the black arrows in Fig. 7.6 are the temperatures at which the magnetic moments during the fc-measurement in 0.1 T were identical when the magnetic field was applied parallel to the surface normal or along the in-plane diagonal. This temperature is shifted to higher temperatures up to a film thickness of 16 nm and decreases again for further thickness enlargement. The thinnest and the thickest thin film of this study do not show perpendicular magnetic anisotropy in the temperature dependent fc magnetization study. While the (preferred in-plane) magnetic anisotropy is comparably weak in case of the 5.5 nm thin film, the in-plane orientation of the magnetization is clearly favorable in case of the 81 nm thin film. Summarizing, the field cooled M(T) measurements indicate that moderate perpendicular anisotropy can be induced in LSMO thin films by the deposition on LSAT and 5% ruthenium substitution in thin films of intermediate thickness, 7.5 nm to 21 nm, at low temperatures.

The thickness- and temperature range in which moderate perpendicular magnetic anisotropy was seen is confirmed by the magnetic field dependent hysteresis loops, which are displayed exemplarily at 10 K in Fig. 7.7 (a), at 100 K in Fig. 7.8, and at 250 K in Fig. 7.7 (b).
Illustrated in Fig. 7.7 are the magnetic hysteresis loops with the magnetic field applied perpendicular to the thin film surface (black) and in the film plane along one of the sample edges (red).

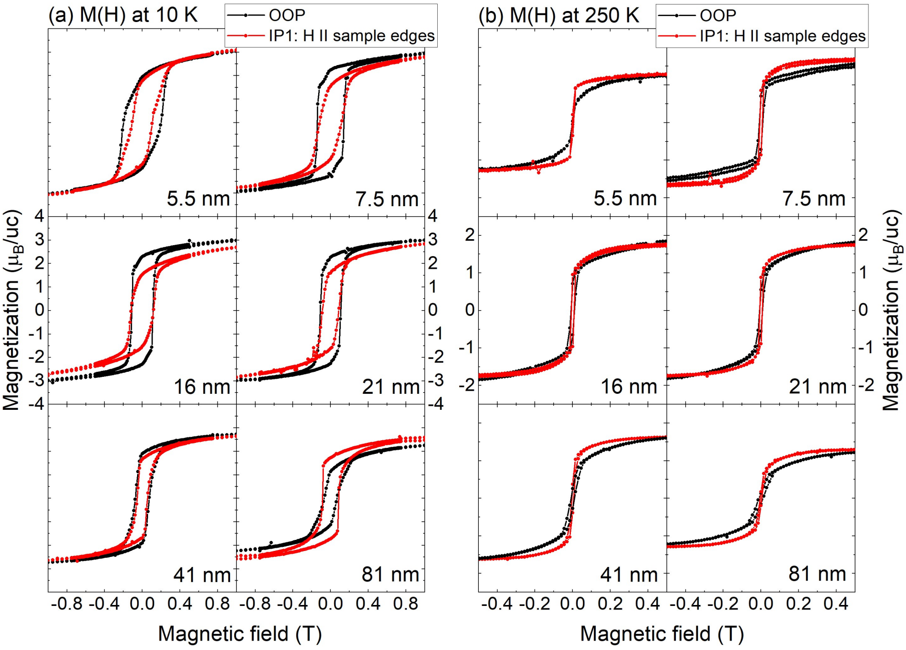

Figure 7.7: Magnetization hysteresis loops of $La_{0.67}Sr_{0.33}Mn_{0.95}Ru_{0.05}O_3$ thin films with thicknesses between 5.5 nm and 81 nm at 10 K (a) and 250 K (b). The measurements were performed with the magnetic field applied parallel to the film surface normal (black) or parallel to the sample edge (red).

The out-of-plane magnetic hysteresis loops of the 7.5 nm, 16 nm, and 21 nm thick $La_{0.67}Sr_{0.33}Mn_{0.95}Ru_{0.05}O_3$ films are more squarish and possess larger magnetization in the remanent state than the corresponding in-plane loops at 10 K, which is in agreement with the moderate perpendicular magnetic anisotropy observed in the temperature dependent magnetization studies. However, the in-plane hysteresis loops still exhibit sizable coercive fields, similar to the out-of-plane loops, and not a clear s-shape. This is an indication that the effective perpendicular magnetic anisotropy is only moderate and the measured in-plane direction is probably not a magnetic hard axis.

The hysteresis loops of the 41 nm thin film possess almost identical magnetic field dependence at 10 K, with a slightly larger remanent magnetization when the magnetic field is applied perpendicular to the thin film surface.

In case of the 81 nm film, the preferred magnetization alignment in the film plane is observed, indicated by the reduced remanent magnetization in the out-of-plane hysteresis loop with respect to the in-plane M(B) loop.

The thinnest film under study has almost identical magnetizations in the remanent state and also similar saturation fields when the magnetic field is applied along the sample edge or parallel to the surface normal. However, the coercive fields as well as the hysteresis loop shapes differ, which might be an indication of variations of the details of the microscopic magnetization reversal.

In contrast to the low temperature M(B)-study, the magnetic hysteresis loops of all the LSMRO films have larger remanent magnetizations when the magnetic field was applied in the film plane at 250 K (presented in Fig. 7.7(b)). This is again in agreement with the preferred in-plane alignment of the magnetization at elevated temperatures which was observed in the M(T) study.

At 100 K (Fig. 7.8), the magnetization loops were measured additionally also with the magnetic field applied along the in-plane diagonal[6] (blue).

The shape of the out-of-plane hysteresis loops of the 7.5 nm and the 16 nm $La_{0.67}Sr_{0.33}Mn_{0.95}Ru_{0.05}O_3$ films is more squarish than of both corresponding in-plane loops, which is consistent with the results from the M(T) study of moderate perpendicular magnetic anisotropy in this temperature and thickness range. In contrast, the 81 nm film clearly exhibits in-plane magnetic anisotropy, according to the large ratio of the magnetization in remanence to the moment in saturation ($M_{\text{rem}}/M_{\text{sat}}$) for the in-plane hysteresis loops and the reduced magnetic moment in remanence in case of the out-of-plane hysteresis loop.

The OOP- and IP2-hysteresis loops of the 21 nm thick LSMRO film show similar magnetic field dependence also at 100 K, which is consistent with the M(T) study in this temperature range. The slightly enhanced $M_{\text{rem}}/M_{\text{sat}}$ ratio of the IP2 hysteresis loop (compared to the OOP loop) in case of the 41 nm thick $La_{0.67}Sr_{0.33}Mn_{0.95}Ru_{0.05}O_3$ film indicates very weak in-plane anisotropy.

---

[6] Due to the required sample mounting with conventional plastic straws for SQUID magnetometry, measurements with more than these orientations could not be performed accurately.

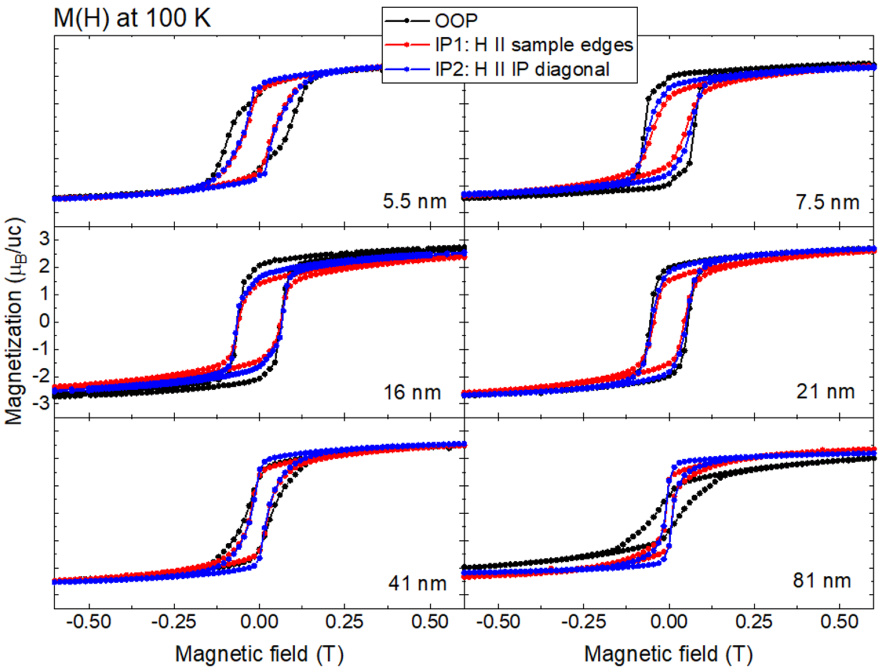

Figure 7.8: Magnetization hysteresis loops at 100 K of $La_{0.67}Sr_{0.33}Mn_{0.95}Ru_{0.05}O_3$ thin films with thicknesses between 5.5 nm and 81 nm. The measurements were performed with the magnetic field applied parallel to the film surface normal (black), parallel to the in-plane diagonal (blue), or parallel to the (in-plane) sample edge (red).

In order to quantify the strength of the magnetic anisotropy, the effective magnetic anisotropy constant K_{eff} was calculated. K_{eff} was estimated from the area between the magnetic out-of-plane and ($[110]_c$) in-plane hysteresis loops in the first quadrant, following the procedure described for instance in Ref. [5]. By definition, K_{eff} is positive if the alignment of the magnetization perpendicular to the film plane is favored over the alignment (along the respective directions) in the film plane.

The thickness dependence of K_{eff} (plotted in purple) and of the ratio of the out-of-plane-magnetization in remanence to the the out-of-plane-magnetization in saturation ($M_{\text{rem}}/M_{\text{sat}}$, black) are displayed in Fig. 7.9.
K_{eff} at 100 K is slightly negative for the 5.5 nm LSMRO film and increases upon thickness increase.

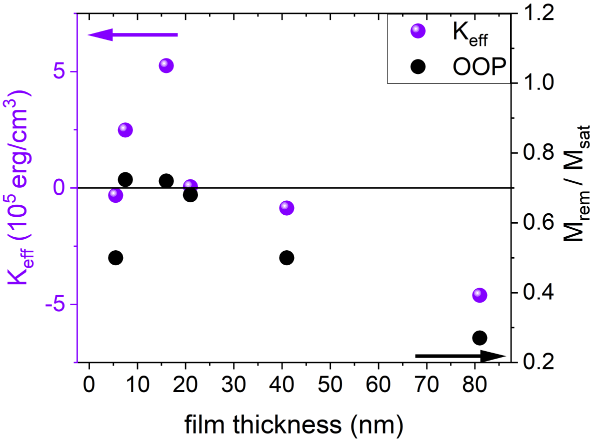

Figure 7.9: Thickness dependence of the effective perpendicular magnetic anisotropy constant K_{eff} (purple) and the ratio of the out-of-plane-magnetization in remanence to saturation $M_{\mathrm{eff}}/M_{\mathrm{sat}}$ (black) at 100 K.

At 100 K, K_{eff} is maximized for a film thickness of 16 nm, which is in agreement with the previously discussed observations from the M(B)- and M(T) investigations. The maximum of K_{eff} is of the order of $5\cdot 10^5$erg/cm^3 and therefore one order of magnitude smaller than it was achieved by octahedral rotation in $La_{1-x}Sr_xMnO_3$-$SrIrO_3$ heterostructures,[5] but is comparable to the effective perpendicular magnetic anisotropy in compressively strained LSMO.[19] With further increasing film thickness, the effective perpendicular magnetic anisotropy at 100 K decreases, it is almost zero for the 21 nm film, and becomes negative for the 41 nm and 81 nm films. The ratio of $M_{\mathrm{rem}}/M_{\mathrm{sat}}$ for the out-of-plane hysteresis loop shows qualitatively similar thickness dependence and is maximized for the 16 nm thin film.

Perpendicular magnetic anisotropy[7] was achieved in LSMO thin films under large compressive strain[3,19,21–27] and attributed to the preferred occupancy of the $3d_{3z^2-x^2}$ orbital.[21] The observed moderate perpendicular magnetic anisotropy is furthermore in agreement with a study by Nakamura *et al.*, who demonstrated that perpendicular magnetic anisotropy can also be induced in

---

[7] Similar induction of moderate perpendicular magnetic anisotropy in LSMO thin films was realized by interfacial modifications in superlattices with $SrTiO_3$[20] or with $SrIrO_3$[5] and attributed to the preferential occupation of the $3d_{3z^2-x^2}$ orbital.[21]

LSMO under weak compressive strain when the manganese is partially (5 % or 10 %) substituted by ruthenium.[10] It was proposed that the PMA was induced by the single-ion anisotropy of the ruthenium, which originated from the compressive-strain-induced lifting of the t_{2g} orbital degeneracy of the doped Ru^{4+}ion and the resulting restorage of orbital momentum in the ruthenium.[10]

The effective magnetic anisotropy constant (at 100 K) shows two spin reorientation transitions as function of thickness: from in-plane to out-of-plane between 5.5 nm and 7.5 nm and back to in-plane above 21 nm. Similar spin reorientation transitions were seen for instance in Cu/Ni films on Cu(001) upon Ni thickness increase.[28] As described in Chapter 2.1 (Equation (2.8)), the effective magnetic anisotropy energy can be written as the sum of the contributions of the bulk (independent of the film thickness t) and a surface and interface contribution that scales with $1/t$. In this way, the spin reorientation from perpendicular magnetization to in-plane magnetization observed in $Fe/Cu_3Au(100)$ films was related to the thickness-increase-related win of the shape anisotropy over the surface anisotropy, which favored the perpendicular magnetization for small thicknesses.[29] If the surface anisotropy of the studied LSMRO thin films is positive, the spin reorientation transition from perpendicular to in-plane magnetization upon thickness increase above 21 nm might originate from such competition of surface and shape anisotropy.

However, the thickness dependence of K_{eff} (cf. Fig. 7.9) cannot be described by this simple $1/t$ scaling in the whole thickness range between 5.5 nm and 81 nm, as two spin reorientations were observed. This indicates that the separation into a thickness-independent bulk term and a single thickness dependent surface contribution is not a proper description of the magnetic anisotropy of the system. Likely, also the bulk terms depend on thickness. As demonstrated in Fig. 7.8, the saturation magnetization weakly increases with film thickness between 5.5 nm and 7.5 nm so that the shape anisotropy is not independent of the thickness.

Furthermore, structural domains that often form in LSMO thin films with bulk rhombohedral structure when they are deposited on cubic substrates (see Chapter 2.2.2 or Ref. [30–32]) might influence the thickness dependence of the magnetic anisotropy. These either unidirectional thickness modulations, unidirectional structural domains,[30] or periodically microtwinned domains[33] were found to impact on the magnetic anisotropy.[34] According to the comparably small ruthenium substitution, the rhombohedral structure of the LSMO film is not expected to be strongly distorted (cf. Chapter 2.2.2). Thus, shear-strain relaxation is expected to take place also in the Ru-substituted LSMO thin films deposited on the cubic LSAT(100) substrates, which induces in-plane biaxial compressive strain. In case of $La_{0.7}Sr_{0.3}MnO_3$ films that were deposited on cubic LSAT substrates, structural domains were observed, with the stripe boundaries along $\{110\}_{\text{cubic}}$ directions.[33] The influence of the formation of structural domains might influence the magnetic anisotropy of the ruthenium substituted LSMO films studied here, as it was observed for instance in ferroelastic $LaCoO_3$ films.[35]

While for the thinner films, the influence of the substrate-induced step-edges might still be relevant, the influence of the existence of elongated terraces on e.g. the shape anisotropy is probably reduced for increased film thickness. The identical shape of the magnetization curves for the magnetic field applied in-plane along $[100]_c$ and $[010]_c$ (parallel to the topographic terraces) for intermediate film thicknesses (see Fig. 7.6) might support this statement. On the other hand, the formation of structural domains and their orientation might become more relevant for increased film thickness.

Structural investigations either by reciprocal space mapping or plane-view TEM would be helpful in order to visualize the formation of structural domains. The improved knowledge about the formation and alignment of structural formations of the films of individual thickness, combined with further angle-dependent measurements would be desirable to improve the understanding of the mechanisms that determine the thickness dependence of the effective perpendicular magnetic anisotropy.

The temperature dependence of the magnetic anisotropy is also related to the distinct temperature dependencies of the contributions of the magnetocrystalline, magnetoelastic, and shape anisotropy as function of temperature. A similar observation of perpendicular magnetic anisotropy only at low temperatures was observed by Xiao *et al.* in compressively strained LSMO and attributed to the preferential occupation of the $3d_{3z^2-x^2}$ orbital and the suppressed transition to the $3d_{x^2-y^2}$ orbital at low temperatures.[21] The shape anisotropy, favoring in-plane alignment, is proportional to the square of the magnetization (cf. Equation (2.7)) and would be maximized at low temperatures. However, only the temperature dependence of the magnetization of the 81 nm thick film could be attributed to the dominance of the shape anisotropy, which might cause the observed increase of the magnetic anisotropy with larger

magnetization along the sample edges and the in-plane diagonal than in the out-of-plane direction. This might be an indication that the compressive epitaxial strain imposed by the LSAT substrates could be partially relaxed in the 81 nm film. However, high resolution XRD studies would be helpful to see whether the film is still fully strained to the substrate.
Temperature-induced spin reorientation in bare LSMO thin films was also attributed to the variation of the relative strength of the biaxial anisotropies (along <110>) and uniaxial contribution along [100].[36] A similar scenario might also influence the temperature dependence of the magnetic anisotropy in the LSMRO thin films under study.

Based on the knowledge of the spin magnetic moment for small (less than 50%) ruthenium substitutions (cf. Chapter 2.2.2, Equation (2.24) or Ref. [37]), the maximum, theoretically expected, saturation magnetization is about 3.4 μ_B/uc for bulk $La_{0.67}Sr_{0.33}Mn_{0.95}Ru_{0.05}O_3$ at low temperatures.[37] For the present thin films, deposited under weak biaxial compressive strain, the magnetization at 100 K is about 2.74 μ_B/uc in case of the 5.5 nm film and 2.9 μ_B/uc for the 16 nm thin film. Even at 10 K, where the saturation magnetization of the 16 nm thin film is about 3.1 μ_B/uc, the observed magnetization values are reduced. However, similar reduction of the magnetization was observed in $La_{0.6}Sr_{0.4}Mn_{1-x}Ru_xO_3$ thin films,[13] in $La_{0.67}Sr_{0.33}MnO_3$ thin films, or LSMO-based heterostructures that exhibit (compressive-strain-induced or interface-induced) perpendicular anisotropy.[5,20,21] Combined XLD and XMCD studies of 30 uc $La_{0.7}Sr_{0.3}MnO_3$ (deposited on LAO) demonstrated the partial lifting of the orbital magnetic moment quenching;[38] with the orbital magnetic moment oriented antiparallel to the spin moment in $La_{0.88}Sr_{0.12}MnO_3$ thin films.[39]
Because of the moderate compressive strain, introduced by the deposition on LSAT in the case of our LSMRO thin films, in combination with the additional elongation of the unit cell in c-direction due to the larger ionic radius of ruthenium, a similar reduction of the magnetic moment due to an antiparallel alignment of spin and orbital Mn moment might be considered. However, also slight off-stoichiometry or the existence of a magnetically dead layer at the film-substrate interface, which is not ferromagnetic, might reduce the overall magnetization.[15] Further possibilities for the reduction might be deviations of the determined and the real film thickness or a possible thickness-dependence of the out-of-plane lattice parameter, which was not calculated individually for every thin film under study.

7.4 Conclusion and outlook

The SQUID magnetometry study of a set of $La_{0.67}Sr_{0.33}Mn_{0.95}Ru_{0.05}O_3$ thin films, which were deposited under small epitaxial strain on LSAT(100) substrates, revealed that moderate perpendicular magnetic anisotropy can be induced by varying the layer thickness. While in-plane anisotropy was observed for the 81 nm thick (5 %) Ru-substituted LSMO film, weak in-plane magnetic anisotropy was seen in a 5.5 nm $La_{0.7}Sr_{0.3}Mn_{0.95}Ru_{0.05}O_3$ thin film. Moderate perpendicular magnetic anisotropy (on the order of 10^5 erg per cm^2 at 100 K) was observed in the intermediate thickness range between 7.5 nm to 21 nm below a layer-thickness-dependent temperature. The observed effective magnetic anisotropy is determined by the competition of the magnetocrystalline anisotropy, shape anisotropy, surface anisotropy, and the magnetoelastic anisotropy. While the shape anisotropy favors in-plane alignment of the magnetization, preferable out-of-plane alignment of the magnetization can be attributed to the compressive strain imposed by the substrate combined with the induced single-ion anisotropy due to the ruthenium substitution. In order to determine the total magnetic anisotropy, detailed angle dependent magnetization or magnetoresistance measurements would be required. In addition to the biaxial anisotropy, a uniaxial contribution along $[001]_O$ was for instance observed in 40 nm $La_{0.7}Sr_{0.3}MnO_3$ films, which were deposited on LSAT(100).[18] Such additional contribution cannot be investigated without detailed angular dependent studies.
Obtaining moderate perpendicular anisotropy, preferably at high temperatures, is desirable in the context of skyrmion creation in thin film heterostructures. Its competition with DMI that is generated at the interface of the ferromagnet and a strong spin-orbit coupled layer was shown to stabilize topologically nontrivial spin textures.[8] The observed moderate perpendicular anisotropy indicates that 5.5 nm to 21 nm thick $La_{0.67}Sr_{0.33}Mn_{0.95}Ru_{0.05}O_3$ films, deposited on LSAT(100), might be suitable candidates to generate magnetically non-trivial structures when the layers are interfaced with a strong spin-orbit coupled material, such as $SrIrO_3$.

The perpendicular magnetic anisotropy can be further enhanced by the increase of the Ru content to 10 %. Shown in Fig. 7.10 are the (fc) temperature dependent magnetization curves of a 2 nm, 6 nm, and a 9 nm $La_{0.7}Sr_{0.3}Mn_{0.9}Ru_{0.1}O_3$ film, which were deposited on LSAT(100).

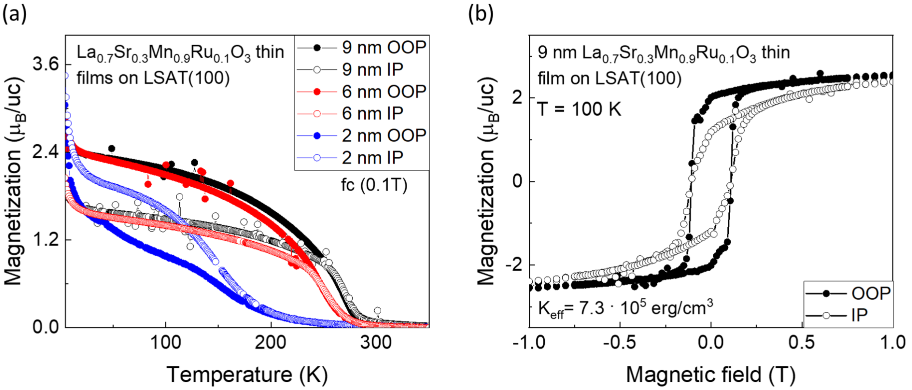

Figure 7.10: (a) M(T)-study of $La_{0.7}Sr_{0.3}Mn_{0.9}Ru_{0.1}O_3$ thin films of 2.5 nm to 9 nm thickness, deposited on LSAT(100). (b) Magnetic hysteresis loops of a 9 nm thick $La_{0.7}Sr_{0.3}Mn_{0.9}Ru_{0.1}O_3$ film at 100 K. The magnetic field was applied perpendicular to the film surface (full symbols) and in-plane along the sample edge (open symbols).

The comparison with the fc measurements of the set of $La_{0.67}Sr_{0.33}Mn_{0.95}Ru_{0.05}O_3$ thin films indicates that the magnetic anisotropy is enhanced and perpendicular magnetic anisotropy can be induced in a broader temperature range for the films of intermediate thickness (6 nm and 9 nm). Furthermore, the magnetic hysteresis loop of the 9 nm film shows a larger $M_{\mathrm{rem}}/M_{\mathrm{sat}}$ ratio at 100 K (cf. Fig. 7.10 (b)) and enhanced effective magnetic anisotropy, compared with the $La_{0.67}Sr_{0.33}Mn_{0.95}Ru_{0.05}O_3$ films in a comparable thickness range. However, the detailed investigations of the thickness dependent magnetic anisotropy are desirable also for this set of LSMO films with 10 % ruthenium substitution. The strong initial decrease of the magnetization in the M(T)-curve and the s-shape contribution around zero magnetic field in the M(B)-curve could be indications of magnetic impurities that impact on the total measured magnetic properties. In order to study the sample characteristics, these contributions need to be reduced, as it was achieved for the $La_{0.67}Sr_{0.33}Mn_{0.95}Ru_{0.05}O_3$ thin film series.

Acknowledgement and own contribution

The presented thin films were deposited and the film morphology was investigated by me. I also performed the corresponding SQUID magnetometry. The presented XRR- and XRD measurements were performed by Brajagopal Das.

References

[1] A.-M. Haghiri-Gosnet and J.-P. Renard: *CMR manganites: physics, thin films and devices*, J. Phys. D: Appl. Phys. **36**, R127 (2003).

[2] H. Meng and J.-P. Wang: *Spin transfer in nanomagnetic devices with perpendicular anisotropy*, Applied Physics Letters **88**, 172506 (2006).

[3] C. Song, X. Li, L. Shen, B. Cui, X. Xu, G. Yu, M. Liu, S. Meng, and K. Wu: *Emergent perpendicular magnetic anisotropy at the interface of an oxide heterostructure*, Physical Review B **104**, 115162 (2021).

[4] R. Sbiaa, H. Meng, and S. N. Piramanayagam: *Materials with perpendicular magnetic anisotropy for magnetic random access memory*, physica status solidi (RRL) – Rapid Research Letters **5**, 413–419 (2011).

[5] D. Yi, C. L. Flint, P. P. Balakrishnan, K. Mahalingam, B. Urwin, A. Vailionis, A. T. N'Diaye, P. Shafer, E. Arenholz, Y. Choi, K. H. Stone, J.-H. Chu, B. M. Howe, J. Liu, I. R. Fisher, and Y. Suzuki: *Tuning Perpendicular Magnetic Anisotropy by Oxygen Octahedral Rotations in* $(La_{1-x}Sr_xMnO_3)/(SrIrO_3)$ *Superlattices*, Physical Review Letters **119**, 077201 (2017).

[6] S. Wu, Y. Zhang, C. Tian, J. Zhang, M. Wu, Y. Wang, P. Gao, H. Yu, Y. Jiang, J. Wang, K. Meng, and J. Zhang: *Prototype Design of a Domain-Wall-Based Magnetic Memory Using a Single Layer* $La_{0.67}Sr_{0.33}MnO_3$ *Thin Film*, ACS Applied Materials and Interfaces **13**, 23945–23950 (2021).

[7] B. Dieny and M. Chshiev: *Perpendicular magnetic anisotropy at transition metal/oxide interfaces and applications*, Review of Modern Physics **89**, 025008 (2017).

[8] A. Fert, V. Cros, and J. Sampaio: *Skyrmions on the track*, Nature Nanotechnology **8**, 152–156 (2013).

[9] N. Nagaosa and Y. Tokura: *Topological properties and dynamics of magnetic skyrmions*, Nature Nanotechnology **8**, 899–911 (2013).

[10] M. Nakamura, D. Morikawa, X. Yu, F. Kagawa, T.-h. Arima, Y. Tokura, and M. Kawasaki: *Emergence of Topological Hall Effect in Half-Metallic Manganite Thin Films by Tuning Perpendicular Magnetic Anisotropy*, Journal of the Physical Society of Japan **87**, 074704 (2018).

[11] M. Ziese, F. Bern, A. Setzer, E. Pippel, D. Hesse, and I. Vrejoiu: *Existence of a magnetically ordered hole gas at the* $La_{0.7}Sr_{0.3}MnO_3/SrRuO_3$ *interface*, The European Physical Journal B **86**, 42 (2013).

[12] S. Hasegawa: Reflection high-energy electron diffraction, *Characterization of materials* (John Wiley & Sons, Ltd, 2012), 1925–1938.

[13] H. Yamada, M. Kawasaki, and Y. Tokura: *Ru-doped* $La_{0.6}Sr_{0.4}MnO_3$ *thin films as a coercivity tunable electrode for magnetic tunnel junctions*, Applied Physics Letters **86**, 192505 (2005).

[14] B. C. Chakoumakos, D. G. Schlom, M. Urbanik, and J. Luine: *Thermal expansion of* $LaAlO_3$ *and* $(La,Sr)(Al,Ta)O_3$*, substrate materials for superconducting thin-film device applications*, Journal of Applied Physics **83**, 1979–1982 (1998).

[15] M. Huijben, L. W. Martin, Y.-H. Chu, M. B. Holcomb, P. Yu, G. Rijnders, D. H. A. Blank, and R. Ramesh: *Critical thickness and orbital ordering in ultrathin* $La_{0.7}Sr_{0.3}MnO_3$ *films*, Physical Review B **78**, 094413 (2008).

[16] H. Boschker, M. Huijben, A. Vailionis, J. Verbeeck, S. van Aert, M. Luysberg, S. Bals, G. van Tendeloo, E. P. Houwman, G. Koster, D. H. A. Blank, and G. Rijnders: *Optimized fabrication of high-quality* $La_{0.67}Sr_{0.33}MnO_3$ *thin films considering all essential characteristics*, Journal of Physics D: Applied Physics **44**, 205001 (2011).

[17] S. K. Chaluvadi: "Influence of the epitaxial strain on magnetic anisotropy in LSMO thin films for spintronics applications", PhD thesis (Normandie Universite, 2017).

[18] H. Boschker, M. Mathews, P. Brinks, E. Houwman, A. Vailionis, G. Koster, D. H. Blank, and G. Rijnders: *Uniaxial contribution to the magnetic anisotropy of* $La_{0.67}Sr_{0.33}MnO_3$ *thin films induced by orthorhombic crystal structure*, Journal of Magnetism and Magnetic Materials **323**, 2632–2638 (2011).

[19] Y. Wu, Y. Suzuki, U. Rüdiger, J. Yu, A. D. Kent, T. K. Nath, and C. B. Eom: *Magnetotransport and magnetic domain structure in compressively strained colossal magnetoresistance films*, Applied Physics Letters **75**, 2295–2297 (1999).

[20] B. Zhang, L. Wu, J. Zheng, P. Yang, X. Yu, J. Ding, S. M. Heald, R. A. Rosenberg, T. V. Venkatesan, J. Chen, C.-J. Sun, Y. Zhu, and G. M. Chow: *Control of magnetic anisotropy by orbital hybridization with charge transfer in* $(La_{0.67}Sr_{0.33}MnO_3)_n/(SrTiO_3)_n$ *superlattice*, NPG Asia Materials **10**, 931–942 (2018).

[21] Z. Xiao, F. Zhang, M. A. Farrukh, R. Wang, G. Zhou, Z. Quan, and X. Xu: *Perpendicular magnetic anisotropy in compressive strained* $La_{0.67}Sr_{0.33}MnO_3$ *films*, Journal of Materials Science **54**, 9017–9024 (2019).

[22] C. Kwon, M. C. Robson, K.-C. Kim, J. Y. Gu, S. E. Lofland, S. M. Bhagat, Z. Trajanovic, M. Rajeswari, T. Venkatesan, A. R. Kratz, R. D. Gomez, and

R. Ramesh: *Stress-induced effects in epitaxial ($La_{0.7}Sr_{0.3}$)MnO_3 films*, Journal of Magnetism and Magnetic Materials **172**, 229–236 (1997).

[23] Y. Suzuki, Y. Wu, J. Yu, U. Ruediger, A. D. Kent, T. K. Nath, and C. B. Eom: *Domain structure and magnetotransport in epitaxial colossal magnetoresistance thin films*, Journal of Applied Physics **87**, 6746–6748 (2000).

[24] J. Dho, Y. N. Kim, Y. S. Hwang, J. C. Kim, and N. H. Hur: *Strain-induced magnetic stripe domains in $La_{0.7}Sr_{0.3}MnO_3$ thin films*, Applied Physics Letters **82**, 1434–1436 (2003).

[25] J. Dho and N. H. Hur: *Thickness dependence of perpendicular magnetic anisotropy in $La_{0.7}Sr_{0.3}MnO_3$ films on $LaAlO_3$*, Journal of Magnetism and Magnetic Materials **318**, 23–27 (2007).

[26] Y. Jiang, G. Y. Gao, Y. Wang, and H. L. W. Chan: *Temperature evolution of anisotropic stress induced highly ordered stripe magnetic domains in $La_{0.7}Sr_{0.3}MnO_3$ thin film on (110) $NdGaO_3$ substrate*, Solid State Communications **150**, 2028–2031 (2010).

[27] J. Wang, S. Wu, J. Ma, L. Xie, C. Wang, I. A. Malik, Y. Zhang, K. Xia, C.-W. Nan, and J. Zhang: *Nanoscale control of stripe-ordered magnetic domain walls by vertical spin transfer torque in $La_{0.67}Sr_{0.33}MnO_3$ film*, Applied Physics Letters **112**, 072408 (2018).

[28] K. Fukumoto, H. Daimon, L. Chelaru, F. Offi, W. Kuch, and J. Kirschner: *Micromagnetic properties of the Cu/Ni crossed wedge film on Cu(001)*, Surface Science **514**, 151–155 (2002).

[29] M.-T. Lin, J. Shen, W. Kuch, H. Jenniches, M. Klaua, C. M. Schneider, and J. Kirschner: *Structural transformation and spin-reorientation transition in epitaxial Fe/Cu_3Au(100) ultrathin films*, Physical Review B **55**, 5886 (1997).

[30] J. E. Boschker, Å. F. Monsen, M. Nord, R. Mathieu, J. K. Grepstad, R. Holmestad, E. Wahlström, and T. Tybell: *In-plane structural order of domain engineered $La_{0.7}Sr_{0.3}MnO_3$ thin films*, Philosophical Magazine **93**, 1549–1562 (2013).

[31] T. F. Zhou, G. Li, X. G. Li, S. W. Jin, and W. B. Wu: *Self-generated in-plane superlattice in relaxed epitaxial $La_{0.67}Sr_{0.33}MnO_3$ films*, Applied Physics Letters **90**, 042512 (2007).

[32] A. Vailionis, H. Boschker, W. Siemons, E. P. Houwman, D. H. A. Blank, G. Rijnders, and G. Koster: *Misfit strain accommodation in epitaxial ABO_3 perovskites: Lattice rotations and lattice modulations*, Physical Review B **83**, 064101 (2011).

[33] S. W. Jin, G. Y. Gao, Z. Huang, Z. Z. Yin, X. Zheng, and W. Wu: *Shear-strain-induced low symmetry phase and domain ordering in epitaxial* $La_{0.7}Sr_{0.3}MnO_3$ *thin films*, Applied Physics Letters **92**, 261901 (2008).

[34] B. Paudel, B. Zhang, Y. Sharma, K. T. Kang, H. Nakotte, H. Wang, and A. Chen: *Anisotropic domains and antiferrodistortive-transition controlled magnetization in epitaxial manganite films on vicinal* $SrTiO_3$ *substrates*, Applied Physics Letters **117**, 081903 (2020).

[35] E.-J. Guo, R. Desautels, D. Keavney, M. A. Roldan, B. J. Kirby, D. Lee, Z. Liao, T. Charlton, A. Herklotz, T. Z. Ward, M. R. Fitzsimmons, and H. N. Lee: *Nanoscale ferroelastic twins formed in strained* $LaCoO_3$ *films*, Science Advances **5**, eaav5050 (2019).

[36] F. Tsui, M. C. Smoak, T. K. Nath, and C. B. Eom: *Strain-dependent magnetic phase diagram of epitaxial* $La_{0.67}Sr_{0.33}MnO_3$ *thin films*, Applied Physics Letters **76**, 2421–2423 (2000).

[37] L. M. Wang, J.-H. Lai, J.-I. Wu, Y.-K. Kuo, and C. L. Chang: *Effects of Ru substitution for Mn on* $La_{0.7}Sr_{0.3}MnO_3$ *perovskites*, Journal of Applied Physics **102**, 023915 (2007).

[38] C. Aruta, G. Ghiringhelli, V. Bisogni, L. Braicovich, N. B. Brookes, A. Tebano, and G. Balestrino: *Orbital occupation, atomic moments, and magnetic ordering at interfaces of manganite thin films*, Physical Review B **80**, 014431 (2009).

[39] Y. Kim, S. Ryu, and H. Jeen: *Strain-effected physical properties of ferromagnetic insulating* $La_{0.88}Sr_{0.12}MnO_3$ *thin films*, RSC Advances **9**, 2645–2649 (2019).

Chapter 8

Anisotropic magnetoresistance and the observation of unidirectional structural domain formation in a Ru-substituted LSMO thin film deposited on LSAT(100)

Contents

In this chapter, the magnetic and magnetotransport investigations of a 42.5 nm $La_{0.67}Sr_{0.33}Mn_{0.95}Ru_{0.05}O_3$ thin film, which was deposited under compressive strain on LSAT(100), are presented. The magnetoresistance exhibits a strong dependence on the angle between the current and the crystallographic axes. Reciprocal space mapping reveals the formation of unidirectional structural domains. Magnetic force microscopy demonstrated the formation of locally ordered magnetic stripe domains that cause domain wall resistance.

8.1 Introduction

The magnetoresistance (MR) of half-metallic strontium-doped lanthanum manganite (LSMO) thin films is the complex result of contributions of the colossal MR, conventional Lorentz MR, domain wall resistance, and anisotropic magnetoresistance.[1] Tailoring of the magnetic properties by engineering of the epitaxial strain state, substrate miscut, or interfacial octahedral coupling was shown to modify the weight of the contributions of the individual MR effects in LSMO thin films.[1–4]

Magnetic stripe domains, locally parallel to each other, were for instance stabilized in $La_{0.7}Sr_{0.3}MnO_3$ films by imposing large epitaxial compressive strain.[5] This caused strong in-plane anisotropy of the magnetoresistance due to the dominant domain wall resistance contribution, which was determined by the angle between the current direction and the domain walls.[5]

Wang *et al.* achieved anisotropic in-plane magnetoresistance by highly anisotropic tensile strain. However, this was detrimental to the ferromagnetic ground state of the LSMO layer.[2] Another way to induce in-plane anisotropic magnetoresistance is the interfacial octahedral coupling when LSMO is deposited on orthorhombic $NdGaO_3$ (110) substrates, as shown by Liao *et al.*[3]

In the subsequently presented study, anisotropic magnetoresistance hysteresis loops are reported, measured for the two orthogonal in-plane directions parallel to the sample edges, when the magnetic field was applied perpendicular to the film surface. This was measured on a 42.5 nm $La_{0.67}Sr_{0.33}Mn_{0.95}Ru_{0.05}O_3$ thin film, which was deposited on LSAT(100). As discussed in Chapter 7, such thin films show significant out-of-plane tilting of the magnetic easy axis. It was furthermore asserted that magnetic skyrmions can form in a similar thin film, a 30 nm thick $La_{0.67}Sr_{0.33}Mn_{0.95}Ru_{0.05}O_3$ film deposited on LSAT(100), inferred from Hall features mimicking a topological Hall effect, magnetic bubble domains in magnetic force microscopy, and supportive Lorentz microscopy images.[6]

In the presented study, the simultaneous measurement of the magnetoresistance and polar MOKE magnetometry, combined with magnetization hysteresis loops acquired by SQUID magnetometry, enabled the connection of the anisotropic magnetoresistance and the anisotropic magnetic properties of the thin film. Furthermore, magnetic force microscopy investigations showed the formation of parallel stripe domains when the magnetic field was applied perpendicular to the film surface. These stripe domains that showed preferential alignment at finite angle perpendicular to the substrate-induced terraces led to significant domain wall resistance and thereby to low field features in the MR hysteresis loops. The structural analysis by x-ray reciprocal space mapping indicated the formation of a unidirectional superlattice structure that likely influenced the magnetic anisotropy and thereby the preferential alignment of the magnetic stripe domains.

8.2 Thin film deposition and topographic investigation

(a)

Deposition parameter	
Temperature	650 °C
O_2 pressure	0.133 mbar
Laser repetition rate	5 Hz
Number of pulses	5100
Laser fluence	2.4 J cm^{-2}

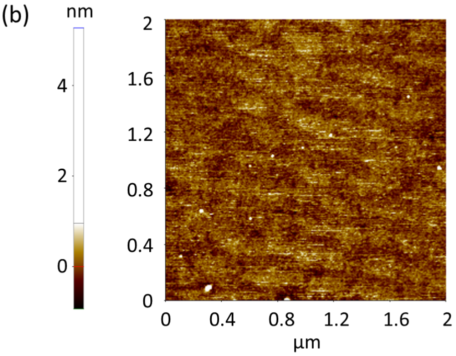

Figure 8.1: (a) Deposition parameters of the 42.5 nm LSMO thin film. (b) Atomic force microscopy scan (2 µm × 2 µm) of the thin film topography after deposition. The AFM image was taken by Lin Yang.

The Ru-substituted $La_{0.67}Sr_{0.33}Mn_{0.95}Ru_{0.05}O_3$ (Ru-LSMO) thin film was grown on an LSAT(100) substrate with the pulsed-laser deposition set-up produced by *SURFACE*. The substrate with a miscut angle of about 0.1° was annealed at 1000 °C for 2 hours in air.

The thin film was deposited from a $La_{0.67}Sr_{0.33}Mn_{0.95}Ru_{0.05}O_3$ target under the conditions summarized in the table in Fig. 8.1 (a).

Based on the x-ray reflectometry of a twin sample and from the deposition parameters, a film thickness of 42.5 nm was estimated.

Atomic force microscopy images taken shortly after growth, presented in Fig. 8.1 (b), confirm the crystallinity of the thin film and the surface smoothness. The thickness modulations with a periodicity of 200 nm to 250 nm likely originate from the imprinted step-and-terrace structure of the miscut substrate.

8.3 Magnetotransport study

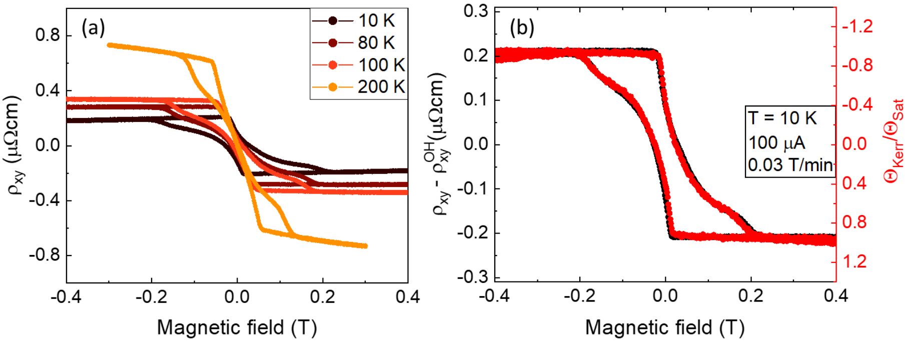

Figure 8.2: (a) Hall resistivity loops of the 42.5 nm $La_{0.67}Sr_{0.33}Mn_{0.95}Ru_{0.05}O_3$ thin film at representative temperatures. (b) Anomalous Hall resistivity (black) and the normalized Kerr rotation angle (red) as function of the applied magnetic field at 10 K. To increase the comparability, the axis of the normalized Kerr rotation angle is reversed.

Motivated by the observation of anomalies in the Hall loops that mimic a topological Hall effect in the study by Nakamura *et al.*[6] (see Fig. 8.3), the Hall hysteresis loops of the investigated 42.5 nm $La_{0.67}Sr_{0.33}Mn_{0.95}Ru_{0.05}O_3$ film were compared with the simultaneously measured MOKE hysteresis loops.

The Hall investigations, displayed in Fig. 8.2, were performed with the home-built MOKE-transport set-up that was described in Chapter 3. The Hall resistivity was measured in van der Pauw geometry with cyclic permutation of the contacts to remove artificial contact and longitudinal magnetoresistance effects.

Under the assumption that the $La_{0.67}Sr_{0.33}Mn_{0.95}Ru_{0.05}O_3$ thin film behaves like a conventional ferromagnet,[7] the total Hall resistivity loops, presented in Fig. 8.2 (a), can be described by the sum of the ordinary Hall resistivity ρ_{xy}^{OH} and the anomalous Hall resistivity ρ_{xy}^{AH}. The ordinary Hall resistivity, dominant in the high magnetic field range when the thin film is saturated and the anomalous Hall effect (AHE) therefore constant, indicates the contribution of multiple conduction channels with p- and n-type charge carriers. While the high field behavior is linear with a positive slope at 10 K, it is almost magnetic field independent at 100 K, and shows a nonlinear negative dependence on the applied magnetic field at 200 K. This temperature dependence of the ordinary Hall resistivity, including a sign change of $d\rho_{xy}^{OH}/dB$, indicates the insufficiency of the explanation in a single-type carrier model. Similar behavior of the ordinary Hall effect was observed experimentally in thin films of the parent compound $La_{0.7}Sr_{0.3}MnO_3$[8] and theoretically predicted by the existence of electron and hole pockets at the Fermi surface.[8,9]

The anomalous Hall constant of the ruthenium-substituted LSMO thin film is negative throughout the investigated temperature range between 10 K and 200 K. An enhancement of the magnitude of the AHE upon temperature increase is observed, despite the temperature-induced decrease of the out-of-plane magnetization (see Fig. 8.9 (d)). This shows that the anomalous Hall constant increases significantly with temperature up to 200 K, which is consistent with the reported behavior of a 30 nm Ru-substituted LSMO thin film in the study by Nakamura *et al.*[6] Similar temperature dependencies of ρ_{xy}^{AH} were furthermore observed in $La_{1-x}Sr_xMnO_3$ single crystals,[10,11] bare LSMO thin films,[8] or $La_{0.7}Sr_{0.3}MnO_3/SrTiO_3$ heterostructures,[12] which indicates that the overall AHE constant of the studied ruthenium-substituted LSMO thin film resembles the characteristics of the parent compound.

The total Hall resistivity loops of the investigated Ru-LSMO thin film[1] do not show any peculiar features between 10 K and 200 K (see Fig. 8.2 (a)), but scale well with the Kerr rotation angle, presented exemplarily in Fig. 8.2 (b) at 10 K.

This is contrary to the study by Nakamura *et al.* on a similar $La_{0.7}Sr_{0.3}Mn_{0.95}Ru_{0.05}O_3$ thin film, who observed hump-like features in the Hall resistivity loops, as depicted exemplarily at 100 K in Fig. 8.3 (a). Bubble-like features were seen in their MFM measurements in the magnetic field range where the magnetic stripe domains of alternating magnetization direction split into smaller domains, which is in agreement with the magnetic field region where the humps appeared in the Hall loop, as presented in Fig. 8.3 (c) and (d). Nakamura *et al.* observed topological Hall resistivities between 5 K and 200 K, on the order of maxmimum 0.65 µΩ cm (cf. Fig. 8.3 (b)), which was not seen for our 42.5 nm thick $La_{0.67}Sr_{0.33}Mn_{0.95}Ru_{0.05}O_3$ film in the temperature range between 10 K and 200 K (cf. Fig. 8.2 (a)). However, the skyrmion-induced topological Hall resistivity is often much smaller than the anomalous Hall resistivity and therefore hardly observable in the overall magnetic field

---

[1] The Hall loops of a twin sample, investigated by Daniel Jansen and Lin Yang, also did not exhibit unconventional features when the magnetic field was swept with similar rates.[13]

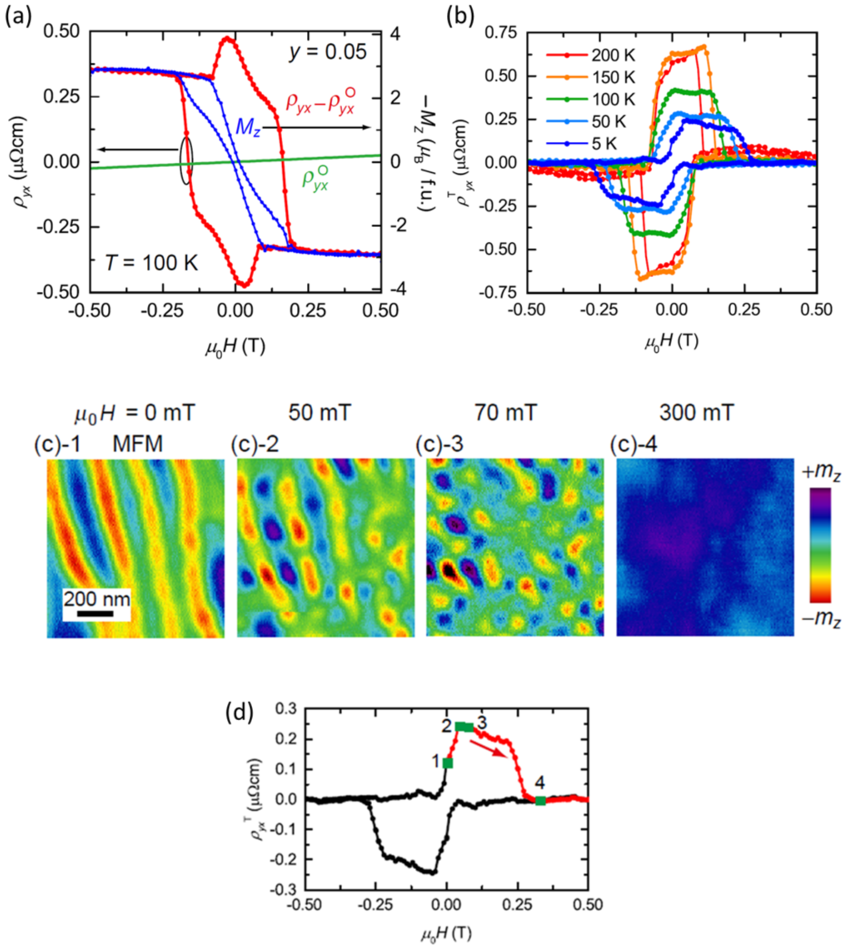

Nakamura *et al.*, JPSJ **87**, 074704 (2018)

Figure 8.3: Hall resistivity and MFM measurements of a 30 nm La$_{0.7}$Sr$_{0.3}$Mn$_{0.95}$Ru$_{0.05}$O$_3$ thin film, which was deposited on LSAT(100). (a) Magnetic field dependence of the ordinary Hall resistivity ρ_{yx}^{O} (green), $\rho_{yx} - \rho_{yx}^{\mathrm{O}}$ (red), and the magnetization M_z (blue). ρ_{yx}^{O} was derived by linear fitting of the $\rho_{yx}(H)$ curve above a magnetic field of 1 T. The scale of the vertical axis for ρ_{yx} and that for M_z are adjusted so that they overlap at 0.5 T. (b) Temperature evolution of the topological Hall resistivity ρ_{yx}^{T} versus H. (c) MFM investigations at 10 K. (d) $\rho_{xy}^{\mathrm{T}}(H)$ curve at 10 K. The red arrows indicate the scan direction and the green data points correspond to the magnetic fields where the MFM measurements were performed. (Sub-)figures are reproduced from Ref. [6], ©(2018) The Physical Society of Japan.

dependence of ρ_{xy} (see for instance Ref. [14]). In order to extract the topological Hall resistivity, the ordinary ρ_{xy}^{OH} and the anomalous Hall resistivities ρ_{xy}^{AH} were subtracted from the total Hall resistivity.[14]

Such subtraction was performed exemplarily for the backward half of the hysteresis loop at 10 K, depicted in Fig. 8.4 (a). The anomalous Hall resistivity was calculated by the scaling of $\rho_{xy} - \rho_{xy}^{OH}$ with the Kerr rotation angle in 0.4 T. The subtraction yields a sharp, peak-like contribution on the order of $-0.023\,\mu\Omega\,\mathrm{cm}$ at around -0.01 T, and thus close to the field of initial domain nucleation, referring to the polar MOKE loop. Compared to the results of Ref. [6] displayed in Fig. 8.3 (b), the peak is much sharper.

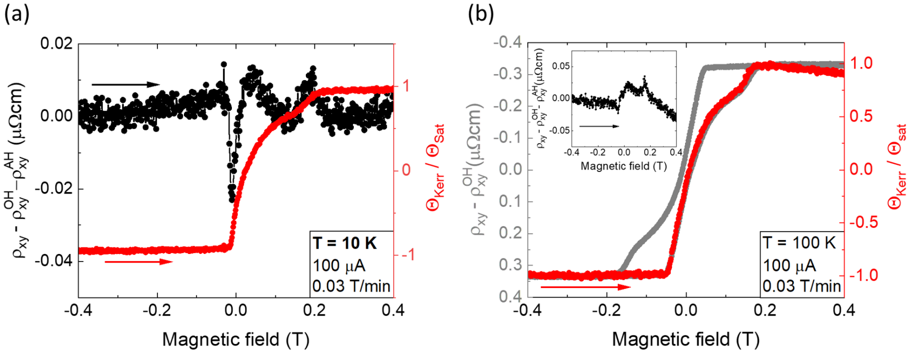

Figure 8.4: (a) Normalized Kerr rotation angle (red) and $\rho_{xy} - \rho_{xy}^{OH} - \rho_{xy}^{AH}$ (black) during the magnetic field sweep from -0.4 T to 0.4 T at 10 K. (b) Magnetic field dependence of $\rho_{xy} - \rho_{xy}^{OH}$ (grey) and the normalized Kerr rotation angle (red) for the magnetic field sweep from -0.4 T to 0.4 T at 100 K. Shown in the inset is $\rho_{xy} - \rho_{xy}^{OH} - \rho_{xy}^{AH}$ (black) during the same magnetic field sweep at 100 K.

Such differences between the Hall properties of the two Ru-substituted LSMO thin films of similar thickness can originate from differences of the sample characteristics, such as exact film thickness, small differences of the stoichiometry, or the LSAT substrate morphology which was shown to impact on the formation of structural domains in LSMO films (see for instance Ref. [15]). It might also originate from the differences of the resistivity measurement set-up. The Hall resistivity was measured in van der Pauw geometry in our case, while Hall bars were patterned in Ref. [6].

Whether the sharp peak in the Hall loop shown in Fig. 8.4 (a) originates from the presence of magnetic skyrmions cannot be concluded based on the Hall measurements exclusively and requires further investigations, such as real space imaging for instance. Even when MOKE and Hall resistivity are measured simultaneously, the small peak-like feature might still be caused by tiny (artificial) variations of the two measurables. Imperfection of the background corrections, required for both quantities, as well as variations of the sensitivity of the two techniques on impurity contributions can lead to such non-vanishing contributions, as it was also observed in ferromagnetic, topologically trivial systems.[16] Furthermore, the Kerr rotation angle measured with the home-built set-up sometimes exhibits a drift of the measurement signal[2], which is visible in the data presented in Fig. 8.4 (b). The (artifical) linear decrease of the normalized Kerr rotation angle above 0.2 T is an indication that this measurement at 100 K was affected by this effect. $\rho_{xy} - \rho_{xy}^{OH} - \rho_{xy}^{AH}$ was calculated again by the subtraction of ρ_{xy}^{AH}, determined from the measured Kerr rotation angle normalized to $\rho_{xy} - \rho_{xy}^{OH}$ at -0.4 T. Thus, also $\rho_{xy} - \rho_{xy}^{OH} - \rho_{xy}^{AH}$, presented in the inset of Fig. 8.4 (b), is influenced by the drift and the observed finite contribution should not be overinterpreted.

Magnetoresistance study

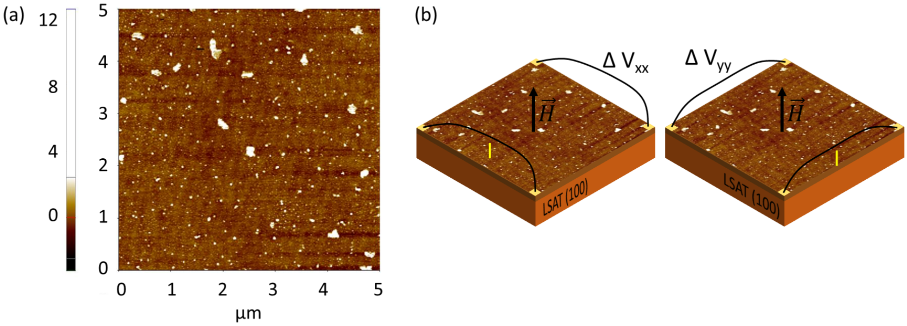

Figure 8.5: Atomic force microscopy images (5 µm × 5 µm) the 42.5 nm thick Ru-substituted LSMO thin film under study, taken after the sample stayed in air for several weeks (a). The definition of the potential differences measured along the two edges of the sample with respect to the topographic terraces is indicated in (b). ΔV_{xx} is measured mainly along the terraces, ΔV_{yy} perpendicular to them.

---

[2] One origin of the drift might be the usage of a thermally non-stabilized PEM. The temporal evolution of the ambient temperature of the PEM was shown to cause thermal drift of the measurement signal, which was demonstrated by the manufacturer *HINDS Instruments*.[17]

Also the subsequently presented longitudinal resistance and magnetoresistance measurements were performed in van der Pauw geometry. The measured voltages are defined as indicated in Fig. 8.5 (b). Due to the miscut of the substrate, making an angle of about 12° ± 2° with respect to the sample edge and therefore to $[100]_c$ or $[010]_c$ direction (cf. AFM image in Fig. 8.5 (a)) , the voltages are not measured exactly parallel or perpendicular to the substrate induced terraces. Thus, the directions will be named as "mainly parallel" or "mainly perpendicular" to the terraces subsequently. ΔV_{xx} is the voltage measured mainly parallel to the topographic terraces (inherent to the vicinal LSAT substrate), which were still clearly visible in the atomic force microscopy image shown in Fig. 8.5 (a), after the sample stayed in air for several weeks. ΔV_{yy} was measured mainly perpendicular to the terraces. The calculation of the corresponding resistivities was performed according to the extension of the van der Pauw method by Price, which is valid for rectangular samples of anisotropic material.[18]

Under the assumption that the current flows everywhere in the sample parallel to the sample plane and ρ_{xx} and ρ_{yy} are the principal resistivities in the plane, the van der Pauw equation is given by:[18]

$$\exp\left(-\frac{\pi d R_{AB,CD}}{(\rho_{xx}\rho_{yy})^{1/2}}\right) + \exp\left(-\frac{\pi d R_{BC,DA}}{(\rho_{xx}\rho_{yy})^{1/2}}\right) - 1 = 0 \tag{8.1}$$

Equation (8.1) can be solved numerically, for instance by the Newton method, in order to calculate $(\rho_{xx}\rho_{yy})^{1/2}$.[18] To determine ρ_{xx} and ρ_{yy}, $(\rho_{xx}/\rho_{yy})^{1/2}$ has to be determined firstly. For squared samples of thickness d, as in the present case, $R_{\mathrm{BC,DA}}$ is given by:[18]

$$R_{\mathrm{BC,DA}} = -\frac{8(\rho_{xx}\rho_{yy})^{1/2}}{\pi d} \times \ln\left(\prod_{n=0}^{\infty} \tanh\left[(\rho_{xx}/\rho_{yy})^{1/2}(2n+1)\frac{\pi}{2}\right]\right) \tag{8.2}$$

and analogously

$$R_{\mathrm{AB,CD}} = -\frac{8(\rho_{xx}\rho_{yy})^{1/2}}{\pi d} \times \ln\left(\prod_{n=0}^{\infty} \tanh\left[(\rho_{yy}/\rho_{xx})^{1/2}(2n+1)\frac{\pi}{2}\right]\right) \tag{8.3}$$

As long as $(\rho_{xx}/\rho_{yy})^{1/2} \not\ll 1$, $(\rho_{xx}/\rho_{yy})^{1/2}$ can be approximated by:

$$(\rho_{xx}/\rho_{yy})^{1/2} = -\frac{1}{\pi}\ln\left(\tanh\left[\pi d R_{\mathrm{BC,DA}}/16(\rho_{xx}\rho_{yy})^{1/2}\right]\right) \tag{8.4}$$

The principal resistivities are then given by:

$$\rho_{xx} = (\rho_{xx}\rho_{yy})^{1/2} \cdot (\rho_{xx}/\rho_{yy})^{1/2} \tag{8.5}$$

$$\rho_{yy} = (\rho_{xx}\rho_{yy})^{1/2} \div (\rho_{xx}/\rho_{yy})^{1/2} \tag{8.6}$$

The longitudinal resistivities of the thin film measured without external magnetic field (zfc), drawn in red in Fig. 8.6 (a), increase upon temperature increase, as commonly observed for the parent compound $La_{0.67}Sr_{0.33}MnO_3$.[19] The metal-to-insulator transition temperature is above room temperature, which is consistent with the ferromagnetic transition temperature that is also above room temperature (compare Fig. 8.9 (d)).

Despite the squarish sample size, the zero-field resistivities possess different values. This could be an indication of structural anisotropy, such as a monoclinic or orthorhombic distortion of the unit cell[20] or structural domain formation,[15,21] as it was observed in undoped LSMO thin films that were deposited on cubic substrates.

The application of 5 T, perpendicular to the thin film surface, leads to the reduction of both longitudinal resistivities, as plotted in black in Fig. 8.6 (a). According to the field dependent magnetization study in Fig. 8.9, the field cooling in 5 T should be sufficient to realize a magnetic single-domain state so that domain wall resistance should not contribute to the overall measured resistivities in 5 T. The temperature dependent magnetoresistance, drawn in blue in Fig. 8.6 (a), was calculated by $\mathrm{MR} = (\rho(5\mathrm{T}) - \rho(\mathrm{zfc}))/\rho(\mathrm{zfc})$. MR is negative over the entire ferromagnetic temperature range, with increasing absolute values upon temperature enhancement. Close to the metal-to-insulator transition, the magnetoresistance of about -20% is maximum, which can be attributed to the dominance of the colossal magnetoresistance (CMR) in this temperature range (e.g. Ref. [1, 19, 22]). The CMR in double-exchange manganites is typically maximum close to the MIT, because the influence of the suppression of spin fluctuations by the application of a magnetic field is maximized in this temperature range.[23]

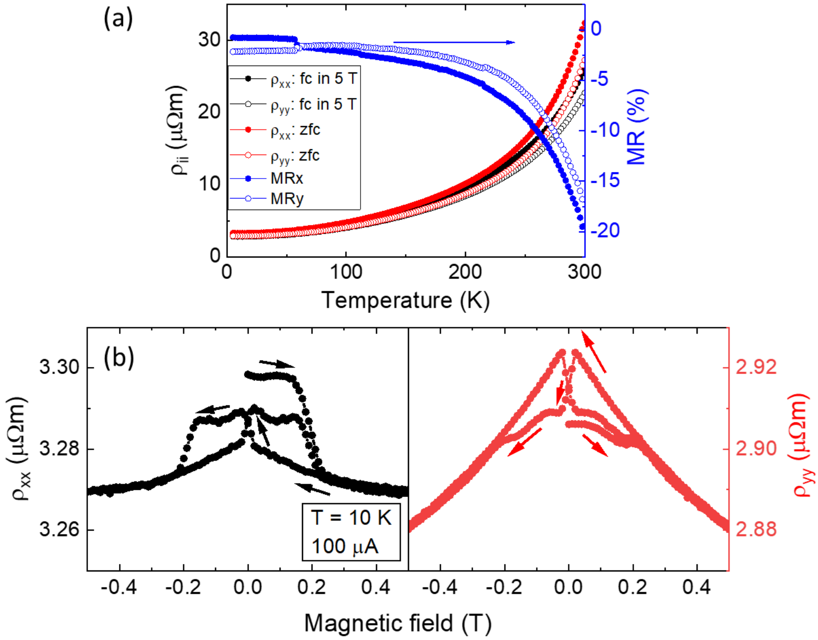

Figure 8.6: (a) Longitudinal resistivities ρ_{xx} (full symbols) and ρ_{yy} (open symbols) as function of temperature in absence of an external magnetic field (red), and in presence of 5 T (black) applied perpendicular to the thin film surface. The magnetoresistance is plotted versus temperature in blue symbols. (b) Magnetoresistivities ρ_{xx} (black) and ρ_{yy} (red) as function of the magnetic field which was applied perpendicular to the film plane at 10 K. Current $I = 100\,\mu\mathrm{A}$ was used for all the resistivity measurements.

Presented in Fig. 8.6 (b) are the magnetic field dependent longitudinal resistivity measurements at 10 K, when the magnetic field was applied perpendicular to the thin film surface. The sweep directions for ρ_{xx} (black) and ρ_{yy} (red) are indicated by arrows. The magnetoresistivity hysteresis loops were taken after cooling the sample to 10 K without external magnetic field. As displayed in Fig. 8.6 (b), the loops show anisotropic magnetoresistivity with low field features that depend on the direction of the applied current. Similar anisotropic magnetoresistivity was observed for a twin sample by Daniel Jansen and Lin Yang.[13] The virgin magnetoresistivity curves decrease for sweeping the magnetic field up to 0.5 T for both current directions. However, the features of the magnetoresistivity virgin curves are mirror-like and the slopes in the magnetic field range above 0.25 T differ, which will be addressed in more detail later.

When the magnetic field is swept back from positive to negative magnetic fields, strong differences of the initial virgin magnetoresistivity and the subsequent magnetoresistivity in zero magnetic field are observed. While the MR in the virgin state is larger than the subsequent magnetoresistivity in zero magnetic field in case of ρ_{xx}, it is smaller for ρ_{yy}. Such differences between the initial zero-field state and the subsequent zero-field magnetoresistivity might be an indication that the domain patterns of the initial zero-field and the subsequent zero-field state differ and therefore different contributions of the domain wall resistance are measured. Such effect was observed for instance in $SrRuO_3$ thin films with strong magnetic anisotropy, where the samples remanent state was still a single domain-state, while zero field cooling led to the formation of a magnetic stripe-domain pattern.[24] Although the magnetic anisotropy in the Ru-substituted LSMO film is smaller than in the case of $SrRuO_3$ thin films, based on the results of Chapter 7, differences in the domain pattern between the initial and subsequent zero-field states might still exist.
A magnetoresistance study of thin films of the parent compound $La_{0.7}Sr_{0.3}MnO_3$, deposited on LAO(001), revealed a similar initial drop of the magnetoresistivity and distinct zero-field magnetoresistivities.[25] It was proposed that grain boundaries that have a non-collinear Mn-spin structure at the LSMO-substrate interface are the origin of the large resistivity in the virgin state, while the application of a magnetic field can align the spins ferromagnetically and thereby decrease the resistivity strongly.[25] In a similar way, also the existence of structural twins that are oriented by the application of an external magnetic field might be a possible origin of the distinct zero-field magnetoresistivities. As it will be shown later in the chapter, undirectional structural domain formation was observed in the 42.5 nm $La_{0.67}Sr_{0.33}Mn_{0.95}Ru_{0.05}O_3$ thin film under study. If these structural domains can be oriented or modified by the application of a magnetic field, similar to the magnetic field control of structural domains in $SrRuO_3$ single crystals,[26] differences of the magnetoresistivities after zero field cooling and in the remanent state would be expected. However, structural x-ray investigations before and after the application of magnetic fields on the order of the saturation field would be helpful to conclude on this speculation.

Not only the virgin curves, but also the magnetoresistivity hysteresis loops exhibit strong dependence on whether the current is applied mainly along (ρ_{xx}) or mainly perpendicular (ρ_{yy}) to the topographic step edges. When the sample was saturated in positive magnetic field, ρ_{xx} shows an almost linear increase close to zero magnetic field values, while ρ_{yy} shows a decrease. At $-17\,\mathrm{mT}$ and $-150\,\mathrm{mT}$, ρ_{xx} has local maxima in the magnetoresistivity and ρ_{yy} local minima. Such mirror-like features often originate from anisotropic magnetoresistance effects due to differences in the angle between the sample magnetization and direction of the electric current.[1,22] In the present case, the magnetic field is always applied perpendicular to the thin film surface. However, as discussed in Chapter 7, the direction of preferential alignment of the magnetization makes a finite angle with the surface normal of the thin film under study. Thus, during the sweeping through the magnetic hysteresis loop, magnetic domains and domain walls will be formed, where the magnetization is rotated away from the surface normal and has finite in-plane components. The angle between these in-plane components of the magnetization and the current direction most likely differs for ρ_{xx} and ρ_{yy} as long as the external magnetic field is insufficient to align the magnetization fully along the surface normal. Another source of an in-plane magnetization component could originate from closure domains, as it was for instance observed in $\mathrm{Fe}_{0.8}\mathrm{Ga}_{0.2}$ thin films.[27,28]

In order to disentangle the various contributions of the overall magnetoresistance (MR), such as the anisotropic MR, CMR, and domain wall magnetoresistance, the magnetization reversal and the details of magnetic domain formation[3] need to be understood. An accurate way to correlate the magnetoresistance with the macroscopic magnetic properties is to measure both quantities simultaneously. This was achieved with our home-built magnetotransport set-up that allowed the simultaneous detection of the magnetoresistance and magneto-optical Kerr effect in polar geometry (p-MOKE). The p-MOKE study was performed with coherent laser light of 491 nm wavelength. The presented hysteresis loops were corrected for the linear background contribution originating from the optical cryostat window. The following magnetoresistance hysteresis loops were calculated by the consideration of the subsequent zero-field state as $\rho(0T)$.

Due to its proportionality to the out-of-plane component of the magnetization, the p-MOKE hysteresis loops, drawn in red in Fig. 8.7, are considered as qualitative measure of the z-component of the macroscopic sample magnetization.

---

[3] The domain formation was investigated by MFM and is addressed in Fig. 8.10.

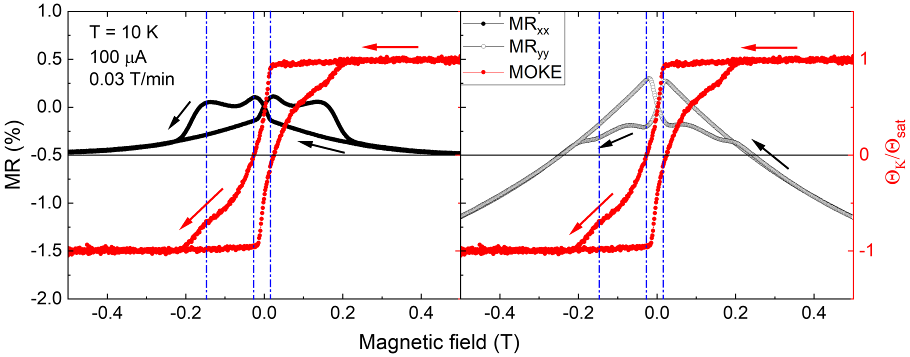

Figure 8.7: Normalized Kerr rotation angle (red), MR_{xx} (black, full symbols), and MR_{yy} (black, open symbols) as function of the external magnetic field, which was applied perpendicular to the thin film surface at 10 K.

Its comparison with the magnetoresistance loops, drawn in black, shows the direct correlation of the low field MR features and the characteristics of the magnetic domain formation imprinted in the macroscopic MOKE hysteresis loop. A similar correlation between the mirror-like features in the magnetoresistance and the MOKE loops were also observed for a twin sample, investigated by Daniel Jansen.[13]

After saturating the sample in large magnetic fields, the initial increase (decrease) in MR_{xx} (MR_{yy}) appears at the same magnetic field for which the first initial decrease is observed in the p-MOKE loop, indicating the formation of magnetic domains with reversed magnetization direction. At the coercive field of around ±0.017 T, determined from the MOKE hysteresis loop, the MR exhibits either a local maximum for MR_{xx}, or local minimum for MR_{yy}. The magnetic field where a plateau is seen in the MOKE hysteresis loops at 150 mT correlates with the second local extremum in the MR loops.

The magnetic field dependence of the MR, possessing multiple local extrema, is most likely related to the existence of magnetic domains that have different switching fields and therefore induce magnetic domains walls and corresponding domain wall resistance, as it was seen in $SrRuO_3$ films that showed regions with distinct local switching fields related to structural twin domains.[29] Similarly, multiple switching events were observed in the magnetoresistance loops of a 60 nm $La_{0.67}Ca_{0.33}MnO_3$ / 5 nm $SrTiO_3$/ 40 nm $La_{0.67}Ca_{0.33}MnO_3$ trilayer, which was attributed to the existence of multiple domains.[30]

Furthermore, the MR and p-MOKE hysteresis loops close consistently at about

±0.22 T. However, even in the magnetic field range above ±0.22 T, both MR channels possess distinct slopes as well as deviations from the linear scaling with the magnitude of the magnetic field that would be expected for pure CMR in LSMO.[22] Therefore, the MR and macroscopic magnetic properties were studied in an enlarged magnetic field range, performed with commercially available PPMS and MPMS3 (both *Quantum Design Inc.*).

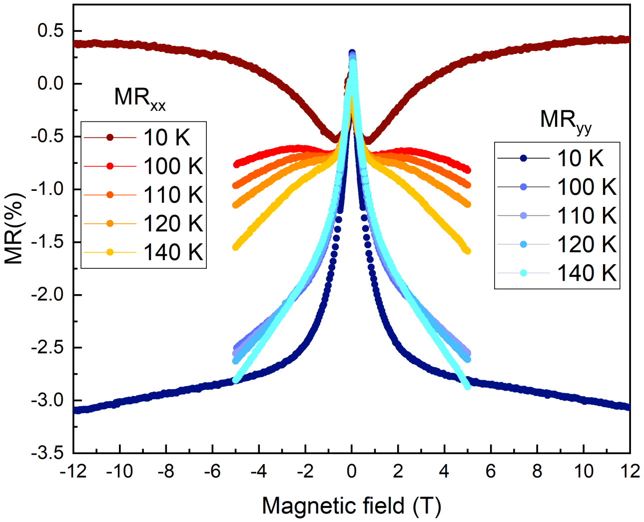

Figure 8.8: Magnetic field dependence of the magnetoresistance measured along the topographic terraces ($\mathrm{MR}_{\mathrm{xx}}$, redish) and perpendicular ($\mathrm{MR}_{\mathrm{yy}}$, bluish) at representative temperatures. The sweep from positive to negative magnetic field values is shown for 100 µA applied current.

As depicted in Fig. 8.8, both magnetoresistance channels $\mathrm{MR}_{\mathrm{xx}}$ and $\mathrm{MR}_{\mathrm{yy}}$ exhibit strong dependence on temperature and the direction of current application, even in magnetic fields up to 12 T.

Generally, the magnetoresistance hysteresis curves can be divided qualitatively into three magnetic field regions, which are determined by distinct main contributions to the MR, respectively. Due to the previous discussion of the low field features, the focus of the subsequent section is on the intermediate and high magnetic field range.

The colossal magnetoresistance typically dominates the MR in the high magnetic field range, where the film is in a magnetic single-domain state and the magnetization macroscopically aligned along the external magnetic field direction so that the contributions of the domain wall resistance and anisotropic magnetoresistance are negligible.[1,22] Except for the $\mathrm{MR_{xx}}$ loop at 10 K, $\mathrm{MR_{xx}}$ and $\mathrm{MR_{yy}}$ scale linearly with $|H|$ in the high magnetic field range (above about 3-4 T), which is typically observed in CMR manganites.[1,22,31,32] Related to the magnetic field induced suppression of spin fluctuations, CMR was observed in bare $La_{0.7}Sr_{0.3}MnO_3$ thin films, deposited on $SrTiO_3$, even up to 60 T.[33] The negative slope of the MR curves in large magnetic fields increases upon temperature enhancement, as visible in Fig. 8.8. This is in accordance with the expectation of the CMR in manganites and the observed MR-temperature dependence displayed in Fig. 8.6 (a).

Also the shapes of the MR curves in the intermediate magnetic field range depend on the direction of the applied current. While $\mathrm{MR_{yy}}$ decreases with the enlargement of the magnetic field, $\mathrm{MR_{xx}}$ has a positive slope in the intermediate magnetic field range. This mirrored behavior can be attributed likely again to anisotropic magnetoresistance effects.[1,22]

The observed anisotropy of the (magneto-)resistances of the two channels hints towards the existence of a magnetic anisotropy within the thin film plane.

SQUID magnetometry (with a MPMS3, *Quantum Design Inc.*) enabled the determination of the magnetization reversal in larger magnetic fields than in case of the p-MOKE set-up, and for different orientations of the applied magnetic field.

The magnetic field was applied perpendicular to the thin film surface for the out-of-plane (OOP) hysteresis loops, and in the film plane along the two sample edges for the two IP hysteresis loops (roughly along $[100]_c$ and $[010]_c$), as sketched in the inset of Fig. 8.9 (a). The shown hysteresis loops were corrected for the diamagnetic contribution of the substrate by linear fitting in the range between ± 6 and 7 T at low temperatures and between ± 4.8 and 7 T at 240 K. As shown in Fig. 8.9 (a), the magnetic hysteresis loop shows significant rotation of the magnetic moment up to about 5 T when the magnetic field is applied along the OOP direction. Such rotation of the magnetic moment indicates that[4] the magnetic moments are still tilted with respect to the external magnetic field direction so that there exists an in-plane component of the magnetization which probably makes distinct angles with the two orthogonal in-plane current directions.

The comparison of the magnetic hysteresis loops in the magnetic field range between ± 0.5 T, displayed in Fig. 8.9 (b), indicates that this thin film does not show (dominant) perpendicular magnetic anisotropy, because the OOP- and IP1-hysteresis loops exhibit very similar shape. This is an indication that the magnetization is canted with similar components in the OOP- and the IP1-directions, which is consistent with the behavior of the 41 nm thin film that was studied in Chapter 7. Angular dependent measurements are required for definite statements about the type of anisotropy and the orientation of the possible easy axis.

The two IP magnetic hysteresis loops, measured with the magnetic field applied in the plane but along the two orthogonal sample edges (along $[100]_c$ and $[010]_c$) are shown in red and orange. The comparison shows that the orientation of the magnetization along the IP2-direction is energetically less favorable than along IP1, since the remanent state of the IP2 hysteresis loop is lower and the overall loop has a more pronounced s-shape (with still significant hysteresis loop opening).

At 240 K (cf. Fig. 8.9 (c)), this anisotropy within the film plane weakens, as the shape of the two in-plane loops are more similar than at low temperatures. However, the magnetization along IP2 is still energetically less favorable than along IP1, indicated by the lower remanence and more s-like shape of the magnetic moment loop. The magnetization component in the OOP direction is smaller than in the two in-plane directions at 240 K, which indicates that the magnetization tends to rotate more towards the film plane at elevated temperatures.

This is reflected in the m(T)-curves during the warming up process in 0.1 T after field cooling in the same magnetic field, shown in Fig. 8.9 (d). While the OOP- and IP1-m(T)-curves increase with temperature decrease, the m(T)-curve with the magnetic field in IP2 direction increases up to about 280 K before it decreases for further temperature decrease. This leads to the situation that the difference of the magnetizations (at 0.1 T) between the OOP- and IP1-curves is reduced for decreasing temperature. In contrast, the difference

---

[4] However, also parasitic paramagnetic contributions from impurities of the substrate might contribute to this rotation of magnetization.

between the magnetizations when the magnetic field is applied along the two sample edges increases upon temperature decrease. As it will be discussed in detail subsequently, this behavior can possibly originate from the existence of unidirectional domain formation so that the corresponding shape anisotropy contributions differ for the two in-plane directions.

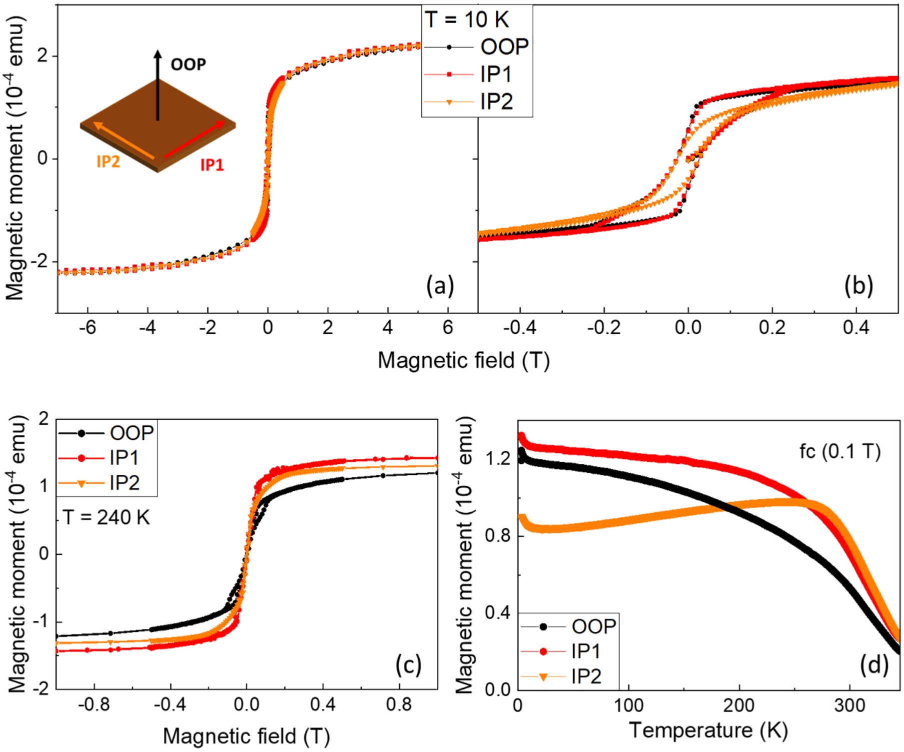

Figure 8.9: Magnetic field dependence of the magnetic moment at 10 K ((a) and (b)). Shown in (b) is a zoom-in between ± 0.5 T to highlight the low field magnetization reversal. The definition of the respective magnetic field orientations is drawn in the inset in (a). Magnetic moment hysteresis loop at 240 K (c). (d) Temperature dependence of the magnetic moment during warming up in 0.1 T after field cooling with the magnetic field applied along three directions, as sketched in the inset in (a).

The comparison of the magnetic moment studies of this 42.5 nm and the 41 nm (cf. Chapter 7) thick $La_{0.67}Sr_{0.33}Mn_{0.95}Ru_{0.05}O_3$ films reveal similarities, but also differences of the magnetic properties. Both thin films of similar thickness exhibit canted magnetization with comparable components for the OOP and IP1 direction (parallel to the sample edges) at low temperatures, as presented in Fig. 7.7 and Fig. 8.9 (a). However, the magnetic hysteresis loops of the 42.5 nm thick film are narrower with smaller coercive fields, which can indicate variations in the details of the magnetic domain formation. Such differences could originate from the distinct annealing procedures of the LSAT substrates and the resulting differences of the substrate topography prior to the deposition. While the substrate used for the 41 nm thick film was annealed as described in Chapter 3.1.2, which created regular step-and-terrace-like structure, the 42.5 nm thick film was deposited on a substrate without well-defined terrace structure due to the annealing at low temperatures of 1000 °C (cf. Fig. 8.1 (b)). As described in detail in Chapter 2, the topography of the substrate, the miscut angle, and the miscut direction are known to impact on the formation of structural twin domains or thickness modulations in LSMO thin films[15] and thereby influence the magnetic anisotropy.[34] In order to improve the understanding of the observed differences, the magnetic properties of a set of Ru-substituted LSMO thin films, which are deposited on substrates with distinct miscut angles, could be compared.

8.4 Correlation of macroscopic and microscopic magnetic properties

The subsequently presented magnetic force microscopy investigations of the 42.5 nm $La_{0.67}Sr_{0.33}Mn_{0.95}Ru_{0.05}O_3$ thin film were performed by the group of Dr. Peter Milde at the Technical University Dresden. A low-temperature non-contact scanning force microscope was used, operated under ultra-high vacuum conditions (2×10^{-10} mbar).[35] The change of the cantilever oscillation frequency was detected in the so-called two-path mode in order to separate the contributions from van der Waals forces between tip and sample and the magnetostatic interactions. Here, the topography was measured first, followed by a second scan with the tip retracted by 20 nm.[35] Both scans were acquired with a hard-magnetic-coated MFM tip. In order to remove artificial background effects, the images were corrected by subtracting the image in high magnetic field (2 T).

Presented in Fig. 8.10 is the comparison of the polar MOKE hysteresis loop (k) and relevant magnetic force microscopy images [(a) - (j)] at 10 K. For both measurements, the external magnetic field was applied perpendicular to the thin film surface.

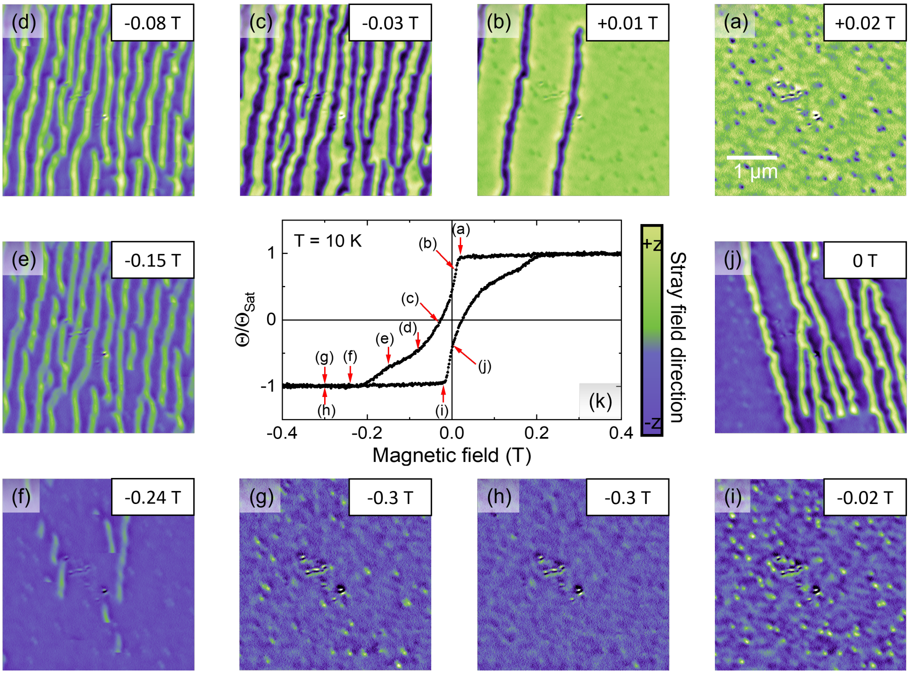

Figure 8.10: Magnetic force microscopy measurements at 10 K with the magnetic field applied perpendicular to the thin film surface. The domain formation is shown at selected magnetic fields during the forward sweep [(a) - (g)] after saturating the sample in 2 T. Presented in [(h) - (j)] are MFM images during the reversed sweep after saturation in -2 T. The color scale corresponds to the measured out-of-plane component of the samples magnetic stray field with green in positive and blue in negative z-direction. (k) Polar MOKE hysteresis loop at 10 K measured with coherent light of 491 nm, normalized to its maximum value in high magnetic fields.

The Kerr rotation angle, proportional to the z-component of the sample magnetization, was normalized to its maximum value at 0.4 T.

The selected MFM images visualize the magnetic domain formation during a magnetic field sweep after saturating the thin film in 2 T. For all the images shown in Fig. 8.10, the measured change of the cantilever oscillation frequency Δf was transformed so that the displayed color code corresponds to the out-of-plane component of the magnetic stray field in positive (green) and negative (blue) z-direction, normalized to the maximum values in ± 2 T.

When the magnetic field is reduced from 2 T towards zero magnetic field, spherical objects with several nanometers diameter form at 20 mT (see Fig. 8.10 (a)).

Except for these objects, the thin film is still homogeneously magnetized parallel to the applied magnetic field with a small, stripy modulation of the magnetic contrast that likely originates from thickness modulations.
At 10 mT (see Fig. 8.10 (b)), initial stripe domains of reversed orientation nucleate, with the out-of-plane stray field component in -z-direction, and lateral extension of about 200 nm to 250 nm. This is in good agreement with the strong decrease of the Kerr rotation angle hysteresis loop that is observed at 0.017 T. When the magnetic field direction is reversed, the number of magnetic stripe domains as well as their elongation increase up to approximately −30 mT, where the areas of stripe domains with the stray field parallel and antiparallel to the applied magnetic field are similar. This is in accordance with the coercive field of −0.027 T determined from the polar MOKE hysteresis loop shown in (see Fig. 8.10 (k)). For magnetic fields larger than −0.03 T, the stripe domains with the OOP-stray field component oriented antiparallel to the applied magnetic field shrink in size until the thin film is homogeneously magnetized at −0.3 T. However, again spherical objects with the stray field aligned antiparallel to the external magnetic field persist still at −0.3 T (see Fig. 8.10 (g)) and can be erased only in large fields of −1 T.
Sweeping the magnetic field back from −2 T to 0 T, the formation of bubble-like features is again observed at −0.02 T. Close to zero magnetic field values, stripe domains are formed again.

The origin of the bubble-like features cannot be clearly pinpointed with our measurement means. However, by the comparison of the MFM images at 0.02 T and at −0.02 T (see Fig. 8.10 (a) and (i)), a memory effect of these bubble-like features is observed. Further comparison with the topography scan, presented in Fig. 8.11, indicates that the bubble-like features are not only formed at the same sites but at positions where topographic defects of maximum 5 nm height are seen. Additional clusters of a few nanometers lateral extension and similar height (3 nm to 4 nm), probably of a different material due to their visibility in the dissipation scan in Fig. 8.11 (c), are seen in the topography image, but are invisible in the MFM image. Thus, it can be assumed that the observed bubble-like features are real magnetic contrast and not an artificial imprint of topographic defects in the MFM images.
These tiny particles of a few nanometers height could originate from the formation of SrO mounds on the LSAT substrates during the annealing process.[36]
When the LSMO thin film is deposited on a substrate with such SrO clusters

on the surface, the material will deposit also on top of these clusters.
This probably leads to local variations of the measured out-of-plane stray field of the thin film surface around these particles.

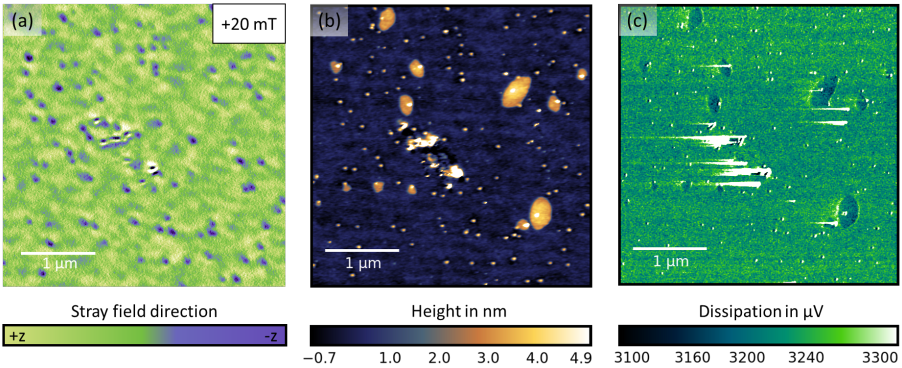

Figure 8.11: Magnetic force microscopy at 10 K in 0.02 T. Corresponding topography (b) and dissipation scan (c) of the thin film at 10 K, acquired at the same position as the MFM image in (a).

These feature are observed in relatively large fields before reaching saturation, or at ±0.02 T before the formation of initial reversed stripe domains. Our Hall measurements did not reveal any THE-like features in these magnetic field ranges. Furthermore, the magnetic field range is not consistent with the peak in the $\rho_{xy} - \rho_{xy}^{OH} - \rho_{xy}^{AH}$-curve (cf. Fig. 8.4 (a)) so that these domains cannot be the origin of the peak. Thus, these spherical objects are likely topologically trivial.
Since the bubble-like objects are observed in a magnetic field range where no hints of reversed domain formation or persistence were observed in the MOKE hysteresis loop, their contribution to the macroscopic magnetization is most likely too weak to be sensed by the MOKE investigations.

The formation of magnetic stripe domains, maze-like or only locally parallel, is often observed in LSMO thin films when perpendicular magnetic anisotropy was realized.[5,32,37–41] If the perpendicular magnetic anisotropy in LSMO thin films was induced by uniaxial compressive strain, for instance by the deposition of relatively thick films on orthorhombic $NdGaO_3$ (110), ordered stripe domains were found in zero field after application of a saturating magnetic field perpendicular to the thin film surface.[38,41] Here, the comparison of the orientation of the magnetic stripe domains with the film topography did not point out any correlation between the alignment and the film surface structure.[41] However, when the PMA was generated in LMSO thin films by inducing biaxial compressive strain, for instance by the usage of $LaAlO_3$ substrates, parallel stripe domains were observed in zero field only after the application of an in-plane saturation magnetic field.[32,38] The domains were then aligned mainly along the direction of the previously applied in-plane magnetic field.[31,32,38] When the magnetic field was applied perpendicular to the thin films, maze-like or locally parallel magnetic stripe domains were seen in the zero-field state,[38,42] which was attributed to the lack of a preferred in-plane orientation of the magnetization in case of biaxially compressively strained LSMO films.[38]

According to the temperature and magnetic field dependent magnetization study, our 42.5 nm $La_{0.67}Sr_{0.33}Mn_{0.95}Ru_{0.05}O_3$ thin film does show neither clear perpendicular magnetic anisotropy, nor magnetically isotropic in-plane behavior. Instead, a significant out-of-plane tilting of the magnetization was seen. Moreover, the in-plane magnetization measurements showed that the orientation of the magnetization along one sample edge is energetically more favorable, while the orientation at 90 degree is magnetically harder.

Thus, the formation of parallel stripe domains could probably be attributed to this combination of out-of-plane tilting of the magnetic easy axis and the anisotropic in-plane behavior. This in-plane magnetic anisotropy might be related to structural anisotropy of the thin film.

In order to investigate the structural characteristics of the thin film, x-ray diffraction off-specular reciprocal space mapping of a twin sample were performed on the $(0\bar{1}3)$,$(\bar{1}03)$,(013), and (103) reflections, as presented in Fig. 8.12.

The Bragg reflections of the LSAT substrate and the ruthenium-substituted LSMO film are located at identical position of $|Q_X|$, in both (0kl) and (h0l) planes, which shows that the thin film is fully strained.[21] Furthermore it indicates that effects due to the relaxation of lattice-mismatch-induced strain are probably negligible.[21] The Q_z values of the (013) and $(0\bar{1}3)$ reflections are enhanced or decreased with respect to the identical Q_z values of the $(\bar{1}03)$ and (103) reflections. This is an indication of the tilting of the pseudocubic c-axis of the thin film with respect to LSAT c-axis.[43] Likely, the Ru-LSMO unit cell is (e.g. monoclinically) distorted, as it was observed in thin films of ferroelastic, rhombohedral $LaCoO_3$ deposited on cubic $SrTiO_3(100)$ substrates.[43]

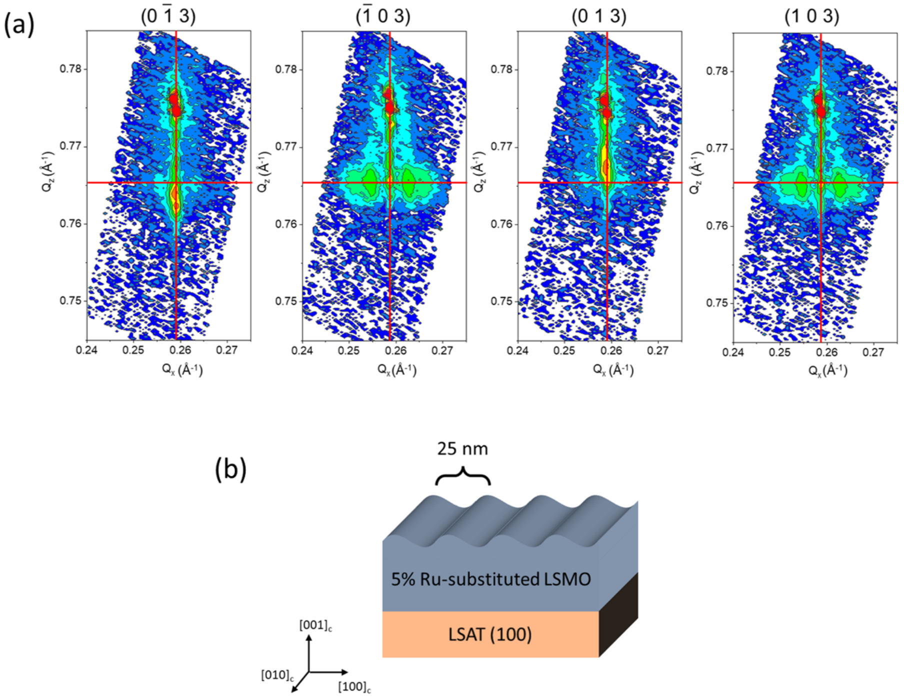

Figure 8.12: (a) X-ray diffraction reciprocal space maps on (0$\bar{1}$3), ($\bar{1}$03), (013), and (103) reflections at room temperature. The red lines are guides to the eye. The presented measurements were performed by Brajagopal Das on a twin sample, which was deposited by Jörg Schöpf. (b) Proposed schematic of the shear-strain-relaxation induced formation of unidirectional structural modulation along $[100]_c$.

Additional satellite peaks, symmetric and broadened with respect to the main peak, are observed in the RSMs in ($\bar{1}$03) and (103) reflections, but are absent for the (013) and (0$\bar{1}$3), indicating the formation of a unidirectional in-plane superlattice.[44] The periodicity of this superlattice in $[100]_\mathrm{c}$ direction was estimated from the spacing of $|Q_X|$ between main and satellite peaks to be 25 nm. However, to visualize the formation of domains on the cubic LSAT substrate microscopically, plan-view TEM images would be required, as shown in Ref. [21].

Similar characteristics were observed in off-specular reciprocal space maps in thin films of the parent LSMO compound.[21,45] Based on the reciprocal space maps[5], the structural domain formation along $[100]_c$ can be sketched as presented in Fig. 8.12 (b).

The monoclinic distortion of the unit cell and the formation of the unidirectional structure is expected to impact on the magnetic anisotropy.[34] Probably the shape anisotropy favors the alignment of the magnetization along the structural domains due to the small width of the structural modulation of about 25 nm.

Combining the angle dependent in-plane magnetization measurements, the observation from MFM that the magnetic stripe domains form perpendicular to the substrate-induced terraces, and the structural investigations, one plausible model[6] is that the unidirectional structural modulation takes place along the terraces so that the structural domain walls are perpendicular to the terraces. Such effect was seen in bare LSMO thin films that were deposited on miscut $SrTiO_3$(100) substrates and attributed to the nucleation at the step edges during the intial growth stage.[15] Also the studied thin film was deposited on a miscut substrate so that this effect might have caused the formation of the structural modulation along the topographic terraces.

Although the attribution of the magnetic stripe domain formation to the unidirectional structural domains is not straightforward, the observation of a unidirectional structural modulation might still be a potential origin of the (weak) preferential alignment of the magnetization along the IP1 direction (cf. Fig. 8.9). Since these unidirectional structural stripes have a width of about 25 nm, much smaller than the elongation of these stripes, the shape anisotropy contribution is expected to be reduced when the magnetization is aligned along these structural domains. Due to the proportionality of the shape anisotropy to the magnetization, its contribution to the effective magnetic anisotropy decreases upon temperature increase. This is in agreement with the observed weakening of the anisotropy in the film plane at elevated temperatures (cf. Fig. 8.9 (c) and (d)).

However, the width of the observed magnetic stripe domains of about 200 - 250 nm at 10 K is much larger than the periodicity of the structural domains (about 25 nm), determined by reciprocal space maps at room temperature.

---

[5] An elaborate structural x-ray study with further conclusions on the details of the structure of this sample was performed by Brajagopal Das and is currently prepared for publication (not shown here).

[6] Brajagopal Das combined XRD investigations with AFM surface topography scanning and SQUID magnetometry (not shown here) in order to investigate the miscut and confirmed that the periodic modulation indeed happens along the terraces.

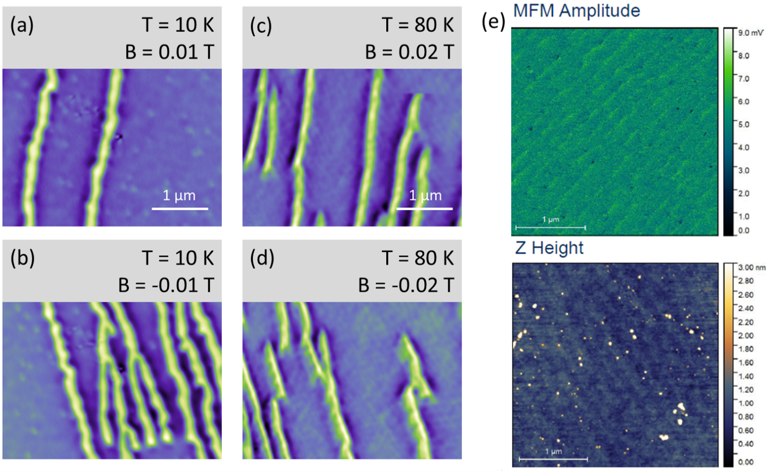

Figure 8.13: (a) - (d) Magnetic force microscopy scans of magnetic stripe domains formed during the hysteresis loops from positive to negative fields ((a) and (c)) and during the backward sweep ((b) and (d)) at 10 K ((a) - (b)) and 80 K ((c) - (d)). (e) MFM amplitude (upper panel) and corresponding topography image (lower scan) at room temperature in absence of an applied magnetic field.

In order to estimate whether the discrepancy originates from the possibility of temperature-induced change of the structural periodicity, magnetic force images were compared at various temperatures. Shown in Fig. 8.13 are MFM images presenting the formation of magnetic stripe domains of reversed orientation during the magnetic field sweeping. Displayed in Fig. 8.13 (e) is the (remanent) room-temperature MFM scan (upper panel) and the topography scan (lower panel), which was recorded with a commercially available AFM (*Park Systems*). The magnetic stripe domains observed at 80 K (Fig. 8.13 (c) and (d)) as well as the still barely visible stripe domains at room temperature still have a domain width of about 200 nm. Hence, the difference of the width of magnetic and structural domains is not related to the distinct temperatures at which the main MFM study and the reciprocal space mapping were conducted.

The origin of the observed discrepancy of the width of the magnetic domains and the structural domains cannot be pinpointed based on the presented data. Magnetic force microscopy studies of bare LSMO thin films, being imposed to compressive strain, demonstrated the formation of magnetic stripe domains without correlation with the film topography.[41,46] It was proposed that magnetostatic interactions account for the observed magnetic domain widths, which were of the order of the respective LSMO film thicknesses.[46] Similarly, it might be that the formation of magnetic stripes as narrow as 25 nm is energetically less favorable than the formation of domains of larger width. However, theoretical analysis, such as micromagnetic simulations, would be helpful in order to estimate the magnetic domain width for the thin film under study.

On the other hand, also the interaction between the magnetic MFM tip and the sample might influence the domain structure locally, as it was seen in other manganite thin films.[47] In order to shed light on this effect, magneto-optical imaging might be considered as a nonpeturpative probe to study the domain formation in such thin films. Alternatively, the MFM studies could be repeated with different magnetic tips that have smaller or larger coercive fields to investigate the influence of the magnetic interactions between the tip and the sample on the magnetic domain formation.

Generally, due to the strong coupling between structural, electronic, and magnetic properties in mixed-valence manganites, the seen unidirectional structural modification is expected to impact on both the magnetic and electronic characteristics of this ruthenium-substituted LSMO thin film. If the structure is unidirectionally distorted, this might also lead to unidirectional distortion of the crystal field of the oxygen octahedra. It thereby might impact on the Mn-O-Mn bond angle and Mn-O bond length, and thus on the exchange interaction. Such asymmetric exchange interaction was induced in LSMO by the deposition on orthorhombic $NdGaO_3$ (110) substrates.[3] Thus, the observed unidirectional anisotropy could possibly also explain the anisotropy of the longitudinal resistivities for the two orthogonal current directions as well as the different MR channels due to the interplay of the various contributions of anisotropic MR and domain wall resistance.

According to our MFM study, the magnetic stripe domains align mainly perpendicular to the substrate-induced terraces and thus mainly along MR_{yy}. In order to remove the main contribution of the anisotropic magnetoresistance, $0.5 \cdot (\Delta\rho_{xx} + \Delta\rho_{yy})$ was calculated, presented in Fig. 8.14 (a).

The sum of the two magnetoresistivities still contains the contribution of the colossal magnetoresistance as well as the domain wall resistance. Displayed in Fig. 8.14 (b) is the domain boundary length that was extracted from the MFM images, plotted versus the applied magnetic field.

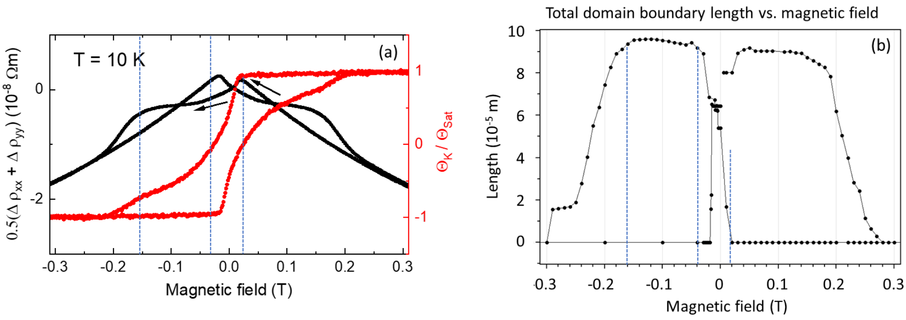

Figure 8.14: Magnetic field dependence of the sum of the two magnetoresistivity channels at 10 K (a). Shown in (b) is the total domain boundary length, extracted from the MFM images by Dr. Milde, as function of the magnetic field at 10 K.

As indicated by the blue lines, the hysteretic features in Fig. 8.14 (a) appear when the domain wall length increases, and shows only a weak field dependence when the domain wall length is almost constant. This emphasizes that the low field features in our MR measurements are indeed related to the domain wall resistance. However, in order to disentangle the domain wall resistance from the colossal magnetoresistance, the subtraction of the CMR, usually determined by linear fitting in the high magnetic field ranges,[1] would be required. Probably, larger magnetic fields are necessary at 10 K, since the overall magnetoresistance showed the expected negative slope of MR(B) only at higher temperatures or in one channel at 10 K, which might indicate that 12 T were insufficient to reach the magnetic field regime where the CMR dominates.

8.5 Conclusion and outlook

Anisotropic magnetoresistance with mirrorlike features for the two in-plane (orthogonal) current directions were observed in a 42.5 nm $La_{0.67}Sr_{0.33}Mn_{0.95}Ru_{0.05}$ thin film, when the magnetic field was applied perpendicular to the surface. This anisotropic MR could be correlated with the magnetic anisotropy of the sample which caused also the formation of parallel magnetic stripe domains, observed by magnetic force microscopy. The domain wall resistance was approximated by summing the two in-plane MR channels in order to remove the contribution from the anisotropic magnetoresistance. The preferential alignment of the magnetization with respect to one of the (in-plane) sample edges is possibly related to the formation of a unidirectional superlattice, indicated by RSM investigations. RSM and SQUID magnetometry of a twin sample confirmed the correlation between the orientation of preferential magnetization alignment and the crystallographic axes. To determine the details of the magnetic anisotropy, such as the exact orientation of the easy axis (in case of uniaxial anisotropy), angular dependent magnetization measurements are required. Referring to the temperature dependence of the magnetization, the in-plane anisotropy of the magnetization vanishes close to 250 K. Magnetoresistance measurements at and above 250 K could yield further information on the possible correlation between the observed anisotropy of the MR channels and the magnetic anisotropy.

In order to shed light on the observed discrepancy between the width of the structural and magnetic domains, structural investigations of the sample in its remanent state would be helpful to study a possible field-induced alignment of the structural domains. Furthermore, magneto-optical Kerr imaging might be considered as technique to exclude the possibility of interactions between the magnetic tip and the sample that influence the magnetic domain width during MFM measurements.

The presented MFM investigations are contrary to a previous study of Nakamura *et al.* on a 30 nm thick $La_{0.7}Sr_{0.3}Mn_{0.95}Ru_{0.05}O_3$ film,[6] who observed the formation of bubble-like objects in the magnetic field range when the magnetic stripe domains of alternating orientation split into smaller domains. This field range coincides with the region where hump-like contributions were seen in the Hall resistivity loop at 10 K.[6] However, we neither observed hump-like features in the Hall loop of the 42.5 nm $La_{0.67}Sr_{0.33}Ru_{0.05}Mn_{0.95}O_3$ thin film, nor clear indications of magnetic bubble-like domains that could be magnetic skyrmions. The discrepancy between the studied thin films might originate from the distinct thicknesses, as the magnetic anisotropy of this system is prone to thickness variations. Furthermore, as we have seen from the sample-to-sample variations, also different LSAT substrates might be a possible origin of the observed differences in the domain formation.

Acknowledgement and own contribution

The magnetic force microscopy study was performed by Dr. Dmytro Ivaneiko and Dr. Peter Milde. The reciprocal space mapping scans were acquired by Brajagopal Das and Dr. Lior Kornblum. The main sample under study was

deposited by Dr. Ionela Lindors-Vrejoiu, and the twin sample for structural investigations by Jörg Schöpf. The initial AFM was taken by Lin Yang. Furthermore, I want to thank Dr. Michael Ziese for fruitful discussions about the magnetoresistance measurements. Moreover I want to thank Lin Yang and Daniel Jansen for their important initial MOKE, Hall, and magnetoresistance investigations of a twin sample.

I performed the shown Hall, magnetoresistance, MOKE, and SQUID measurements, and made the corresponding analysis. The SQUID study was performed with kind assistance from Sven Ilse (MPI Stuttgart). The MOKE, Hall, and magnetoresistance measurements were performed with significant assistance from Jörg Schöpf. Furthermore, I want to thank Brajagopal Das and Dr. Lior Kornblum for their elaborate work on the structural investigations of this sample.

References

[1] P. Perna, D. Maccariello, F. Ajejas, R. Guerrero, L. Méchin, S. Flament, J. Santamaria, R. Miranda, and J. Camarero: *Engineering Large Anisotropic Magnetoresistance in* $La_{0.7}Sr_{0.3}MnO_3$ *Films at Room Temperature*, Advanced Functional Materials **27**, 1700664 (2017).

[2] B. Wang, L. You, P. Ren, X. Yin, Y. Peng, B. Xia, L. Wang, X. Yu, S. Mui Poh, P. Yang, G. Yuan, L. Chen, A. Rusydi, and J. Wang: *Oxygen-driven anisotropic transport in ultra-thin manganite films*, Nature Communications **4**, 2778 (2013).

[3] Z. Liao, M. Huijben, Z. Zhong, N. Gauquelin, S. Macke, R. J. Green, S. Van Aert, J. Verbeeck, G. Van Tendeloo, K. Held, G. A. Sawatzky, G. Koster, and G. Rijnders: *Controlled lateral anisotropy in correlated manganite heterostructures by interface-engineered oxygen octahedral coupling*, Nature Materials **15**, 425–431 (2016).

[4] Z. L. Liao, G. Koster, M. Huijben, and G. Rijnders: *Experimental evidence for anisotropic double exchange interaction driven anisotropic transport in manganite heterostructures*, Scientific Reports **7**, 2654 (2017).

[5] J. Wang, S. Wu, J. Ma, L. Xie, C. Wang, I. A. Malik, Y. Zhang, K. Xia, C.-W. Nan, and J. Zhang: *Nanoscale control of stripe-ordered magnetic domain walls by vertical spin transfer torque in* $La_{0.67}Sr_{0.33}MnO_3$ *film*, Applied Physics Letters **112**, 072408 (2018).

[6] M. Nakamura, D. Morikawa, X. Yu, F. Kagawa, T.-h. Arima, Y. Tokura, and M. Kawasaki: *Emergence of Topological Hall Effect in Half-Metallic Manganite Thin Films by Tuning Perpendicular Magnetic Anisotropy*, Journal of the Physical Society of Japan **87**, 074704 (2018).

[7] E. M. Pugh and N. Rostoker: *Hall Effect in Ferromagnetic Materials*, Reviews of Modern Physics **25**, 151 (1953).

[8] I. M. Dildar, C. Beekman, X. He, and J. Aarts: *Hall effect measurements on strained and unstrained thin films of* $La_{0.7}Ca_{0.3}MnO_3$ *and* $La_{0.7}Sr_{0.3}MnO_3$, Physical Review B **85**, 205103 (2012).

[9] W. E. Pickett and D. J. Singh: *Chemical disorder and charge transport in ferromagnetic manganites*, Physical Review B **55**, R8642–R8645 (1997).

[10] A. Asamitsu and Y. Tokura: *Hall effect in* $La_{1-x}Sr_xMnO_3$, Physical Review B **58**, 47–50 (1998).

[11] V. V. Mashkautsan, R. I. Zainullina, N. G. Bebenin, V. V. Ustinov, and Y. M. Mukovskii: *Hall Effect in* $La_{1-x}Sr_xMnO_3$ *Crystals*, Physics of the Solid State **45**, 494–498 (2003).

[12] L. M. Wang: *Anomalous Hall Effect in* $La_{0.7}Sr_{0.3}MnO_3/SrTiO_3$ *Superlattices: Hopping Transport and a Probe of Dimensionality*, Physical Review Letters **96**, 077203 (2006).

[13] D. Jansen: "Magneto-optical and Magneto-transport Investigations of Ru Substituted $\mathrm{La_{0.7}Sr_{0.3}MnO_3}$ Epitaxial Films", Bachelor thesis (University of Cologne, 2020).

[14] A. Soumyanarayanan, M. Raju, A. L. G. Oyarce, A. K. C. Tan, M. Y. Im, A. P. Petrović, P. Ho, K. H. Khoo, M. Tran, C. K. Gan, F. Ernult, and C. Panagopoulos: *Tunable room-temperature magnetic skyrmions in Ir/Fe/Co/Pt multilayers*, Nature Materials **16**, 898–904 (2017).

[15] J. E. Boschker, Å. F. Monsen, M. Nord, R. Mathieu, J. K. Grepstad, R. Holmestad, E. Wahlström, and T. Tybell: *In-plane structural order of domain engineered* $La_{0.7}Sr_{0.3}MnO_3$ *thin films*, Philosophical Magazine **93**, 1549–1562 (2013).

[16] L. Wysocki, J. Schöpf, M. Ziese, L. Yang, A. Kovács, L. Jin, R. B. Versteeg, A. Bliesener, F. Gunkel, L. Kornblum, R. Dittmann, P. H. M. van Loosdrecht, and I. Lindfors-Vrejoiu: *Electronic Inhomogeneity Influence on the Anomalous Hall Resistivity Loops of* $SrRuO_3$ *Epitaxially Interfaced with 5d Perovskites*, ACS Omega **5**, 5824–5833 (2020).

[17] https://www.hindsinstruments.com/products/photoelastic-modulators/ pem-100/pem-atc/, last accessed:03/04/22.

[18] W. L. V. Price: *Electric potential and current distribution in a rectangular sample of anisotropic material with application to the measurement of the principal resistivities by an extension of van der Pauw's method*, Solid-State Electronics **16**, 753–762 (1973).

[19] A.-M. Haghiri-Gosnet and J.-P. Renard: *CMR manganites: physics, thin films and devices*, J. Phys. D: Appl. Phys. **36**, R127 (2003).

[20] H. Boschker, M. Mathews, P. Brinks, E. Houwman, A. Vailionis, G. Koster, D. H. Blank, and G. Rijnders: *Uniaxial contribution to the magnetic anisotropy of* $La_{0.67}Sr_{0.33}MnO_3$ *thin films induced by orthorhombic crystal structure*, Journal of Magnetism and Magnetic Materials **323**, 2632–2638 (2011).

[21] S. W. Jin, G. Y. Gao, Z. Huang, Z. Z. Yin, X. Zheng, and W. Wu: *Shear-strain-induced low symmetry phase and domain ordering in epitaxial* $La_{0.7}Sr_{0.3}MnO_3$ *thin films*, Applied Physics Letters **92**, 261901 (2008).

[22] Z. Liao, M. Huijben, G. Koster, and G. Rijnders: *Uniaxial magnetic anisotropy induced low field anomalous anisotropic magnetoresistance in manganite thin films*, APL Materials **2**, 096112 (2014).

[23] S. Blügel, Lecture Notes, Ferienkurs Jülich 1999, title: Magnetische Schichtsysteme.

[24] L. Klein, Y. Kats, A. F. Marshall, J. W. Reiner, T. H. Geballe, M. R. Beasley, and A. Kapitulnik: *Domain Wall Resistivity in* $SrRuO_3$, Physical Review Letters **84**, 6090–6093 (2000).

[25] U. K. Sinha, B. Das, and P. Padhan: *Interfacial reconstruction in* $La_{0.7}Sr_{0.3}MnO_3$ *thin films: giant low-field magnetoresistance*, Nanoscale Advances **2**, 2792–2799 (2020).

[26] S. Kunkemöller, D. Brüning, A. Stunault, A. A. Nugroho, T. Lorenz, and M. Braden: *Magnetic shape-memory effect in* $SrRuO_3$, Physical Review B **96**, 220406(R) (2017).

[27] M. Granada, S. Bustingorry, D. E. Pontello, M. Barturen, M. Eddrief, M. Marangolo, and J. Milano: *Magnetotransport properties of* $Fe_{0.8}Ga_{0.2}$ *films with stripe domains*, Physical Review B **94**, 184435 (2016).

[28] B. Pianciola, S. Flewett, E. De Biasi, C. Hepburn, L. Lounis, M. Vásquez-Mansilla, M. Granada, M. Barturen, M. Eddrief, M. Sacchi, M. Marangolo, and J. Milano: *Magnetoresistance in* $Fe_{0.8}Ga_{0.2}$ *thin films with magnetic stripes:*

The role of the three-dimensional magnetic structure, Physical Review B **102**, 054438 (2020).

[29] W. Wang, L. Li, J. Liu, B. Chen, Y. Ji, J. Wang, G. Cheng, Y. Lu, G. Rijnders, G. Koster, W. Wu, and Z. Liao: *Magnetic domain engineering in* $SrRuO_3$ *thin films*, npj Quantum Materials **5**, 73 (2020).

[30] J. Z. Sun, W. J. Gallagher, P. R. Duncombe, L. Krusin-Elbaum, R. A. Altman, A. Gupta, Y. Lu, G. Q. Gong, and G. Xiao: *Observation of large low-field magnetoresistance in trilayer perpendicular transport devices made using doped manganate perovskites*, Applied Physics Letters **69**, 3266–3268 (1996).

[31] Y. Wu, Y. Suzuki, U. Rüdiger, J. Yu, A. D. Kent, T. K. Nath, and C. B. Eom: *Magnetotransport and magnetic domain structure in compressively strained colossal magnetoresistance films*, Applied Physics Letters **75**, 2295–2297 (1999).

[32] Y. Suzuki, Y. Wu, J. Yu, U. Ruediger, A. D. Kent, T. K. Nath, and C. B. Eom: *Domain structure and magnetotransport in epitaxial colossal magnetoresistance thin films*, Journal of Applied Physics **87**, 6746–6748 (2000).

[33] W. Niu, X. Wang, M. Gao, Z. Xia, J. Du, Y. Nie, F. Song, Y. Xu, and R. Zhang: *Unsaturated magnetoconductance of epitaxial* $La_{0.7}Sr_{0.3}MnO_3$ *thin films in pulsed magnetic fields up to 60 T*, AIP Advances **7**, 056404 (2017).

[34] B. Paudel, B. Zhang, Y. Sharma, K. T. Kang, H. Nakotte, H. Wang, and A. Chen: *Anisotropic domains and antiferrodistortive-transition controlled magnetization in epitaxial manganite films on vicinal* $SrTiO_3$ *substrates*, Applied Physics Letters **117**, 081903 (2020).

[35] G. Malsch, D. Ivaneyko, P. Milde, L. Wysocki, L. Yang, P. H. M. van Loosdrecht, I. Lindfors-Vrejoiu, and L. M. Eng: *Correlating the Nanoscale Structural, Magnetic, and Magneto-Transport Properties in* $SrRuO_3$*-Based Perovskite Thin Films: Implications for Oxide Skyrmion Devices*, ACS Applied Nano Materials **3**, 1182–1190 (2020).

[36] J. H. Ngai, T. C. Schwendemann, A. E. Walker, Y. Segal, F. J. Walker, E. I. Altman, and C. H. Ahn: *Achieving A-site termination on* $La_{0.18}Sr_{0.82}Al_{0.59}Ta_{0.41}O_3$ *substrates*, Advanced Materials **22**, 2945–2948 (2010).

[37] C. Kwon, M. C. Robson, K.-C. Kim, J. Y. Gu, S. E. Lofland, S. M. Bhagat, Z. Trajanovic, M. Rajeswari, T. Venkatesan, A. R. Kratz, R. D. Gomez, and R. Ramesh: *Stress-induced effects in epitaxial* $(La_{0.7}Sr_{0.3})MnO_3$ *films*, Journal of Magnetism and Magnetic Materials **172**, 229–236 (1997).

[38] J. Dho, Y. N. Kim, Y. S. Hwang, J. C. Kim, and N. H. Hur: *Strain-induced magnetic stripe domains in* $La_{0.7}Sr_{0.3}MnO_3$ *thin films*, Applied Physics Letters **82**, 1434–1436 (2003).

[39] J. Dho and N. H. Hur: *Thickness dependence of perpendicular magnetic anisotropy in* $La_{0.7}Sr_{0.3}MnO_3$ *films on* $LaAlO_3$, Journal of Magnetism and Magnetic Materials **318**, 23–27 (2007).

[40] T. W. Olson, J. M. W. Olson, A. Scholl, and Y. Suzuki: *Magnetic domain structure of colossal magnetoresistance thin films and islands*, Journal of Applied Physics **95**, 7354–7356 (2004).

[41] Y. Jiang, G. Y. Gao, Y. Wang, and H. L. W. Chan: *Temperature evolution of anisotropic stress induced highly ordered stripe magnetic domains in* $La_{0.7}Sr_{0.3}MnO_3$ *thin film on (110)* $NdGaO_3$ *substrate*, Solid State Communications **150**, 2028–2031 (2010).

[42] M. Liebmann, A. Schwarz, U. Kaiser, R. Wiesendanger, D.-W. Kim, and T.-W. Noh: *Magnetization reversal of a structurally disordered manganite thin film with perpendicular anisotropy*, Physical Review B **71**, 104431 (2005).

[43] E.-J. Guo, R. Desautels, D. Keavney, M. A. Roldan, B. J. Kirby, D. Lee, Z. Liao, T. Charlton, A. Herklotz, T. Z. Ward, M. R. Fitzsimmons, and H. N. Lee: *Nanoscale ferroelastic twins formed in strained* $LaCoO_3$ *films*, Science Advances **5**, eaav5050 (2019).

[44] D. Lan, P. Chen, C. Liu, X. Wu, P. Yang, X. Yu, J. Ding, J. Chen, and G. M. Chow: *Interfacial control of domain structure and magnetic anisotropy in* $La_{0.67}Sr_{0.33}MnO_3$ *manganite heterostructures*, Physical Review B **104**, 125423 (2021).

[45] T. F. Zhou, G. Li, X. G. Li, S. W. Jin, and W. B. Wu: *Self-generated in-plane superlattice in relaxed epitaxial* $La_{0.67}Sr_{0.33}MnO_3$ *films*, Applied Physics Letters **90**, 042512 (2007).

[46] M. Liebmann, U. Kaiser, A. Schwarz, R. Wiesendanger, U. H. Pi, T. W. Noh, Z. G. Khim, and D.-W. Kim: *Tilted magnetization of a* $La_{0.7}Sr_{0.3}MnO_3/LaAlO_3$ *(001) thin film*, Journal of Magnetism and Magnetic Materials **280**, 51–59 (2004).

[47] G. Jung, M. Indenbom, V. Markovich, C. J. van der Beek, D. Mogilyansky, and Y. M. Mukovskii: *Magneto-optics observation of spontaneous domain structure in ferromagnetic* $La_{0.78}Ca_{0.22}MnO_3$ *single crystal*, Journal of Physics: Condensed Matter **16**, 5461 (2004).

Part IV

Summary and outlook

Summary and outlook

This dissertation discusses the magnetic and magnetotransport properties of different perovskite oxide thin films. The focus lies on the ferromagnets strontium ruthenate and ruthenium-substituted lanthanum strontium manganite. Both materials are promising candidates in the view of the creation of topologically non-trivial structures, such as magnetic skyrmions. This originates from the possibility to modify the magnetic properties, such as the magnetic anisotropy, for instance by layer thickness variations and interfacial engineering.

After the first observation of hump-like features that resemble a topological Hall effect in $SrRuO_3$-$SrIrO_3$ bilayers, several studies aimed to unravel the origin of these anomalies. If skyrmions indeed form in such $SrRuO_3$-$SrIrO_3$ heterostructures, the magnetic coupling between the magnetic layers will be of particular relevance, since the coupling of the skyrmions across the multilayer stack would be desirable. This question was addressed in the framework of the thesis by the artificial design and investigation of $SrRuO_3$-$SrIrO_3$ heterostructures. For 2 MLs thick insulating spacer, only very weak coupling between the individual magnetic $SrRuO_3$ layers was observed, whereas no coupling was observed for thicker $SrIrO_3$ spacers. Such magnetic decoupling of the $SrRuO_3$ is undesirable in the view of the coupling of skyrmions across the multilayer stack. Thus, alternative perovskite oxides should be considered as spacer materials in order to achieve ferromagnetic coupling of the $SrRuO_3$ layers. Since enhanced ferromagnetic coupling was observed when the $SrRuO_3$ layers were separated by metallic $LaNiO_3$ spacers, a similar heterostructure design with strong spin-orbit coupled, but metallic spacers might be of future research interest.

Due to the experimental challenges in the imaging of nanosized skyrmions, Hall effect measurements are frequently used to detect fingerprints of magnetic skyrmions. When conduction electrons get scattered by skyrmions, the topological Hall effect (THE) can be detected with technically simple experimental

set-ups. However, it is problematic that also other phenomena, such as multiple, parallel (anomalous) Hall channels, can generate features that resemble a topological Hall effect. This issue was emphasized by different examples within this thesis.
The magnetic force microscopy (MFM) study of an ultrathin $SrRuO_3$-$SrIrO_3$ bilayer, capped by $SrZrO_3$, showed that peak-like features can be observed in Hall measurements without the existence of skyrmions. The MFM investigations revealed variations of the local layer thickness and corresponding differences of the switching fields in a bare $SrRuO_3$ thin film. These thickness variations were also seen in the trilayer and expected to lead to band structure variations of the anomalous Hall constant. Within the model of multiple anomalous Hall channels, these local variations of switching field and AHE constant can explain the THE-like features.

It was demonstrated in a second study that hump-like anomalies can be generated in the Hall loops in $SrRuO_3$-based heterostructures, when the individual $SrRuO_3$ layers possess distinct switching fields and anomalous Hall constants. For this purpose, heterostructures with two $SrRuO_3$ layers of different thickness and therefore with different anomalous Hall constants and coercive fields were investigated. Here, the total Hall voltage can be written as the sum of the Hall voltages of the individual layers. This emphasizes that the conclusion about the presence of skyrmions based on transport measurements only, can be faulty. This further highlights the importance of techniques that are capable to proof the existence of skyrmions, such as real space imaging.

In the second part of this dissertation, ruthenium-substituted lanthanum strontium manganite ($La_{0.67}Sr_{0.33}Mn_{0.95}Ru_{0.05}O_3$) films, grown under moderate compressive strain on LSAT(100) substrates, were investigated. A nonmonotonic dependence of the magnetic anisotropy on the layer thickness was observed and attributed to the distinct temperature dependencies of the individual contributions of the magnetic anisotropy.
Finally, strong in-plane anisotropic magnetoresistance was seen in a 42.5 nm $La_{0.67}Sr_{0.33}Mn_{0.95}Ru_{0.05}O_3$ thin film deposited on LSAT(100). This anisotropic magnetoresistance, with mirrorlike features for the two orthogonal current directions, could be related with the magnetic anisotropy. The macroscopic magnetic behavior is in good agreement with the formation of parallel magnetic stripe domains, which were observed in a magnetic force microscopy study.

The preferential alignment of the magnetic stripe domains furthermore explained the current-direction dependent contribution of magnetic domain wall resistance to the overall magnetoresistance. However, the understanding of the connection between the size and orientation of the magnetic stripe domains and the structural domains still needs to be improved.

In contrast to the investigated $SrRuO_3$ films which typically show strong perpendicular magnetic anisotropy, when it is interfaced with $SrIrO_3$ or $SrZrO_3$, the $La_{0.67}Sr_{0.33}Mn_{0.95}Ru_{0.05}O_3$ films under study possessed a weak magnetic anisotropy with preferential magnetization alignment perpendicular to the thin film surface in a thickness-dependent temperature range. This is promising in the view of the tailoring of the magnetic state by small distortions of the (magnetic) energetic balance by modifications of the heterostructure design. The interfacing of Ru-substituted LSMO layers with a strong spin-orbit coupling material, such as $SrIrO_3$, is therefore a possibility that might stabilize magnetically non-trivial structures and is considered as promising research topic in the future.

Kurzzusammenfassung und Ausblick

Diese Dissertation behandelt die magnetischen und magneto-elektrischen Eigenschaften verschiedener oxidischer Perovskitdünnschichtsysteme. Hierbei liegt der Fokus auf den zwei Ferromagneten Strontium Ruthanat sowie Rutheniumsubstituiertem Lanthanum Strontium Manganat. Beide Materialien sind vielversprechende Kandidaten im Hinblick auf die Erzeugung topologisch nicht-trivialer Strukturen, wie z.B. magnetischer Skyrmionen. Dies ist dadurch bedingt, dass die magnetischen Eigenschaften, wie beispielweise die magnetische Anisotropie, durch Schichtdickenvariation oder Modifikation der Grenzflächen kontrolliert werden können.

Nach der ersten Beobachtung von Peaks in den Hallmessungen von $SrRuO_3$-$SrIrO_3$ Bilagen, die einem topologischen Halleffekt ähnelten, wurden viele Studien durchgeführt, die den Ursprung dieser Peaks evaluieren wollten.

Unter der Annahme, dass tatsächlich Skyrmionen in diesem System erzeugt werden können, ist die magnetische Kopplung der Skyrmionen innerhalb der Heterostruktur im Hinblick auf potentielle Anwendungsmöglichkeiten essenziell. Die Thematik der Stärke der magnetischen Kopplung der einzelnen Lagen wurde im Rahmen dieser Dissertation betrachtet. Hierfür wurden asymmetrische $SrRuO_3$-$SrIrO_3$ Heterostrukturen hergestellt und im Hinblick auf ihre magnetischen Eigenschaften untersucht. Trotz der geringen Dicke der trennenden $SrIrO_3$ Schicht konnte nur eine sehr geringe (antiferromagnetische) Kopplung der Strontium Ruthanat Schichten realisiert werden. Da dies im Hinblick auf die bevorzugte Kopplung der Skyrmionen innerhalb der Heterostruktur nicht gewünscht ist, sollten andere Materialen als mögliche Trennschicht betrachtet werden. Die erfolgreiche ferromagnetische Kopplung der Strontium Ruthanat Schichten durch metallisches $LaNiO_3$ könnte hierbei als erster Anhaltspunkt gewählt werden, sodass zukünftig metallische Trennschichten, die zusätzlich eine starke Spin-Bahn Kopplung besitzen sollten, untersucht werden können.

Bei der Detektion von magnetischen Skyrmionen, dessen experimentelle Darstellung aufgrund ihrer Größe im Nanometerbereich herausfordernd ist, haben Hall-Messungen eine besondere Bedeutung. In Anwesenheit von Skyrmionen werden die Leitungselektronen durch das skyrmiongenerierte Magnetfeld abgelenkt, was einen zusatzlichen Beitrag in den Hall-Messungen erzeugt, den sogenannten topologischen Hall-Effekt. Problematisch ist hierbei, dass Beiträge, die einem topologischen Hall-Effekt ähneln, auch durch andere Phänomene wie z.B. multipel anomale Hall-Kanäle generiert werden können. Dies konnte im Rahmen dieser Thesis anhand mehrerer Beispiele gezeigt werden. In ultradünnen gecappten $SrRuO_3$-$SrIrO_3$ Bilagen verdeutlichte unsere Magnetic Force Microscopy Studie, dass peakähnliche Strukturen in Hall-Messungen auch ohne die Existenz von Skyrmionen beobachtet werden können. Weiterhin wurden lokale Variationen in der Schichtdicke der Strontium Ruthanat-Lage entdeckt, die zu lokal verschiedenen Koerzitivfeldern sowie vermutlich unterschiedlichen anomomalen Hall-Konstanten geführt haben. Im Rahmen des Modells der verschiedenen anomalen Hall-Kanäle kann dies die beobachteten Anomalien erklären.

In einer weiteren Studie konnten wir zeigen, dass peakähnliche Strukturen in den Hall-Messungen von Heterostrukturen gezielt erzeugt werden können, wenn die einzelnen $SrRuO_3$ Lagen verschiedene Koerzitivfelder und anomale Hall-Konstanten besitzen. Hierzu wurden wiederum asymmetrische Heterostrukturen betrachtet, die zwei ferromagnetische $SrRuO_3$ Schichten mit unterschiedlichen magnetischen und Hall Eigenschaften besaßen. Die effektiv gemessene Hallspannung konnte hierbei als Summe der beiden einzelnen Schichten dargestellt werden. Die hierbei entdeckten, scharfen Peaks in den Hall-Messungen konnten so auf die Existenz mehrerer Kanäle und nicht auf die Existenz von Skyrmionen zurückgeführt werden. Damit konnte gezeigt werden, dass die finale Schlussfolgerung der Existenz von Skyrmionen ausschließlich basierend auf Hall-Messungen nicht hinreichend ist. Die Ergebnisse verdeutlichen weiterhin die Relevanz von Messmethoden, die Skyrmionen tatsächlich nachweisen können, wie z.B. bildgebende Verfahren im Realraum.

In einem weiteren Kapitel dieser Thesis wurden Ruthenium-substituierte Lanthanum Strontium Manganat $La_{0.67}Sr_{0.33}Mn_{0.95}Ru_{0.05}O_3$ Dünnschichten untersucht. Diese zeigten eine nichtmonotone Schichtdickenabhängigkeit der magnetischen Anisotropie aufgrund der verschiedenen Temperaturabhängkeiten der einzelnen Beiträge zur magnetischen Anisotropie. Weiterhin wurde in einem 42.5 nm dicken $La_{0.67}Sr_{0.33}Ru_{0.05}Mn_{0.95}O_3$ Film, der auf LSAT unter epitaktischer, biaxialer, kompressiver Spannung gewachsen wurde, ausgeprägte Anisotropie des Magnetotransports in der Filmebene beobachtet. Dieser anisotrope Magnetowiderstand für die zwei orthogonalen Stromrichtungen konnte auf die magnetische Anisotropie in der Filmebene zurückgeführt werden. Das makroskopische magnetische Verhalten ist hierbei in guter Übereinstimmung mit der Bildung magnetischer Streifendomänen, die im Rahmen unserer MFM Studie beobachtet wurden. Die bevorzugte Ausrichtung der parallen Streifendomänen erklärt außerdem die Existenz des stromrichtungsabhängigen Beitrags des Domänenwandwiderstands zum gesamten Magnetowiderstand.

Während die untersuchten Strontium Ruthanat Filme typischerweise eine starke senkrechte magnetische Anisotropie zeigten, wenn sie Grenzflächen mit $SrIrO_3$ oder $SrZrO_3$ besaßen, zeigten die untersuchten Ruthenium-substituierten LSMO Filme eine vergleichsweise geringe senkrechte magnetische Anisotropie, die temperatur- und schichtdickenabhängig war. Dies ist im Hinblick auf die mögliche Steuerung der magnetischen Struktur vielversprechend. Die Ergebnisse machen Hoffnung, dass die magnetische Anisotropie durch kleine Modifikationen der Heterostruktur modifiziert werden kann. Das Grenzflächenengineering mit $SrIrO_3$ ist hierbei als Möglichkeit für zukünftige Forschungen zu erwähnen, da an der Grenzfläche mit dem Spin-Bahn gekoppelten Material, eventuell eine Dzyaloshinskii–Moriya Wechselwirkung induziert werden könnte.

List of Figures

Publications and preprints

The publications marked with an (*) are addressed within this thesis.

- Xuanyi Zhang, Aubrey N. Penn, **Lena Wysocki**, Zhan Zhang, Paul H. M. van Loosdrecht, Lior Kornblum, James M. LeBeau, Ionela Lindfors-Vrejoiu, Divine P. Kumah, Thickness and temperature dependence of the atomic-scale structure of $SrRuO_3$ thin films, APL Materials **10**, 051107 (2022)
- **Lena Wysocki**, Sven Erik Ilse, Lin Yang, Eberhard Goering, Felix Gunkel, Regina Dittmann, Paul H.M. van Loosdrecht, Ionela Lindfors-Vrejoiu, Magnetic interlayer coupling between ferromagnetic $SrRuO_3$ layers through a $SrIrO_3$ spacer, Journal of Applied Physics **131**, 133902 (2022).
- Julian Wagner, Anuja Sahasrabudhe, Rolf B. Versteeg, **Lena Wysocki**, Zhe Wang, Vladimir Tsurkan, Alois Loidl, Daniel I. Khomskii, Hamoon Hedayat, and Paul H. M. van Loosdrecht, Magneto-optical study of metamagnetic transitions in the antiferromagnetic phase of α-$RuCl_3$, npj quantum materials **7**, nr.28 (2022)
- Lin Yang, Lei Jin, **Lena Wysocki**, Jörg Schöpf, Daniel Jansen, Brajagopal Das, Lior Kornblum, Paul H. M. van Loosdrecht, and Ionela Lindfors-Vrejoiu, Enhancing the ferromagnetic interlayer coupling between epitaxial $SrRuO_3$ layers, Physical Review B **104**, 064444 (2021)
- Lin Yang, **Lena Wysocki**, Jörg Schöpf, Lei Jin, András Kovács, Felix Gunkel, Regina Dittmann, Paul H. M. van Loosdrecht, and Ionela Lindfors-Vrejoiu, Origin of the hump anomalies in the Hall resistance loops of ultrathin $SrRuO_3$/$SrIrO_3$ multilayers, Phys. Rev. Mat. **5**, 014403 (2021)
- Yannic Falke, Boris V. Senkovskiy, Niels Ehlen, **Lena Wysocki**, Tomas Marangoni, Rebecca A. Durr, Alexander I. Chernov, Felix R. Fischer, and Alexander Grüneis, Photothermal Bottom-up Graphene Nanoribbon Growth Kinetics, Nano Lett. **20**, 4761-4767 (2020)

- **Lena Wysocki**, Lin Yang, Felix Gunkel, Regina Dittmann, Paul H. M. van Loosdrecht, and Ionela Lindfors-Vrejoiu, Validity of magnetotransport detection of skyrmions in epitaxial $SrRuO_3$ heterostructures, Phys. Rev. Mat. **4**, 054402 (2020) (*)

- **Lena Wysocki**, Jörg Schöpf, Michael Ziese, Lin Yang, András Kovács, Lei Jin, Rolf B. Versteeg, Andrea Bliesener, Felix Gunkel, Lior Kornblum, Regina Dittmann, Paul H. M. van Loosdrecht, and Ionela Lindfors-Vrejoiu, Electronic Inhomogeneity Influence on the Anomalous Hall Resistivity Loops of $SrRuO_3$ Epitaxially Interfaced with 5d Perovskites, ACS Omega **11**, 5824-5833 (2020)

- Gerald Malsch, Dmytro Ivaneyko, Peter Milde, **Lena Wysocki**, Lin Yang, Paul H. M. van Loosdrecht, Ionela Lindfors-Vrejoiu, and Lukas M. Eng, Correlating the Nanoscale Structural, Magnetic, and Magneto-Transport Properties in $SrRuO_3$-Based Perovskite Thin Films: Implications for Oxide Skyrmion Devices, ACS Applied Nano Materials **3**, 1182-1190 (2020) (*)

- **Lena Wysocki**, Ramil Mirzaaghayev, Michael Ziese, Lin Yang, Jörg Schöpf, Rolf B. Versteeg, Andrea Bliesener, Johannes Engelmayer, András Kovács, Lei Jin, Felix Gunkel, Regina Dittmann, Paul H. M. van Loosdrecht, and Ionela Lindfors-Vrejoiu; Magnetic coupling of ferromagnetic $SrRuO_3$ epitaxial layers separated by ultrathin non-magnetic $SrZrO_3$/ $SrIrO_3$, Applied Physics Letters **113**, 192402 (2018)

Erklärung zur Dissertation gemäß der Promotionsordnung vom 12. März 2020

„Hiermit versichere ich an Eides statt, dass ich die vorliegende Dissertation selbstständig und ohne die Benutzung anderer als der angegebenen Hilfsmittel und Literatur angefertigt habe. Alle Stellen, die wörtlich oder sinngemäß aus veröffentlichten und nicht veröffentlichten Werken dem Wortlaut oder dem Sinn nach entnommen wurden, sind als solche kenntlich gemacht. Ich versichere an Eides statt, dass diese Dissertation noch keiner anderen Fakultät oder Universität zur Prüfung vorgelegen hat; dass sie - abgesehen von unten angegebenen Teilpublikationen und eingebundenen Artikeln und Manuskripten - noch nicht veröffentlicht worden ist sowie, dass ich eine Veröffentlichung der Dissertation vor Abschluss der Promotion nicht ohne Genehmigung des Promotionsausschusses vornehmen werde. Die Bestimmungen dieser Ordnung sind mir bekannt. Darüber hinaus erkläre ich hiermit, dass ich die Ordnung zur Sicherung guter wissenschaftlicher Praxis und zum Umgang mit wissenschaftlichem Fehlverhalten der Universität zu Köln gelesen und sie bei der Durchführung der Dissertation zugrundeliegenden Arbeiten und der schriftlich verfassten Dissertation beachtet habe und verpflichte mich hiermit, die dort genannten Vorgaben bei allen wissenschaftlichen Tätigkeiten zu beachten und umzusetzen. Ich versichere, dass die eingereichte elektronische Fassung der eingereichten Druckfassung vollständig entspricht."

Teilpublikationen

- Gerald Malsch, Dmytro Ivaneyko, Peter Milde, **Lena Wysocki**, Lin Yang, Paul H. M. van Loosdrecht, Ionela Lindfors-Vrejoiu, and Lukas M. Eng, Correlating the Nanoscale Structural, Magnetic, and Magneto-Transport Properties in $SrRuO_3$-Based Perovskite Thin Films: Implications for Oxide Skyrmion Devices, ACS Applied Nano Materials **3**, 1182-1190 (2020)

- **Lena Wysocki**, Lin Yang, Felix Gunkel, Regina Dittmann, Paul H. M. van Loosdrecht, and Ionela Lindfors-Vrejoiu, Validity of magnetotransport detection of skyrmions in epitaxial $SrRuO_3$ heterostructures, Phys. Rev. Mat. **4**, 054402 (2020)
- **Lena Wysocki**, Sven Erik Ilse, Lin Yang, Eberhard Goering, Felix Gunkel, Regina Dittmann, Paul H.M. van Loosdrecht, Ionela Lindfors-Vrejoiu, Magnetic interlayer coupling between ferromagnetic $SrRuO_3$ layers through a $SrIrO_3$ spacer, Journal of Applied Physics **131**, 133902 (2022)

Die im Zuge dieser Dissertation gemessenen Daten und deren Analysen sind auf den Servern des II. Physikalischen Instituts im Ordner \\files \AGPvL \Lena gespeichert. Zusätzliche Daten, die im Rahmen der Promotion aufgenommen wurden, wurden auf DVD gespeichert und an Dr. Lindfors-Vrejoiu übergeben.

Lena Wysocki
Köln, den 19.12.2022

Acknowledgment

Without the support and help of many extraordinary people, this thesis could not have been accomplished. I want to thank everybody who supported me during my phd time, by scientific discussions, technical help, advice, and guidance.

First, I want to thank Prof. Paul van Loosdrecht for giving me the opportunity to work in his research group. With his enthusiasm for physics and research, he set up a great example and motivated me to always give my best.

I want to thank Dr. Ionela Lindfors - Vrejoiu for the extraordinary direct supervision of my thesis, for giving me the opportunity to focus my research on highly actual materials and topics, and for her guidance during the project. I am thankful for everything that she has taught me, especially that I had the chance to learn the epitaxial oxide thin film growth by PLD from her, one of the world-wide experts in the field. Furthermore, I want to thank her for giving me the opportunity to present our work on many (international) conferences.

Special thanks go to the members of my dissertation committee: Prof. Kathrin Dörr for being the second reviewer of this thesis, Prof. Jan Jolie for taking over the committee chair, and Dr. Andrea Bliesener for being the minutes-taker.

During the last years, I was given the chance to work with many outstanding scientists, not only from the University of Cologne, but from several research facilities. I enjoyed the successful scientific collaboration with Prof. Lior Kornblum and Brajagopal Das from the Technion-Israel Institute of Technology. I also appreciate the great cooperation we had with the magnetic force microscopy group of Dr. Peter Milde, together with Dr. Dmytro Ivaneyko, and Gerald Malsch from the Technical University of Dresden. I want to thank Prof. Regina Dittmann, Dr. Felix Gunkel, and their students for the support and the opportunity to grow my thin films in their laboratory as well as the ongoing fruitful collaboration on $SrRuO_3$ thin films. Furthermore, I want to thank Prof. Michael Ziese for his support and insights into the broad topic of the techniques and understanding of SQUID magnetometry and magnetotransport. I want to thank Dr. András Kovács and Dr. Lei Jin for their dedication for high quality STEM and TEM investigations of our epitaxial heterostructures.

I want to thank Sven Ilse and Dr. Eberhard Goering for our great project on FORC investigations of the magnetic interlayer coupling. Additionally, I am very grateful for their help with SQUID magnetometry in the Max Planck Institute for Intelligent Systems, when our own instrument broke down for several weeks.
Furthermore, I want to thank Prof. Divine Kumah for the collaboration on high resolution XRD measurements of $SrRuO_3$ films. I would like to thank Dr. Marjana Ležaić, Prof. Yuriy Mokrousov, Dr. Kartik Samanta, and Prof. Stefan Blügel for providing theoretical understanding of the Hall effect phenomena in $SrRuO_3$ crystals and ultrathin films, as well as ideas on future projects.
I am very grateful to all my colleagues from the AG-PvL, especially to my "office-mates" Chris Reinhoffer, Julian Wagner, Semyon Germanskiy (and previously Dr. Yu Mukai, Dr. Fumiya Sekiguchi, and Suqin He). I want to thank you for the good time together during the last years! A special thanks goes to my colleagues from our small subgroup: Lin Yang, Jörg Schöpf, Ramil Mirzaaghayev, and Daniel Jansen. I enjoyed all the time we spent together on beamtimes, inside and outside of the labs.
I am thankful that I had the opportunity to work with and share the experiences of a PhD with great colleageaus also from other research groups. I would like to thank Dr. Johannes Engelmayer, Dr. Christoph Grams, Thomas Schunk-Born, and Prof. Thomas Lorenz for their help with magnetotransport measurements. I want to thank Dr. Andrea Bliesener for her scientific support with atomic force microscopy, spincoating, and transport measurements, but also mental guidance and motivation.

I further want to thank the many people working "in the background", without whom the research work would not be possible. I am very grateful for the technical help from Jens Koch and Timur Zent, for the help from the technical and electrical workshop. I am grateful that Rolf Dommel, Dr. Harald Kierspel and the rest of the helium-team ensured the continuous supply of liquid helium, even during the official holidays and weekends. I want to thank also Susanne Heijligen for her "24/7-support" in the SQUID lab.
A special thanks goes to Dr. Ralf Müller. I can call myself lucky that I had the chance to do my internship in our institute in 2010, supervised by Ralf. Without this great experience, I am sure that I would not have studied physics in Cologne.

Die letzten Worte dieser Danksagung möchte ich den wichtigsten Menschen in meinem Leben widmen, meinem Partner, meiner Familie und meinen Freunden. Danke für die Unterstützung an jedem einzelnen Tag dieser Promotion, danke für Euer Verständnis und die emotionale Unterstützung auch in schwierigen Zeiten! Ohne Euch wäre diese Arbeit nicht möglich gewesen.